Coherent Terahertz Control and Ultrafast Spectroscopy of Layered Antiferromagnets

by

Batyr Ilyas

B.S. Physics, Nazarbayev University, 2017

Submitted to the Department of Physics
in partial fulfillment of the requirements for the degree of

DOCTOR OF PHILOSOPHY

at the

MASSACHUSETTS INSTITUTE OF TECHNOLOGY

September 2024

© 2024 Batyr Ilyas. All rights reserved.

The author hereby grants to MIT a nonexclusive, worldwide, irrevocable, royalty-free license to exercise any and all rights under copyright, including to reproduce, preserve, distribute and publicly display copies of the thesis, or release the thesis under an open-access license.

Authored by:	Batyr Ilyas Department of Physics August 16, 2024
Certified by:	Nuh Gedik Professor of Physics, Thesis Supervisor
Accepted by:	Lindley Winslow Professor of Physics Associate Department Head of Physics

Coherent Terahertz Control and Ultrafast Spectroscopy of Layered Antiferromagnets

by

Batyr Ilyas

Submitted to the Department of Physics
on August 16, 2024 in partial fulfillment of the requirements for the degree of

DOCTOR OF PHILOSOPHY

ABSTRACT

The central theme of modern condensed matter physics is to understand the emergent phenomena arising from interactions among Avogadro's number of particles in quantum materials, alongside efforts to control their properties. While powerful transport, thermodynamic, and spectroscopic tools have been developed, they often fall short to reveal the intricate interplay among electronic, spin, orbital, and lattice degrees of freedom. A promising approach involves selectively perturbing one degree of freedom while observing responses in others, made possible by ultrafast lasers with femtosecond time resolution. These advancements not only showcase the capability of ultrafast experiments in understanding complex material properties but also demonstrate the manipulation of ordered phases at ultrafast timescales, thereby opening a laboratory for studying materials in nonequilibrium regime.

This dissertation contributes to the ongoing effort of developing new ultrafast spectroscopy tools, utilizing them to probe lattice, magnetic, and electronic properties, and gaining active control over them. Specifically, it investigates the induction of a new magnetic state with net magnetization using intense low-energy terahertz (THz) pulses in the van der Waals antiferromagnet $FePS_3$. Critical fluctuations near the phase transition are found to enhance both the magnitude and the lifetime of this new state. Additionally, a broadband two-dimensional (2D) THz spectroscopy technique is developed and employed to study interactions among low-energy collective excitations and to directly identify phonons that induce the new magnetic phase. Furthermore, time-resolved spectroscopy in the visible and near-infrared spectral range is utilized to detect a bound state between phonon and electronic states in the sister compound $NiPS_3$, and to capture a magnetostriction effect in $FePS_3$ using coherent phonon spectroscopy, that was elusive to conventional diffraction experiments. Finally, second harmonic generation spectroscopy with microscale spatial resolution, is employed to study the multiferroic material NiI_2, demonstrating its persistence down to the single atomic layer — a first of its kind.

These findings and tools can potentially be extended to frustrated quantum magnets to control their magnetic phases and potentially detect their collective modes. The 2D nonlinear spectroscopy utilized in this dissertation is gaining attention both theoretically and experimentally as a promising tool for detecting fractionalized spin excitations.

Thesis supervisor: Nuh Gedik
Title: Professor of Physics

Acknowledgments

First and foremost, I would like to express my deepest appreciation to Professor Gedik for all the guidance and support he has provided me. Nuh is a brilliant physicist with a profound understanding of the current frontiers of condensed matter physics, and knows down to the minute technical details of our experiments. I felt comfortable approaching him with any questions I had. At the same time, he always respects the project ideas we proposed and the solutions we suggested to certain issues in our projects. His trust in the group members instilled a confidence in ourselves, which I now recognize as a great way of nurturing future scientists. Whenever he noticed that our proposals, ideas, or interpretations of the data seemed off, he would gently ask us few questions. For example, he often said, *"This might be unlikely, but what if such and such a scenario is taking place instead?"* It would sometimes take me days to answer or to realize my flaws. Nuh has a unique approach to tackling pressing questions in current condensed matter topics, always seeking innovative experimental tools to solve long-standing problems. I hope to carry this approach into my future research endeavors. Besides being a great scientist, Nuh has an endearing and humble personality and radiates an aura of kindness. I learned a lot from Nuh not only during our discussions but also by observing how he resolved issues and interacted with others. He sincerely cares about each and every member of the group and is always ready to help, particularly with their future careers.

I extend my gratitude to Prof. Riccardo Comin and Prof. Martin Zwierlein for serving on my committee. During my initial years in graduate school, I audited two of Martin's courses and learned fundamental topics in light-matter interaction, which were directly relevant to my studies. His enthusiasm for science is truly inspiring and ignites interest in anyone he teaches. Riccardo has always been available for discussing physics or offering career advice. I had the opportunity to join a remarkable project initiated by him, which yielded excellent results. I am also very grateful for his support during my postdoc application period and for guiding me towards promising research directions and labs.

Prior to coming to MIT, I did not have any experimental experience. In retrospect, I can now appreciate Nuh's wisdom in allowing me to work with Emre Ergecen and Mehmet Burak Yilmaz. I feel incredibly fortunate to have learned from such masters of their trades and deeply value their mentorship. Emre is a brilliant individual with a unique approach to experiments, always brimming with smart and novel ideas. He knows a lot of tricks in optics and ultrafast experiments and knows how to apply these tools to modern problems in condensed matter physics. Mehmet is a wise person with a great personality. He was always happy to teach me fundamental skills, whether it was coding tricks in Python or designing clean and clever projects in LabView. Mehmet's mentorship was invaluable during the early

and most crucial stages of my PhD journey.

In the later part of my studies, I had the honor of working with Michael (Tianchuang) Luo, an exceptionally talented individual skilled in every aspect of experimental science. At the beginning of our collaboration, I was concerned that I might not be able to be a good mentor to a first-year graduate student. However, Michael quickly proved that my worries were unnecessary. He was already well-trained in many areas. In fact, I learned a great deal from him, including contemporary topics in solid state physics, coding in LabView, machining, and simulations. Together, we built a new setup for intense terahertz excitation and two-dimensional THz spectroscopy, which turned out to be a highly productive tool. Later, Jack (John) Maier joined our team, bringing motivation and talent. Jack is unafraid of any challenges and always thinks outside the box, coming up with original solutions. The whitelight microscopy setup is undoubtedly in great hands with him.

With the arrival of new postdocs to the lab, I had the opportunity to collaborate with Alex von Hoegen and Honglie Ning. Both of them taught me many things, including topics in nonlinear phononics and symmetry analysis. After each of our conversations, I came away with new knowledge or corrected misunderstandings.

I would like to thank Bryan Fichera and Dongsung Choi. The three of us started in the Gedik lab around the same time, learning many things together, from problem sets of 8.511 to handling the various challenges of graduate school as young researchers. I will cherish our hangouts and the single badminton game we played together. Bryan has always amazed me with his knack for automating experiments and the skills he has in doing so. Dongsung is one of the kindest people in the lab, always ready to help and who also shouldered the responsibility of the tr-ARPES setup. I also had an extended overlap with Cliff Allington and Yifan Su in the lab, who are experts in a broad range of topics. Cliff has a great personality and a wonderful sense of humor, and we could quickly agree on matters such as sharing laser beam time or other instruments. Yifan is one of the rare people with whom I could discuss about soccer. And all five of us are departing the group about the same time.

I want to thank our group's senior students, Changmin Lee, Ozge Ozel, Alfred Zong, and Carina Belvin, who made the Gedik lab a very welcoming space for us. They were always ready to provide their support and expert opinions on technical matters. Alfred has been a source of inspiration during our time together in the lab. His work ethic, immense knowledge, and his pleasant way of interacting with others have always reminded me of the room for improvement in myself. I am also thankful to our former postdocs in the lab: Zhanybek Alpichshev, Tim Rohwer, Nikesh Koirala, Anshul Kogar, Suyang Xu, Edoardo Baldini, Baiqing Lyu, Masataka Mogi, and Doron Azoury. Most of them are now professors and have started their own labs, while others are working in leading industry fields. I could approach any of them with my questions or for career advice. I used to hear about Zhanybek since my high school days; he inspired many young scientists in Kazakhstan. Later, I had the opportunity to discuss research topics with him, and anyone who speaks with him immediately realizes his high standards for research projects and his vast knowledge, not only in physics but also in history, philosophy, and other branches of natural sciences.

The beauty of working in the Gedik lab lies in the diverse skills and knowledge that each person brings, providing continuous opportunities for learning. The younger generation of students in the lab — Kyoung Hun Oh, Zongqi Shen, Tommy Tai, and Haoyu Xia — alongside current postdocs Jacob Pettine and Shuyu Cheng, have infused the lab with a new

wave of ideas and enthusiasm. They are poised to tackle new big questions.

The second floor of Building 13 is a hub of condensed matter experimental research, where new big discoveries occur almost every week or month. I am grateful to Professors Riccardo Comin, Joseph Checkelsky, Long Ju, Raymond Ashoori, and Pablo Jarillo Herrero for creating an exceptional scientific environment and serving as role models and sources of inspiration. They have been incredibly open and supportive, providing invaluable guidance during my PhD and as I transitioned into postdoctoral studies. I had the privilege to collaborate with Qian Song and Connor Occhialini from the Comin lab, who were always ready to assist us with Raman and other experimental techniques. Denis Bandurin, Tonghang Han, Jixiang Yang, and Junseok Seo were always willing to help with device fabrication, wire bonding, or just chat about science. Monica Wolf, Lars Llorente, and Gerry Miller would always find time to assist us with reimbursements, travel arrangements, and room reservations. The APO team—Catherine Modica, Sydney Miller, and Shannon Larkin were there to support us, welcome us and send their warm words in person or via email. Thank you all very much!

I am grateful to our collaborators, without whom our projects would not have been possible. Professor Angel Rubio and Emil Viñas Boström were instrumental in our $FePS_3$ projects, providing invaluable theoretical support. Professor Dominik Juraschek, with his extensive knowledge in nonlinear phononics, symmetry, and chiral phonons, has been a constant inspiration for our experimental endeavors. Professor Je-Geun Park and his group members — Jaena Park, Youjin Lee, Junghyun Kim, and Chaebin Kim — were generous in providing us with the highest quality crystals in the world. Professor Jayakanth Ravichandran and his students, Huandong Chen and Boyang Zhao, played a crucial role in our $BaTiS_3$ project. Our monthly meetings with Professors Xiaodong Xu, Di Xiao, and Haidan Wen were incredibly fruitful and enlightening, resulting in several joint works. Professor T. Senthil and his group members, Dan Mao and Hoi Chun Po, helped us interpret our observations in $NiPS_3$. Professor Keith Nelson and Zhuquan Zhang supported us with measurements and taught us optical techniques for terahertz experiments. During several conferences and other meeting I had a pleasure to discuss about physics and learn from these brilliant people: Claus Ropers, Mirco Cinchetti, Fahad Mahmood, Pavel Dolgirev, Frank Gao, Omar Mehio, Yinming Shao, Yoseob Yoon, Sudi Chen, Zuocheng Zhang, and Yue Sun. I extend my sincere thanks to all of you!

My high school teachers Yasin Yogurtcu, Aidyn Tussupzhanov, Prof. Askar Davletov and Daniyar Saparov opened the doors to physics for me and ignited my interest in this beautiful field of science. They were more than just teachers; they were mentors, coaches, and friends. They trained me to participate in various physics competitions, which later laid a solid foundation for my future studies.

During my college years at Nazarbayev University, Professors Daniele Malafarina, Boris Fine, Zhandos Utegulov, Giorgios Tsironis, Vassilios Kovanis, Sergiy Bubin, Ernazar Abdikamalov, Constantinos Valagiannopoulos, and Aikaterini Mandilara supervised me, guided my first steps into research, and provided invaluable support during my graduate school applications. Thanks to our department's support, many of us from our class have started our graduate studies in the US, and coped with its nuances and challenges together. With my classmates Murat Yessenov, Alisher Duspayev, Nikolay Yegovtsev, Azamat Zhaksylykov, Amir Bralin, Danat Issa, Zhenisbek Tagay, Aidar Zhetessov, Kaisarbek Omirzakhov, Zhanibek

Rysbek, and many others, we would travel together, visit each other and have discussion on broad range of topics. Thank you all very much!

My social life during my seven years in Cambridge would not have been possible without my friends here. Rassul Aitassov, Zhanat Zhapparov, Altynbek Murat, Aibolat Koishybay, Kenessary Seitkhanov, Gafur, Olzhas, Beibit Zharylkassyn, Nurbek Aitzhanov, Bauyrzhan Primkulov, Arman Amirzhan, and many others, along with their families, were always ready to support me and my family in every way. I will always cherish the wonderful times spent with my roommates, who later became my very close friends: Ulugbek Barotov, Ali Shtarbanov, Gadam Myratgeldiyev, Inan, and Sami. I feel blessed to be surrounded by such friends.

I am deeply thankful to my loving parents Kamal and Gulzhamal for their unconditional love and care. They have always been ready to support my studies, cover my expenses, and create an environment for me to focus on my academic pursuits. My dad's advice to excel in our chosen fields resonates deeply with me. I cannot thank you enough. My brothers Abzal and Akhan, along with their wives Madina and Aruzhan, are incredibly caring people. Thanks to them, I have had fewer worries about our parents.

It is thanks to my wife and the love of my life, Gulnar, her unwavering support, patience, and motivation, that I have been able to get things done. I feel incredibly lucky and blessed to have met you. After long and tiring experiments or other works in the lab, seeing your smile, and that of our lovely son Amir, immediately fills me with energy. Thank you for everything!

This dissertation is dedicated to my mom, Gulzhamal, who unfortunately passed away during the later years of my PhD. She taught me how to read and write, took me to primary, secondary, and high school, and traveled with me for my college applications. She was always there supporting and motivating me. If my PhD work brings even the smallest benefit to humanity, the rewards should definitely go to my mother.

Batyr Ilyas
Cambridge, MA
Summer, 2024

Contents

List of Figures

List of Tables

In memory of my lovely mother, Gulzhamal

Chapter 1

Introduction

> *So the triumph of the reductionism of the Greeks is a pyrrhic victory: We have succeeded in reducing all of ordinary physical behavior to a simple, correct Theory of Everything only to discover that it has revealed exactly nothing about many things of great importance.*
>
> — Robert B. Laughlin and David Pines

Contents

1.1 A comprehensive description of solids

A solid is a state of matter in which its constituting atoms arranged in a particular ordered fashion. Depending on the types and numbers of elements, solids can exhibit a vast array of physical phenomena that are not only fundamentally important, but also have direct implications for various technological applications. To describe these materials, which consist of ions and electrons, we cab write the relevant and sufficient equations. The Hamiltonian,

which includes the kinetic energies of valence electrons (those outside the last closed shell) and ions, as well as the Coulomb interactions among them, can be expressed as:

$$\mathcal{H} = -\sum_{i}^{N_e} \frac{\hbar^2}{2m}\nabla_i^2 - \sum_{\alpha}^{N_i} \frac{\hbar^2}{2M}\nabla_\alpha^2 - \sum_{i}^{N_e}\sum_{\alpha}^{N_i} \frac{Z_\alpha e^2}{|\vec{r}_i - \vec{R}_\alpha|} + \frac{1}{2}\sum_{i\neq j}^{N_e} \frac{e^2}{|\vec{r}_i - \vec{r}_j|} + \frac{1}{2}\sum_{\alpha\neq\beta}^{N_i} \frac{Z_\alpha Z_\beta e^2}{|\vec{R}_\alpha - \vec{R}_\beta|} \quad (1.1)$$

here m, N_e and M, N_i are the masses and the total numbers of electrons and ions, respectively. $\hbar$ is a reduced Planck constant. $\vec{r}_i$ and $\vec{R}_\alpha$ are the spatial coordinates of electrons and ions respectively, and Z_α is the atomic number of the ions.

To determine the quantum state of this ensemble of ions and electrons at a given point in time, we solve the Schrodinger's equation. Although this might seem quite simple, it is essentially all needed to describe the physical properties of materials in our daily life. Laughlin and Pines have referred to this as a "Theory of Everything" [1]. Indeed, apart from phenomena involving relativistic, gravitational or nuclear forces, the Eq. 1.1 is sufficient to comprehensively describe the world around us.

However, solving the Schrodinger's equation for the given Hamiltonian (Eq. 1.1) is tremendously expensive and cannot be solved either analytically or with state-of-the-art numerical tools. Numerical methods can solve systems with particle number fewer than 10, but when it comes to Avogadro number of particles, the problem becomes intractable. So, even though have the equations needed to describe the entire physics in solids, they are practically useless since we have no way of solving them. This is nicely described by Laughlin and Pines, *"So the triumph of the reductionism of the Greeks is a pyrrhic victory: We have succeeded in reducing all of ordinary physical behavior to a simple, correct Theory of Everything only to discover that it has revealed exactly nothing about many things of great importance"* [1].

What can we do now? There are two pieces of good news: i) for this exact reason, there is still active and exciting research being conducted around the world in the fields of atomic molecular and optical (AMO) and condensed matter physics; ii) it particularly highlights the importance of experimental observations in proving or disproving various approximate models (see section 1.2) and providing a guidance to these models. Again in words of Laughlin and Pines *"For better or worse we are now witnessing a transition from the science of the past, so intimately linked to reductionism, to the study of complex adaptive matter, firmly based in experiment, with its hope for providing a jumping-off point for new discoveries, new concepts, and new wisdom"*.

An alternative approach to this problem is to not focus on the microscopic details, but rather to look at the collective behavior of the system. Astonishingly, for many physical

properties of solids, atomic-scale information is not always relevant. In other words, the reductionist ideology fails to describe macroscopic emergent phenomena. For example, consider water and ice. If we zoom into these two substances down to atomic length scales, they appear identical. However, differences emerge when we start to zoom out. In ice, we begin to see beautifully organized water molecules in an almost perfect arrangement, whereas in water, the molecules are more chaotic. Other macroscopic properties also become distinct, such as rigidity and low-energy collective modes, like sound waves in ice. This is similar to the French impressionist style of painting: you understand the picture only when viewed from a distance, not up close. To summarize, at each level of complexity, there are higher-order principles that govern physical behavior, which are not necessarily deduced from the lower level.

1.2 Approximated models: A band theory

As mentioned in the previous section, we cannot solve the state equation for the given Hamiltonian (Eq. 1.1). Therefore, we must reformulate our task. Specifically, we simplify the Hamiltonian by assuming certain approximations and then try to capture various experimental observations. This approach shifts the problem from a fully deterministic theoretical one to a synergistic interaction between experiment and theoretical analysis. New approximate theories must be refined to explain observations, and, conversely, experiments need to be designed to test the predicted physics.

In fact, while formulating our Hamiltonian, we have already made certain approximations. One such approximation is assuming the ion to be a spherically symmetric point charge when writing the Coulombic interaction between the valence electron and the ion. In reality, ions have internal structures. Nevertheless, we aim to keep our models as simple as possible, provided they accurately describe the physical behavior. Fortunately, physicists over the past few decades have made significant achievements in developing sufficiently simple models. The most popular and surprisingly powerful model is the band theory, introduced by Swiss physicist Felix Bloch [2]. In this model, certain terms in the Hamiltonian are ignored. For instance, due to their large masses, ions have small kinetic energy, which we neglect. Additionally, the interaction between the itinerant electrons and the relatively stationary ions is captured by a periodic electrostatic potential, while the interaction among the electrons is approximated by a Hartree potential. In its simplest form, the equation for a free single electron under a periodic potential can be written as follows:

$$\mathcal{H} = \frac{\hbar^2}{2m}\nabla^2 + V(\vec{r}) \tag{1.2}$$

where $V(\vec{r})$ is periodic function in space. Bloch has shown [2] that the solution of the Schrodinger equation in this case will be a plane wave with a spatial periodic modulation, given by:

$$\psi(\vec{r}) = e^{i\vec{k}\cdot\vec{r}}u(\vec{r}) \tag{1.3}$$

here the exponential prefactor is a plane wave, and $u(\vec{r})$ is periodic function in space. Now, given that we have the wavefunction (Eq. 1.3), we can calculate various types of observables.

Even though the treatment we have made above may seem like an oversimplification, this model has proven to be tremendously powerful in reproducing the main characteristics of many materials. An outstanding example is semiconductors, such as silicon and germanium. More importantly, these and similar materials form the core of many functional devices that we use in our daily lives, including the memory components and microprocessors of smartphones and computers.

1.3 Strong interactions

Like any toy model, band theory has a finite range of applicability and may fall short under certain conditions. One obvious limitation arises from ignoring electron-electron interactions, encapsulated in the Hartree potential. While this simplification might initially seem to complicate matters, it also holds the promise that phenomena emerging from strong interactions could lead to novel and enhanced functionalities. Although there is no universally accepted definition, materials that cannot be described by band theory and exhibit strong electronic correlations, alongside complex interactions with magnetic, lattice, and orbital degrees of freedom, are now referred to as *"Quantum Materials"*.

Strong interactions can lead to various types of physical phenomena. One prominent example is a *Mott insulator*. A Mott insulator is a phase that, according to band theory, should be metallic. However, due to strong electron correlations, it undergoes a metal-to-insulator transition. This deviation from band theory necessitates the development of more sophisticated approximate models. One such model is the *Hubbard model*. To understand the essence of the Hubbard model, let's consider a one- or two-dimensional lattice with one electron per site. Ignoring electron interactions, except for the Pauli exclusion principle, the electrons will occupy the lowest energy levels in the band. Due to the Pauli exclusion principle, half of the electrons will have spin-up, and the other half will have spin-down. According to band theory, there are higher energy states available with no energy gap, implying the system should be metallic. However, when an electron at site i wants to jump onto site j, which has an electron with an opposite spin, the Coulomb energy penalty (U) for

two electrons occupying the same site must be considered. If this energy penalty dominates over the kinetic energy, the electrons will tend to localize at their own sites. This interplay transforms the expected metal into an insulator, known as a Mott-Hubbard insulator. The mathematical description of the Hubbard model is as follows:

$$\mathcal{H} = -t \sum_{\langle i,j \rangle, \sigma} c^{\dagger}_{i,\sigma} c_{j,\sigma} + U \sum_{i} n_{i,\uparrow} n_{j,\downarrow} \tag{1.4}$$

here t is the hopping matrix element, $c^{\dagger}_{i,\sigma}, c_{j,\sigma}$ are creation and annihilation operators of electrons at site i and j, U is an on-site Coulomb interaction, n_i is an electron density at each site. The first term describes the kinetic energy of the electrons, while the second term is an on-site Coulomb repulsion.

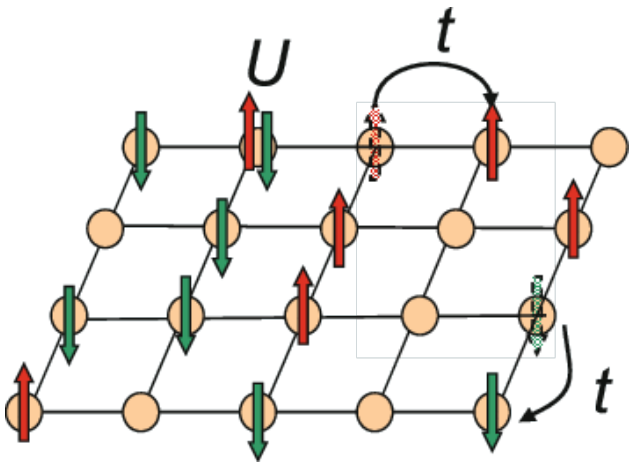

Figure 1.1: A Hubbard model on a 2D square lattice. An electron can hop to a neighbouring site with a hopping transfer integral t at the penalty of Coulomb repulsion U. Adapted from Wikipedia.

If U remains small in comparison to t, then we can capture the electronic behavior using free electron band theory as discussed in section 1.2. On the other hand, if U becomes dominant, we are dealing with a strongly correlated electronic system. In this scenario, the system will exhibit an antiferromagnetic (AFM) ground state at half filling. This is because the strong on-site Coulomb repulsion forces the electrons to localize in a manner that minimizes their energy, resulting in alternating spin alignment on adjacent lattice sites.

A Mott-Hubbard insulator is a prototypical correlated system and is believed to be the core of many other exotic phases in quantum materials. For example, the AFM Mott insulator, as discussed above, is the parent compound of high-temperature superconducting cuprates. Upon changing the temperature and external parameters such as doping or pressure, this parent state exhibits a plethora of complex phases, as depicted in Figure 1.2. These

phases include superconductivity with remarkably high transition temperatures, charge order, pseudogap, and others. As we can see, strong correlation effects give rise to rich physics alongside with promising practical applications.

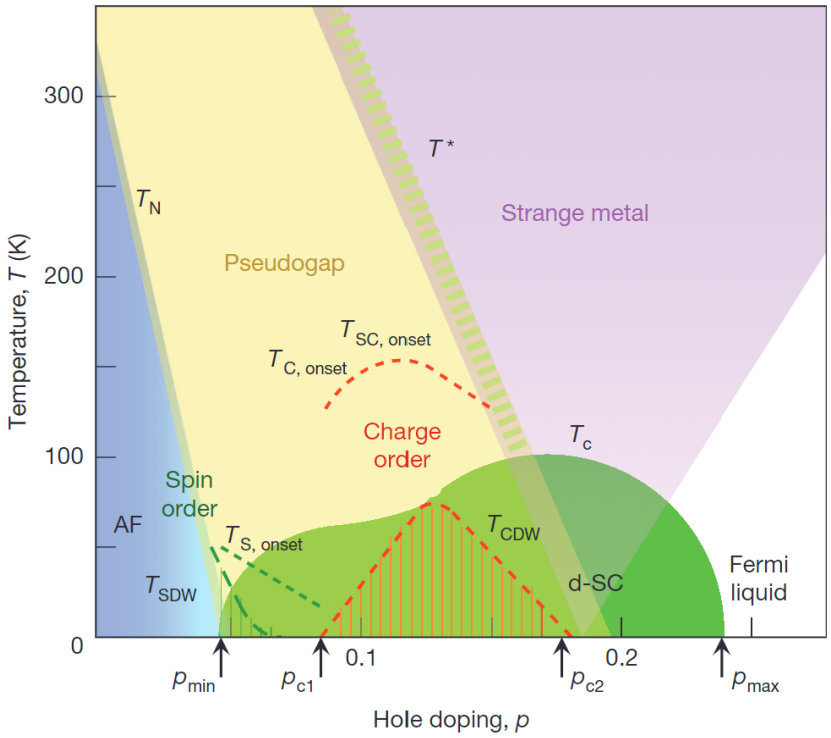

Figure 1.2: Phase diagram of cuprate superconductors. A blue region on the left is AFM Mott insulating state, which undergoes a series of phase transitions upon hole doping. This include superconductivity with remarkably high transition temperature, charge order, pseudogap and other phases. Adapted from ref. [3].

A natural question that arises is: what are the requirements for materials to host correlated quantum phases? Based on our understanding from the Hubbard model, the kinetic energy must be small, while the electron interaction U must be large. Controlling the Coulomb repulsion energy is typically challenging, but one can search for or modify the electron hopping matrix element t. Therefore, systems with flat electronic bands are expected to give rise to novel physics. A notable recent example is the bilayer graphene system. Bistritzer and MacDonald's continuum Dirac model calculations on bilayer graphene showed that there are specific twist angles between the two layers of graphene that result in perfectly flat bands [4]. Following this breakthrough, experimental work has demonstrated that at these magic angles, bilayer graphene exhibits correlated insulating states [5] and superconductivity [6].

A few years later, another major discovery occurred. Two layers of transition metal dichalcogenide (TMD), $MoTe_2$, twisted by about 3 degrees, showed a fractional quantum

Hall effect at zero magnetic field [7]. In this case, the flat bands induced by the twisting of the layers cause a band inversion and spontaneous breaking of time-reversal symmetry, which eventually induces quantum anomalous Hall states. Here, another major topic, *topology*, comes into play. We will not delve into this field in this dissertation. While the integer quantum anomalous Hall effect can be understood using a single-particle picture with topological band structures, the fractional states require strong electronic correlations. Although the higher-level contributions of topology and electronic correlations might seem to complicate matters, they are leading to new and unforeseen discoveries, making this an exciting research area.

1.4 Elementary excitations in solids

As mentioned earlier, there are no exact solutions to our problem at hand. However, thanks to extensive research over the past few decades, we can treat solids as collections of elementary excitations, as will be discussed below. For instance, in the Bloch theorem discussed earlier, electronic quasiparticles are treated as non-interacting excitations. Besides electronic quasiparticles, other types of elementary excitations in solids also play a crucial role, provided they have long lifetimes. Generally, these excitations can be classified into bosonic and fermionic modes, each exhibiting distinct energy and momentum distribution probabilities.

For instance, we can expand the last term in Eq. 1.1 and retain only the quadratic terms in atomic displacements. This allows us to describe the ionic part of the Hamiltonian as a sum of harmonic oscillators, or *phonons*. Higher-order terms introduce phononic anharmonicities that account for scattering among phonons themselves. We can also expand the third (electron-ion) term in Eq. 1.1, which leads to interactions between phonons and electrons, providing an additional decay channel for phonons. On the other hand, the interaction between electrons and phonons can lead to exotic behaviors. Under certain conditions, phonons can effectively induce an attractive force between electrons, resulting in bound Cooper pairs and giving rise to superconductivity in metals. This mechanism of phonon-mediated superconductivity is known as conventional or BCS (Bardeen, Cooper, and Schrieffer) theory [8]. When considering electronic quasiparticles in metals, it is important to note that only those sufficiently close to the Fermi level will be well-defined quasiparticles with long lifetimes.

Besides phonons, there are other types of low-energy collective excitations. One of the most relevant excitations for the purposes of this dissertation is spin waves. In a ferromagnet or antiferromagnet, at low but finite temperatures, the spins fluctuate, and the quantized versions of these spin waves are called *magnons*. Although magnetism originates from quantum effects, it can be treated semi-classically in the long-wavelength limit. This approach is

known as linear spin wave theory (LSWT), which is a powerful tool for calculating spin wave dispersion relations when supplemented with experimentally obtained magnetic constants of the system. Applying this technique to a chain of spins that are either ferromagnetically or antiferromagnetically coupled predicts distinct behaviors. Let's write down the equations for this. For simplicity, we will assume a magnetic interaction only between nearest-neighbor spins. For such a system with Heisenberg interactions:

$$\mathcal{H} = -J \sum_{\langle ij \rangle} \vec{S}_i \cdot \vec{S}_j \tag{1.5}$$

here $J > 0$ is a ferromagnetic interaction, while $J < 0$ describe the antiferromagnetic interaction. For the ferromagnetic case, the ground state is characterized by all spins being aligned in the same direction. This problem can be solved either semi-classically or fully quantum mechanically, with both methods yielding the same results. In the semi-classical treatment, we first determine the effective magnetic field at site i induced by the two neighboring sites. This field generates a torque on the spin at site i. We then write the equations of motion for the spin components based on the torque-induced changes in spin components over time. Solving these equations provides the dispersion relation for ferromagnetic magnons. In the long-wavelength limit, or near the zone center, the magnon energy varies quadratically with its momentum. In contrast, a similar treatment for an antiferromagnetic chain results in a linear dispersion relation. A more realistic consideration of other magnetic interactions in the system, will necessitate the inclusion of terms such as magnetic anisotropy and demagnetization field, and the corresponding dynamics are captured by Landau-Lifshitz-Gilbert (LLG) equation. Comprehensive discussions along these lines can be found in Ref. [9].

The simple Heisenberg Hamiltonian used above can be further modified to capture more realistic behaviors in materials. For example, the assumption of only nearest-neighbor interactions can be relaxed to include second or third nearest-neighbor interactions. In cases of mixed types of magnetic interactions, where nearest neighbors are ferromagnetically coupled and next-nearest neighbors are antiferromagnetically coupled, new types of spin structures may emerge. In such scenarios, the spins might become frustrated and form noncollinear spin structures, such as helical or spiral patterns. Although the microscopic mechanism may differ, similar noncollinear spin ordering will be discussed in the context of a new multiferroic material with proper-screw helical spin order, NiI_2, in Chapters 5 and 8.

Moreover, other anisotropic terms, such as single-ion anisotropy or exchange anisotropy, can further alter the magnetic ordering and their excitations. The dispersion relations of magnons are typically measured with inelastic neutron scattering spectroscopy, while mode energies at the zone center can be investigated using Raman or infrared spectroscopies. In

Chapters 4 and 6, we discuss the layered antiferromagnetic material $FePS_3$, where strong single-ion anisotropy in the out-of-plane direction forces all spins to align along this direction, resulting in a magnetic Hamiltonian close to the Ising universality class. This anisotropy term also opens up a large gap in the spin-wave spectrum, exceeding 15 meV. More detailed discussions will be presented in the respective chapters of this dissertation.

Besides phonons and magnons, there are other types of elementary excitations. We will briefly describe some of them here.

Plasmons. Plasmon is a quantum of collective excitations of electronic density. One cannot derive density oscillations from non interacting system of electrons. Near the Brillouin zone center the energy of plasmons are given by:

$$\omega_{\text{pl}} = \sqrt{\frac{4\pi n e^2}{m}} \tag{1.6}$$

here n is electron density. In most of the metals the plasmons energies are about several 10 meV, and correspondingly they minimally contribute to the thermodynamic properties of the system.

Polarons. In polar insulators, an electron can strongly couple to the optical phonon modes, forming a cloud of phonons around the electron. Although there may not be universally accepted definitions, other types of quasiparticles can also be called polarons when they strongly couple with phonons. For example, in the case of $FePS_3$, a magnon mode gets hybridized with phonons that are close in energy. As will be discussed in Chapter 4, such a quasiparticle is called a magnon-polaron.

Polariton. If the elementary excitations discussed in the preceding sections are polar in nature, they can interact with light, resulting in a new hybrid particle called a polariton. Polaritons are formed when the energy and momenta of the matter mode, such as a magnon or phonon, match those of light. Under such conditions, light propagates through the material, resonantly driving the polar modes. These modes will oscillate and re-emit within the matter medium. Given the typical energy scales of matter modes, light has relatively small momentum, making the dispersion of matter modes almost flat relative to light. At the crossing point of the dispersions, an avoided crossing occurs, resulting in modes that are hybrids of light and matter. Depending on the type of matter mode, the polariton can take various forms, such as phonon-polaritons, magnon-polaritons, exciton-polaritons, and many others [10].

There are several experimental approaches for creating polaritons and measuring their dispersion relations. In the terahertz spectral range, time-domain terahertz spectroscopy can be used. However, the amount of momentum provided by free-space photons is limited. An

alternative approach involves bringing a sharp metallic tip close to the sample surface and shining light on the tip-sample junction. In such cases, larger momenta can be transferred to modes in the sample, with the amount defined by the inverse of the tip radius. In Chapter 5, we discuss the details of phonon-polaritons and demonstrate a new method for measuring their dispersion.

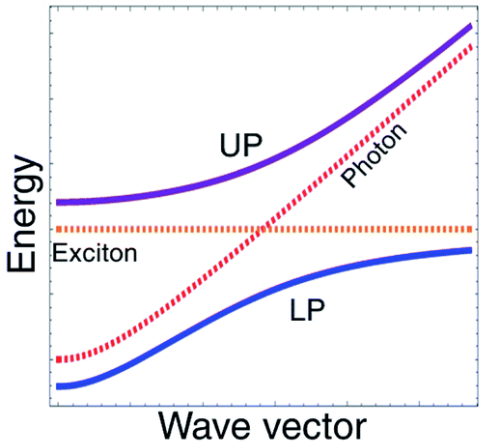

Figure 1.3: Dispersion relation of exciton-polariton. Dispersion relation of an exciton-polariton. The orange dashed line is a bare exciton, and the red dashed line is a photon dispersion. Solid line depict upper and lower polaritons with an avoided crossing. Adapted from ref. [11].

Exciton. In insulators or semiconductors, an electron in the conduction band and a hole in the valence band can form a bound state known as an exciton. Depending on the binding energy of excitons, their energies can lie deep within the band gap. Excitons can be of various types. For example, Wannier-Mott excitons have extended wavefunctions that span several unit cells. This occurs due to the large dielectric constant in semiconductors, which reduces the binding energy. The recent discovery of monolayer semiconductors, such as MoS_2, shows that when thinned down to atomic thickness, the reduced Coulomb screening leads to large excitonic oscillator strengths. Additionally, reducing the layer number modifies the electronic band structure, and in the single atomic layer limit, it becomes a direct bandgap semiconductor.

Another type of exciton is the Frenkel exciton, found in systems with relatively smaller dielectric constants, which increases the binding force between electrons and holes. Consequently, Frenkel excitons have wavefunctions typically localized within a single unit cell. In this dissertation, Chapter 7, we will discuss a new type of exciton that is intimately linked to the magnetic order in $NiPS_3$. This exciton has a record-breaking sharp linewidth and only becomes visible below the magnetic ordering temperature. In the same chapter, we will also

discuss d-d transitions among the d-orbitals of nickel ions. These transitions among tightly bound d-shell orbitals are sometimes referred to as Frenkel excitons.

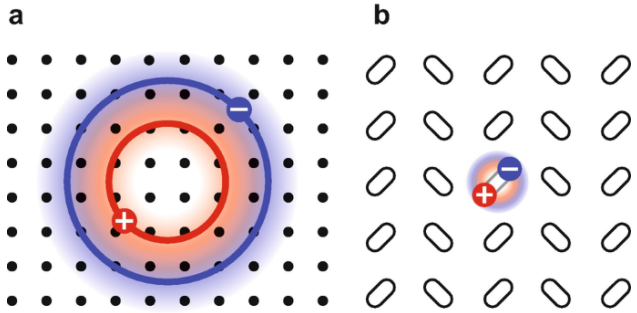

Figure 1.4: Wannier-Mott and Frenkel excitons. a. A Wannier-Mott exciton with extended wavefunctions that span several unit cells. **b.** Frenkel exciton wavefunctions typically localized within a single unit cell. Adapted from ref. [12].

There are several different methods for probing the properties of excitons. The most commonly used methods are photoluminescence and optical absorption. However, these techniques are limited to zero-momentum, electric dipole, and spin-allowed excitons. More comprehensive information about excitons can be obtained from photoemission experiments, which provide details about the dispersion relation of excitons, including dark excitons [13].

1.5 Coherent excitation of collective modes

So far, we have discussed elementary excitations in the context of their thermal population. Let's consider phonons. At a given temperature, the phonon energy levels in a sample are thermally occupied, but these oscillators have random phases. Coherent oscillation occurs when all these oscillators are synchronized with an external stimulus, such as ultrashort laser pulses, and acquire the same phase. Such phase synchronization, together with large mode amplitudes of phonons, leads to new physics in nonequilibrium settings. Recent works, including some in this dissertation, have shown that this approach can be used to control the macroscopic properties of materials. Prominent examples include possible light-induced superconductivity [14], ferroelectricity [15], [16], and magnetism [17]. The purpose of this section is to introduce the effects and use cases of coherent oscillations, as well as various methods for their generation.

1.5.1 Coherent phonons

The beauty of coherent phonons was revealed with the invention of ultrafast lasers. These lasers are used in two ways. First, they trigger the normal modes of atoms so that they all

start to oscillate in perfect synchrony. This occurs over a macroscopic volume of the solid, defined by the laser spot size. The second use of ultrafast lasers is that we can not only induce coherent phonons but also probe them in real time, as the periodicity of some optical phonons is on the picosecond timescale. Such *pump-probe* experiments were performed in the early 1990s and observed oscillations in reflectivity [18]. Other types of probing schemes can also be used, such as polarization changes, second harmonic generation, and others.

Coherent phonons can be used both as a spectroscopic tool and as a method of manipulating the system via the lattice. For example, in an iron-based superconductor, a multi-messenger probe, time-resolved ARPES, and time-resolved X-ray diffraction were utilized to trace the modulation of the electronic band and the lattice simultaneously [19]. This lock-in type of measurement with well-defined oscillations allows for accurately estimating the electron-phonon coupling strength.

Moreover, in Chapter 6, we will discuss another example of spectroscopy with coherent phonons. In this case, we track the phase information of the phonons as we lower the temperature across T_N. We observe a sudden π phase jump of the phonons upon magnetic ordering, a manifestation of the magnetostriction effect [20].

Regarding phonon-induced phases, a new field called nonlinear phononics is emerging, allowing for mode-selective excitation of phonons, which in turn coherently modify electron-phonon coupling, magnetic exchange couplings, and other energy scales. In Chapter 4, we will discuss an example of phonon-modulated magnetic energy scales that induces a net magnetization. This type of mode-selective excitation is particularly attractive for overcoming the longstanding challenge of heating effects in ultrafast experiments.

1.5.2 Generation mechanisms of coherent phonons

When discussing the mechanisms of coherent phonon generation, we should divide them into two categories:

- With high-energy photons in the near-infrared and visible range, where $\omega_{\text{photon}} \gg \omega_{\text{phonon}}$.
- With low-energy photons in the mid-infrared and terahertz (THz) range, where $\omega_{\text{photon}} \simeq \omega_{\text{phonon}}$.

Let's start with the first category. If the solid is insulating and the photon energy is smaller than the band gap, the generation mechanism is *impulsive stimulated Raman scattering* (ISRS). Because the laser pulse is ultrashort, the uncertainty principle requires it to have a broad spectral width. If the phonon energy is smaller than the spectral width

of the laser (see Figure 1.5a), it can be generated coherently. For example, for two given frequencies within the laser's spectral content, ω_1 and ω_2, the following condition must be satisfied: $\omega_1 - \omega_2 = \omega_{\text{ph}}$. As the name suggests, the ISRS mechanism is limited to Raman active modes and cannot excite infrared active modes.

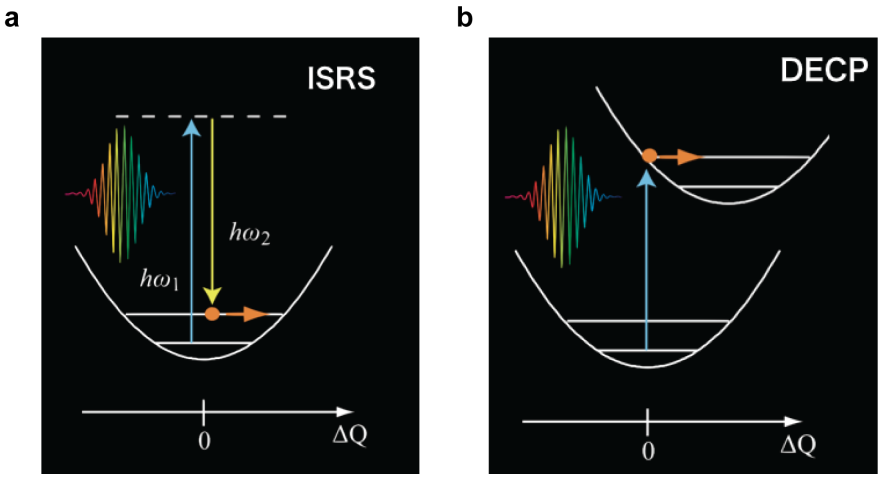

Figure 1.5: Impulsive and displacive generation of coherent phonons. a. ISRS mechanism of generating coherent optical phonons. Here the spectral bandwidth of the laser pulse exceeds the energy of the phonon **b.** Displacive excitation of coherent phonons. In metals, an ultrashort laser pulse generates many electron-hole pairs, shifting the energy landscape of phonons. Upon relaxation, a set of coherent phonons can be generated. Adapted from Ishioka lab, NIMS, Japan.

The other type of excitation is called *displacive excitation of coherent phonons* (DECP), which mostly occurs in metals or, more generally, in materials where the laser can generate a sufficient number of electron-hole pairs. In this mechanism, the photo-generated electrons and holes displace the lattice landscape (see Figure 1.5b), triggering coherent oscillations. Since the electron-hole pairs do not assume any broken symmetry after photoexcitation and quickly thermalize within the first few femtoseconds, the force they exert on the lattice will be symmetric. Consequently, only fully symmetric Raman modes can be driven via the DECP mechanism. In group theoretic language, these modes are typically of A_{g} symmetry.

Distinguishing between these two mechanisms can sometimes be ambiguous. One potential method is by examining their initial phase. If the lifetime of the generated phonons significantly exceeds their periodicity, the ISRS mechanism exhibits a sine function in time, whereas the DECP mechanism shows a cosine function in time. Another way to identify the excitation mechanism is by analyzing the dependence of the mode amplitude on the polarization angle of the incident light. In the ISRS case, this dependence follows the Raman tensor elements and reflects the symmetry of the respective Raman mode. In contrast, the displacive mechanism is independent of the light polarization.

Next, we discuss the case with low photon energies in the mid-IR and THz range, which are resonant or close to optical phonon energies. The simplest case is the *resonant excitation* of infrared-active phonons. The corresponding equations of motion can be written as:

$$\ddot{Q}_{\mathrm{IR}} + 2\Gamma\dot{Q}_{\mathrm{IR}} + \Omega_0^2 Q_{\mathrm{IR}} = gE_{\mathrm{THz}}(t) \tag{1.7}$$

here, Q_{IR} is a mode coordinate (phonon amplitude) of the IR-active phonon, Γ is a phonon linewidth, Ω_0 is a phonon frequency, $E(t)$ is an external drive field, which is in our case a THz pulse, and g is a coupling constant. The THz field can be modeled by the following analytical expression:

$$E_{\mathrm{THz}}(t) = E_0 \exp\left(-4\ln 2\frac{(t-t_0)^2}{\tau^2}\right)\cos\left(\omega_0 t + \psi_{\mathrm{CEP}}\right) \tag{1.8}$$

where E_0 is a THz peak electric field, τ is a pulse duration, ω_0 is a central frequency and ψ_{CEP} is a carrier-envelope phase.

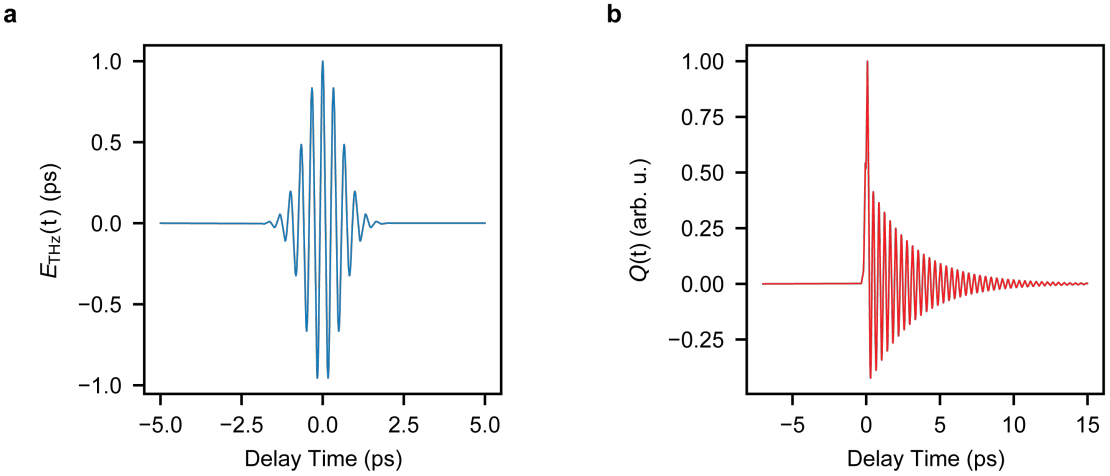

Figure 1.6: Terahertz field profile and resonantly excited infrared phonon. a. Time trace of the model THz field, as given in Eq. 1.8, with a center frequency resonant with the infrared phonon. **b.** Time domain oscillation of the generated phonon.

The time profile of the THz field, resonant with the phonon mode, and the driven infrared-active phonon dynamics are shown in Figure 1.6.

Infrared-active modes with a finite dipole moment can be directly excited through resonant excitation. However, generating coherent Raman modes requires going beyond the linear regime, necessitating higher field strengths. The nonlinear aspect of the excitation opens several different pathways. This can involve purely *photonic* mechanisms, or lattice modes can mediate the excitation. For simplicity, let's consider the photonic case. Similar to resonant excitation, we can write the equations of motion as follows:

$$\ddot{Q}_{\mathrm{R}} + 2\Gamma\dot{Q}_{\mathrm{R}} + \Omega_0^2 Q_{\mathrm{R}} = \epsilon_0 R E_{\mathrm{THz}}^2(t) \tag{1.9}$$

here ϵ_0 is the vacuum permittivity constant, R is a Raman tensor element.

Even though we now have a different force term, the induced dynamics will be similar to those shown in Figure 1.6b. However, this changes when we consider a new mechanism that involves lattice modes due to the different lifetimes of the THz field and the induced phonon. The idea of the so-called *ionic* mechanism is as follows: the driving photon field induces oscillations of the infrared phonons, which in turn facilitate the excitation of the Raman phonon. We can write the equations of motion as follows:

$$\ddot{Q}_{\mathrm{R}} + 2\Gamma\dot{Q}_{\mathrm{R}} + \Omega_0^2 Q_{\mathrm{R}} = c Q_{\mathrm{IR},1}(t) Q_{\mathrm{IR},2}(t) \tag{1.10}$$

here $Q_{\mathrm{IR},1}(t)$ and $Q_{\mathrm{IR},2}(t)$ are the phonon amplitudes of the infrared phonon. Each of these IR phonons will have lifetimes typically much longer than the light pulse width. This means such ionic mechanism allows to displace the lattice towards one direction for an extend time, as defined by the lifetime of mediator infrared modes.

To amplify the amplitude of the Raman mode, it is important for either the sum or the difference of the energies of the infrared phonons to match that of the Raman phonon. All these various mechanisms are summarized in Figure 1.7.

Finally, nonlinear excitation is not limited to only photonic or phononic mechanisms; it can also be of a mixed nature. For instance, one photon and one phonon can together act as an external force on a damped harmonic oscillator. This mechanism, known as *infrared resonant Raman scattering* (IRRS), has been considered theoretically [22] and has several experimental observations [23].

For completeness, we can also lift the assumption of only phonon mode involvement. Essentially, all our previous discussions based on phonons can also apply to other elementary excitations in solids. For example, in CoF_2, a high-energy Raman phonon was observed to be excited via a magnon mode with a smaller energy [24].

Identifying the actual mechanism of nonlinear excitation can become nontrivial in some cases. The most powerful technique suited for this problem is two-dimensional coherent terahertz spectroscopy. Combined with various control experiments involving temperature, fluence, polarization, and other factors, this method allows for pinpointing the exact mechanism. We will discuss more details of this method in Chapter 2.

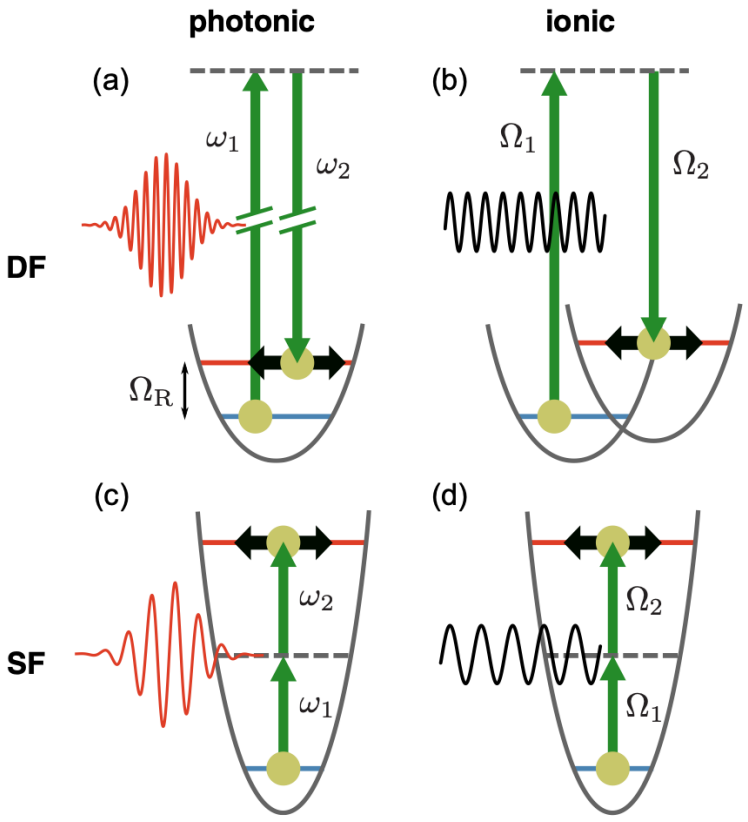

Figure 1.7: Summary of photonic and ionic Raman scattering mechanisms. In the photonic (**a**, **c**) and ionic (phononic) (**b**, **d**) mechanisms induced either via sum- or difference-frequency process of either the external light or phonons. Adapted from ref. [21].

1.6 Outline of this Dissertation

In Chapter 2, we review both static and time-resolved optical probes that are routinely used in the study of quantum materials. We further discuss how ultrafast techniques can be used not only as spectroscopy tools but also as methods to control the macroscopic properties of solids. Finally, we survey emerging ultrafast techniques that open new opportunities in the field.

In Chapter 3, we discuss two dimensional magnets, starting with their initial discovery and emergence of new family of materials. We review physics of magnetism in two dimensions, as well as their promising practical applications.

Chapter 4 focuses on our recent discovery of metastable magnetization in $FePS_3$. It provides a detailed discussion of the experimental methods used, the microscopic mechanisms involved, and the theoretical and numerical analyses conducted.

In Chapter 5, we present our new method for measuring the dispersion relation of phonon

polaritons, which does not require any fine-tuning of external parameters.

In Chapter 6, we demonstrate the use of coherent phonon spectroscopy in $FePS_3$, which enabled us to detect a magnetostriction effect that was elusive to many conventional scattering probes.

In Chapter 7, we present a magnetically brightened electron-phonon bound state using transient absorption and coherent phonon spectroscopies. We provide unambiguous identification of the bosonic component of this bound state.

Finally, in Chapter 8, we discuss the discovery of a multiferroic phase in the monolayer limit of NiI_2. Using a suite of optical spectroscopic probes, we trace the multiferroic order parameter as a function of temperature and atomic layer number.

Chapter 2

Ultrafast phenomena in quantum materials

The duty of the man who investigates the writings of scientists, if learning the truth is his goal, is to make himself an enemy of all that he reads, and attack it from every side. He should also suspect himself as he performs his critical examination of it, so that he may avoid falling into either prejudice or leniency.

— Alhazen (The Book of Optics)

Contents

With the advent of ultrafast lasers, a new avenue for time-resolved experiments has opened. The primary advantage of such ultrashort lasers, where the laser power is localized in time, is that it becomes possible to reach high field strengths without overheating the system, unlike with continuous wave lasers. Consequently, nonlinear optical processes can be explored, offering a promising probe for hidden broken symmetries [25]. Furthermore, ultrafast lasers enable the formation of light-dressed states in matter. Examples include Floquet engineering of electronic band structures [26] and the creation of novel hybrid light-matter polariton modes [10]. With these intense and ultrashort pulses, we can capture electronic, magnetic, and lattice dynamics with unprecedented time resolutions, ranging from picoseconds down to attoseconds. Finally, these intense electromagnetic fields allow for active control over macroscopic properties of materials by dressing the electronic states or dynamically modulating the microscopic interaction energies [27].

2.1 Static and time-resolved optical spectroscopies

In this section, we will overview some common optical spectroscopy tools, both static and time-resolved, most of which were employed in the studies of this thesis. These include reflectivity, circular dichroism, magneto-optical effects, and second harmonic generation. The power of optical methods lies in their versatility and applicability to a wide range of material systems. For the purposes of this dissertation, we will focus on the magnetic origins of the optical properties of the crystals, such as magnetic linear dichroism or birefringence, which give rise to Faraday or Kerr effects. There are several motivations for studying these magneto-optical effects in quantum materials. First is the investigation of magnetic properties, whether in equilibrium or out of equilibrium. Secondly, these techniques are very powerful in detecting time-reversal symmetry breaking orders.

2.1.1 Magneto-optical effects

Magneto-optical effects refer to the changes in the polarization state of the laser upon interaction with a magnetic medium. More broadly, a medium that can rotate the polarization plane of light is called optically active, where right and left circularly polarized light propagate at different speeds. For instance, linearly polarized light (e.g., horizontally polarized) can be decomposed into two circularly polarized components.

$$\begin{bmatrix}1\\0\end{bmatrix} = \frac{1}{2}\begin{bmatrix}1\\-i\end{bmatrix} + \begin{bmatrix}1\\i\end{bmatrix} \tag{2.1}$$

After travelling a distance d in the medium, two circular components acquire different phases:

$$\frac{1}{2}\begin{bmatrix}1\\-i\end{bmatrix} e^{ik_{\mathrm{L}}d} + \begin{bmatrix}1\\i\end{bmatrix} e^{ik_{\mathrm{R}}d} \tag{2.2}$$

After doing some change of variables, we can rewrite the expression above as [28]:

$$e^{\frac{i(k_{\mathrm{R}}+k_{\mathrm{L}})d}{2}} \begin{bmatrix}\cos\theta\\\sin\theta\end{bmatrix} \tag{2.3}$$

where $\theta = \frac{1}{2}(k_{\mathrm{R}} - k_{\mathrm{L}})d$. Here, the transmitted light represents a polarization rotated by an angle of θ. The wavevector of light in the medium can be expressed in terms of the refractive index as $k = \frac{n\omega}{c}$. As we can see, the polarization rotation in this situation is induced by the difference of refractive indices for the two opposite helicities of the light. In on other words, *circular birefringence* rotates the plane of the polarization.

There are other similar terminologies regarding the optical properties of the media that alter the polarization state of light. We discussed *circular birefringence*, which is the difference in refractive indices of the right and left circularly polarized light. In contrast, the difference in absorption of opposite helicities is called *circular dichroism*. Similarly, for linearly polarized light, if light travels at different speeds when polarized linearly along two orthogonal axes, then we call it a *linearly birefringent* medium, and the different absorption is called a *linearly dichroic* medium. All these distinct optical properties of the medium induce different changes in the polarization state. To be more precise, we can write down the dielectric tensor in two dimensions as:

$$\begin{bmatrix}\epsilon_{xx} & \epsilon_{xy}\\\epsilon_{yx} & \epsilon_{yy}\end{bmatrix} \tag{2.4}$$

The dielectric function defines the propagation speed of light in the medium ($v_p = \frac{c}{\sqrt{\epsilon\mu}}$, with μ being the magnetic permeability), which consequently alters its polarization state. Here, the nonzero off-diagonal tensor elements indicate a broken time-reversal symmetry. Therefore, precise and careful measurement of these quantities is important. Our ultimate

observables are either polarization rotation (the Kerr effect in reflection, the Faraday effect in transmission), or circular dichroism. In the first case, we are sensitive to the real part of $\epsilon_{xy} = \epsilon'_{xy} + \epsilon''_{xy}$, while in circular dichroism, we are sensitive to the imaginary part of the off-diagonal element. In both situations, the signal indicates broken time-reversal symmetry.

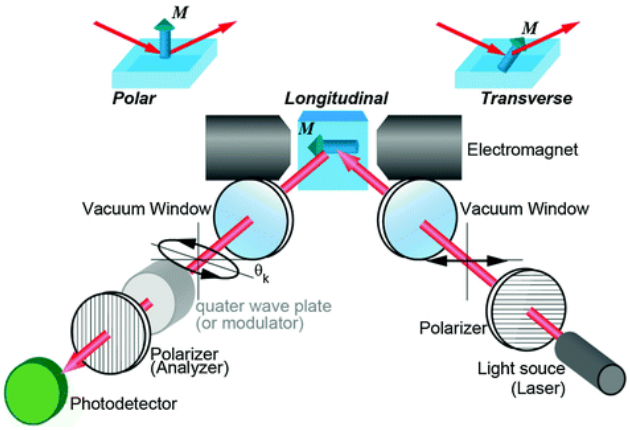

Figure 2.1: Schematics of the magneto-optic Kerr measurements. There are two types of Kerr measurements based on the direction of magnetization: the polar Kerr effect, where the magnetization direction is out of the plane, and the transverse Kerr effect, where the magnetization direction is in the plane. When linearly polarized light interacts with the magnet, it becomes elliptical. The detection optics then quantify the amount of induced ellipticity. Adapted from ref. [29].

Importantly, one has to be careful about certain subtleties when performing these types of polarization sensitive measurements. The most trivial scenario could be due to optical anisotropies in the experimental setup. For example, the reflectivity from a 45-degree mirror for s- and p-polarized light can differ, inducing an artificial polarization rotation. Even though the nominal values of such anisotropies might seem minute, they can still give rise to significant errors in the experiment. Besides other possible sources of optical anisotropies in the experimental elements, this particular problem can be mitigated by using an equal number of mirrors placed either for s- or p-polarized light.

Furthermore, if the medium is linearly dichroic ($\epsilon_{xx} \neq \epsilon_{yy}$), deciphering the origin of polarization rotation becomes nontrivial. To address such situations, one approach is to measure the rotation as a function of the polarization angle. For a time-reversal symmetric but linearly dichroic medium, the expected behavior is a sine or cosine-like dependence of the rotation angle with respect to the crystal orientation. This method allows you to distinguish the contributions from linearly dichroic effects and true polarization rotation.

$$\Delta\theta = \theta_{\mathrm{B}} \sin\left(2\phi - \phi_0\right) \tag{2.5}$$

where ϕ is the polarization angle of the light with respect to the easy axis of the medium. For example, at the principal axes of the crystal, the polarization of the light should not rotate. If we introduce a time-reversal symmetry-breaking order, such as ferromagnetism, on top of the linear dichroism, we need to repeat the measurement to isolate the pure Kerr or Faraday signal. In this case, the expected behavior will be similar to the nonmagnetic case, but with an additional constant that corresponds to the Kerr rotation.

$$\Delta\theta = \theta_{\mathrm{B}} \sin\left(2\phi - \phi_0\right) + \theta_{\mathrm{Kerr}} \tag{2.6}$$

Such a situation was recently discussed in the context of the kagome superconductor material CsV_3Sb_5. In this system, the parent charge density wave state is hypothesized to break time-reversal symmetry, inducing a so-called loop current order [30]. Similar experiments have been conducted to test this hypothesis. For instance, the angle dependence of polarization rotation has provided evidence for such a time-reversal symmetry-breaking order [31]. On the other hand, another type of powerful magneto-optical Kerr effect (MOKE) experiment based on a Sagnac interferometer did not find the same results [32]. Although this is a separate debate in itself, it highlights potential difficulties one may face with these types of MOKE experiments, and thus, extra care must be taken. Speaking of Sagnac interferometers, they are a very powerful technique for detecting time-reversal symmetry breaking, with an unprecedented sensitivity of about 30 nanoradians!

Measurement schemes for the polarization state of light

In this section we will derive, how two different balanced detection schemes implemented to measure the polarization rotation, as well the ellipticity change. Further, we will show how these measured values can be related to the real and imaginary part of the complex refractive index of the exemplary material, $FePS_3$. The polarization of light field propagating along the z-direction is described by the Jones vector:

$$\boldsymbol{E} = \begin{pmatrix} E_{0x} \\ E_{0y} e^{i\delta} \end{pmatrix}. \tag{2.7}$$

where $E_{0\mathrm{x}}$ and $E_{0\mathrm{y}}$ are the amplitude of the electric field along x and y directions, and δ is their phase difference. We define $\tan\alpha = \frac{E_{0y}}{E_{0x}}$ to characterize the ratio between y and x electric field amplitudes. In general, Eq. 2.7 describes an elliptically polarized light. An ellipse is defined by the polarization angle ψ (the angle between the major axis of the ellipse and the x axis) and ellipticity angle χ (the ratio between the minor and major axis), which

are related to α and δ by [33]:

$$\tan(2\psi) = \tan(2\alpha)\cos\delta \tag{2.8}$$

$$\sin(2\chi) = \sin(2\alpha)\sin\delta, \tag{2.9}$$

To measure the static dielectric properties of $FePS_3$, a vertically polarized light impinges on the sample and the polarization of the transmitted light is measured by balanced detection schemes. In the first scheme, the transmitted light passes through a half-wave plate (HWP) with its fast axis aligned along 22.5° with the y axis. We then separate the x and y components of the light with a Wollaston prism and measure their intensities I_x and I_y. We define the balanced detection signal as

$$\frac{\Delta I}{I} = \frac{I_y - I_x}{I_y + I_x}. \tag{2.10}$$

$\frac{\Delta I}{I}$ can be related to elliptical polarization parameters (ψ, χ) of the light transmitted through the sample as derived in the following. The polarization state of the light after the HWP is given by

$$R\left(-\frac{\pi}{8}\right)\begin{pmatrix}1 & 0\\ 0 & e^{i\pi}\end{pmatrix}R\left(\frac{\pi}{8}\right)\boldsymbol{E} = \begin{pmatrix}\frac{\sqrt{2}E_{0x}}{2} + \frac{\sqrt{2}E_{0y}e^{i\delta}}{2}\\ \frac{\sqrt{2}E_{0x}}{2} - \frac{\sqrt{2}E_{0y}e^{i\delta}}{2}\end{pmatrix}, \tag{2.11}$$

where R is the two-dimensional rotation matrix and the 2×2 matrix in the middle is a Jones matrix for HWP. The balanced detection signal is then given by

$$\left(\frac{\Delta I}{I}\right)_{\text{HWP}} = -\frac{2E_{0x}E_{0y}\cos\delta}{E_{0x}^2 + E_{0y}^2} = -\tan(2\psi)\cos(2\alpha). \tag{2.12}$$

In the second scheme, we replace the HWP by a quarter-wave plate (QWP) with its fast axis aligned 45° with y axis. Now the polarization state after the QWP is

$$R\left(-\frac{\pi}{4}\right)\begin{pmatrix}1 & 0\\ 0 & e^{i\frac{\pi}{2}}\end{pmatrix}R\left(\frac{\pi}{4}\right)\boldsymbol{E} = \begin{pmatrix}\frac{(1-i)\left(iE_{0x}+E_{0y}e^{i\delta}\right)}{2}\\ \frac{(1-i)\left(E_{0x}+iE_{0y}e^{i\delta}\right)}{2}\end{pmatrix}, \tag{2.13}$$

here the 2×2 matrix in the middle is a Jones matrix for QWP. And the balanced detection signal in this case is:

$$\left(\frac{\Delta I}{I}\right)_{\text{QWP}} = -\frac{2E_{0x}E_{0y}\sin\delta}{E_{0x}^2 + E_{0y}^2} = -\sin(2\chi) \tag{2.14}$$

In the limit of small sample modulation of optical properties $\alpha - \frac{\pi}{2} \ll 1$, $\delta \ll 1$, we have

$$\left(\frac{\Delta I}{I}\right)_{\text{HWP}} \approx 2\psi - \pi \tag{2.15}$$

$$\left(\frac{\Delta I}{I}\right)_{\text{QWP}} \approx -2\chi. \tag{2.16}$$

Therefore we can directly probe the polarization angle, ψ and the ellipticity angle, χ, of the light transmitted through the sample by using HWP and QWP, respectively, in the balanced detection scheme.

Relating the ellipticity and polarization angle to the complex refractive index

To relate the ellipticity χ and polarization ψ angles to the optical properties of a solid we consider the complex transmission coefficient through a slab of material with complex refractive index $\widetilde{n} = n + ik$,

$$T = \tau_1 \tau_2 \exp\left(-ik_0 n \cdot l\right) \tag{2.17}$$

where $\tau_i = 1 + \rho_i$ are the elementary transmission coefficients and $\rho_i = \pm\frac{n-1}{n+1}$ are the elementary transmission coefficients of front and back interfaces, respectively. l is the slab thickness and k_0 is the wavenumber of the transmitted light in vacuum. As outlined above, in the limit of small δ we have $\psi \approx \alpha$ and the polarization angle ψ is then determined by the two electric field components as $\tan\psi_0 = \frac{E_{0y}}{E_{0x}}$ and therefore the polarization angle of the transmitted light is determined by the ratio of the absolute values of $\frac{|T_y|}{|T_x|}$, and is given by:

$$\tan\psi = \tan\psi_0 \times \frac{|\tau_{1,y}||\tau_{2,y}| \exp\left(-k_0 k_y \cdot l\right)}{|\tau_{1,x}||\tau_{2,x}| \exp\left(-k_0 k_x \cdot l\right)} \tag{2.18}$$

$$= \tan\psi_0 \times \sqrt{\frac{n_y^2 + k_y^2}{n_x^2 + k_x^2}} \times \frac{(n_x+1)^2 + k_x^2}{(n_y+1)^2 + k_y^2} \times \exp\left(-k_0(k_y - k_x) \cdot l\right) \tag{2.19}$$

$$\approx \tan\psi_0 \times \exp\left(-k_0(k_y - k_x) \cdot l\right) \tag{2.20}$$

The last step involves make use of $\widetilde{n}_y \approx \widetilde{n}_x$, which is typically a good approximation even for dichroic or birefringent materials. Moreover, in this limit the prefactor of the exponential $\sqrt{\frac{n_y^2+k_y^2}{n_x^2+k_x^2}} \times \frac{(n_x+1)^2+k_x^2}{(n_y+1)^2+k_y^2}$ will be close to 1 for the experimental values of $n \approx 3$ and $k \approx 0.1$ [34]. The factor in the exponential $k_0 \cdot l$ is in the order to 1000 for the thickness of the sample ($\sim$ 200 μm) and probe wavelength (800 nm). *Therefore, the polarization angle* $\Delta\psi = \psi - \psi_0$ *is determined by the imaginary part of the refractive index in a material with*

a linear dichroism $k_y \neq k_x$. Similar arguments can be made for the ellipticity angle χ. From the above discussion we know, that χ is proportional to the retardation difference δ of the two orthogonal electric field components. After propagating through the material slab the retardation difference is given by the difference of the argument of the complex transmission coefficient along x and y,

$$\Delta\delta = \arg(T_y) - \arg(T_x) = \arg\left(\frac{T_y}{T_x}\right) \tag{2.21}$$

This can be derived as,

$$\Delta\delta = k_0(n_y - n_x) \cdot l + \arg\left(\frac{n_y + ik_y}{n_x + ik_x} \cdot \frac{(n_x + 1 + ik_x)^2}{(n_y + 1 + ik_y)^2}\right) \tag{2.22}$$

with the same argument as above ($n_y \approx n_x$ and $k_0 \cdot l$ is large), this can be approximated as:

$$\Delta\delta = k_0(n_y - n_x) \cdot l \tag{2.23}$$

This result shows that ellipticity angle χ is determined by the real part of the refractive index in a material with a linear birefringence $n_y \neq n_x$.

2.1.2 Nonlinear spectroscopy

If the previously discussed Kerr or Faraday measurements are commonly sensitive to broken time-reversal symmetry, this section will address another type of nonlinear optical spectroscopy called second harmonic generation (SHG), which is sensitive to broken inversion symmetry. The basic principle of SHG is as follows: a light with frequency ω impinges on the sample, transiently polarizing it, and reemits light at its higher harmonics. Typically, these higher-order harmonics are weak, so pulsed lasers are preferred for such experiments. By analyzing the second harmonic of the fundamental pulse at 2ω and its angle dependence with respect to the sample orientation, one can map out the second-order susceptibility tensor elements. This can be expressed as:

$$P_i = \chi_{ij}^{(1)} E_j + \chi_{ijk}^{(2)} E_j E_k + ... \tag{2.24}$$

where P_i is the induced polarization, E_i is an electric field component, $\chi_{ij}^{(1)}$ and $\chi_{ijk}^{(2)}$ are first and second order susceptibility tensors, respectively. By tuning the incident light polarization angle, the SHG polarimetry can be obtained, which is determined by the $\chi_{ijk}^{(2)}$ tensor elements. This experimental method is a powerful probe of broken lattice or electronic symmetries. To acquire the polarimetry pattern in quicker and to improve the signal-to-noise ratio (SNR) of

the experiments, a new and fast way of rotation of polarization optics has been engineered [35], known as rotational anisotropy SHG (RA-SHG) (see Figure 2.2), that lad to several discoveries about correlated states. These include an inversion symmetry-broken state in cuprates [25] and a potential odd-parity hidden state in iridates [36].

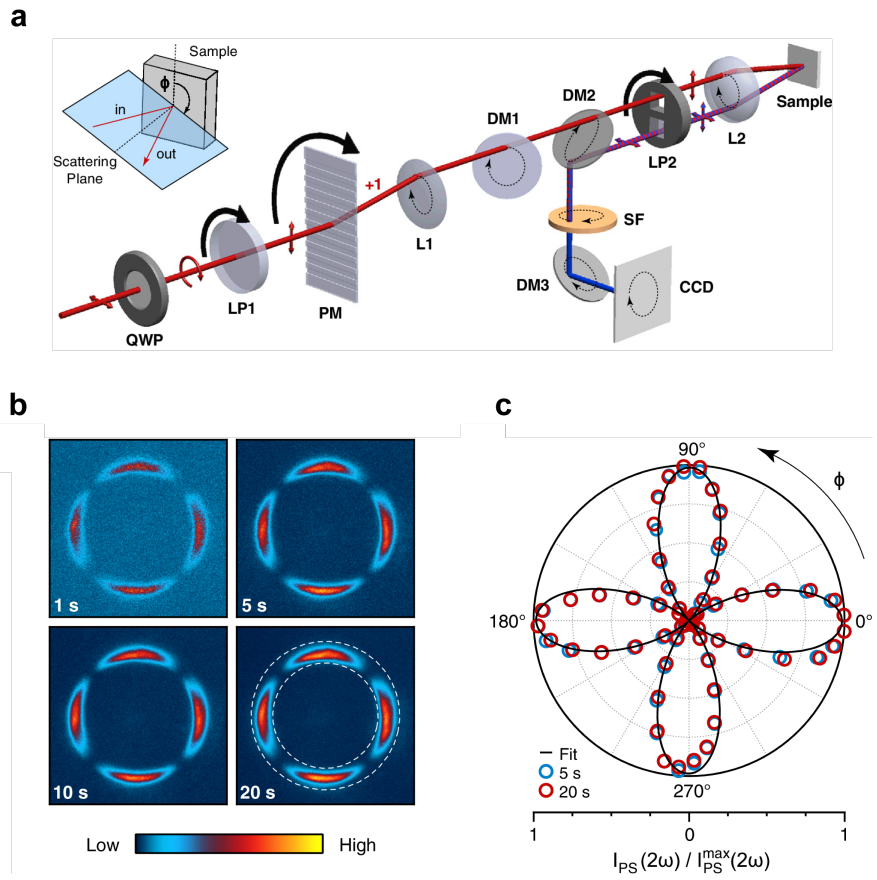

Figure 2.2: Schematics of the RA-SHG setup. a. Detailed schematics of the RA-SHG setup involve mechanically rotating all the polarization control optics together, which allows for fast data acquisition. The emitted second harmonic light and the fundamental beam are reflected back, with the SHG component isolated using a set of dichroic mirrors and detected with a two-dimensional charge-coupled device (CCD). The detected image on the CCD from (001) GaAs is shown in panel **b**, after various integration times. Panel **c** presents a polar plot of the RA-SHG patterns. Adapted from ref. [35].

Similar to the MOKE measurements discussed in the previous section, there are several important aspects of SHG experiments that one must be cautious about. As mentioned earlier, the underlying symmetry of the lattice, magnetic ordering, and electronic ordering defines the tensor elements. A higher symmetry system imposes constraints, such that some tensor elements may be zero or satisfy specific relationships among nonzero elements. Consequently, in highly symmetric systems, it is easier to determine the origin of the SHG

and identify potential broken symmetries. However, if the symmetry of the system is too low, the elements of $\chi^{(2)_{ijk}}$ become more independent, making the SHG fitting process more challenging and potentially leading to overfitting.

Further complications can arise due to several sources of SHG. A comprehensive review of these processes and a more detailed analysis can be found in ref. [37]. As light propagates through the medium, it induces electric polarization, magnetization, and quadrupole polarization. All these contributions add to the source term, which can be expressed as:

$$\vec{S}(2\omega) = \mu_0 \frac{\partial^2 \vec{P}(2\omega)}{\partial t^2} + \mu_0 \big(\nabla \times \frac{\partial \vec{M}(2\omega)}{\partial t}\big) - \mu_0 \big(\nabla \frac{\partial^2 \vec{Q}(2\omega)}{\partial t^2}\big) \tag{2.25}$$

The SHG intensity is given by

$$I(2\omega) \sim |\vec{S}(2\omega)|^2 \tag{2.26}$$

here μ_0 is a magnetic permeability. The first term corresponds to the electric dipole (ED) contribution, which is the dominant contributor in many systems. In centrosymmetric materials, the ED term must be zero. The second term is the magnetic-dipole (MD) contribution, and the last is the electric quadrupole (EQ) contribution. All these sources can also interfere with each other [38]. In inversion-broken systems, the ED term is typically the leading contributor to SHG. Since the surface of materials intrinsically breaks inversion symmetry, surface SHG must also be considered when analyzing experimental observations. As mentioned earlier, these various contributions can make SHG analysis complex, particularly in cases with low symmetry and multiple intertwined orders.

Moreover, if both the crystalline lattice and spin ordering break inversion symmetry, the electric dipole term can have contributions from two sources.

$$\vec{P}(2\omega) = \epsilon_0(\chi^{(i)} + \chi^{(c)})\vec{E}(\omega)\vec{E}(\omega) \tag{2.27}$$

$\chi^{(i)}$ is a time invariant (i-type) tensor, that is determined by the crystal lattice, and $\chi^{(c)}$ is time noninvariant (c-type) tensor, governed by the magnetic ordering symmetry. In cases when the incident light is absorbed by the crystal, the tensor elements can also be complex numbers, which further may lead to interference effects [37].

The purpose of these discussions is not to discourage SHG measurements but to emphasize the importance of careful analysis. Indeed, SHG measurements are very powerful, versatile, and can be sensitive to various degrees of freedom. To further elucidate the microscopic origin of the observed SHG response, one can investigate its dependence on the energy of the fundamental light, temperature, or external magnetic field. At certain wavelengths, the fitting analysis can be significantly simplified. For instance, when there is no absorption,

the tensor elements are real, and the magnetic dipole contribution is weak [37]. Finally, the ultra-sensitivity of SHG to various degrees of freedom and its versatility make it an excellent imaging tool. For example, SHG imaging can resolve 180-degree antiferromagnetic domains in a prototypical magnetoelectric system, such as Cr_2O_3 (see Figure 2.3).

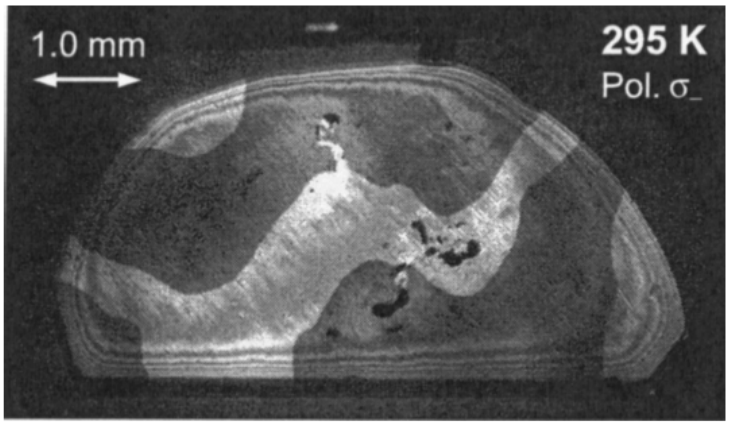

Figure 2.3: SHG imaging of antiferromagnetic domains. 180 degree antiferromagnetic domains in Cr_2O_3, measured with a circularly polarized 2.1 eV light at room temperature. The domain sizes exceed 1 mm. Adapted from ref. [37].

One particular example of SHG imaging, including the contributions from electric and magnetic dipoles, as well as temperature and layer dependence, will be discussed in Chapter 8. In this chapter, we demonstrate the power of SHG spectroscopy and microscopy in identifying the monolayer multiferroic order in NiI_2.

2.2 Controlling materials with light

The light-induced dynamics in materials can vary widely. At low to medium excitation intensities, the the ground state may oscillate gently around the free energy potential minimum. The frequency of these oscillations can provide insights into the shape of the energy landscape and its coupling with other degrees of freedom. For example, one can excite the system with light and use different probes sensitive to various degrees of freedom. In a seminal work by S. Gerber *et al.* [19], a near-infrared light pulse was used to induce phonon oscillations with A_{1g} symmetry. Subsequent measurements with a lattice probe (X-ray diffraction) and an electronic probe (ARPES) revealed oscillations with the same frequency in both probe channels, allowing for precise quantification of the electron-phonon coupling strength.

Beyond gentle excitations, a system may undergo a phase transition following photoexcitation. In such cases, the energy barrier for the transition can be significantly larger than the thermal energy, requiring a nonthermal external stimulus such as light. This scenario

is schematically depicted in the free energy landscape in Figure 2.4b. We will explore more examples of such phenomena in the next section.

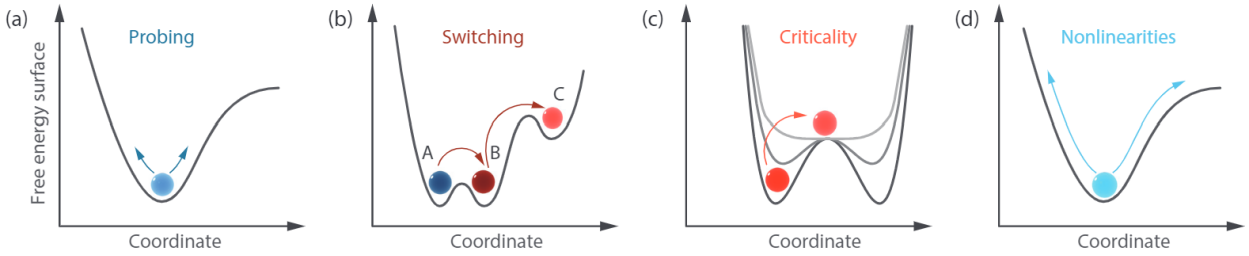

Figure 2.4: Laser triggered ultrafast phenomena. a. Probing the free energy landscape with gentle light excitation and the induced oscillatory modes. **b.** Switching the macroscopic state into new state with light, that is not existent in equilibrium. **c.** The critical behavior near dynamics phase transition. **d.** Inducing anharmonicities with intense field drives. Adapted from ref. [39].

2.2.1 Tipping the balance of competing orders

Another manifestation of intertwined degrees of freedom in quantum materials is the competition among different possible ground states. This competition can lead to behaviors such as frustration, high susceptibility, or phase separation. In such cases, a light pulse can act as a selector or favor one of the competing phase over the other. The new phase may either decay back quickly or persist indefinitely.

For example, in *1T*-TaS_2, an ultrashort laser pulse can convert the low-temperature insulating state into a metallic one, which is metastable [40] (see Figure 2.5). This observation holds great promise for practical applications, such as memory devices, where the "written" memory can be erased via thermal cycling. Not only ultrashort laser pulses but also electrical pulses with durations ranging from 40 ps to 1 s have been found effective in switching to the metastable magnetic state [41]. The underlying mechanism is still under active study, with one hypothesis suggesting the creation of topological defects, where domain boundaries act as conductive channels.

A similar phenomenon of laser-induced metal-to-insulator transition was discovered in VO_2 [42]. In this case, a high-temperature metallic phase with a rutile crystal structure undergoes a first-order phase transition to a monoclinic insulating phase.

Another important example of competing orders is the charge order that impedes the onset of superconductivity in cuprates at higher temperatures. A direct demonstration of this competition was achieved using ultrashort lasers to reduce superconducting condensation by creating quasiparticles. As the superconducting state weakens, the charge order is expected

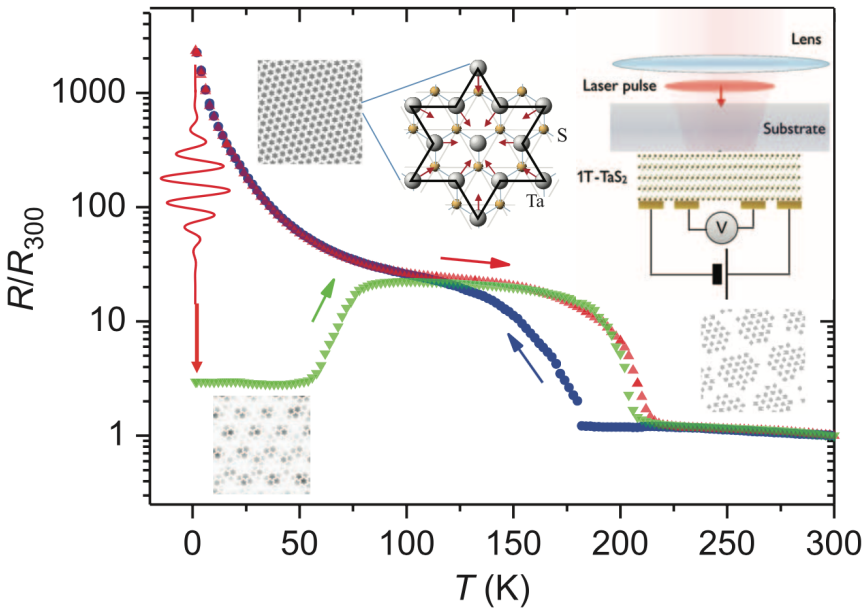

Figure 2.5: Light induced metastable metal to insulator transition in *1T*-TaS_2. *1T*-TaS_2 undergoes several charge density wave orderings. At room temperature the crystal form a nearly commensurate ordering, and at low temperatures a commensurate CDW sets in. The resistance undergoes a jump at around 200K. Interestingly, a single laser pulse can convert the insulating phase into a metallic phase at low temperatures, and this metallic state can persist for extended periods. Adapted from ref. [43].

to increase in amplitude and coherence length [44]. In such experiments, an infrared laser is used to quench superconductivity in $YBa_2Cu3O6 + x$, followed by a resonant soft X-ray pulse to trace the charge density wave (CDW) diffraction peak [45]. The quenched superconductivity resulted in an enhanced CDW coherence length, directly demonstrating the phase competition.

In rare earth tritellurides, a prototypical CDW material, the system can exhibit either one or two competing CDW transitions, depending on the rare earth element. In some cases, only one transition is observed, with the onset of a potential second CDW transition believed to occur at very low temperatures, which may be experimentally inaccessible. Following a similar approach of selectively weakening one of the competing orders to stabilize the other, this situation has been observed in $LaTe_3$.

In Figure 2.6a, the crystal structure of $LaTe_3$ is shown, with CDW ordering occurring in bilayer tellurium sheets. The Fermi surface in the high-temperature metallic state is depicted, along with the nesting vector $\vec{q}_c$. The experimental setup involves intense near-infrared light pulses hitting the sample, followed by ultrafast electron diffraction to trace the resulting lattice dynamics. As illustrated in Figure 2.6c, before laser excitation (left side), the diffraction pattern shows only horizontal CDW superlattice peaks (blue), corresponding

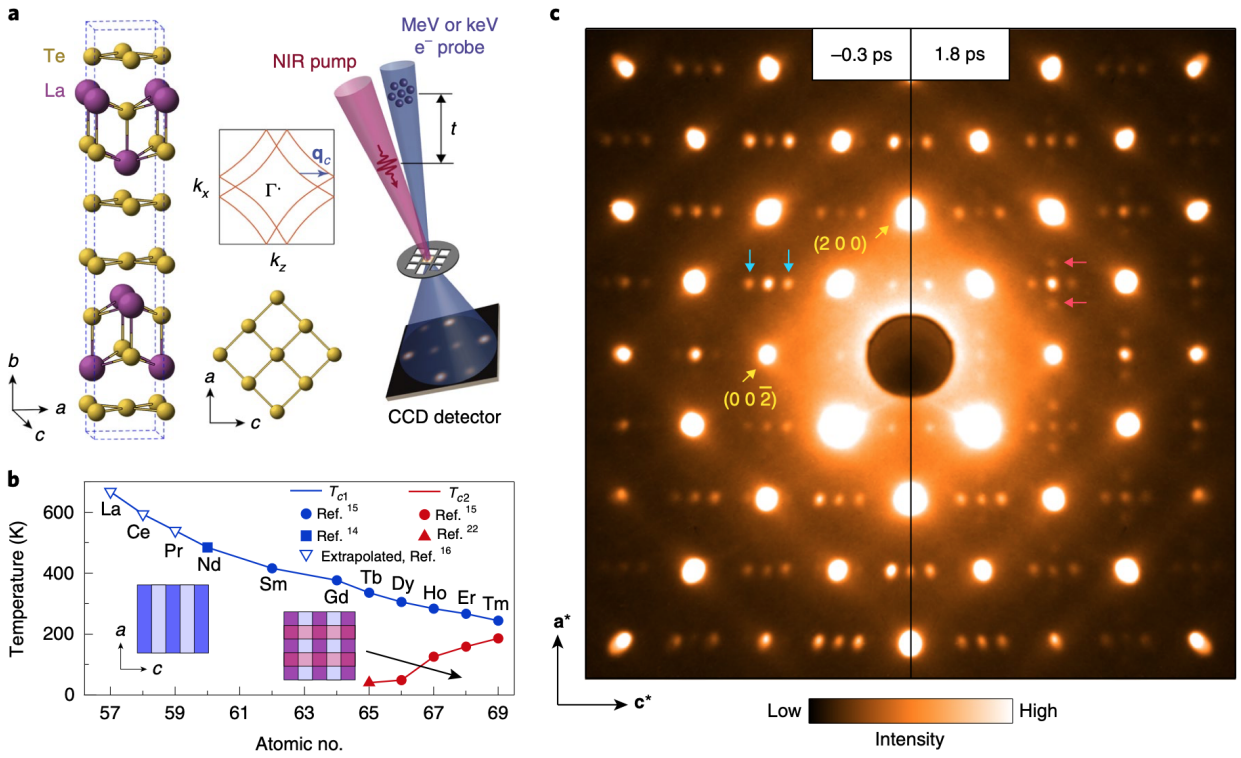

Figure 2.6: Competing charge density wave orders. a. Lattice structure, Fermi surface in the metallic phase of $LaTe_3$. Schematics of the near infrared pump, and ultrafast electron diffraction probe experiments. **b.** Two charge density wave orders in rare earth tritellurides. As the atomic layer number increased, the transition temperature of the higher CDW state T_{c1}, decreases. Opposite behavior takes place for the second CDW phase. According to the trend, the second CDW should occur at negative temperatures for La-based compound. **c.** Electron diffraction patterns before (left half), and after (right half) photoexcitation. The first CDW peaks (blue) are weakened, and the second CDW peak (red) has emerged. Adapted from ref. [46].

to the first high-temperature phase. After photoexcitation (right side), the dominant CDW peaks are weakened, and a new CDW peak in the perpendicular direction (red) emerges.

In Chapter 4, we will discuss a related discovery metastable state induced by an intense THz pulse in $FePS_3$, as well as the coherently generated magnons and phonons in the same material system.

2.2.2 Nonlinear phononics and generation of tunable terahertz pulses

The primary challenge in ultrafast control of phases in condensed matter systems is the undesired heating effect. Rather than achieving precise tuning of specific parameters in materials, ultrashort pulses often induce simultaneous changes across multiple degrees of freedom. This typically occurs when the light is significantly absorbed by the sample, leading

to the generation of a large number of electron-hole pairs or disrupting the underlying order. Such effects significantly hinder the deterministic control of materials using light.

One approach to mitigating this issue is to use low-energy laser pulses in the terahertz (THz) or mid-infrared (mid-IR) range. This spectral range encompasses most of the relevant collective modes, allowing for mode-selective excitations. However, radiation sources in these energy ranges are scarce, and high-power commercial options are nearly non-existent. Recent technological advancements have significantly reduced the barriers to obtaining intense THz to mid-IR laser pulses. New developments in amplified pulse lasers for the mid-IR range have been reported [47], but these technologies are still in the early stages of development and are not yet commercially available.

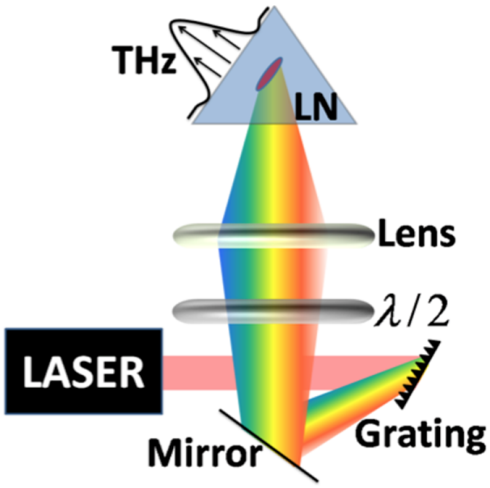

Figure 2.7: Tilted pulse front method of generating intense THz fields. 800 nm pulse from an amplified laser sent to a grating, that tilts the pulse front. Further the beam is focused on a $LiNbO_3$ crystal, where the crystal's surface is almost parallel with the pulse front. Adapted from Nelson lab at MIT.

The general framework for generating low-energy pulses involves difference frequency generation (DFG) or rectification nonlinear processes. Optimizing power in this context requires the searching for new nonlinear crystals with high efficiencies and high damage thresholds. Recent investigations have identified new nonlinear organic crystals [48], [49] that are pushing the boundaries of intense terahertz (THz) generation. The current benchmark for intense THz generation is still set by the tilted-pulse front technique using $LiNbO_3$ crystals [50], where field strengths exceeding MV/cm have been achieved (see Figure 2.7). This method remains highly efficient for the commercially available wavelength of amplified lasers at 800 nm. Conversely, while new organic crystals may achieve similar field intensities, they operate more efficiently in the infrared range, necessitating additional parametric amplification. Compared to $LiNbO_3$, organic crystals typically produce a much broader THz

spectral content. In Chapters 4 and 5, we utilize both of these THz generation schemes.

The aforementioned THz sources have limited tunability. For ultimate mode-selective excitations, narrowband and tunable light sources are desired. In the continuous wave regime, recent work has demonstrated THz quantum cascade lasers with tunable central frequencies [51]. However, the power levels of these lasers are still insufficient to enter the nonlinear regime in materials. A new free electron laser beamline facility, TELBE, in Dresden has demonstrated a tunable THz source with frequencies ranging from 0.1 THz to 2.5 THz and field strengths of approximately 1 MV/cm [52]. Notably, this beamline operates at a repetition rate of 100 kHz, significantly enhancing the signal-to-noise ratio (SNR) of experiments. For example, this capability has enabled the observation of highly efficient high harmonic generation in graphene [53].

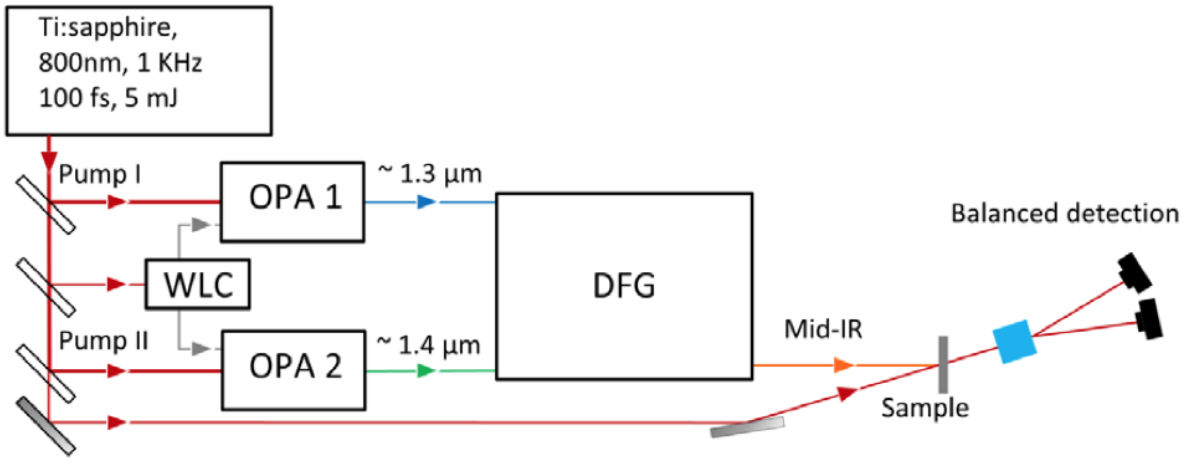

Figure 2.8: Generation of CEP stable mid-IR pulses. A CEP stable and tunable mid-IR pulse is generated by mixing the outputs of two OPAs in a GaSe crystal. The field profile is sampled using electro-optical sampling method. To ensure the stability of CEP, both of the OPA are seeded by the same whitelight continuum (WLC). Adapted from ref. [54].

So far, we have discussed THz-range light sources, which typically cover frequencies up to 6-7 THz. An alternative approach is to obtain light sources in the higher energy range, up to mid-infrared (mid-IR). This method also relies on the difference frequency generation (DFG) process in nonlinear crystals. For tunability purposes, optical parametric amplifiers (OPAs) are employed. The outputs of two OPAs are mixed in a crystal, such as GaSe, where the generated light is the difference between the two incident beams from the OPAs. To ensure stability of the carrier-envelope phase (CEP), both OPAs must be seeded by the same white light source [55] (see Figure 2.8).

This approach works effectively at energies higher than about 10 THz. However, for the

range between 6-7 THz and 10 THz, the method illustrated in Figure 2.8 produces broad radiation, which compromises the selectivity advantage. To address this issue, the outputs from the two OPAs are first chirped, and an additional delay is introduced before mixing in the nonlinear crystals. This scheme, known as the chirp-and-delay method, enables narrowband radiation. Additionally, for this spectral range, a different type of organic crystal, DSTMS, has been found to be more efficient (see Figure 2.9). Consequently, an intense, narrowband, and highly tunable laser source in the range between 4 THz and 18 THz has been achieved [56], as shown in Figure 2.9.

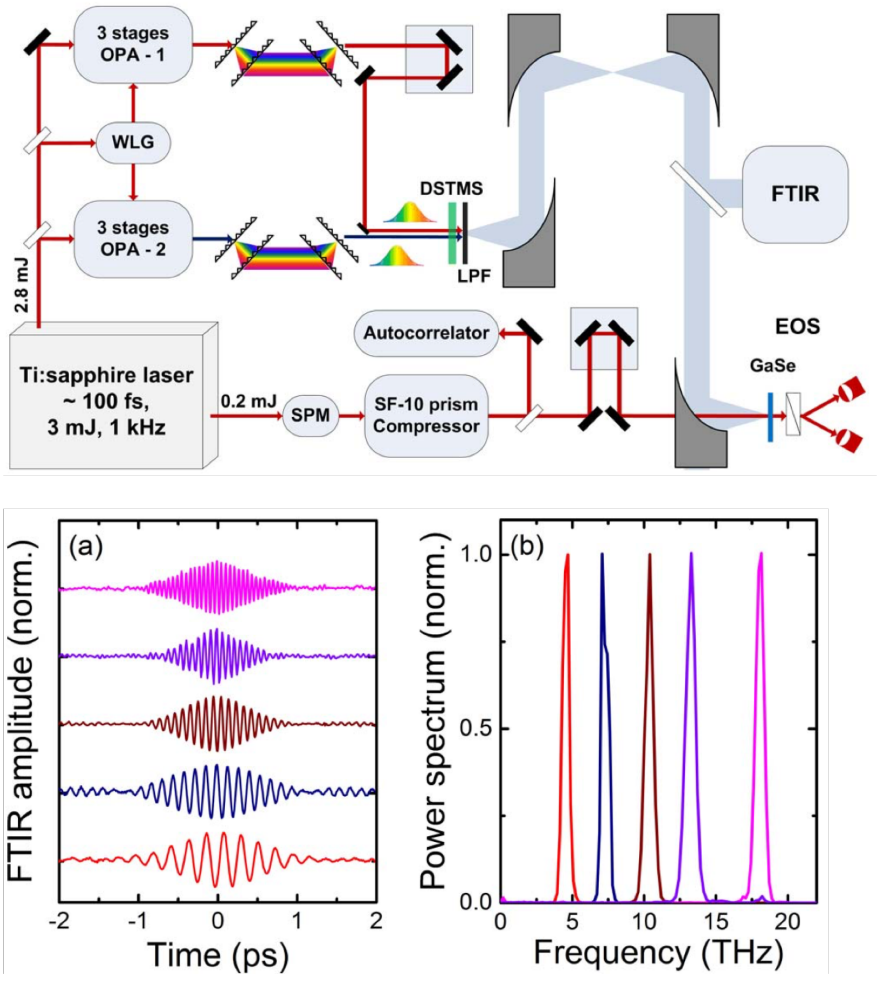

Figure 2.9: Generation of tunable and CEP stable THz pulses. (Top) schematics of experimental setup. The OPA outputs are chirped and delayed before mixing in the nonlinear crystal DSTMS. (Bottom) The time traces and spectral contents of the representative THz fields in the range between 4 THz and 18 THz. Adapted from ref. [56].

Next, we discuss several notable cases where nonlinear phononics, enabled by the various intense THz and mid-IR generation techniques discussed above, creates new phases of matter that have no equilibrium counterparts.

Possible light induced superconductivity. Among the various nonequilibrium orders created by THz or mid-IR fields, superconductivity is undoubtedly the most intriguing. The first reports of such phenomena date back to 2011 [57]. In this study, conducted on a stripe-ordered superconductor $La1.675Eu0.2Sr_0.125CuO_4$ (LESCO), a mid-IR pulse at 15 μm, resonant with the in-plane Cu-O stretching mode, was used. At a temperature where the system was not superconducting, the mid-IR drive induced a three-dimensional superconducting state, as evidenced by an out-of-plane Josephson plasma resonance. Later, in 2016, similar observations were reported for the organic superconductor K3C60 powders [14]. Here, mid-IR pulses ranging from 6 μm to 15 μm, resonant with vibrational molecular modes or the metallic plasma, were employed. Subsequent THz conductivity probe measurements revealed a gap feature in the real part of the conductivity (σ_1) and divergent behavior in the imaginary part (σ_2), reminiscent of superconductivity. Although these results were promising, they were initially insufficient to confirm the onset of a superconducting state. Traditionally, a system is considered a superconductor if it meets two crucial criteria: i) zero resistance and ii) the Meissner effect. Initially, it seemed challenging to verify these criteria, but the authors of these studies made significant efforts to demonstrate both features.

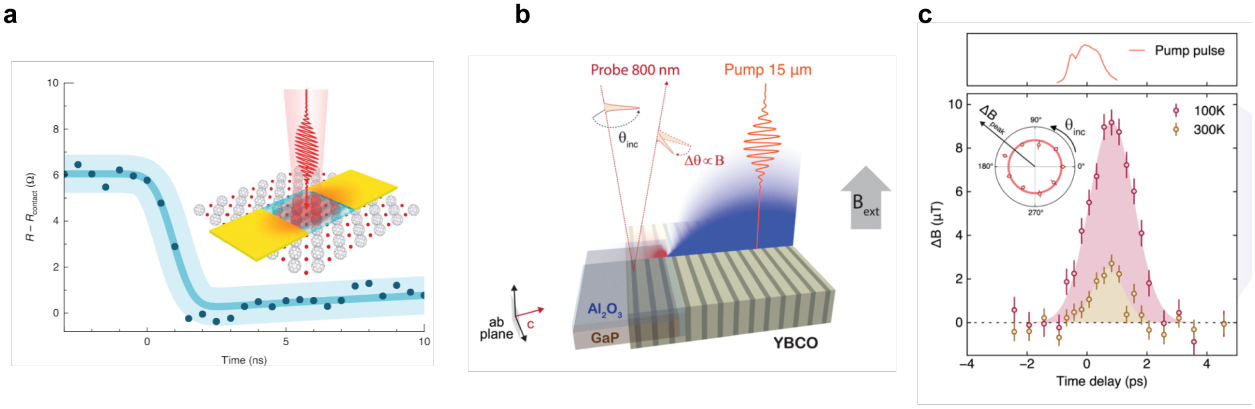

Figure 2.10: Photoinduced zero resistance and Meissner effect. a. Zero resistance state after photoexcitation in an organic superconductor K_3C_{60}. **b.** and **c.** Photoinduced magnetic field repulsion in YBCO, indicative of the Meissner effect. **a** is adapted from ref. [58], **b** and **c** are adapted from [59].

The first challenge was that transport measurements were not fast enough to capture the ultrafast dynamics. To address this, the authors made significant advancements in laser technology, achieving mid-IR pulses with tunable durations ranging from picoseconds to nanoseconds [58]. The extension of pulse duration allowed for transport measurements that demonstrated vanishingly small resistance (see Figure 2.10a). Additionally, the same group developed a method to measure magnetic field expulsion from the photoinduced, potentially superconducting region (see Figure 2.10b and c) [59]. These experiments were conducted on

$YBa_2Cu3O6.48$ (YBCO). These efforts provided compelling evidence for the photoinduced superconducting phase, importantly demonstrated across various systems, highlighting the widespread occurrence of the phenomenon.

THz field-induced ferroelectricity. $SrTiO_3$ is a quantum paraelectric material where large quantum oscillations of Ti ions at very low temperatures prevent ferroelectric ordering. The system's tendency to form long-range dipolar order has been observed in previous experiments involving chemical doping, strain, and pressure [60]–[62]. Two independent groups have explored nonequilibrium methods to stabilize ferroelectric fluctuations. In the first study [63], a soft phonon mode was targeted and driven resonantly with intense terahertz fields. In the second study [64], a higher-frequency vibrational mode was excited using an approximately 15 μm field. In both cases, second harmonic generation of a subsequent probe pulse was employed to detect the ferroelectric order, which was observed to persist for hours after photoexcitation and up to room temperature. The underlying mechanism of this transition remains unclear, but recent time-resolved X-ray diffraction measurements [65], [66] are providing new insights into the phenomenon.

THz field-induced magnetism. In addition to the previous examples, selective mode driving has also proven to be an effective method for controlling the magnetic order parameter. In CoF_2, the space group permits the piezomagnetic effect, and it has been found that the magnetic structure can be manipulated through strain engineering [67], [68]. However, strain control is limited by the symmetries it can access and the relatively low levels of applicable strain. Some fragile material systems may fail before even reaching 0.1% strain levels. Mode-selective dynamical strain offers a solution to these challenges, as it allows for a much larger symmetry space for distortion compared to static strain. This method enables the driving of any phonon mode with a finite dipole moment, with the amplitude of distortion limited by the Lindemann instability criterion. According to this criterion, crystals begin to melt if the distortion exceeds 10% of the interatomic distance [69].

In a recent study on CoF2 [70], a mid-IR pulse at 12 THz was used to resonantly drive two degenerate Eu infrared modes with mutually perpendicular polarizations. The elegance of nonlinear phononics becomes particularly evident in this case. The two infrared modes exert a force on a third, Raman-active, phonon mode. The equations of motion for this system can be written as:

$$\ddot{Q}_{\mathrm{R}} + 2\Gamma\dot{Q}_{\mathrm{R}} + \Omega_0^2 Q_{\mathrm{R}} = cQ_{\mathrm{IR},1}(t)Q_{\mathrm{IR},2}(t) \tag{2.28}$$

By tuning the polarization angle of the driving field, each infrared mode can be selectively excited, or both can be driven simultaneously by setting the polarization to an intermediate

angle. The initial phases of the individual infrared phonons can be controlled by the polarization state of the driving field. In **b**, when the phonons are in phase, the Raman mode is displaced in the positive direction. In contrast, in **c**, when the infrared phonons are out of phase, the Raman mode is displaced towards the negative side. This method allows for significant lattice displacements, inducing a ferrimagnetic state in the parent antiferromagnetic phase, with magnetic moments reaching approximately 0.2 μ_B.

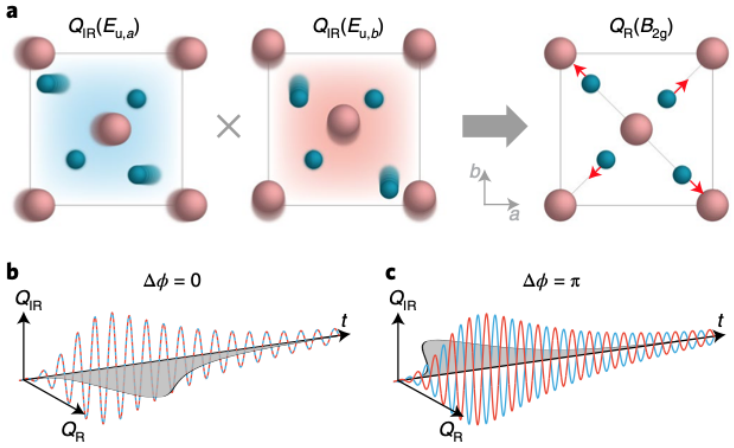

Figure 2.11: Nonlinear phononics for manipulating magnetism in CoF_2. a. Atomic motions of two infrared active phonons, when combined has a symmetry that imposes a force on the Raman active phonon (on the left). The initial phases of the individual infrared phonons can be set by the polarization state of the driving field. In **b**, they are in phase, leading to the displacement of the Raman mode along the positive direction, whereas in **c**, the infrared phonons are out-of-phase, displacing the Raman mode towards the negative side. Adapted from [70].

Similarly, a ferromagnetic state in $YTiO_3$ has been stabilized at temperatures significantly higher than the intrinsic Curie temperature [17]. In this case, high-temperature magnetic and orbital fluctuations typically hinder magnetic long-range ordering. However, by employing resonant lattice excitations, it is possible to favor one magnetic state over another, overcoming these fluctuations.

In Chapter 4, we explore a similar phenomenon where we displace the lattice along a specific phonon direction, thereby modifying the underlying magnetic exchange interactions. This results in a state with net magnetization and notably long lifetimes.

2.3 Emerging ultrafast spectroscopy tools

In this section, we provide a brief overview of emerging ultrafast spectroscopy tools. The selected spectroscopies are my personal picks, and undoubtedly, some other methods will be

missing. The criteria for selecting these techniques are based on their potential to address the following pressing questions, in no particular order:

- Will the response of materials beyond linear be able to provide us new insights into strongly correlated physics?
- In emerging platforms of strongly correlated systems, based on 2D materials that are prone to disorder and lattice reconstruction, can we probe nonequilibrium and nonlinear responses at the single atomic and/or moiré site to be able to capture disorder-free physics?
- The size restrictions of 2D materials and their heterostructures impose significant barrier to probing their low energy collective modes and dynamics. Can we overcome this barrier?
- The current resolutions of time-resolved experiments on solids are still commonly limited by tens of femtoseconds. To be able to disentangle the electronic and lattice dynamics, and correspondingly to understand the defining mechanisms of nonequilibrium phase transitions, it is crucial to have a better time resolutions, down to tens to hundreds of attoseconds.

2.3.1 2D Coherent terahertz spectroscopy

2D infrared spectroscopy is a well-established technique commonly used in physical chemistry to study molecular vibrational modes [71]. It has also been widely applied in semiconductor physics. To closely probe the low-energy nonlinear response function of new quantum materials, the terahertz spectral range is highly desired. Due to the technical challenges of terahertz technology and the relatively scarce radiation sources, nonlinear terahertz spectroscopies were developed later. One of the first applications of nonlinear THz spectroscopies was on semiconducting nanostructures [72] to probe the correlation spectra of optical intersubband optical phonons, and on canted antiferromagnets [73] to investigate the third-order magnon signals.

This methodology has seen a surge in activity in recent years. For instance, one group pioneered a new data acquisition scheme, single-shot detection, which significantly sped up measurement durations [75]. This improvement enabled temperature, intensity, and polarization-dependent measurements (see Figure 2.12) within practical timeframes and revealed new magnon-magnon nonlinear interaction channels [74], [76]. Furthermore, two-dimensional terahertz spectroscopy has proven invaluable in disordered correlated electron systems, where it has been possible to directly quantify both longitudinal and transverse

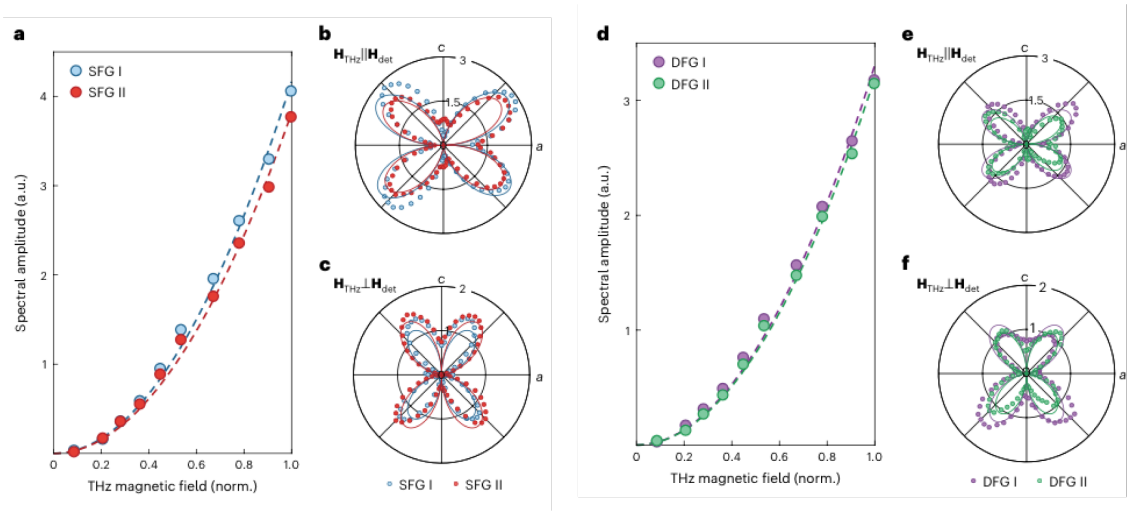

Figure 2.12: Fluence and polarization dependent nonlinear spectra in $YFeO_3$. Owing to the single-shot extension of the 2D THz spectroscopy, the fluence (**a** and **b**) and THz polarization (**b**, **c**, **e**, and **f**) dependence of the nonlinear peaks are made possible within reasonable data acquisition durations. Adapted from [74].

relaxation times, demonstrating the presence of marginal Fermi glass behavior in the system [77].

The basic working principle of nonlinear spectroscopy is as follows. Two pulses of THz fields (E_1 and E_2) propagate together and transmit through the sample under study. The transmitted pulses are further sampled in a reference crystal. The nonlinear signal is extracted as:

$$E_{\mathrm{NL}}(t,\tau) = E_{12}(t,\tau) - E_1(t,\tau) - E_2(t) \tag{2.29}$$

The timings of both pulses (t and τ) are scanned over a certain range. The Fourier transform along the two time axes generates a two-dimensional nonlinear THz spectrum. The off-diagonal peaks in these spectra directly indicate nonlinear couplings among low-energy collective modes.

Arguably, the most exciting theoretical prediction regarding the potential detection of new collective modes using 2D THz spectroscopy is the observation of fractionalized spin excitations [78]. Experimental verification likely awaits the development of new quantum magnets with strong third-order susceptibilities, as well as the use of stronger light fields and experimental geometries that allow for pronounced nonlinear signals near the temporal overlap of the THz pulses [79].

2.3.2 Ultrafast scanning tunneling microscopy

Most nonequilibrium optical experiments excite and probe regions on the micron to millimeter length scales. While these probes are already quite powerful, they often fall short for emerging two-dimensional materials with sizes on the order of $\lesssim 30$ μm. In these materials, moiré disorder and lattice reconstruction can significantly alter the underlying physics at macroscopic length scales. Consequently, local time-resolved probes with spatial resolutions capable of resolving individual moiré sites are highly desired. Scanning tunneling microscopy (STM) is an extremely powerful technique for this purpose. Although STM and ultrafast experiments might initially seem incompatible due to the slow electronics of STM, significant advancements have been made toward ultrafast STM, achieving resolutions down to several femtoseconds [80] (see Figure 2.13).

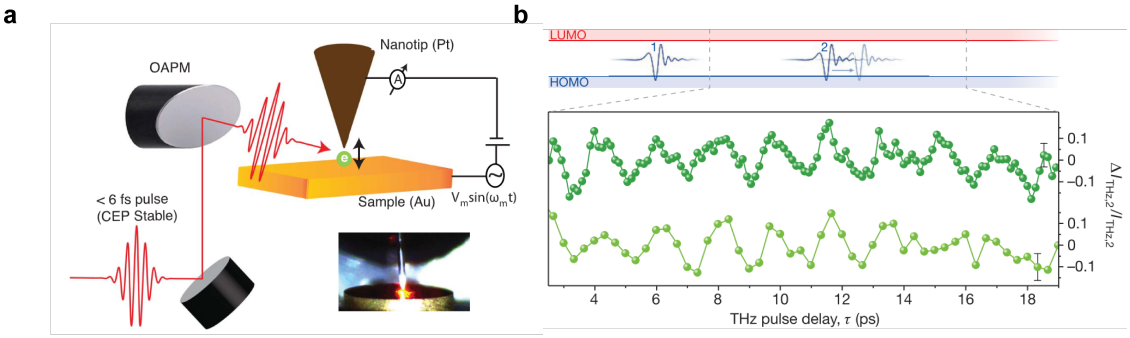

Figure 2.13: Ultrafast STM with 6 fs time resolution. a. Sub-6 fs carrier envelope phase (CEP) stable pulses coherently control the tunnelling currents at the junction. OAPM - off axis parabolic mirror. **b.** Vertical vibrational mode of a single pentacene molecule, with 0.5 THz frequency, detected using THz-STM. **a** is adapted from [80], **b** is adapted from [81].

The concept behind time-resolved tunneling currents relies on the autocorrelation principle. Two ultrashort pulses are directed to the tunnel junction between a nanotip and the sample. These optical or terahertz pulses can either act as a transient bias voltage or as an additional AC voltage superimposed on the DC background voltage. This approach has been used to resolve the vertical vibrational modes of a single pentacene molecule at a frequency of 0.5 THz. Currently, there are very few laser-based STM studies conducted on solids, and exploring local optical and nonequilibrium spectroscopies using ultrafast STM principles would be a promising area for investigating electronic correlations.

2.3.3 THz spectroscopy of 2D materials

Earlier, we emphasized the importance of the THz-range electromagnetic response of solids. Most collective excitations, single-particle excitations, and correlated band gaps fall within

this spectral interval. Since the discovery of single-layer graphene, a plethora of new topological and strongly correlated phases of matter have been identified in 2D materials. However, a significant challenge arises because the length scales of THz radiation ($\gtrsim 300$ μm) and the thicknesses of few-layer samples ($\lesssim 30$ μm) are quite different, making THz spectroscopy measurements on these systems challenging.

This led to the development of chip-based spectroscopy techniques. First discovered by David H. Auston in the 1960s [82], a photoconductive switch is based on a semiconductor that is initially insulating. Upon light excitation, the semiconductor becomes metallic. If a bias is applied under these conditions, the device functions as a photoconductive switch, which generates a short current pulse when illuminated. One can further design a waveguide through which the generated current pulse travels, inducing an electric field within the waveguide (see Figure 2.14). This setup can be used as a THz spectrometer by placing the sample under study in the waveguide and measuring the transmitted current with another identical photoconductive switch.

Such an experimental setup has been used to study monolayer graphene nanoribbons to investigate scale invariance in the quantum critical regime of the Dirac liquid phase [83]. Additionally, a similar approach led to the discovery of collective electronic modes in graphene, such as hydrodynamic plasmons and energy waves [84].

There are several challenges to overcome with this technique. First, the THz spectral bandwidth is currently limited to about 1.5 THz in available waveguides, necessitating new waveguide design principles. Second, the absorption cross section of THz radiation in semiconductors is relatively small, making it particularly challenging to study transition metal dichalcogenide (TMD) devices, where many new phenomena have been discovered. This challenge is compounded by the dominant contribution of gating layers, such as graphite. However, there are potential solutions to these issues, and they are indeed the focus of ongoing and future research.

In addition to the THz spectroscopy of small flakes using waveguides, several other approaches can be considered. For example, scanning near-field scattering can achieve spatial resolutions on the order of 100 nm and analyze the interaction of the sample with free-space THz radiation. This technique can detect collective excitations [85], though extracting THz complex conductivity remains challenging due to the complexities of modeling the tip-sample junction. Another approach involves spintronic emitters [86], where visible light is focused on a micron-sized spot, generating THz radiation from that small region. By blocking this radiation with the sample of interest, it is possible to extract THz-range complex conductivity spectra.

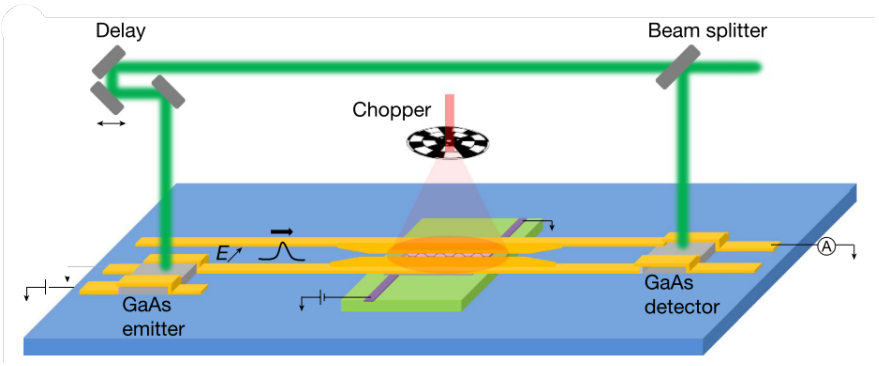

Figure 2.14: On-chip THz spectroscopy of a graphene nanoribbon. An optical pulse (green) is split into two arms. The first arm directed the pulse to a GaAs-based Auston switch emitter, which generates a short pulse of electrical current. To enhance the local field strength, the waveguide is narrowed close to the sample. After transmission through the sample, the pulse is sampled at the second switch. The electronic temperature is controlled using another pulsed laser (red). Adapted from [84].

2.3.4 Attosecond spectroscopy

One of the primary motivations for time-resolved experiments on ultrafast timescales is to disentangle the dynamics of various degrees of freedom in the time domain. For example, lattice dynamics are typically several orders of magnitude slower than electronic relaxation. Although the lasers currently in use are short enough for certain problems, they are still unable to capture the dynamics occurring during the birth of new nonequilibrium orders, which can happen on even shorter timescales. This brings us to attosecond science, where light pulses can be as short as tens of attoseconds and have pulse energies in the tens of electron volts. Such capability enables us to monitor the dynamics during the establishment of nonequilibrium orders. In particular, the electronic response to external perturbations can be captured while the lattice effectively remains in its equilibrium state, providing clues about the microscopic mechanisms of order in nonequilibrium conditions.

Such short pulses with high energies in the soft X-ray regime offer the opportunity to investigate element-specific dynamics. Photon energies in the X-ray window of the spectrum can induce electronic excitations from core levels to the conduction band, where transitions between different atomic core levels are well-resolved spectrally, allowing selective excitation or probing of different elements. Notably, in contrast to the energy-time uncertainty principle, attosecond pulses provide high time and energy resolution simultaneously. Moreover, their broad spectral content can sometimes encompass several elemental transition lines without the need for tuning and calibrating the light source each time. This approach allows the overall light-induced dynamics to be parsed into distinct degrees of freedom, as well as different atomic species present in the system.

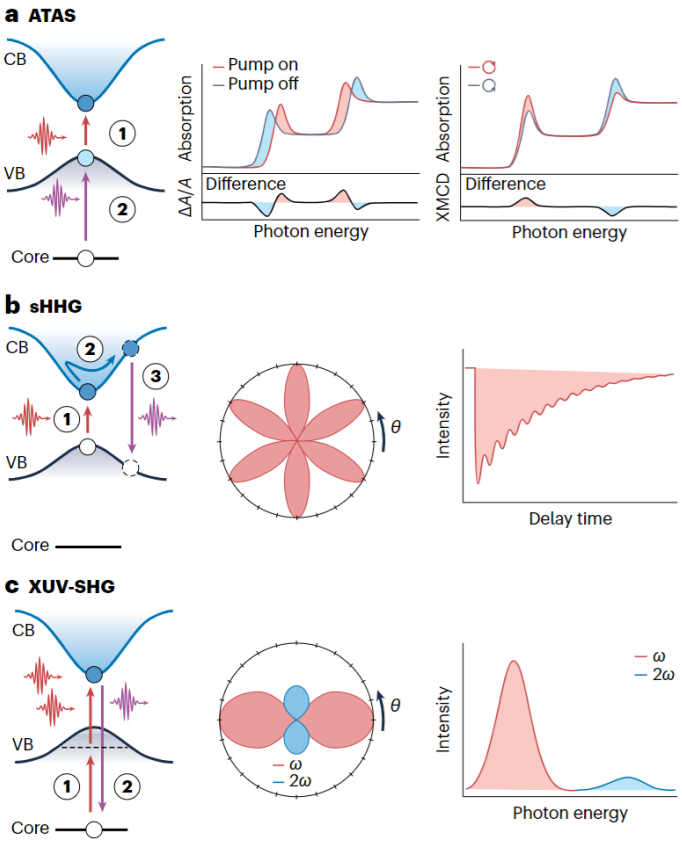

Figure 2.15: An overview of new experimental techniques based on short high energy lasers. a. Attosecond transient absorption spectroscopy (ATAS) enables the highest time resolution and offers spectral resolution in the soft and hard X-ray photon energy ranges. **b.** Solid-state high harmonic generation (sHHG) can be sensitive to both the electronic response and the topological properties of the electronic bands. **c.** XUV-SHG is an extension of nonlinear spectroscopy from optical spectral range to the high energy X-ray photons, which allows probing the element specific nonlinear response functions. Adapted from [87].

Besides attosecond dynamics and element specificity, short pulses with high energies can probe the electronic and lattice symmetries and the topological properties of electronic bands in a system. The experiments designed for such purposes are called extreme ultraviolet second-harmonic generation (XUV-SHG) and solid-state high harmonic generation (sHHG). An overview of these emerging techniques is provided in Fig. 2.15, and excellent detailed discussions about their advantages and limitations can be found in Ref. [87].

Chapter 3

Layered magnets: A highly tunable platform of magnetism

What we observe is not nature in itself but nature exposed to our method of questioning.

— Werner Heisenberg

Contents

3.1 Ordering in two dimensions

While discussing various phenomenologies in quantum materials, it might initially seem that they require independent mathematical or physical treatments to describe their behavior. However, an elegant theory by Landau and Ginzburg enables capturing the macroscopic properties at phase transitions by expressing the free energy in terms of a complex *order parameter*, without involving any microscopic parameters. This allowed the description of second-order phase transitions of various types, such as magnetism, superconductivity, or ferroelectricity, within a *unified theory*.

Using the concept of an order parameter, Landau postulated that crystalline phases cannot exist in one and two dimensions. This idea extends beyond crystal ordering and applies to a broader class of second-order phase transitions that involve the breaking of continuous symmetry. In 1968, N. D. Mermin provided a more rigorous argument supporting this theorem using the Bogoliubov inequality [88]. However, in the previous chapter, and more generally within the condensed matter community, we frequently discuss the discovery of two-dimensional materials, such as graphene and transition metal dichalcogenides. So, what accounts for this apparent inconsistency?

Before we attempt to resolve this dichotomy, let us first examine the reasoning behind this statement. Intuitively, long-range fluctuations in one or two dimensions require very little energy to be created, which destroys any onset of ordering. To understand why this occurs in one and two dimensions, but not in higher dimensions, let's consider the following energetic argument.

The lowest energy excitation in a chain of N spins can be visualized as a twisted rubber band, where the spins at the two ends of the chain point in opposite directions. If the angle between adjacent spins changes smoothly from one end to the other, the angle between any two neighboring spins will be approximately $\frac{\pi}{N}$. The interaction energy between these neighboring spins is then $E \sim \frac{\pi^2}{N^2}$. The total energy of the chain is therefore $E_{\text{tot}} \sim N\frac{\pi^2}{N^2}$. In the thermodynamic limit, where $N \to \infty$, the energy cost of long-wavelength excitations in one dimension approaches zero and large fluctuation created at no cost will destroy the order. A similar argument applies in two dimensions. However, in three dimensions, the energy required for these fluctuations increases with the system size, creating an energy barrier that prevents such fluctuations and thereby allows for ordering in three dimensions.

A keyword in the theorem's definition is the *thermodynamic limit*, which refers to systems of infinite size. In two dimensions, atomic fluctuations increase logarithmically with system size, and in the thermodynamic limit, these large fluctuations are sufficient to melt the crystalline order. However, for these fluctuations to reach a scale comparable to interatomic distances, the system would need to be as large as the entire solar system. This implies that for laboratory samples, typically on the millimeter or micrometer scale, the theorem becomes largely irrelevant. In fact, the discovery of the first two-dimensional material, graphene, was a groundbreaking achievement, though it wasn't entirely surprising in light of Mermin's theorem.

Another important theorem, known as the Mermin-Wagner theorem, was formulated by Mermin, Wagner, and Hohenberg. It states that in systems with dimensions less than 3 ($d < 3$), with finite-range Heisenberg-type magnetic interactions, ferromagnetic or antiferromagnetic ordering cannot occur at any nonzero temperature [89]. However, it is crucial to

consider the underlying assumptions of this theorem. Specifically, the Heisenberg interaction in this context is isotropic. This means that in the presence of more generalized interactions or anisotropies, the Mermin-Wagner theorem may not necessarily apply.

3.2 Discovery of two-dimensional magnets

The realization and discovery of two-dimensional magnets happened relatively recently. As previously mentioned, magnetic Hamiltonians with anisotropy are not necessarily prohibited by the Mermin-Wagner theorem from forming long-range magnetic order in two dimensions. In fact, many magnetic materials are better described by non-Heisenberg Hamiltonians, such as the Ising model. Thus, the primary challenges in realizing monolayer magnets were rather technical nature than due to any fundamental physical limitations.

For instance, many material systems are sensitive to air and degrade when reduced to a few layers. Additionally, their transition temperatures often decrease as the layer number is reduced. To achieve magnetic ordering at a practical temperature in a single atomic layer, the bulk material must possess a relatively high critical temperature and have weak interlayer interactions. Moreover, because exfoliated monolayer crystals have small lateral dimensions, the techniques used to probe magnetization must be highly sensitive and compatible with the limited sample size. Overcoming these technical challenges was crucial for the realization of the first single atomic layer magnet.

Various layered magnetic materials have been investigated in the quest to find magnetism in the 2D limit. Notably, the first calculations suggesting that ferromagnetism could persist down to the monolayer limit in CrI_3 date back to 2014 [90]. Subsequent first-principles calculations have indicated that a family of transition metal trichalcogenides, including $CrSiTe_3$, $CrGeTe_3$, $MnPS_3$, and $MnPSe_3$, could also retain magnetic order in their single atomic layers [91]. Experimental evidence supporting this was soon provided for $CrSiTe_3$ through layer-dependent Raman spectroscopy [92]. However, direct confirmation of such a magnetic phase requires magnetometry measurements, such as SQUID, and in the case of ferromagnets, the observation of a hysteretic effect would further substantiate the evidence.

In 2017, research groups at the University of Washington and the University of California, Berkeley, directly demonstrated monolayer ferromagnetism in CrI_3 [93] and $CrGeTe_3$ [94], respectively. Both studies employed the magneto-optical Kerr effect as the experimental probe. In the case of CrI_3, magnetism is layer-dependent; the monolayer exhibits ferromagnetic ordering. However, due to interlayer antiferromagnetic coupling, the system shows a layer-dependent net magnetization, as illustrated in Figure 3.1.

This discovery opens up numerous opportunities for magnetic nanodevices, where the

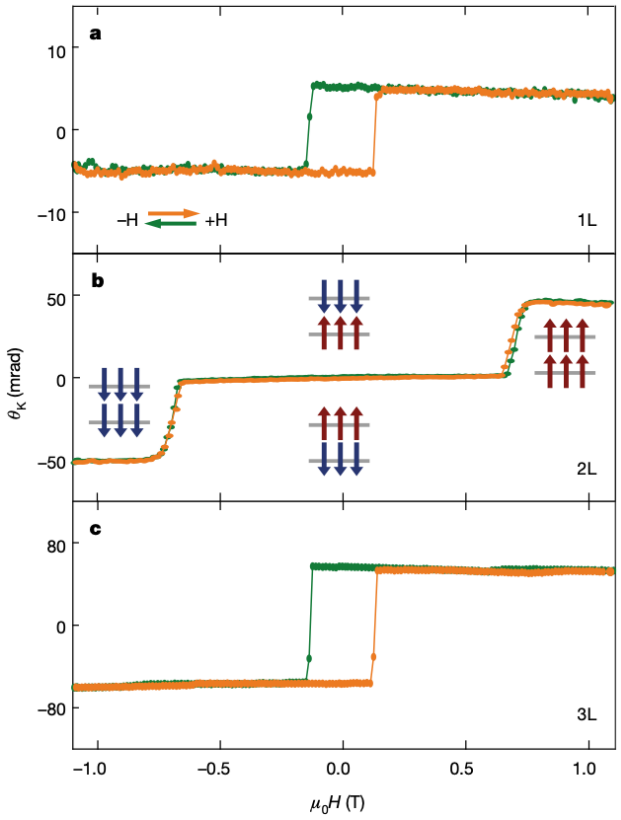

Figure 3.1: Magnetic ordering in mono- and few-layer CrI_3. a. Hysteretic Kerr rotation signal from monolayer CrI_3. The magnetic field is applied in the out-of-plane direction. The states on the two sides of the plot correspond to up and down pointing spin orderings. **b.** Same as in **a** for bilayer system. Near zero magnetic field, the spins in the two layers are anti-aligned, resulting in zero net magnetization, and correspondingly no Kerr signal. As the field exceeds spin-flop transition strength, it induces a ferromagnetically aligned spin in both layers. **c.** Same for the trilayer sample, with a finite net magnetization. Adapted from ref. [93].

high tunability of two-dimensional materials can be exploited. For instance, interface and stacking engineering of magnetism are now feasible, and giant magnetoresistance and spin-filtering effects have been demonstrated in chromium trihalide structures [95]. Additionally, rotating two layers of the same crystal relative to each other can create a periodic stacking pattern. This approach has been shown to produce periodic domain structures with alternating ferromagnetic and antiferromagnetic orderings [96]. Another significant achievement is the electrical control of the magnetic phase. By applying electrostatic gating, researchers have successfully switched between ferromagnetic and antiferromagnetic states [97].

3.3 Layered antiferromagnets

3.3.1 Discovery of monolayer antiferromagnetism

In contrast to their ferromagnetic counterparts, antiferromagnets (AFMs) present additional challenges for detecting magnetic order due to their zero net magnetization. Standard experimental techniques, such as the Kerr effect and magnetometry, are not suitable for AFMs. However, it is precisely this compensated spin structure that grants AFMs several advantages from an application perspective. For instance, with zero net magnetization, AFM states are robust against external magnetic fields and produce no stray fields, making them ideal for magnetic storage devices. Additionally, the spin dynamics in AFMs are much faster than in ferromagnets, with the lowest magnon modes occurring in the terahertz (THz) range, which can significantly enhance magnetic reading and writing processes. Beyond these promising applications, ultrathin AFM systems also serve as a rich platform for exploring magnetic phenomena in two dimensions.

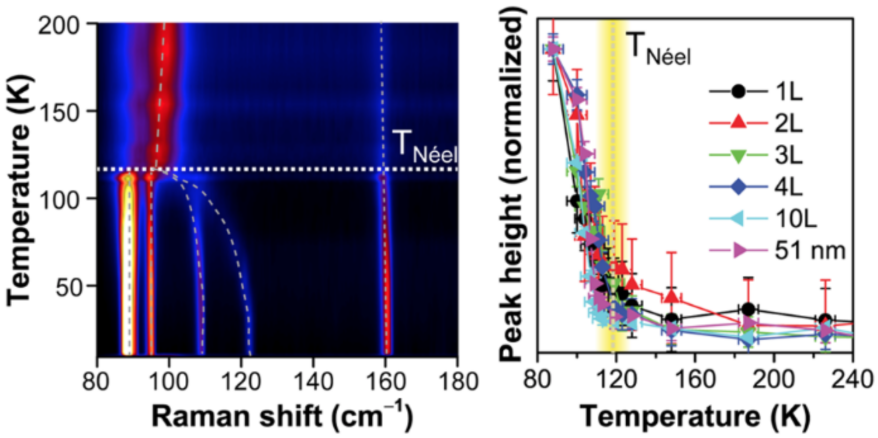

Figure 3.2: Persistence of antiferromagnetism in $FePS_3$ down to monolayer limit. (Left) Temperature dependent Raman spectra of bulk $FePS_3$. Below AFM ordering temperature (∼118K) a magnon mode near 120 cm^{-1} and other low energy phonon modes emerge, serving as a proxy of the AFM ordering temperature. (Right) Dependence of the back-folded phonon intensity on the layer number, and the AFM order persists down to the monolayer limit. Adapted from ref. [98].

Despite the challenges in detecting the antiferromagnetic (AFM) order parameter, a monolayer AFM state was discovered in $FePS_3$, slightly before ferromagnetism in other layered magnets [98], [99]. This discovery leveraged the strong spin-lattice coupling in the material, where magnetic ordering alters the low-energy phonon spectra, allowing Raman spectroscopy to trace the evolution of magnetic order as the layer number decreases. Specifically, the magnetic order doubles the magnetic unit cell, leading to a smaller Brillouin zone.

If the spin-lattice interaction is strong enough, changes in spin ordering will affect the structural degrees of freedom, resulting in zone-folded phonons. These phonons were detected and found to persist down to the monolayer limit. Notably, the transition temperature for monolayer antiferromagnetism is close to that of the bulk, indicating weak interlayer magnetic interactions. In addition to Raman experiments, it was later discovered that the zig-zag type AFM ordering in $FePS_3$ induces significant optical anisotropy [100], with reflectivity differing greatly along the zig-zag and armchair axes. This property has opened up new opportunities for experiments, such as time-resolved spectroscopy, where linear dichroism can be used as a sensor of antiferromagnetism.

As discussed earlier, the Mermin-Wagner theorem prohibits antiferromagnetic (AFM) or ferromagnetic (FM) order for Heisenberg-type magnetic interactions in 1D and 2D systems [89]. However, this theorem does not apply to $FePS_3$, which exhibits Ising-type discrete symmetry breaking. Similar to CrI_3 and $CrGeTe_3$, the strong magnetic anisotropy in $FePS_3$ forces the spins to align in the out-of-plane direction, resulting in a large magnon gap of about 14 meV, and making the system well-described by Ising interactions. Other significant manifestations of the strong spin-lattice coupling in $FePS_3$, such as magnetostriction and the dynamic control of the magnetic state via the lattice, will be discussed in Chapters 4 and 6.

3.3.2 Family of low dimensional antiferromagnetic materials

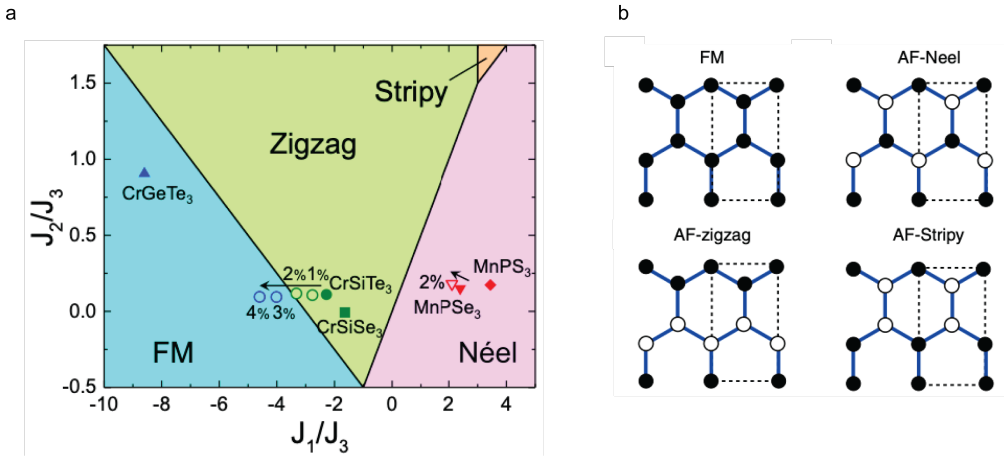

Figure 3.3: Phase diagram of ground state of MPX_3 with the given spin model. **a.** The ground state phase diagram of the spin model give by Eq. (3.1). Various types of spin ordering can be realized, depending on the relative strength and sign of the exchange couplings. **b.** Schematics of the possible orderings on the hexagonal lattice. These are ferromagnetic, Néel-type, stripya and zig-zag AFM. Adapted from ref. [91].

In a broader context, the MPX_3 material family encompasses various members with

different types of magnetic interactions, making it an important platform for investigating magnetism in low-dimensional systems. In these materials, the metal (M) can be Fe, Ni, Mn, Co, or other elements, while the chalcogen (X) can be S or Se. The metal ions with magnetic moments form a hexagonal lattice. To analyze the potential magnetic ground states, the Heisenberg Hamiltonian can be used, taking into account not only nearest-neighbor interactions but also interactions up to the third nearest neighbor, without yet considering detailed anisotropy terms. This Hamiltonian can be expressed as:

$$H = \sum_{\langle ij \rangle} J_1 \vec{S}_i \cdot \vec{S}_j + \sum_{\langle\langle ij \rangle\rangle} J_2 \vec{S}_i \cdot \vec{S}_j + \sum_{\langle\langle\langle ij \rangle\rangle\rangle} J_3 \vec{S}_i \cdot \vec{S}_j \tag{3.1}$$

here J_1, J_2 and J_3 are first, second and third nearest neighbour exchange interactions.

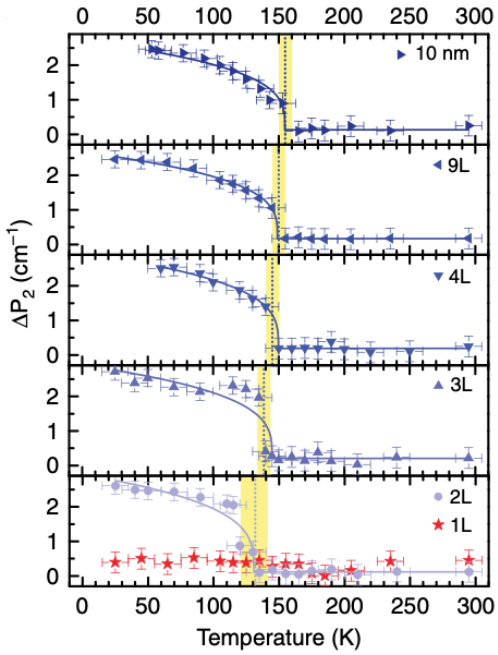

Figure 3.4: Layer dependence of the Néel temperature in $NiPS_3$. The onset of the AFM order in $NiPS_3$ is sensed via energy shift of a particular phonon peak in Raman spectrum. Such magnetic phase transition has been observed down to bilayer limit, whereas the monolayer does not exhibit any change. Vertical yellow lines mark the transition temperature, which changes by small amount with layer number, implying weak interlayer coupling. Adapted from ref. [101].

Depending on the strength and sign of the exchange interactions, a diverse set of magnetic ground states can be realized, as illustrated in Figure 3.3a. These states include ferromagnetic, Néel-type AFM, zig-zag AFM, and stripy AFM, with the respective spin arrangements depicted in Figure 3.3b. Notably, by simply substituting the metal ion, one can alter the magnetic ground state. For example, $MnPS_3$ exhibits a Néel-type AFM ordering with spins

almost aligned in the out-of-plane direction. The exchange couplings in $MnPS_3$ are nearly isotropic, making it well-described by the Heisenberg Hamiltonian. In contrast, $NiPS_3$ exhibits a zig-zag type order, with spins primarily oriented in-plane. $NiPS_3$ is believed to be described either by the XXZ model ($J_x = J_y \neq J_z$) or the XY model ($J_x = J_y, J_z = 0$) [101]. This universality class exhibits unique behaviors in the 2D limit. Berezinskii [102], along with Kosterlitz and Thouless [103], demonstrated that 2D XY models host an unusual ground state characterized by algebraic order, also known as the Berezinskii-Kosterlitz-Thouless (BKT) transition. With these exfoliable layered magnets, such transitions can now be directly studied. Raman experiments on $NiPS_3$ have shown that, unlike other related compounds, $NiPS_3$ maintains its magnetic order down to the bilayer limit, while in the monolayer, strong fluctuations prevent ordering [101] (see Figure 3.4).

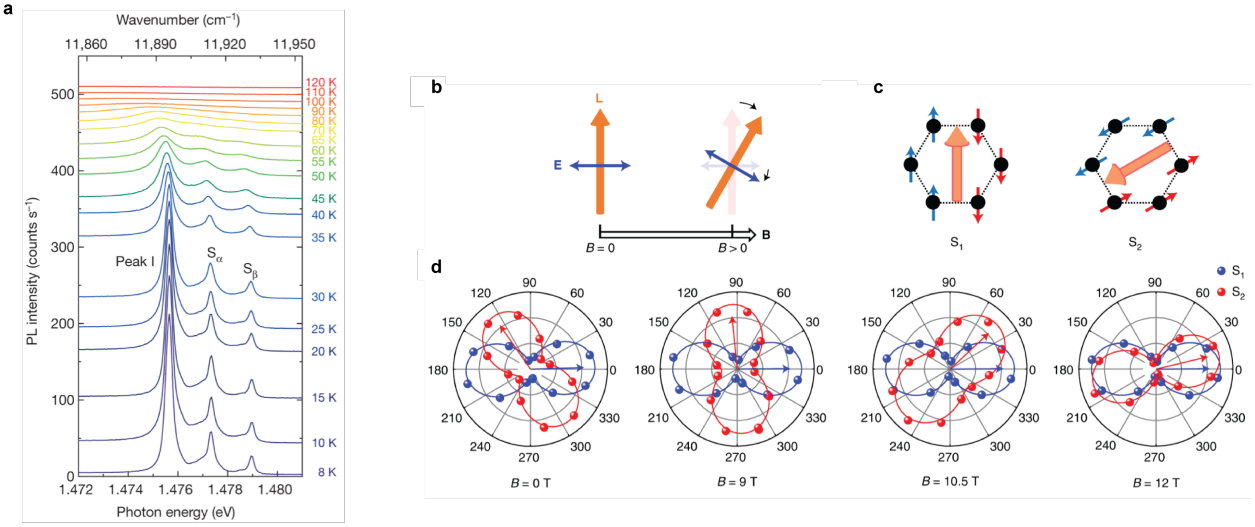

Figure 3.5: Zig-zag order induced polarized emission from $NiPS_3$. a. Temperature dependent PL spectra. Peak I is a spin-orbit entangled exciton, and the side peaks labeled as S_α and S_β are identified as magnon sidebands. **b.** Illustration of Néel vector (L) canting with external magnetic field. **c.** Initial spin alignments of two different samples (S_1 and S_2). The Néel vector of S_1 is oriented perpendicular to the magnetic field. Therefore, it will not be canted with magnetic field. **d.** Polarization resolved PL response, integrated near the exciton resonance. The orientation of the emission from S_2 smoothly follows the orientation of the magnetic field. **a** is adapted from ref. [104], **b** is adapted from [105].

In addition to strong spin-lattice coupling, these materials exhibit optomagnetic properties, adding to their intriguing characteristics. A suite of spectroscopic tools, including resonant inelastic X-ray scattering, photoluminescence, and optical absorption, has revealed a coherent many-body localized exciton in $NiPS_3$ arising from strong spin-orbit coupling [104]. This coherent state is marked by an extremely sharp linewidth (300 μeV) in the photoluminescence spectrum, which emerges below the Néel temperature. Moreover, the

zig-zag spin ordering induces anisotropy in the photoluminescence emission, with stronger emission when the polarization is parallel to the zig-zag chain and weaker emission when it is perpendicular. The intrinsic connection between the polarized emission and the underlying magnetic structure has been further demonstrated by examining the emission under strong in-plane magnetic fields, which can reorient the individual spin orientations. Notably, the photoluminescence polarization follows the direction of spin canting under these conditions [105] (see Figure 3.5).

3.3.3 Noncollinear layered antiferromagnets

Noncollinear magnetism, where spins are neither fully aligned nor anti-aligned with each other, is an important area of study in nanomagnetism. One of the most notable examples is magnetic skyrmions, which are particularly attractive for topologically protected magnetic storage device applications. In addition to skyrmions, there are various other magnetic textures and long-range spin orderings, such as helical and spiral configurations. The emergence of noncollinear magnetism typically results from the competition among different magnetic energy scales. For instance, in a simple chain of spin-1/2 moments with Heisenberg interactions, if the nearest-neighbor and next-nearest-neighbor exchange couplings have opposite signs, a spiral ordering can arise (Figure 3.6a). More generally, other factors such as anisotropy terms, Dzyaloshinskii-Moriya interactions, or geometric and exchange frustrations can lead to diverse types of noncollinear orderings.

One important implication of noncollinear magnetic order is the potential for magnetism-induced ferroelectricity in systems with sufficient spin-lattice coupling. The coexistence of these two different ferroic orderings is referred to as multiferroicity. Specifically, when ferroelectricity emerges as a secondary order due to magnetic ordering, it is known as a type-II multiferroic. A prominent example of such behavior in layered magnets is NiI_2. Pyroelectric current measurements at various temperatures and magnetic fields have demonstrated that NiI_2 and other dihalides are multiferroic [107]. In Chapter 8, we will explore other spectroscopic experiments and demonstrate that the multiferroicity in NiI_2 persists down to the monolayer limit.

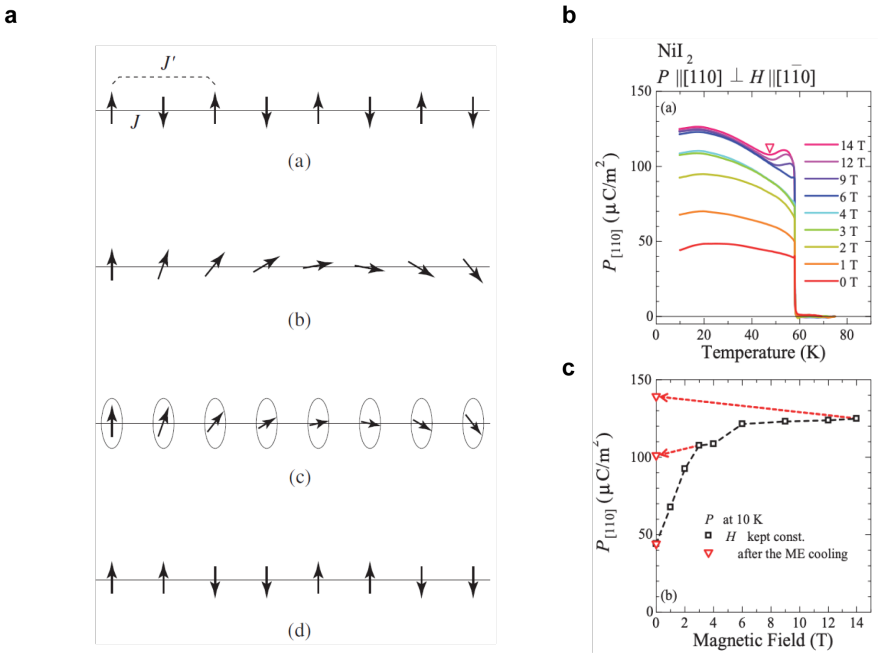

Figure 3.6: Noncollinear spin ordering in a 1D chain. a. Possible types of orderings with various strength and signs of the nearest and next nearest neighbour exchange interactions. These include Néel type AFM, spiral, helical and collinear AFM order with different periodicites. **b** and **c** are temperature and magnetic field dependence of the ferroelectric polarization in NiI_2, indicating a type-II multiferroic order. **a** is adapted from ref. [106], **b** and **c** are adapted from [107].

Chapter 4

THz field-induced metastable magnetization near criticality in $FePS_3$

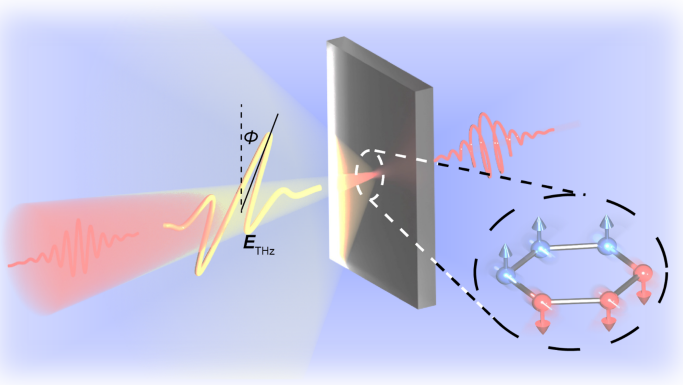

Contents

Controlling the functional properties of quantum materials with light has emerged as a frontier of condensed matter physics, leading to discoveries of various light-induced phases of matter, such as superconductivity [108], ferroelectricity [63], [64], magnetism [70], [109], [110] and charge density waves [46]. However, in most cases, the photoinduced phases return to equilibrium on ultrafast timescales after the light is turned off, limiting their practical applications. In this study, we use intense terahertz pulses to induce a metastable magnetization with a remarkably long lifetime of over 2.5 milliseconds in a van der Waals antiferromagnet, $FePS_3$. The metastable state becomes increasingly robust as the temperature approaches

the antiferromagnetic transition point, suggesting a significant role played by critical order parameter fluctuations in facilitating extended lifetimes. By combining first principles calculations with classical Monte Carlo and spin dynamics simulations, we find that the displacement of a specific phonon mode modulates the exchange couplings in a manner that favors a ground state with finite magnetization close to the Néel temperature. This analysis also clarifies how the critical fluctuations of the dominant antiferromagnetic order can amplify the magnitude and the lifetime of the new magnetic state. Our discovery demonstrates the efficient manipulation of the magnetic ground state in layered magnets through non-thermal pathways using terahertz light, and establishes the regions near critical points with enhanced order parameter fluctuations as promising areas to search for metastable hidden quantum states.

This chapter is based on the following unpublished work:

B. Ilyas†, T. Luo†, A. V. Hoegen†, E. V. Boström† *et al.* Terahertz field-induced metastable magnetization near criticality in $FePS_3$. *Under Review*, (2024)

The author of this dissertation contributed to the following aspects of the work: conceiving the study, designing and constructing the experimental setup, conducting the experiments, analyzing and interpreting the experimental data, and writing the manuscript.

4.1 Light as a novel tuning knob of controlling quantum materials

Thermal, quantum and order parameter fluctuations all play a critical role in shaping the phase diagrams of quantum materials. They typically arise close to phase transitions where the relative energy scales of different microscopic degrees of freedom become comparable. These strong fluctuations can hinder or facilitate the emergence of long-range order. For example, the antiferromagnetic fluctuations in underdoped cuprates are suggested to be the origin of the enigmatic pseudogap phase [111]–[113]. On the other hand, strong quantum fluctuations of the atomic positions in $SrTiO_3$ prevent a long-range ferroelectric ordering at any temperature [114]. Fluctuations also offer the ability to actively control the material properties by applying external stimuli such as pressure, strain, electric fields, or by tailoring the materials dielectric environment [115], [116], which can tune the relative energy scales of the system in favor of a new ground state.

In addition to these static tuning knobs, photo-excitation by intense light pulses has emerged as a novel dynamical method of control, resulting in numerous light-induced symmetry broken states of matter. However, the lifetimes of these phases are predominantly in the picoseconds to nanoseconds range [46], [63], [70], [108], [117], with few examples of metastable

cases [17], [40], [64], [109]. Finding viable strategies for stabilizing non-equilibrium states remains an ongoing and complex task. Moreover, high photon energy laser pulses, used in most of the experiments, deposit significant amount of thermal energy and perturb the underlying order, impeding deterministic control [39]. In this respect, terahertz pulses have recently garnered wide attention. The low photon energy of these sources enable selective excitation of collective modes to large amplitudes while keeping the orbital and electronic degrees of freedom in the ground state.

In this chapter, we demonstrate a light-induced metastable magnetization in the layered antiferromagnetic insulator $FePS_3$, with a lifetime of 2.5 milliseconds. We achieve this by resonantly driving its low-energy magnon and phonon modes to high amplitudes through illumination with intense terahertz (THz) pulses. This in turn modifies the exchange parameters driving the system into a state with a finite magnetization. The THz photon energy (< 25 meV) is orders of magnitude smaller than the electronic gap of $FePS_3$ ($\sim$1.6 eV) [118] and therefore preserves the low-energy physics and strong spin-lattice coupling. We find that the lifetime and amplitude of the terahertz-light induced magnetization diverges close to the Néel temperature, as a result of its coupling to the static and dynamic critical fluctuations of the dominant antiferromagnetic order parameter. Our results thereby highlight the crucial role that critical order parameter fluctuations play in stabilizing this non-equilibrium state.

4.2 Experimental methods

4.2.1 THz pump and magneto-optical probe experiments

Output of Ti-sapphire amplifier (35 fs pulse duration, 800 nm wavelength, 1 kHz repetition rate) is split into pump and probe arms. Pump arm seeds an optical parametric amplifier (OPA), and the signal output of OPA at 1300 nm wavelength is used to generate THz radiation via optical rectification in an organic crystal. A set of parabolic mirrors are used to guide the THz beam and focus tightly on a diffraction limited spot of size 180 ± 10 μm full width at half maximum (FWHM) on the sample surface at normal incidence. The THz beam spot size is measured using a THz camera (Rigi S2, Swiss Terahertz). An optical chopper was placed in the OPA beam path to measure polarization rotation $\Delta\theta$ and ellipticity change $\Delta\eta$ of the probe induced by pump (THz) pulse. The spot size of the 800 nm probe beam is 54 ± 2 μm, measured using a CMOS camera at the sample location. The entire path of THz beam propagation and the organic crystal are kept in a box purged with dry air to avoid water absorption of THz. A translation stage placed on the probe arm (800 nm) is used to control the time delay between THz and probe pulses. For polarization rotation and ellipticity change measurements a half wave-plate (HWP) and a quarter wave-plate (QWP) were used,

respectively. A Wollaston prism is placed on the path of the transmitted beam after the HWP/QWP, and the two split beams with orthogonal polarizations were detected with a pair of silicon photodetectors. For circular dichroism (CD) measurements in transmission a QWP was placed on the probe path before the sample, and the transmitted beam was detected directly by a single photodetector. The purity of the probe polarization state, both linear and circular, were carefully analysed at the sample position by using a polarizer and a powermeter. The cryostat window was placed on the path during the polarization characterization process to take into account the effect of the window on the polarization. The detailed schematics of the experimental setup is shown in Figure 4.1.

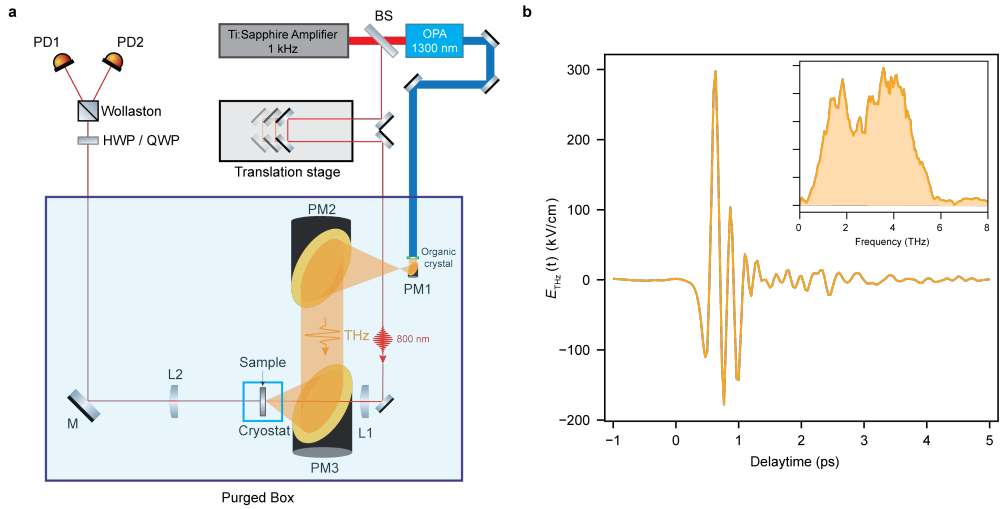

Figure 4.1: Experimental setup for intense THz excitation. a. Detailed schematics of the experimental setup. The abbreviations used here: BS - beam splitter; OPA - optical parametric amplifier; PM - parabolic mirror; L - lens; HWP - half wave plate; QWP - quarter wave plate; PD - photo-diode. **b.** Field profile of the THz pulse. Peak field strength is ∼300 kV/cm. Fourier spectrum of the field is shown in the inset. .

4.2.2 Sample preparation

We synthesized $FePS_3$ crystals using a chemical vapor transport method. All the powdered elements (purchased from Sigma-Aldrich): iron (99.99% purity), phosphorus (99.99%) and sulfur (99.998%), were prepared inside an argon-filled glove box. After weighing the starting materials in the correct stoichiometric ratio, we added an additional 5 wt of sulfur to compensate for its high vapor pressure. After the synthesis, we carried out the chemical analysis of the single-crystal samples using a COXEM-EM30 scanning electron microscope equipped with a Bruker QUANTAX 70 energy dispersive X-ray system to confirm the correct stoichiometry. We also checked the XRD using a commercial diffractometer (Rigaku Miniflex

II). We cleaved samples before placing them into high vacuum ($\sim 10^{-7}$ torr) to expose a fresh surface without contamination and oxidation. The sample thicknesses used in these experiments ranged from 20 μm to 60 μm, as determined using a profilometer.

4.3 Family of layered antiferromagnets

4.3.1 Magnetic and lattice structure of $M\mathrm{PS}_3$

$M\mathrm{PS}_3$ (where M = Fe, Ni, or Mn) is a group of honeycomb lattice van der Waals antiferromagnetic (AFM) materials, which host stable AFM orders down to atomically thin limits [98], [101], [119], [120]. The specific choice of the transition metal M determines the strength and the sign of the exchange interactions which gives rise to diverse types of spin orderings [91], [121], [122]. The spin structure exhibits a complex interplay with other degrees of freedom such as the lattice and orbital ordering, which manifested as distinct fingerprints in recent experiments [98], [104], [123]–[129]. FePS_3 stands out among the other members of the $M\mathrm{PS}_3$ family in two characteristics. First, it features a pronounced single-ion anisotropy [130], [131] arising from spin-orbit coupling enabled by unquenched orbital moments of Fe^{+2} ions. Together with a ferromagnetic nearest neighbor and antiferromagnetic third nearest neighbor exchange interaction, this results in a zig-zag AFM ground state below $T_\mathrm{N} = 118$ K. The large single-ion anisotropy forces the magnetic moments to align in the out of plane direction, which then arrange ferromagnetically within the zig-zag chains (a-axis), and antiferromagnetically between the adjacent chains (see Figure 4.2a, the structure in the circle, d, e, f). Second, FePS_3 exhibits a particularly strong spin-lattice interaction [98], [122], [123], [132], which is exemplified by recent magneto-Raman experiments that revealed strong hybridization between the low energy magnon and phonon modes [100], [133]–[135]. This may offer an effective pathway to manipulate the magnetic order by distorting the crystal lattice either statically by applying strain or pressure or dynamically by driving the relevant lattice modes to large amplitudes.

4.3.2 Resonant excitation of low energy collective modes

Recent experiments tried to leverage the dynamical approach to achieve an ultra-fast manipulation of the magnetism in FePS_3 through excitation of the electronic subsystem with high photon energy light pulses [123], [124], [132], [137], [138]. This excitation couples only indirectly to the lattice, yet is still effective in driving coherent oscillations of the lattice (phonons) and spins (magnons) and demonstrated an ultra-fast weakening of the antiferromagnetic order. Here we use an alternative strategy to leverage the strong spin-lattice

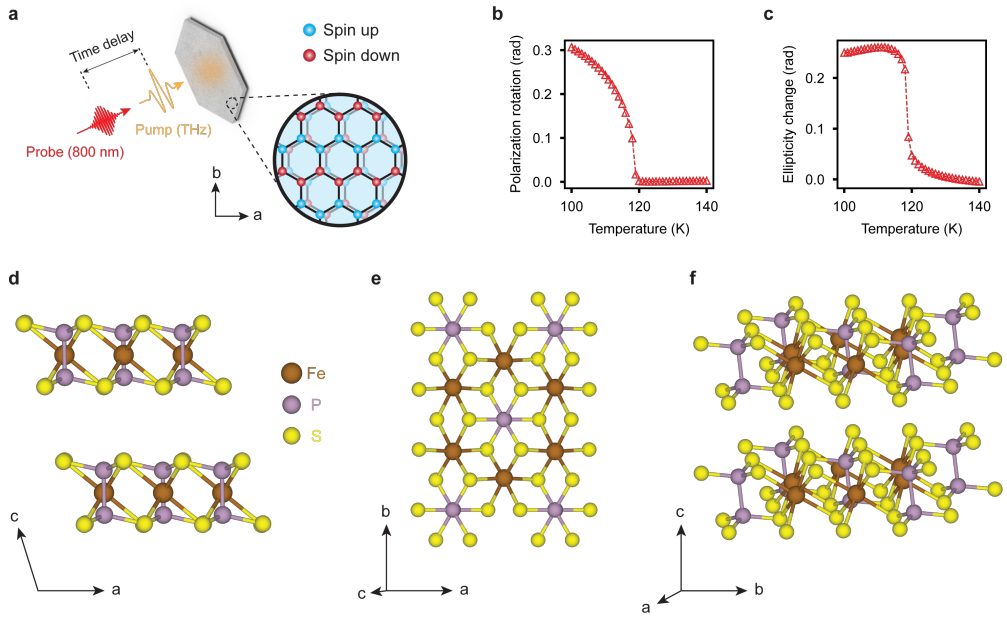

Figure 4.2: Experimental schematics and static optical anisotropy. a. Intense THz pulse (orange) drives low energy collective excitations in $FePS_3$ and the induced transient changes in optical properties are probed with 800 nm probe pulse (red). Fe^{2+} ions form a hexagonal lattice and their spins arrange ferromagnetically along the zig-zag chain (a-axis) and antiferromagnetically between the adjacent chains (the structure in the circle). The magnetic coupling between the layers is antiferromagnetic together with a small interlayer shear distortion along the a-axis. **b.** and **c.** are temperature dependencies of polarization rotation and ellipticity change signals in equilibrium, respectively. **d.** Crystal structure schematics of the a-c plane projected along $\mathbf{b}^*$-axis. **e.** a-b plane projected along $\mathbf{c}^*$-axis. **f.** 3D view of the crystal structure. All the structures were generated by VESTA software [136].

coupling. We drive the hybridized spin and lattice modes directly with intense THz pulses. To study the role of resonant driving, we use two THz sources generated via optical rectification in different nonlinear crystals (see Experimental methods section above). For resonant excitation, we use a THz field with a broad spectrum that covers the range of 0.2 - 6 THz (Figure 4.3b, shown in orange, labeled as "THz_1"), with a peak field of $\sim$ 300 kV/cm (Figure 4.1b). For off-resonant excitation, we use a THz source with a spectrum primarily concentrated at energies below $\sim$ 2 THz (Figure 4.3b, shown in brown, labeled as "THz_2"), which is not resonant with any of the lattice or spin excitations. The peak field in this case is $\sim$ 600 kV/cm. We monitor the ensuing dynamics induced by the THz pump pulse by using a weak near-infrared (800 nm) probe pulse with variable time delay Δt and analyzing the polarization state of the transmitted beam (see Figure 4.2a). Specifically, we measure the ultra-fast polarization rotation and ellipticity of the initially linearly polarized probe pulses.

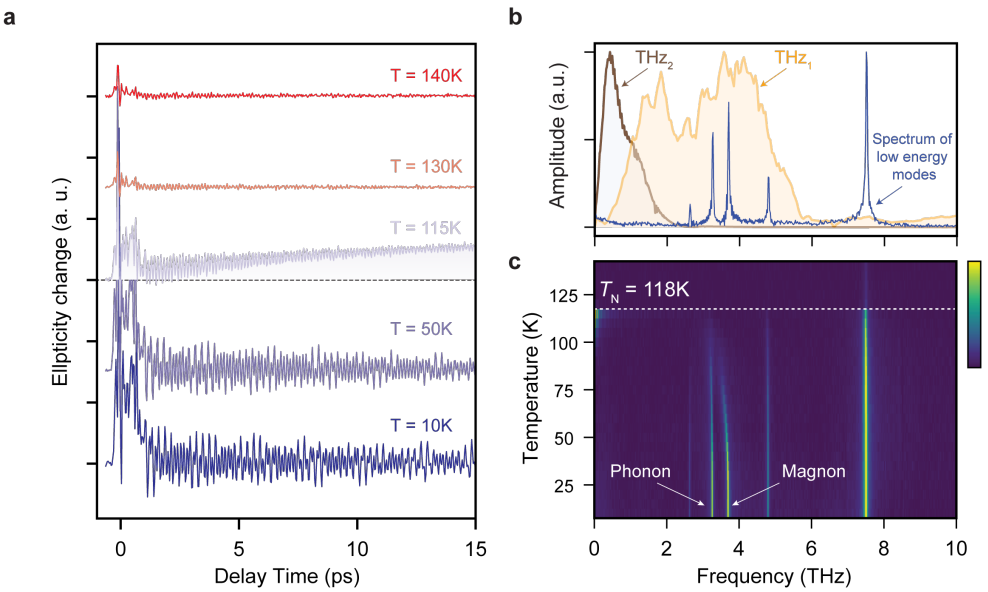

Figure 4.3: THz field-driven low energy modes. a. Probe ellipticity change signal traces at selected temperatures exhibit coherent oscillations induced by THz-field. As temperature approaches the transition point (e.g. at $T = 115$K), the time traces start to build a net-positive response. **b.** Fourier transform of the oscillations at $T = 10$K (dark blue) contains 5 prominent peaks that correspond to a magnon and phonon modes. The spectral content of the excitation pulse is shown in orange, labeled as THz_1. For additional experiments a THz field generated from a different source is used, with a spectrum shown in brown and labeled as THz_2, and it is not resonant with any of the modes. **c.** Temperature evolution of the Fourier spectrum. Colorbar is normalized. A notable change in the spectra occurs below the Néel temperature ($T_\text{N} = 118$ K) and the magnon mode softens upon increasing temperature.

4.3.3 Optical anisotropy probes as a proxy of the zig-zag AFM order

We establish the relationship between these polarization characteristics and the underlying magnetic order by measuring the temperature dependence of their equilibrium values. The static polarization rotation signal, $\theta_{\text{st.}}(T)$, sets on below the transition temperature T_N and has an order parameter-like behavior (Figure 4.2b), indicating its sensitivity to the AFM order. The static ellipticity change of the near-infrared light, $\eta_{\text{st.}}(T)$, on the other hand, has a markedly different temperature dependence. Below the Néel temperature, $\eta_{\text{st.}}(T)$ is strongly enhanced, but it also shows a finite tail above T_N which is absent in the polarization rotation signal, suggestive of sensitivity to magnetic fluctuations (Figure 4.2c). Quantitatively, the ellipticity change and polarization rotation measure the anisotropy in the real and imaginary parts of the complex refractive index, respectively (see Section 2.1.1). Therefore, by measuring these two quantities, we can comprehensively study the THz-induced magnetic

dynamics in $FePS_3$. We note that similar measurements in equilibrium were performed on other systems [105], [129], [139], and have established these optical anisotropy probes as a good proxy of the zig-zag AFM order.

4.4 THz induced magnetic and lattice dynamics

4.4.1 Low temperature coherently driven collective modes

Figure 4.3a shows representative traces of the time-resolved ellipticity change at selected temperatures. The transient changes induced by the broadband THz pulse ("THz_1") consist of fast oscillations and a strong positive signal near time zero. The positive signal near zero time delay, with a positive background, occurs as a result of the so called terahertz Kerr effect and marks the temporal overlap of pump and probe pulses [140]. This is followed by oscillatory features at later times. The Fourier transform of these oscillations at 10 K is shown in Figure 4.3b (blue). We can identify four distinct phonon modes and a magnon, the frequencies of which are in good agreement with Raman [134] and infrared spectroscopies [100] (see Figure 4.4). Most of these modes are spectrally covered by our broad THz excitation spectrum (Figure 4.3b in orange). We note that several phonons observed in our experiments are found to be visible both in Raman and infrared spectra, despite the fact that $FePS_3$ preserves inversion symmetry [141]. This is explained by the strong hybridization of the magnon and phonon modes, which alters the selection rules [100] and allows these modes to be visible in both of these experimental probes. The defining features of the transient ellipticity signal at low temperatures are in qualitative agreement with the polarization rotation signal.

4.4.2 Temperature dependence of the coherent modes

Next, we turn to the temperature dependence of the coherent modes (see Figure 4.3c) and the dynamics close to the Néel temperature. The spectrum of the coherent oscillations undergoes an abrupt change below the Néel temperature and the magnon mode softens upon temperature increase. In particular, the observed phonon modes with energies below ~ 5 THz are found to vanish above T_N, indicating that they are zone-folded modes induced by the zigzag AFM order. Notably, as we approach the transition temperature, a long-lived signal starts to build up in response to the THz pump, as can be seen in the 115 K trace in Figure 4.3a. This signal manifests as a low frequency spectral weight near T_N in Figure 4.3c.

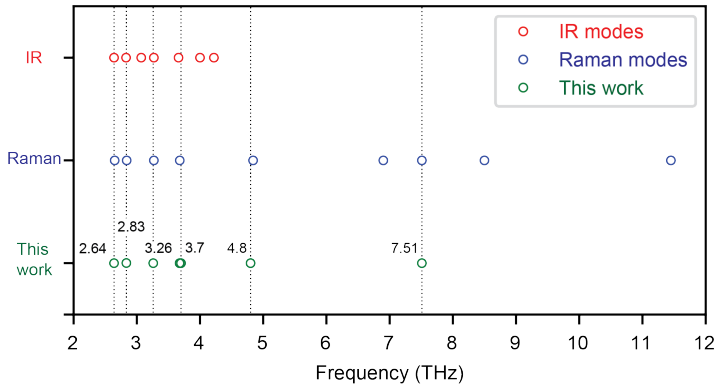

Figure 4.4: List of low energy modes. Mode frequencies as detected by Raman [98] and infrared [100], [135] spectroscopies. Out of seven modes observed in this work, 4.8 THz and 7.51 THz modes are only observed in Raman spectra, whereas the other three phonon modes (2.64 THz, 2.83 THz, and 3.27 THz) and two magnon modes near 3.69 THz appear in both Raman and infrared measurements. Error bars are smaller than the marker sizes.

4.5 Nonequilibrium state with a net magnetization

4.5.1 Changes in polarization state

To further analyze the nature of this long-lived state, we extend the delay time window up to a maximum of ~ 175 ps and observe that at $T_N = 118$ K the signal is still growing with no sign of saturation, both in the polarization rotation $\Delta\theta(t)$ (Figure 4.6a) and the ellipticity change $\Delta\eta(t)$ (Figure 4.6d) channels. Figure 4.6b and e show the maximum values of these quantities extracted at $t = 175$ ps, $\Delta\theta_0(T)$ and $\Delta\eta_0(T)$, as a function of temperature. Both quantities peak at the Néel temperature, however they display distinct behaviors: $\Delta\theta_0(T)$ has an asymmetric shape across T_N, whereas $\Delta\eta_0(T)$ is symmetric.

To identify the degrees of freedom that are responsible for the long-lived signal, we first consider the possibility of electronic excitations. In our experimental setting, there are two potential pathways of carrier excitation: (i) multiphoton absorption and (ii) tunneling. The multiphoton absorption process is highly suppressed due to the $2-3$ orders of magnitude mismatch in energies of the gap (~ 1.6 eV) [118] and THz photons (< 25 meV). To explore the tunneling scenario, which is more efficient at higher electric fields, we repeat the experiments with more intense single-cycle THz pulses which spectrally do not overlap with any of the low energy modes (see Figure 4.3b, "THz_2"). For this purpose a strong THz pulse is generated by tilted-pulse front technique in $LiNbO_3$ [50] and the polarization rotation is measured in the same way as described above. The details of the experimental setup has been reported elsewhere [142]. The spectrum of the generated pulse is given in Figure 4.7a (blue). As

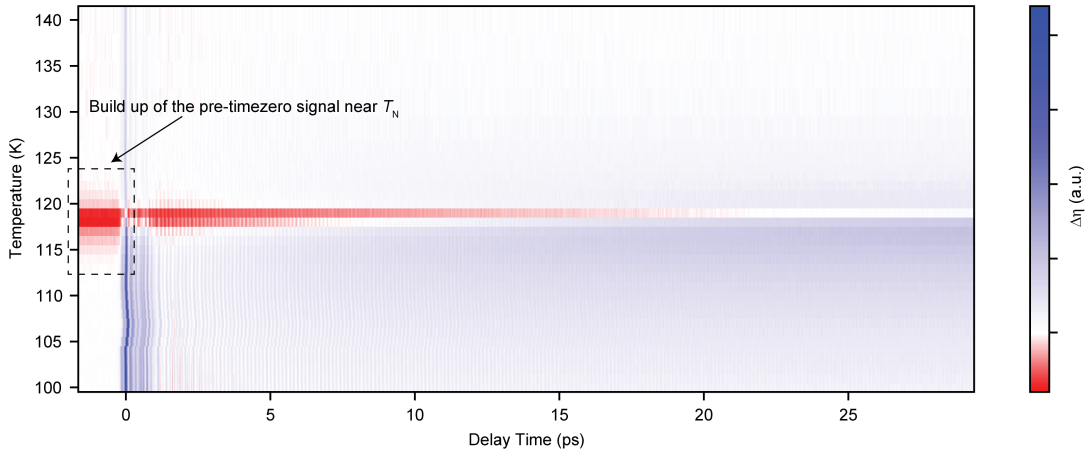

Figure 4.5: Temperature dependence of ellipticity change time traces. Raw data of temperature dependent $\Delta\eta$ experiments performed near Néel temperature with fine steps. It shows a marked change near transition point. A box with black dashed lines marks the region near transition a build-up of pre-time zero signal. Figure 4.6e is obtained by measuring the signal amplitude at long time delays (∼170 ps). The pre-timezero signal decreases with temperature for $T < 118K$, whereas it increases with increasing temperature for higher temperatures.

can be seen in Figure 4.7b, the long-lived signal is not observed when the driving field is off-resonant. This observation rules out the possibility of carrier generation upon pumping with THz as discussed in the text, which in turn indicates that the long-lived signal must be triggered by resonant excitation of the low energy modes. This observation highlights the fundamental difference between the THz drive and the previous works with above-gap photo-excitations [124], [138].

4.5.2 Nonthermal dynamics

Since the THz spectrum covers several mode resonances, the temperature increase in the lattice or in the spin subsystems, and consequently the reduction of the order parameter cannot be ignored. To understand the role of this heating effect, we compare the THz-induced dynamics and the static optical responses. For this purpose, we integrate the temperature dependent functions $\Delta\theta_0(T)$ and $\Delta\eta_0(T)$ (Figure 4.6b and e) from a high temperature cut-off T_{high} down to the temperature T, and plot the resulting functions $\theta_{\text{int}}(T) = \int_T^{T_{\text{high}}} \Delta\theta_0(T)$ and $\eta_{\text{int}}(T) = \int_T^{T_{\text{high}}} \Delta\eta_0(T)$ together with the static values $\theta_{\text{st.}}(T)$ and $\eta_{\text{st.}}(T)$. In the polarization rotation channel, the static and the integrated dynamic responses are nearly identical to each other (Figure 4.6c) indicating that the change $\Delta\theta_0(T)$ is mainly due to a THz-induced change in temperature. Since $\theta_{\text{st.}}(T)$ is sensitive to the AFM order parameter, $\Delta\theta_0(T)$

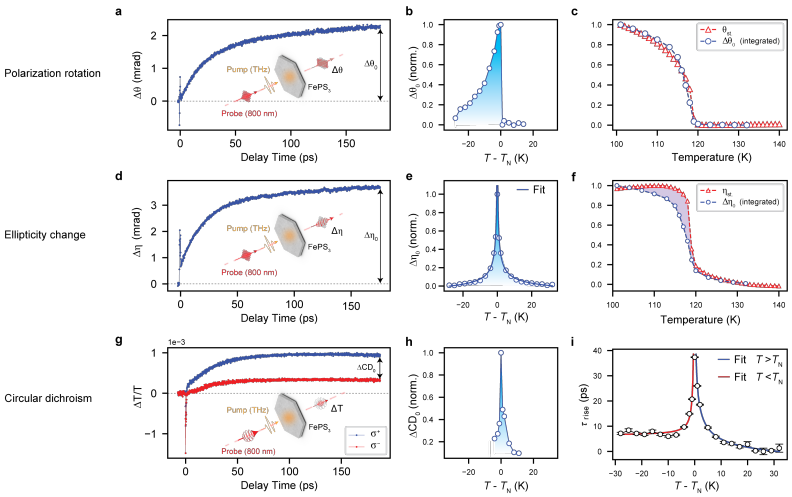

Figure 4.6: THz field-induced nonequilibrium state with a net magnetization. THz field induced long-lived polarization rotation **a**, ellipticity change **d**, and circular dichroism **g** signals, all measured at 118K. Note: all three time traces are shifted vertically, so that the pre-time zero signal is at zero level. The temperature dependent raw data are provided in Figure 4.5. The temperature dependence of the maximum signal values labeled as $\Delta\theta_0(T)$, $\Delta\eta_0(T)$, and $\Delta\mathrm{CD}_0(T)$, measured at ∼170 ps, are given in **b**, **e**, and **h**, respectively. To analyze the THz induced heating effect, we measured static polarization rotation and ellipticity change signals, as shown in **c** and **f** (red). Further, we integrate the dynamic changes in of these optical properties (**b**, **e** and **h**) in temperature and compare with static values. In the case of polarization rotation the static and dynamic responses (integrated) coincide well, indicating THz induced response is mostly due to heating effect. In the case of ellipticity change, there is a sizeable contrast between the two responses, hinting at an additional non-thermal effect. This observation together with ΔCD response in **h**, imply a nonequilibrium state with a net magnetization. The $\Delta\eta_0(T)$ in **i**, is fit by a power law and the exponent is 0.56 ± 0.05. **i.** The critical behavior of the rise time dynamics is fit with a power law, and the obtained critical exponents are $\nu z = 1.07 \pm 0.27$ and $\nu z = 0.44 \pm 0.07$, for temperatures below and above T_N, respectively.

can be assigned to a thermal reduction of the AFM order parameter. Additionally, lattice distortions due to nonlinearly excited phonons can also reduce the AFM order and lead to a polarization rotation signal. On the other hand the behavior in the ellipticity channel is distinct (Figure 4.6f). There is a considerable deviation of the THz-induced response from the static signal, which implies the presence of an additional non-thermal contribution. Notably, the sharp divergences of $\Delta\theta_0(T)$ and $\Delta\eta_0(T)$ near T_N indicate an infinitesimal increase in the spin temperature induced by the THz field, since a significant heat deposition would lead to a broad peak shifted away from T_N, as observed in works with above gap excitation [138].

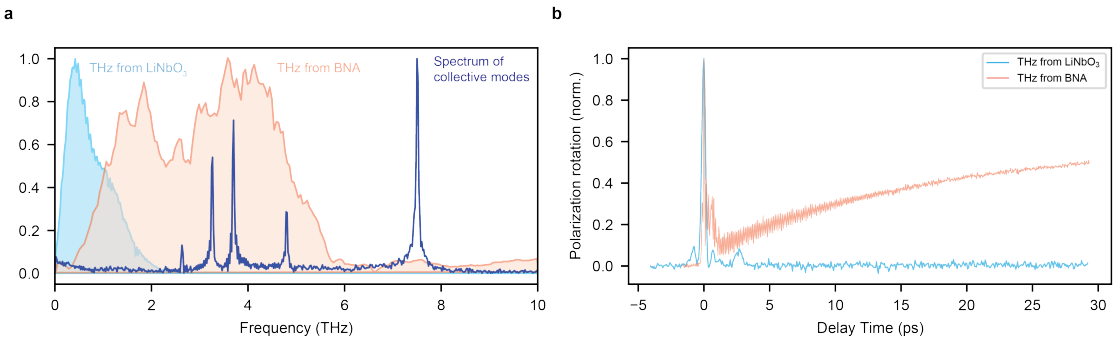

Figure 4.7: Importance of nonlinearly excited low energy modes. We repeat the same experiment with single-cycle THz excitation pulses generated from $LiNbO_3$ by tilted-pulse-front technique [50]. The THz spectrum is given in **a** (blue), that is below the lowest phonon observed in $FePS_3$. In **b** we compare signals induced by two different THz pulses generated by organic crystal (BNA) and $LiNbO_3$ at T =118 K, and in the case of $LiNbO_3$ we did not observe any long-lived signal.

4.5.3 Circular dichroism

The ellipticity of our initially linearly polarized light can be caused by two distinct optical mechanisms, linear birefringence and circular dichroism (CD). However, in a fully-compensated antiferromagnet with zero net magnetization, such as $FePS_3$, we do not expect an equilibrium CD in the optical range. Moreover, a CD response can only occur in certain nonmagnetic media, such as in systems with a chiral lattice structure. However, detailed characterizations of the crystal structure of $FePS_3$ [124], [143] show no sign of chiral behavior. To investigate the possibility of a nonequilibrium CD, we study the response of circularly polarized probe pulses to THz excitation. We find a significant difference in the relative transmission of left- (σ_-) and right-handed (σ_+) circularly polarized light (Figure 4.6g), i.e. a circular dichroism, with a slow rise-time similar to the transient ellipticity. Additionally, the temperature dependence of the transient CD (Figure 4.6h) resembles that of the ellipticity, suggesting that the ellipticity signal is indeed caused by a THz-induced CD. The observed out-of-equilibrium dichroism signal, $\Delta\mathrm{CD}(T)$, therefore indicates that the new photoinduced state has a net out-of-plane magnetization, which coexists with the weakly suppressed but still dominant zig-zag AFM order.

4.6 Decay dynamics of the nonequilibrium magnetic state

4.6.1 Pre-time zero signal

We examine the dynamics of the induced nonequilibrium magnetic state. We note that in Figure 4.6a, d, and g, the time traces are shifted vertically, such that all the traces are set to zero before time zero. However, in the raw data shown in Figure 4.8a and Figure 4.5, as we approach T_{N}, a significant amount of pre-time zero signal develops. The existence of a pre-time zero signal hints at a relaxation time τ_{decay} comparable with the separation time between the probe and pump pulses (1 ms and 2 ms). In this case, the effects of consecutive pump pulses accumulate and lead to an ellipticity change of the probe even in the pump-off region. A larger ratio between the pre-time zero signal and the maximal signal after time zero indicates a slower decay of the pump induced $\Delta\eta$. From the modeling as detailed in the next section, τ_{decay} can be extracted, and its temperature evolution is shown in Figure 4.8b. A clear divergence around 118 K is observed. However, we note that the value of τ_{decay} extracted here is an overestimation since the maximal value of the signal after time zero is not reached in the measurement time window (30 ps). To further substantiate our model and obtain a more accurate τ_{decay}, we extend the temporal separation between the THz pulses (τ_{pump}) from 2 ms to 5 ms (the orange trace in Figure 4.8c), allowing the system to fully relax to equilibrium conditions before the arrival of the subsequent THz pulse. As we vary the time of the probe in the pump-off region (τ_{probe}) from 1 ms to 4 ms, the pre-time zero signal gradually decays (Figure 4.8d), corresponding to the decay of $\Delta\eta$ in the pump-off region (the blue trace in Figure 4.8c). By fitting the pre-time zero signal for different τ_{probe} with the same model (see next section), we find the relaxation time of the metastable state at 118 K to be $\tau_{\mathrm{decay}} \sim 2.5$ ms. Therefore the THz-induced state with a net magnetization has a remarkably long lifetime.

4.6.2 Extraction of relaxation time of the metastable state

THz pump and $\Delta\eta(T)$ probe signal is measured as a difference between the probe ellipticity in pump-on and pump-off regions. As illustrated in Figure 4.8c, if the relaxation time of the metastable state exceeds one millisecond, the pump-off state (white region in Figure 4.8c) will carry the tail of pump-on region signal, therefore giving rise to a pre-time zero difference between pump-on and pump-off regions.

The connection between the relaxation time (τ_{decay}) and the pre-time zero signal can be modeled as follows. We assume each pump pulse will induce a change in ellipticity signal that decays in time as $Ae^{-\frac{t}{\tau_{\mathrm{decay}}}}$, where t is the time duration after the pump. Then the

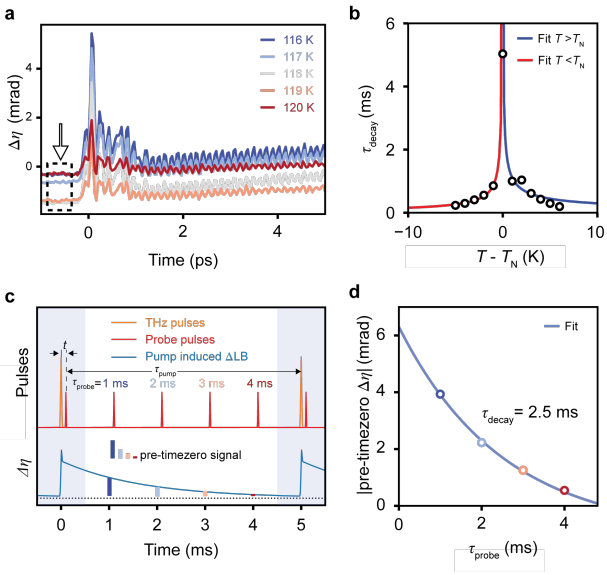

Figure 4.8: Decay time of the photoinduced state exceeds 2 ms. a. Pre-time zero signal (dashed square under the arrow) around T_{N} in the ellipticity channel.**b.** Metastable state decay time obtained from the pre-time zero signal. The red and blue lines are power law fits which gives $z\nu = 0.89$ and 0.56. **c**. Studying the decay dynamics with a different THz repetition rate. The upper panel shows the train of THz pump (orange) and optical probe (red) pulses. The pump pulses are separated by $\tau_{\mathrm{pump}} = 5$ ms. The probe pulse separation are chosen between $\tau_{\mathrm{probe}} = 1$ ms, 2 ms, 3 ms, and 4 ms. t labels pump-probe time delay. The experimentally accessible region of t is much shorter than pulse-to-pulse separations. The blue shaded region is the pump-on region, and the unshaded region is pump-off. The lower panel shows the pump induced $\Delta\eta$. The cumulative effect of the pump pulses leads to a net offset from zero. The colored bars label the strength of the pre-time zero signal in this measurement configuration, obtained by the difference between pump-on (shaded) and pump-off (unshaded) region. **d**. The fitting of pre-time zero signal as a function of τ_{probe}, which gives an estimation of the intrinsic relaxation time τ_{decay} of the metastable state. Colored markers are the absolute values of the pre-time zero signal in **c**.

ellipticity signal before time zero for the pump-on region is given by the sum of repetitive pulses as $\sum_{n=1}^{\infty} Ae^{-\frac{n\tau_{\mathrm{pump}}}{\tau_{\mathrm{decay}}}}$, where τ_{pump} is the temporal separation between the THz pump pulses. The pump-off state signal is similarly given by $\sum_{n=0}^{\infty} Ae^{-\frac{\tau_{\mathrm{probe}}+n\tau_{\mathrm{pump}}}{\tau_{\mathrm{decay}}}}$, where τ_{probe} is the temporal separation between the probe pulses in the pump-on and pump-off regions. The measured pre-time zero signal is then given by:

$$\text{pre-time zero } \Delta\eta = A\frac{e^{-\frac{\tau_{\mathrm{pump}}}{\tau_{\mathrm{decay}}}} - e^{-\frac{\tau_{\mathrm{probe}}}{\tau_{\mathrm{decay}}}}}{1 - e^{-\frac{\tau_{\mathrm{pump}}}{\tau_{\mathrm{decay}}}}}. \tag{4.1}$$

In Figure 4.8c, we set $\tau_{\mathrm{pump}} = 5$ ms and $\tau_{\mathrm{probe}} = 1, 2, 3, 4$ ms. The pre-time zero signal as a

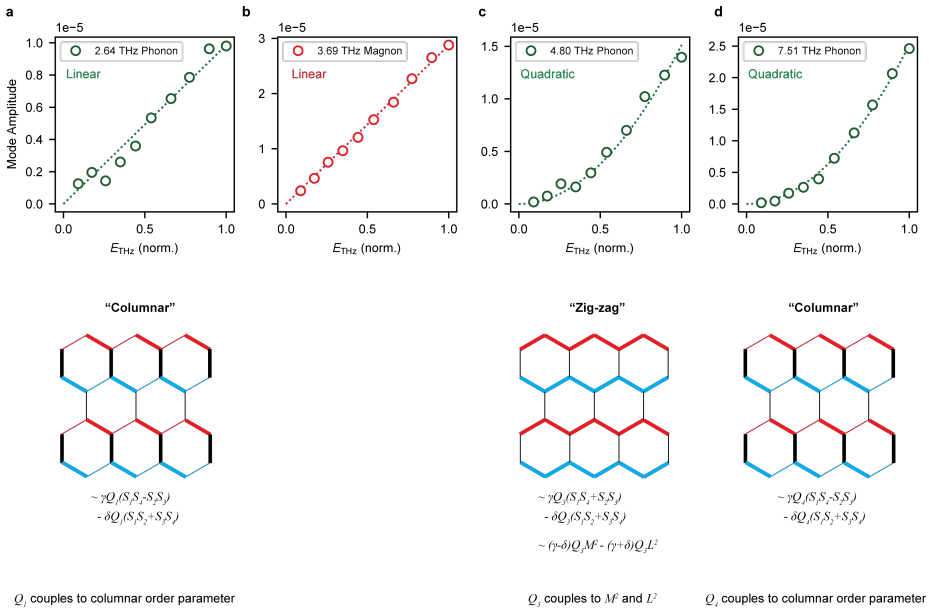

Figure 4.9: Field strength dependencies of other low energy modes. **a**, **b**, **c**, and **d** are THz field strength dependencies of the 2.64 THz phonon, 3.69 THz magnon, 4.80 THz phonon, and 7.51 THz phonon mode amplitudes, respectively. Dashed lines in **a** and **b** are linear fits, whereas in **c** and **d** the fits are quadratic. The lower panels are the modulation patterns of the nearest-neighbour exchange interactions under the corresponding phonon displacements. The Q_1 (2.64 THz) and Q_4 (7.51 THz) phonons induce so called columnar modulations. Since the columnar phase is far from the zig-zag phase, the contributions of these two phonons to the Ginzburg-Landau free energy can be neglected. The Q_3 (4.80 THz) phonon has a "zig-zag" type modulations, and it couples individually to M^2 and L^2. Unless there is a mechanism that breaks the degeneracy between opposite signs of magnetization, the Q_3 is also not expected to generate a net magnetization. These findings are further supported by spin Monte Carlo simulations (see section 4.7.4), and therefore, we neglect their contributions in the text.

function of τ_{probe} are fitted by Eq. 4.1 in Figure 4.8d which yields $\tau_{\text{decay}} = 2.5$ ms. The ratio between the pre-time zero signal and the maximal signal after time zero is

$$\frac{\text{pre-time zero } \Delta\eta}{\text{maximal } \Delta\eta} = \frac{e^{-\frac{\tau_{\text{pump}}}{\tau_{\text{decay}}}} - e^{-\frac{\tau_{\text{probe}}}{\tau_{\text{decay}}}}}{1 - e^{-\frac{\tau_{\text{probe}}}{\tau_{\text{decay}}}}}. \tag{4.2}$$

τ_{decay} as a function of temperature can then be obtained by numerically solving Eq. 4.2. The results for the case with $\tau_{\text{pump}} = 2$ ms and $\tau_{\text{probe}} = 1$ ms are shown in Figure 4.8b.

4.6.3 Importance of phonon excitations

The comparison between a resonant and off-resonant excitation of the low energy modes (Figure 4.7), as performed above, highlights the importance of large amplitude displacements of these modes in inducing the long-lived magnetic state. In contrast, linear excitation of infrared-active phonons results in an oscillatory motion of the atoms around their equilibrium positions, and cannot give rise to the accumulation of net positive signal over long delay times ($\sim$ 100 ps). A net positive or negative signal instead requires a net average distortion of the lattice, which can be realized through various nonlinear excitation pathways [21]. To identify the modes that are nonlinearly driven, we analyze the field strength dependence of mode amplitudes. The lowest energy phonon mode (Ω_1 = 2.64 THz), as well as the magnon (Ω_m = 3.69 THz), exhibit a linear field dependence, whereas the Ω_3 = 4.80 THz and Ω_4 = 7.51 THz phonons show a quadratic dependence on the field (see Figure 4.9). The linear dependence of the magnon indicates a direct excitation by the magnetic component of the THz field. Remarkably, the field strength dependence of the phonon mode at Ω_2 = 3.27 THz cannot be fit by either a linear or quadratic function, but instead displays a superposition of linear and quadratic behavior. In Figure 4.10a), we show the dependence of the 3.27 THz phonon amplitude on THz electric field. The fit function we used has both linear and quadratic terms ($|aE_{\mathrm{THz}}+bE^2_{\mathrm{THz}}|$), whereas these terms individually cannot fit the field dependence. Since both magnetic and lattice structures of $FePS_3$ preserves inversion symmetry [143], phonons are either Raman-active or infrared-active, but not both. The origins of linear and nonlinear excitation mechanisms are as follows. The 3.27 THz mode is Raman active, and hence can be excited nonlinearly with THz via two photon absorption or other nonlinear pathways, which more generally can be classified as sum- or difference-frequency generation of photonic or ionic modes [21]. As the Q_2 mode is also hybridized with a magnon even at zero external magnetic field [100], it can be linearly excited through magnon. The fact that the field dependence is curved down tells us about the destructive interference between these two driving forces on Q_2 mode. Therefore the nonlinearly excited phonon modes Ω_2, Ω_3, and Ω_4 are the main candidates to explain the induced magnetization.

4.7 Identifying the microscopic mechanism of induced magnetization

4.7.1 Magnetic Hamiltonian

To better understand how nonlinear driving of these low-energy modes leads to metastable state with finite magnetization, we formulate a microscopic theory of the spin and lattice

degrees freedoms in $FePS_3$. The magnetic structure is governed by the Hamiltonian [100], [144]

$$H = \sum_{ij} J_{ij} \mathbf{S}_i \cdot \mathbf{S}_j - \Delta \sum_i S_{iz}^2, \tag{4.3}$$

where $\mathbf{S}_i$ is the spin of the Fe ion at lattice site i, and J_{ij} is the exchange coupling between spins at sites i and j. The first term of H represents the Heisenberg interaction, while the second term corresponds to an Ising-type single-ion anisotropy. When a phonon mode is excited this results in a change of the inter-ionic distances, which in turn modifies the exchange parameters. For small displacements the exchange interaction can be expanded as $J_{ij}(Q) \approx J_{ij} - \alpha_{ij} Q$, where α_{ij} quantifies the modulation of the magnetic interaction and Q is the phonon displacement. The model is completely parameterized from first principles, and the calculated values of J_{ij} and α_{ij} (see Table 4.1) are found to correctly reproduce the equilibrium magnetic properties [100] (see also section 4.7.4). In particular, from calculations within the frozen phonon approximation the spin-phonon couplings α_{ij} are found to decay rapidly with inter-atomic distance, and to be significant only for nearest neighbor spins.

	Equilibrium exchange coupling (meV)			
	J_1	J_2	J_3	J_4
	-0.81	-1.38	-0.81	-1.38

	Spin-phonon coupling (meV/Å)			
Mode	α_1	α_2	α_3	α_4
Q_1	-5.4	-5.0	5.7	3.7
Q_2	17.1	0.5	-17.6	-0.4
Q_3	9.7	-20.7	9.7	-20.8
Q_4	-30.0	-29.0	26.1	26.4

Table 4.1. Nearest neighbor exchange interactions and spin-phonon couplings in $FePS_3$. Calculated magnetic exchange interactions of the four inequivalent nearest neighbor bonds indicated in Figure 4.10b, as well as the spin-phonon coupling coefficients α_i labeled in correspondence with J_i.

4.7.2 First principles calculations

To obtain the spin-phonon coupling of bulk $FePS_3$, we performed first principles simulations with the ABINIT electronic structure code [145]–[148]. We used the local density approximation with projector augmented wave (PAW) pseudopotentials, a plane wave cut-off of 20

Ha and 40 Ha respectively for the plane wave and PAW part, and included an empirical Hubbard U of 2.7 eV on the Fe d-orbitals as self-consistently determined in the OCTOPUS electronic structure code via the ACBN0 functional. A Γ-centered Monkhorst-Pack grid with dimensions $8 \times 6 \times 8$ was used to sample the Brillouin zone.

The ground state was found to have zig-zag antiferromagnetic order with spins aligned along the z-axis. The DFT wave functions were mapped onto effective localized orbitals via the WANNIER90 code, and the spin parameters were calculated by the PYTHON package TB2J employing the magnetic force theorem [149], [150]. The resulting spin parameters are in good agreement with recent neutron scattering data [131].

Phonon frequencies and eigenvectors were calculated with ABINIT for a ferromagnetic interlayer coupling, after relaxing the atomic positions and stresses to below 10^{-6} Ha/Bohr. We identify four relevant phonon modes at $\Omega_1 = 2.67$ THz, $\Omega_2 = 3.27$ THz, $\Omega_3 = 4.77$ THz and $\Omega_4 = 7.48$ THz, in excellent agreement with our experimental THz and Raman scattering data (see also Table 4.2). The spin-phonon couplings for these four modes were calculated in the frozen phonon approximation and are given in Table 4.1. These large spin-phonon couplings are consistent with previous works on magnon-phonon hybridization [100], [134], [135], and they likely arise from the same origin as the large single-ion anisotropy, i.e. the unquenched Fe orbital magnetic moments as reported in Ref. [151].

Mode	Q_1	Q_2	Q_3	Q_4
$\Omega^{(c)}$ (THz)	2.67	3.27	4.77	7.48
$\Omega^{(c)}$ (meV)	11.1	13.5	19.8	31.0
Irrep.	B_g	A_g	A_g	B_g

Table 4.2. Phonon properties of $FePS_3$. Calculated mode frequencies and irreducible representations of the Raman active phonon modes of $FePS_3$, with C_{2h} point group. Phonons proximate to the lower magnon branch at 3.69 THz are listed.

4.7.3 Phonon modulated exchange interactions

The spatial patterns in which the phonons modulate the exchange parameters are shown in Figure 4.10b and Figure 4.9. These spatial modulations are coarse grained to obtain a coupling between the phonon modes and the macroscopic magnetic variables $L = S_1 - S_2 - S_3 + S_4$ and $M = S_1 + S_2 + S_3 + S_4$, corresponding to the AFM and ferromagnetic (FM) order parameter, respectively. Here S_i denotes the four spins of the magnetic unit cell, labeled according to Figure 4.10b. From the coarse grained theory we find that only

the $\Omega_2 = 3.27$ THz phonon mode can lead to a finite magnetization, via a coupling of the form $H_{\mathrm{m-ph}} = gLMQ_2$. The real space motions of the atoms corresponding to this mode modifies the bond lengths between the Fe atoms as shown in Figure 4.10b, which enhances the exchange interaction within one of the FM chains while it weakens within the adjacent chain. This phonon induced magnetization, as well as the form of the coupling, is corroborated by Monte Carlo simulations of the microscopic spin Hamiltonian (Eq. 4.3), where the magnetic interactions are modulated according to the phonon displacement patterns (see section 4.7.4 and Figure 4.9). We therefore conclude that the nonlinear driving of the 3.27 THz phonon is responsible for the THz-induced magnetization observed here. Considering the spectrum of the THz pulse and the energies of linearly driven modes, the nonlinear excitation of 3.27 THz mode can happen via purely photonic or via infrared resonant Raman scattering processes [22]. The purely ionic process is unlikely to take place due to energy matching constraints. On the other hand, since the magnetization is induced by the displacement of the 3.27 THz mode, this type of rectification process can also be mediated by infrared-active phonons [21]. This type of dynamical modulation of the exchange coupling parameters can be broadly applied to other magnetic materials exhibiting strong spin-phonon coupling [152], [153].

4.7.4 Spin Monte Carlo simulations

To validate the exchange parameters obtained from first principles calculations, as well as the effective spin-phonon Hamiltonian, we performed simulated annealing using the Monte Carlo Metropolis algorithm. The calculations were done for a monolayer or thin bulk (up to 10 layers) of $FePS_3$ using the equilibrium spin parameters of Table 4.3 and a spin length $S = 2$, for in-plane supercells of linear sizes between $L = 10$ or 20. The simulated annealing was initialized at a temperature $T \approx 170$ K and performed down to a target temperature $T_0 = 70$ K in steps of $\Delta T \approx 2$ K. At each temperature we performed 2000 Monte Carlo sweeps to thermalize the system, followed by 4000 measurements performed at an interval of 50 sweeps to obtained thermodynamic averages. Our calculations find a magnetic transition from the paramagnetic to the zigzag antiferromagnetic state at $T_{\mathrm{N}} \approx 115$ K, in good agreement with experiment, thereby validating the calculated equilibrium spin parameters.

To assess the effects of a spin-phonon coupling we modified the magnetic parameters according to the spatial modulation patterns shown in Figure 4.10b and Figure 4.9. Such a simulations corresponds to a frozen phonon approximation, and reveals the expected magnetic properties for a fixed phonon displacement Q. For modes 1, 3 and 4 no qualitative effect is seen on the order parameters L and M, or on the transition temperature. In contrast, for a finite displacement of phonon mode 2 (i.e. for $Q_2 \neq 0$), a finite magnetization appears in connection with the magnetic phase transition (see Figure 4.11), an effect which is

J_1^F	J_1^A	J_2^F	J_2^A	J_3	Δ
-0.56	-1.40	0.01	0.43	0.53	2.46

Table 4.3. Equilibrium magnetic interaction parameters of $FePS_3$. The magnetic exchange interactions for nearest neighbor (subscript 1), next nearest neighbor (subscript 2) and third nearest neighbor interactions (subscript 3) used to obtain the equilibrium properties of $FePS_3$ via simulated annealing. The superscript denotes the interactions on intra-chain (ferromagnetic, F) and inter-chain (antiferromagnetic, A) bonds. The single-ion anisotropy is denoted by Δ.

independent of system size and thus expected to survive in the thermodynamic limit. This strongly indicates a significant coupling between the phonon coordinate $Q = Q_2$ and the macroscopic order parameters L and M.

To determine the form of the interaction, we note that the magnetization grows linearly with the phonon coordinate Q_2 (see Figure 4.11). Further, we find that the sign of the magnetization is sensitive to the sign of both Q_2 and L, and determined by the sign of the product Q_2L (see Figure 4.11). Due to Raman-activity and its intricate connection to the AFM ordering, the sign displacement of the Q_2 phonon depends on underlying order (L), rendering the sign of magnetization independent of the THz field polarization (see section 4.7.5 for a detailed discussion). The lowest order interaction term consistent with these results is of the form $\gamma Q_2 LM$, in agreement with the coarse-graining performed in the previous section. We note that here we did not introduce the effect of critical fluctuations and therefore cannot capture the behavior at $T > T_N$.

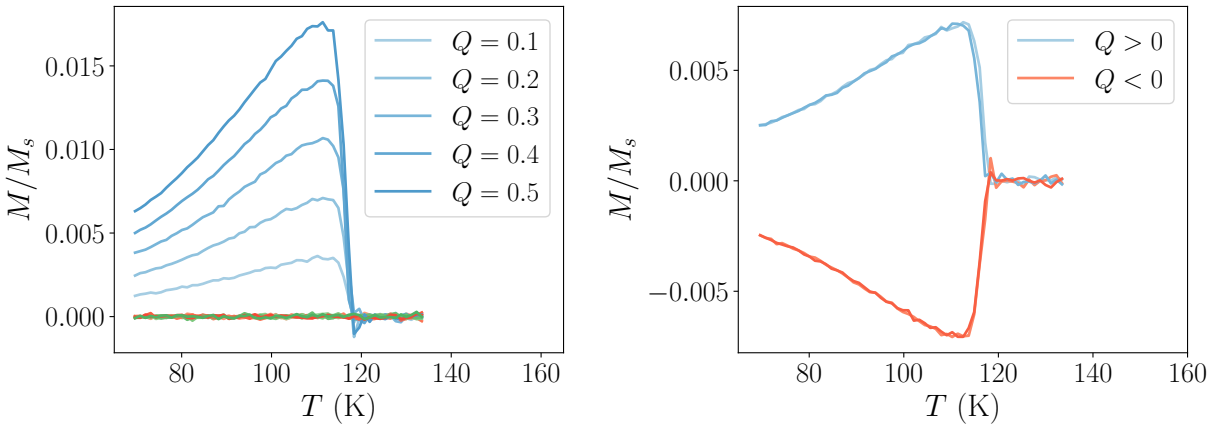

Figure 4.11. Temperature and phonon displacement dependence of induced magnetization in $FePS_3$. Temperature dependence of the phonon-induced magnetization of $FePS_3$, as a function of amplitude and sign of the phonon coordinate $Q = Q_2$. The phonon modulations are given in terms of the basic unit $Q_0 = 0.43$ pm. These results are consistent with a spin-phonon coupling of the form Q_2LM. We did not introduce the effect of critical fluctuations here and therefore cannot capture the behavior at $T > T_N$.

4.7.5 The sign of THz-induced magnetization

In a bulk sample, the system consists of a magnetic unit cell containing a total of 8 Fe ions, accounting for the zigzag antiferromagnetic order within each layer as well as the antiferromagnetic interlayer coupling. A change in sign of all spins, corresponding to a change in sign of L, is therefore equivalent to a translation of the system along the interlayer direction c by a distance $c/2$. Since the choice of unit cell should not affect any physical properties, this means that we also need to change the sign in the definition of the phonon displacement Q_2. This follows from the fact that Q_2 is a Raman mode and has to be even under inversion symmetry. For the magnetization order parameter, no change in sign is necessary between the unit cells. Therefore, reversing the sign of L should be associated with a simultaneous change of sign in Q_2, ensuring that the coupling term $gLMQ_2$ remains invariant. This property indeed has important consequences for the stability of the observed effect, implying that it is insensitive to domain formation.

To illustrate this insensitivity to the domain structures more closely, we consider two domains with $L > 0$ and $L < 0$ (Figure 4.12). As explained earlier, the lattice distortions in the neighboring layers have to be in opposite directions due to Raman activity of the mode. For instance, in the upper layer (Layer 1) of Domain 1 (Figure 4.12a), the zig-zag chains with up spins (shown in red) acquire stronger magnetic exchange interactions under

the distortion, whereas the chains with down spins acquire weaker magnetic interactions. This results in a net positive (up) magnetization. Meanwhile, in the lower layer (Layer 2), the distortion occurs in the opposite direction, again leading to positive magnetization. All these magnetizations add up. A domain with opposite sign of antiferromagnetic (AFM) order parameter (Domain 2), has to be distorted with the opposite Q_2 (Figure 4.12b), also leading to positive (up) magnetization ($M > 0$).

4.7.6 Ginzburg-Landau free energy

An effective Ginzburg-Landau free energy can then be written as

$$F = \frac{a_L(T)}{2}L^2 + \frac{b_L}{4}L^4 + \frac{a_M(T)}{2}M^2 + \frac{b_M}{4}M^4 + \frac{\Omega^2}{2}Q_2^2 + gLMQ_2, \tag{4.4}$$

where only the effects of the Q_2 phonon are considered. The free energy landscape as a function of L and M, with and without a distortion along the Q_2 mode, is illustrated in Figure 4.10c and d. The phonon distortion leads to a new displaced minimum with a net magnetization, $M \neq 0$ (red line), whose sign is determined by the sign of Q_2L. Therefore the application of an external magnetic field will not flip the sign of M, as opposed to common expectation for ferromagnets in equilibrium. Furthermore, the sign of the induced magnetization is insensitive to domain formation. This is attributed to the fact that the sign of lattice distortion, Q_2, is connected to the sign of L (see section 4.7.5 for a detailed explanation), such that the product Q_2L is set by material parameters only.

4.7.7 Criticality near phase transition

As demonstrated below, this Ginzburg-Landau theory can explain the temperature dependence of both the magnitude and lifetime of the THz-induced magnetization. Minimizing the free energy with respect to M and Q_2, assuming L is constant, the global energy minimum is reached for nonzero values of both M and Q_2. In particular, the magnetization of the global minimum is proportional to the variance of AFM order parameter, $M \sim \sqrt{\langle L^2 \rangle}$ (see section 4.7.4). Since the variance of L is proportional to the spin structure factor, which in turn is related to magnetic susceptibility of the zigzag order, the magnetization is expected to scale with temperature as $M \sim \sqrt{\chi_{zz}}$. As a result, the magnitude of the nonequilibrium

magnetization is expected exhibit a critical divergence near T_N [122], such that

$$M(T) \sim |T - T_N|^{-\gamma/2}. \tag{4.5}$$

Here γ is the critical exponent of the magnetic susceptibility. Here we note that near the transition point, the critical fluctuations dominate the dynamics, and fluctuations of the Q_2 phonon are also present above T_N. To compare the response expected from the 3-D Ising universality class with the experimental values, we assume that $\Delta\eta_0(T)$ acts as a probe of the magnetization. This assumption is further corroborated by the similar temperature dependencies of $\Delta\eta_0(T)$ and ΔCD_0, the latter of which is a direct measure of $M(T)$. The power-law fit to the temperature dependence (see below) of the observed $\Delta\eta_0(T)$ gives a critical exponent $\gamma/2 = 0.56 \pm 0.05$ (see Figure 4.6e), which is in good agreement with the expected value $\gamma/2 = 0.62$ [154].

4.7.8 Fitting and extracting the critical constants of the magnetization, rise time and the decay time

For the temperature dependence of the magnetization amplitude we fit with a power law as:

$$M(T) = A|T - T_N|^{-\gamma/2} + \text{const.} \tag{4.6}$$

were A, γ and "const." are free parameters. We assume $M(T)$ to be proportional to $\Delta\eta_0(T)$. $\Delta CD_0(T)$ data can also be equivalently used for the fits, however we worked with ellipticity change signal instead, as it has more data points and is intrinsically less noisy, owing to its differential type detection scheme. We fit the $T > T_N$ and $T < T_N$ regions separately, and the obtained critical constants are $\gamma/2 = 0.53 \pm 0.05$ and $\gamma/2 = 0.56 \pm 0.05$, respectively (see Figure 4.6e). These are in good agreement with the expected critical exponent of 3D Ising model.

Next we extract the rise time constants from the same set of data by fitting the time traces with an exponential function:

$$\Delta\eta(t, T) = A\exp(-\frac{t}{\tau_{\text{rise}}}) + B \tag{4.7}$$

the initial few picosecond window of the trace with a spike due to THz Kerr effect is omitted. Further we fit the obtained $\tau_{rise}(T)$ separately high and low temperature sides of T_N with a

power law given as:

$$\tau_{\text{rise}}(T) = \tau_0 \left| \frac{T_{\text{N}}}{T - T_{\text{N}}} \right|^{\nu z} + \text{const.} \tag{4.8}$$

The obtained critical exponents for rise time are $\nu z = 1.07 \pm 0.27$ and $\nu z = 0.44 \pm 0.07$, for $T < T_{\text{N}}$ and $T > T_{\text{N}}$, respectively (see Figure 4.6i). We fit the temperature dependence of the decay time with the same power law (Eq.4.8), and the exponents are $\nu z = 0.72$ and $\nu z = 0.56$, for low and high temperature sides (see Figure 4.8b). The lower temperature side critical behavior is close to the expected value from 3D Ising model ($\nu z = 1.27$).

To explain the long-lived nature of the induced magnetization, we note that the Ginzburg-Landau theory in fact predicts a degenerate pair of shallow free energy minima at $\pm(M, Q_2)$, as shown in Figure 4.10e (upper panel). In thermal equilibrium, the order parameter will fluctuate between the two minima, preventing a build-up of net magnetization in equilibrium. This is similar to how quantum fluctuations prevent ferroelectric ordering in $SrTiO_3$ [114]. However, when the system is driven into an asymmetric configuration by the THz-induced finite phonon displacement close to transition point (Figure 4.10e middle panel), the fluctuating order parameters L and M are stabilized and start to migrate, such that M localizes in the free energy minimum selected by the sign of $Q_2 L$ (Figure 4.10e lower panel). This mechanism is supported by extensive microscopic spin dynamics simulations, showing a build-up of magnetization in response to dynamical phonon displacement.

The slow decay of the induced perturbations will eventually bring the system back to thermal equilibrium. However, close to a second order phase transition, the relaxation of perturbations in the dominant order parameter are expected to show a critical slowing down following the exponential form $\delta L(t) \sim e^{-t/\tau(T)}$, with a lifetime $\tau(T) \sim |T - T_{\text{N}}|^{-\nu z}$ diverging as $T \to T_{\text{N}}$ [155]. Both the solution of the stochastic Ginzburg-Landau equations and the analytic solution of the deterministic equations show that for $T \to T_{\text{N}}$ the induced magnetization $M(t)$ quickly relaxes to the free energy minimum determined by δL, and then adiabatically follows the free energy minimum back to equilibrium. Crucially, the relaxation of the free energy minimum is determined by the dynamics of the antiferromagnetic order, and therefore exhibits a critical slowing down. At long times the magnetization is therefore given by $M(t) \approx g/\sqrt{\Omega b_M}\delta L(t) \sim \exp(-t/\tau)$, such that $M(t)$ inherits its critical behavior from δL. In particular, the magnetization shows a diverging relaxation time close to T_{N} with the same dynamical exponents as δL. Analyzing the temperature dependence of both the rise time (Figure 4.6i) and decay time (Figure 4.8b), the dynamical critical exponents in the region $T < T_{\text{N}}$ are close to the expected values from 3-D Ising model.

4.7.9 Multiscale modeling of dynamics

The time scales involved in our experiments span the range from typical magnetic scales of ps to relaxation dynamics happening over several ms. As there is no single method that can access all these timescales, we have used a multi-scale approach where different methods are combined to cover different regimes. Our microscopic methods (spin Monte Carlo and Landau-Lifshitz dynamics) are restricted to $\sim$ 1 ns, while solutions to the stochastic Ginzburg-Landau equations can be obtained up to $\sim$ 10 ns. These methods were used to address the short to intermediate time scales, covering the initial excitation and the build-up of the THz-induced magnetization. We note that all these theories agree in the prediction that a finite magnetization appears if and only if the phonon mode Q_2 is displaced away from equilibrium, either in a static (as corroborated by thermal Monte Carlo simulations) or in dynamic fashion (as corroborated by Landau-Lifshitz and Ginzburg-Landau dynamics). To understand the nature and microscopic dynamics of the magnetized state up to time scales of $\sim$ 10 ns, these methods are therefore both accurate and sufficient.

To address the long-time dynamics, we combine results from the theory of dynamic critical phenomena with analytical and numerical solutions of the (stochastic) Ginzburg-Landau equations. These methods are expected to provide an accurate description of the relaxation dynamics, which is dominated by the interplay of long-wavelength excitations and thermal fluctuations and therefore insensitive to microscopic details. Specifically, as all our theories find the dominant antiferromagnetic order parameter L to be largely unaffected by the sub-dominant ferromagnetic order parameter M and the phonon displacement Q_2, the critical dynamics of L (in the region $T \sim T_\mathrm{N}$) is determined solely by its intrinsic dynamics. We can therefore employ the standard theory of dynamical critical phenomena [155], which predicts that perturbations of the dominant order parameter decay as $\delta L(t) \sim \exp(-t/\tau)$ with $\tau \sim |T - T_\mathrm{N}|^{-\nu z}$.

As discussed in the next section, we find that the coupling term $gLMQ_2$ leads to a critical slowing down also in the dynamics of M. This is supported by numerical solutions of the stochastic Ginzburg-Landau equation for M (for times up to $\sim$ 10 ns). Therefore, for times $t \gtrsim 1$ ns but $t < \tau$, we have $M(t) \sim \exp(-t/\tau)$ with the same lifetime as L.

4.7.10 Critical slowing down of magnetization dynamics

An intuitive way to understand the critical slowing down of M is to note that for $T \to T_N$, the fast order parameter (M) quickly decays to the local minimum defined by the slow order parameter (L). Once M has reached this minimum, it adiabatically follows it back to equilibrium, such that $M(t) \approx \sqrt{(g^2 L(t)^2/\Omega - a)/b}$. Here we have suppressed the subscripts

on a_M and b_M. Since the relaxation of the free energy minimum is determined by the dynamics of the antiferromagnetic order, it exhibits a critical slowing down. More precisely, for slow variations of L close to criticality, we can approximately solve the deterministic Ginzburg-Landau equation for M by replacing a with $a - g^2 L(t)^2/\Omega$. Assuming that $L(t) = L(0)e^{-t/\tau}$, as is well known from the theory of dynamical critical phenomena [155], and defining $\lambda^2 = g^2 L(0)^2/\Omega$, the solution is then

$$M(t) \approx \sqrt{\frac{\lambda^2 e^{-t/\tau} - a}{b}} \left[1 - e^{2at - 2\lambda^2 \tau e^{-t/\tau}} \left(1 + \frac{\lambda^2 e^{-t/\tau} - a}{bM(0)^2}\right)\right]^{-1/2} \tag{4.9}$$

The leading order term of this equation recovers the simple adiabatic approximation discussed above, while the sub-leading terms show that there is a crossover at $at \approx \lambda^2 \tau e^{-t/\tau}$ to a regime of intrinsic exponential decay $M(t) \sim e^{-at}$. Importantly, close to the critical temperature, $M(t)$ will decay with with a diverging relaxation time $\tau \sim |T - T_N|^{-\nu z}$. Therefore, for times $t \gtrsim 1$ ns but $t < \tau$, we have $M(t) \sim \exp(-t/\tau)$ with the same lifetime as L. We provide further evidence of the critical slowing down of the magnetization, and how it is inherited from the critical dynamics of L, based on numerical solutions of the stochastic Ginzburg-Landau equations.

4.8 Conclusions

In summary, we discovered a hidden state with finite magnetization induced by an intense THz field. This nonequilibrium phase emerges as a result of the nonlinear driving of a specific phonon mode, leading to significant modifications in the in-plane distances between the magnetic ions. We find that the equilibrium and dynamical critical fluctuations of the underlying antiferromagnetic order respectively enhance the magnitude of the nonequilibrium magnetization and facilitate its metastability. Remarkably, our theoretical analysis captures all aspects of the experimental observations. Notably the magnetization mechanism in this case is distinct from the dynamic piezomagnetic effect [70], [156], as the magnetic point group of $FePS_3$ ($2/m1'$ [141]) prohibits piezomagnetism. All these findings present an interesting new angle of phase transitions by showing that the regions near critical points in the phase diagram, with enhanced order parameter fluctuations, are promising areas to search for metastable hidden states. While the optical probes used in this study, such as polarization rotation, ellipticity change and circular dichroism, are sufficient to characterize and verify the new non-equilibrium state with a net magnetization, further characterizations via time-resolved X-ray diffraction or X-ray magnetic circular dichroism [157]–[159] would provide valuable details of the new magnetic order. Moreover, experimental confirmation of the

phonon mode involved in inducing the new order, as well as validation of an equilibrium state with two degenerate minima, as obtained within our Ginzburg-Landau theory, would be useful to corroborate our understanding. Lastly, as the lifetime of the state exceeds 2 ms, conventional transport probes such as Hall resistivity can also be employed, thereby establishing its potential for future spintronic applications.

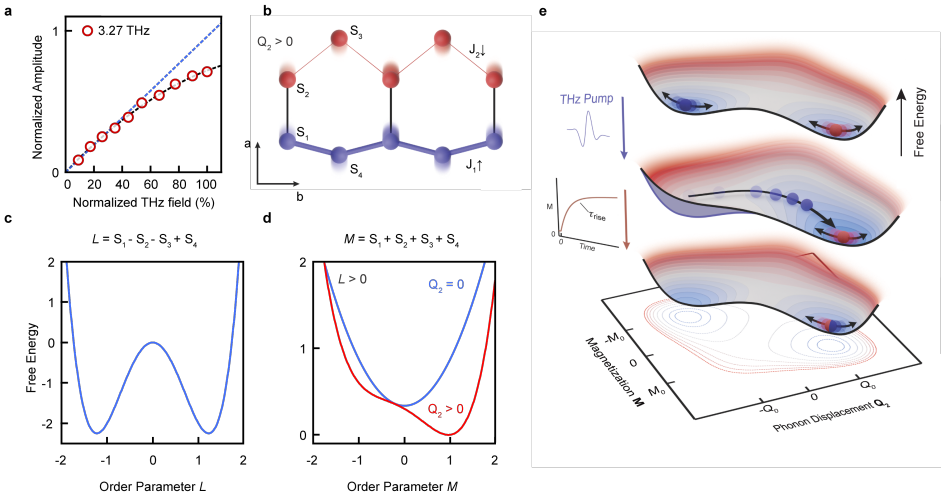

Figure 4.10: Nonlinear excitation of Q_2 phonon triggers a net magnetization and the critical fluctuations facilitate its metastability. Field strength dependence of the 3.27 THz (**a**) phonon mode amplitude. The 3.27 THz phonon has both linear and quadratic components, that interfere destructively, which is manifested in the "curved down" shape of the field dependence. **b.** Real-space motions of the Fe^{2+} ions due to excitation of the Q_2 phonon and the spatial pattern of the phonon-modulated exchange couplings. An enhancement of the magnetic interaction on a given bond is illustrated by a thick line and up-pointing arrow, whereas a decrease is shown by a thin line a down-pointing arrow. Labels S_i and J_i denote the relevant spin and exchange parameters of the magnetic unit cell. **c** and **d** are the magnetic free energy landscapes as a function of zig-zag AFM order parameter L and magnetization M, respectively. For a fixed 3.27 THz phonon displacement Q_2, the system develops to degenerate energy minima at finite L and M, such that the sign of M is determined by the signs of Q_2 and L through a term Q_2LM in the free energy. **e.** Equilibrium free energy landscape obtained from effective Ginzburg-Landau theory. In thermal equilibrium the order parameter fluctuates between the two degenerate minima, thereby preventing the build-up of a finite magnetization (upper panel). When driven into an asymmetric configuration by distorting the lattice (middle panel), a single minimum is favored leading to a net magnetization (lower panel). The subsequent dynamics are governed by the critical fluctuations, which results in a critically slowed down relaxation back to equilibrium.

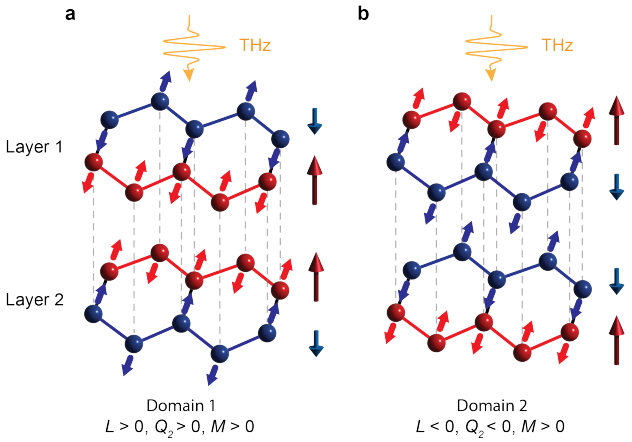

Figure 4.12. The sign of THz-induced magnetization a. A lattice distortion of Domain 1 with $L > 0$, under the nonlinear excitation of the Q_2 phonon. Two neighboring layers are depicted. Under such distortion, upper and lower layers have opposite phase of the distortion, leading to $M > 0$ in each layer. **b**. same for Domain 2, with $L < 0$ and correspondingly $Q_2 < 0$.

Chapter 5

Time-of-flight detection of terahertz phonon-polariton

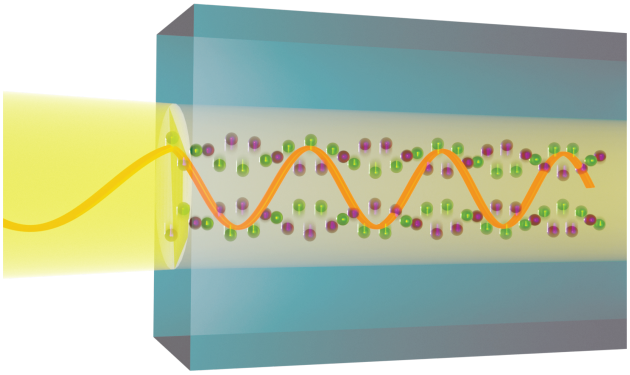

Contents

A polariton is a fundamental quasiparticle that arises from strong light-matter interaction, garnering significant scientific and practical interest. When light is strongly coupled to the crystal lattice, it gives rise to phonon-polaritons (PPs), which have proven useful in the dynamic manipulation of quantum materials and the advancement of terahertz technologies. However, current methods for detecting and characterizing polaritons remain limited. Traditional techniques such as Raman scattering or transient grating require fine-tuning of external parameters or complex phase extraction procedures. To overcome these limitations, we propose and demonstrate a technique based on time-of-flight measurement of PPs. In our method, we resonantly launch broadband PPs with intense terahertz fields and measure the time-of-flight of each spectral component using time-resolved second harmonic generation. This time-of-flight information, combined with the PP attenuation, enables us to resolve the real and imaginary parts of the PP dispersion relation. We demonstrate this technique in the van der Waals magnets NiI_2 and $MnPS_3$, revealing a hidden magnon-phonon interaction. We believe that this approach will open new avenues for studying polaritons across diverse material systems and enhance our understanding of strong light-matter interactions.

This chapter is based on the following published work:

T. Luo†, B. Ilyas†, A. v. Hoegen†, *et al.* Time-of-flight detection of terahertz phonon-polariton. *Nature Communications* **15** (1), 1-8 (2024) [160]

The author of this dissertation contributed to the following aspects of the work: designing and constructing the experimental setup, conducting the experiments, analyzing and interpreting the experimental data, and writing the manuscript.

5.1 Quasiparticles of strong light-matter interactions

5.1.1 Types of polaritons

Exposing crystals to a strong external electromagnetic (EM) field can induce highly nontrivial dynamics [161]–[164]. Under such conditions, a new type of quasiparticle, the polariton, can emerge [10], [165]. Polaritons are hybrid light-matter modes arising from strong light-matter interaction, carrying crucial information about the interaction strength and holding promising potential in applications such as high-speed, low-loss communication [166], [167]. Polaritons can manifest in various forms, including phonon-polaritons (PPs) [168], magnon-polaritons [169]–[171], exciton-polaritons [172], [173], and others [165], depending on the nature of the light-matter interaction. Phonon-polaritons (PPs) arise when light strongly couples with the crystal lattice's collective excitations, i.e., phonons, as illustrated in opening figure of this Chapter. When an EM wave propagates inside a crystal, it can induce coherent oscillation of infrared-active lattice vibrations if they fall within the EM field spectral bandwidth. This interaction with dipolar vibration affects the medium's dispersive properties. The dipolar motion of the infrared-active vibration leads to re-radiation of the EM wave, which propagates and re-excites the dipolar vibration, resulting in propagating hybrid light-lattice modes, i.e., PPs. These modes have been actively explored as platforms for THz waveguides [174], [175] and tools for studying nonlinear phononic effects and dynamically controlling material properties [176]–[178].

5.1.2 Dispersion relation of phonon polaritons

The physics of phonon-polaritons (PPs) is described by their dispersion relation (Figure 5.1c). The real part of the PP dispersion relation features an avoided crossing (color-coded line in Figure 5.1c), whose magnitude provides information about the coupling strength. Correspondingly, the imaginary part of the dispersion (blue line in Figure 5.1c), which describes the damping of the PP during propagation, exhibits a resonant peak around the phonon frequency, indicating rapid dissipation of electromagnetic field energy through the phonon mode. However, determining the PP dispersion relation is a highly nontrivial task, primarily due to the difficulty in identifying the wavevector (momentum) of each spectral component of the PPs.

The small wavevector range (1 mm^{-1} – 1 μm^{-1}), where photon and phonon momenta intersect, makes optical techniques particularly sensitive to PP dispersion relations. Traditional methods such as Raman scattering [179], [180] and transient grating spectroscopy [177], [181] require careful tuning of the photon's incidence angle to determine the polariton's

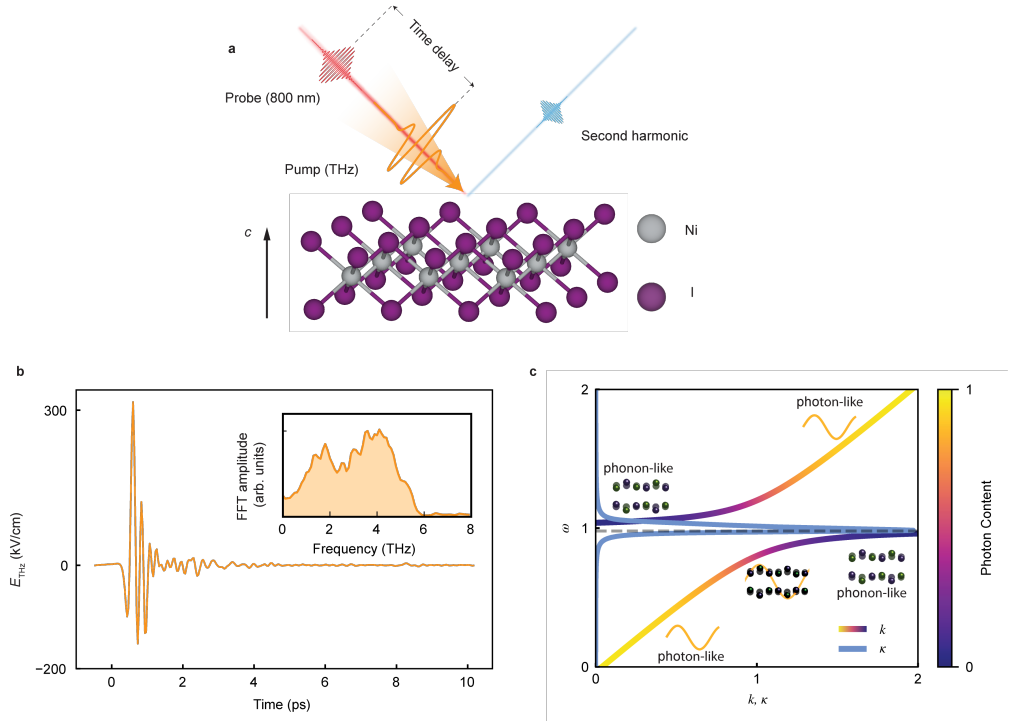

Figure 5.1: Experimental configuration and illustration of PP. a. Schematics of the experimental setup. Intense THz pump (orange) and the 800 nm probe (red) pulses are incident on the *ab* surface of the NiI_2 sample at 45°. The second harmonic of the 800 nm probe reflected from the *ab* surface (blue) is collected as the probe signal. **b.** The profile of the terahertz field. Inset: the spectrum of the terahertz, which covers the range of 0 - 6 THz. **c.** A typical dispersion relation of PP with schematics illustrating the photon and phonon components in different regions of the dispersion relation. The real part (k) of the dispersion curve is color-coded by the photon weight. The imaginary part (κ) of the dispersion is shown in blue.

wavevector. These methods are only applicable to inversion-symmetry broken systems where the polaritons are Raman active. Other techniques extract the polariton wavevector by satisfying the phase-matching condition [182], [183], necessitating a frequency sweep to map out the dispersion. Recent advances in generating stable terahertz (THz) laser pulses have opened new possibilities for directly measuring the polariton dispersion using time-domain THz spectroscopy (TDTS) [184]. However, this method determines the PP wavevector by measuring the exact phase delay of the THz electromagnetic wave inside the sample, requiring electro-optic sampling in an external crystal and careful phase referencing. Additionally, free-space TDTS is suitable only for macroscopic samples due to the large diffraction limit of the THz electromagnetic wave. These methods also face difficulties in obtaining the phonon oscillation amplitude carried by the PPs, which is crucial for studying lattice nonlinearities.

5.1.3 New method of measuring the polariton dispersion

In this chapter, we propose a method to measure the PP dispersion based on the time-of-flight of coherent PPs. Here, we resonantly launch PPs within the wide bandwidth of an ultrashort THz pulse and measure the time required for each frequency component to travel through the sample's bulk to directly obtain the real part of the dispersion relation.

5.2 Experimental methods

5.2.1 Sample preparation

Single crystal NiI_2 was synthesized via a chemical vapor transport method. Nickel powder (99.99%, Sigma-Aldrich) and iodine (99.99%, Alfa Aesar) were mixed in the stoichiometric ratio and sealed in an evacuated quartz tube. The quartz tube was placed in a two-zone furnace with a temperature configuration of 750°C (hot zone) and 720°C (cold zone) for seven days. The quality and crystallinity of the synthesized crystals were verified using energy-dispersive x-ray spectroscopy (EDX) and powder x-ray diffraction (XRD). The thickness of the NiI_2 samples under study is (250±20) μm, as characterized by a Bruker Dektak DXT-A stylus profilometer.

Single crystal samples of $MnPS_3$ were synthesized by a similar chemical vapor transport method. A quartz ampoule containing the raw materials was placed in a horizontal two-zone furnace with a temperature configuration of 780°C (hot zone) and 730°C (cold zone). The sample thickness was measured to be (85±10) μm, as characterized by the profilometer.

5.2.2 THz pump, SHG probe spectroscopy

The broadband THz pump is generated by pumping an N-benzyl-2-methyl-4-nitroaniline (BNA) crystal with a 1300 nm output from an optical parametric amplifier (OPA) operating at a repetition rate of 1 kHz. An 800 nm pulse from a Ti-Sapphire amplifier, co-propagating with the THz pump pulse, is focused onto the sample to probe the lattice and polariton dynamics. Both the THz and 800 nm pulses are incident at an angle of 45°. The THz pump is *s*-polarized, with its electric field oriented along the in-plane direction. The probe pulse is polarized to maximize the static second harmonic (SH) signal. The SH generation from the 800 nm pulse is separated from the fundamental beam by a pair of dichroic mirrors and a narrow band bandpass filter, and then directed to a photomultiplier tube (PMT). The output signal from the PMT is collected by a data acquisition (DAQ) card. A schematic of the experimental setup is shown in Figure 5.2. The peak-to-peak THz electric field at

the sample position is 350 kV/cm and the spectral weight is centered around 3 THz with a bandwidth of 6 THz (Figure 5.1b)

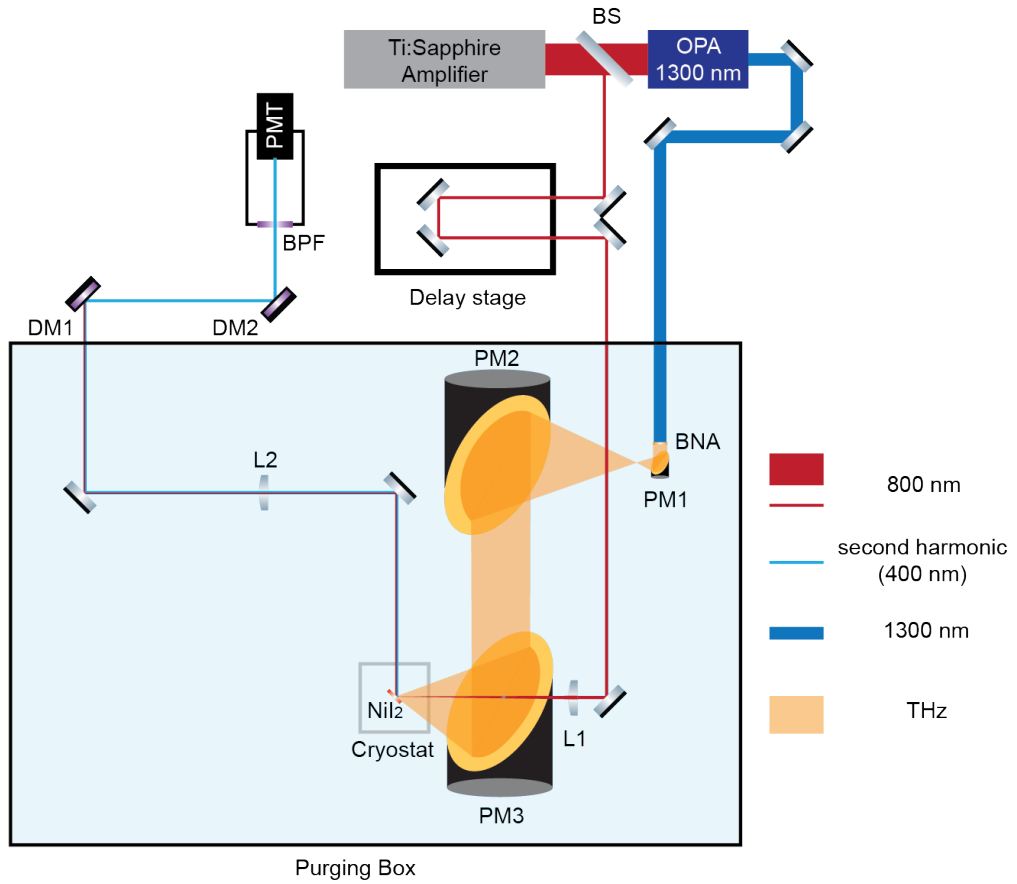

Figure 5.2: Experimental scheme of the THz pump-SHG probe setup. BS: beam splitter; PM1, PM2, PM3: gold coated parabolic mirrors; L1, L2: lenses; DM1, DM2: dichroic mirrors; BPF: band pass filter.

5.3 Detection of phonon-polaritons in NiI_2

5.3.1 The principles of time-of-flight detection

The idea behind this approach is the equivalence of the dispersion relation and the group velocity as a function of frequency.

$$v_g(\omega) = \frac{d\omega}{dk}. \tag{5.1}$$

A similar time-of-flight technique has been employed to measure the dispersion of near-infrared (NIR) exciton polaritons [185]. By integrating this concept with state-of-the-art THz

techniques, we demonstrate a time-of-flight study of the phonon-polariton (PP) dispersion in van der Waals (vdW) layered magnetic materials. The amplitude and phase-resolved detection is realized with time-resolved optical second harmonic (SH) generation of a NIR probe pulse. The reflected SH light intensity as a function of the time delay between the THz excitation and NIR probe captures the arrival time of the PPs at the surface (see Figure 5.1a). This approach can map out the PP dispersion relation without the need for any external adjustment parameter, phase referencing, or external electro-optic sampling. The imaginary part of the dispersion can also be obtained by comparing the SH generation amplitude of the PP before and after traversing the sample. Unlike conventional TDTS techniques, detection at NIR wavelengths allows us to extend this approach to measure microscopic samples below the THz diffraction limit.

As a proof-of-concept, we apply this time-of-flight method to the layered multiferroic material NiI_2. Below 59 K NiI_2 develops a multiferroic ground state, which can persist down to atomic monolayer limit [186]. Static magnetoelectric responses of NiI_2 have been studied[187], however its dynamical counterpart, the coupling between magnons and phonons, has not been reported. Understanding such interactions is important for identifying effective pathways for the control of macroscopic properties, with potential applications such as high-speed storage devices. The broken inversion symmetry of the NiI_2 multiferroic ground state leads to a finite $\chi^{(2)}$ optical nonlinearity, which results in a static SH generation from the NIR probe pulses. Any coherently oscillating infrared-active mode will dynamically modulate $\chi^{(2)}$ and will therefore be visible as changes in the SH intensity as a function of time delay $\Delta I_{\mathrm{SH}}(t) \sim \Delta\chi^{(2)}(t)$ at the frequencies of those modes.

5.3.2 THz field induced SHG and its modulation by phonons

During the initial few picoseconds of the THz pump SHG probe trace we observe a few sharp spikes and an incoherent background that offsets the oscillation from zero (Figure 5.3a). They can be attributed to THz field induced SHG. THz electric field E_{THz} breaks the inversion symmetry and leads to a change in SH intensity:

$$\begin{aligned}\Delta I_{\mathrm{SH}} &\propto |\chi^{(3)} E_{\mathrm{THz}} E^2_{\mathrm{probe}} + \chi^{(2)} E^2_{\mathrm{probe}}|^2 - |\chi^{(2)} E^2_{\mathrm{probe}}|^2 \\ &= \chi^{(3)2} E^2_{\mathrm{THz}} E^4_{\mathrm{probe}} + 2\chi^{(2)}\chi^{(3)} E_{\mathrm{THz}} E^4_{\mathrm{probe}}. \end{aligned} \tag{5.2}$$

where $\chi^{(2)}$ and $\chi^{(3)}$ are second and third order nonlinear susceptibility and E_{probe} is the probe electric field. Therefore, we expect ΔI_{SH} components both linear and quadratic to E_{THz}. When the THz pump field is present, the first term in Eq. 5.2 above results in the incoherent background, and the second term gives rise to spikes near time zero. Moreover,

the quadratic term leads to small spectral weight in the high frequency region in the FFT spectrum, which is beyond our THz spectral content. This is due to the fact that quadratic term doubles the frequency.

Following the THz pulse, ΔI_{SH} is dominated by the excited phonon modes. Eq. 5.2 can be applied in this case by replacing E_{THz} with phonon induced polarization P_{ph}. Since the phonon induced change in $\chi^{(2)} = \chi^{(3)} P_{\mathrm{ph}}$ is much smaller than the static $\chi^{(2)}$ in our experiment, we mainly detect the second term in Eq. 5.2 oscillating at the frequency of the phonon mode.

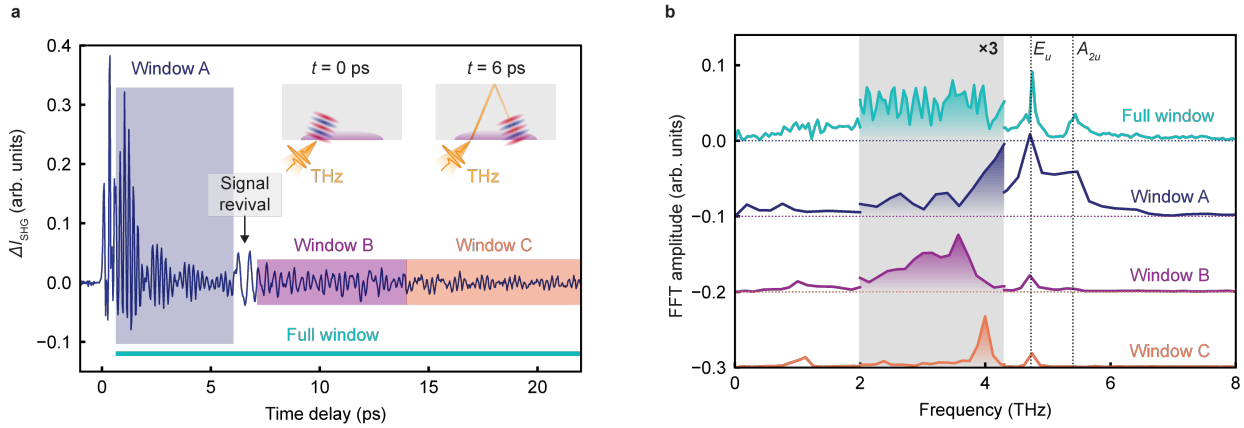

Figure 5.3: THz field induced SHG in NiI_2. a. THz field induced SHG in NiI_2 as a function of delay time between THz pump and NIR probe pulses. The inset shows the schematics of the dominant contribution to the signal before and after the signal revival. The grey rectangle is the sample. The orange pulse is the THz pump, and the purple shaded region is the sensing area of the SHG probe. The periodic wave in red and blue is the excited PP. The blue horizontal line and the shaded regions color-code different time windows used to perform FFT. **b.** FFT of the pump probe time trace within different time windows. Two vertical dashed lines indicate the frequencies of the E_{u} mode (4.7 THz) and the $A_{2\mathrm{u}}$ mode (5.3 THz). Three time magnification is applied in the shaded region for clarity.

Figure 5.3a shows the THz-field induced change of the SH intensity of NiI_2 at 7 K, deep in the multiferroic state. Near zero time delay, when the THz pump and the NIR probe pulses are temporally overlapped, we observe THz-field induced SH generation (TFISH), as discussed in the previous section. At later times, we observe coherent oscillations with multiple frequencies, resulting in a beating pattern (Figure 5.3a, Window A). These oscillations can be ascribed to infrared-active collective modes of the lattice (phonons) and the spins (magnons) [186], [188]. Notably, following the initial decay of the oscillations, we observe a sudden revival of the oscillation amplitude at around 6 ps time delay.

The coherent oscillations and the revival can be understood in the following way. NiI_2 is opaque to the SH of our NIR probe pulses ($\hbar\omega_{\mathrm{SH}} = 3.1$ eV) and therefore the reflected

SH intensity is sensitive only to changes of $\chi^{(2)}$ close to the sample surface within the penetration depth of the SH light [189], [190]. Therefore, the initial coherent oscillations can be understood as non-propagating collective modes in the system, which are probed close to the sample's surface (Figure 5.3a, left inset). The revival of the oscillations at 6 ps can not be reconciled with non-propagating modes. Replicas of pump or probe pulses outside the sample can also be ruled out since such revival is not observed in our electro-optic sampling traces (see Figure 5.1b). Therefore, such a signal suggests a propagating wavepacket of PPs that got reflected from the sample's back surface and reached the front surface after around 6 ps (Figure 5.3a, right inset). We note that since the penetration depth of SH is smaller than the THz wavelength, the phase-matching condition is unimportant for the detection of PP in our case.

We reveal unconventional dynamics of the coherent oscillations by obtaining the Fourier spectrum of the time trace in Figure 5.3a. Figure 5.3b shows the fast Fourier transform (FFT) with a time window that excludes the initial TFISH signal (labeled as Full window). The result (Figure 5.3b, shown in green) shows two sharp peaks at 4.7 THz and 5.4 THz, which have been previously assigned to infrared-active E_{u} and $A_{2\mathrm{u}}$ modes in the high temperature phase, respectively [188]. In addition, we observe a dense set of peaks between 1 THz and 4.5 THz (Figure 5.3b, shaded region), in stark contrast to the phonon modes and is reminiscent of interference of two time-delayed wavepackets. In this case, we expect different Fourier spectra from different time windows. To test this hypothesis, we performed FFT analysis for different time windows (see Figure 5.3a and b). The Fourier spectrum of time window A (before the oscillation revival) shows a clear phonon spectrum with two peaks. These peaks are broadened due to the shorter time window. As described above, this observation agrees well with non-propagating phonon modes. For window B (after the signal revival), we additionally observe a broad peak between 2 and 4 THz, with a lineshape very different from that of the phonons. At larger time delays, this feature sharpens and moves to higher frequencies (window C).

5.3.3 Time-frequency analysis

Next we perform a complete time-frequency analysis utilizing a wavelet transform of the time-dependent SH trace to better understand the spectral weight between 2 to 4 THz (see Figure 5.5a). The wavelet transform convolves the time trace with a sliding wavelet at different scales and better resolves the time-frequency relation compared to short-time FFT (STFT), as shown in Figure 5.4. This analysis yields the instantaneous spectrum for each delay in the SH time trace. Close to zero delay we observe our excitation spectrum and its second harmonic frequencies (see previous section). The frequencies of the E_{u} and $A_{2\mathrm{u}}$

modes appear as horizontal lines along the time axis. After $t = 6$ ps, coincidental with the revival of the coherent oscillations in Figure 5.3a, a chirped feature emerges. Its frequency increases with time, starting below 2 THz and gradually saturates to around 4 THz at larger delays. This chirped feature corresponds to the peak between 2 and 4 THz in the FFT of window B and C (Figure 5.3b) and does not depend on the strength of the THz driving field Figure 5.6, establishing it as the linear response of the system. We can therefore assign this chirped mode to the spread-out PP wavepacket that was subject to its dispersion relation.

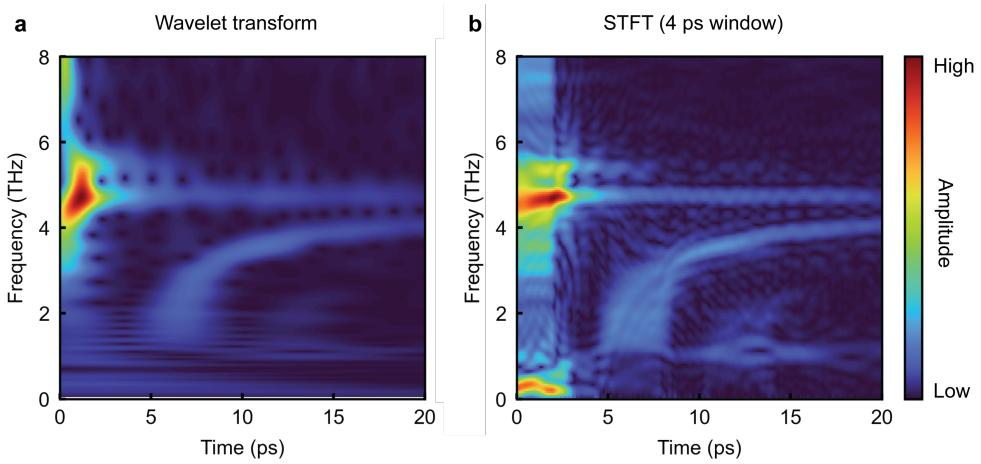

Figure 5.4: Wavelet transform **a** and STFT **b** of the THz induced SH time trace in Figure 5.3a.

5.3.4 Time and frequency resolution from the spectrogram

In this section we analyze the time and frequency resolution in extracting a peak from the spectrogram. The time-frequency resolution is related to the wavelet chosen for the wavelet transform. We chose the generalized Morse wavelet (GMW) with parameters $\beta = 120$, $\gamma = 3$ as the mother wavelet. As can be seen from the representative wavelets in Fig. 5.7a left and bottom panels, the time-frequency resolution varies with frequency. At the low frequency side of the PP (1.5 THz) the frequency resolution is 0.06 THz and the time resolution is 1.4 ps (Fig. 5.7a, red wavelets), whereas at the high frequency side, these values are 0.15 THz and 0.5 ps (4 THz) (Fig. 5.7a, blue wavelets), respectively. The time and frequency uncertainties of the wavelets are shown as the light-shaded region in Fig. 5.7d. Here the resolution of the wavelet is defined by the square root of its variance.

On the other hand, the temporal step size in our measurements is 0.033 ps, and the measurement time window of 20 ps allows a frequency resolution of 0.05 THz. Because of this oversampling, we can further improve the time/frequency uncertainty by fitting constant

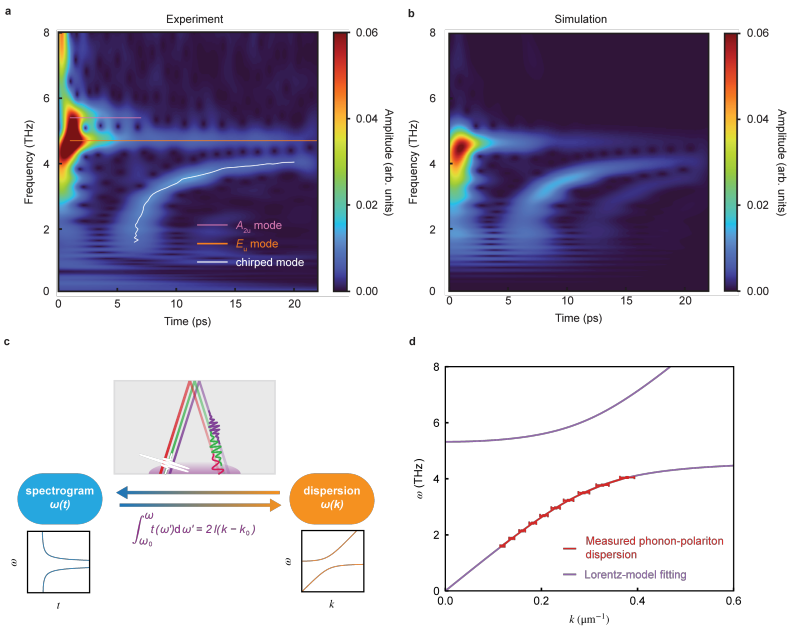

Figure 5.5: Obtaining the real part of the PP dispersion relation. a. Spectrogram of the THz pump SHG probe time trace in Figure 5.3a. White line is the extracted peaks of the chirped mode. Orange and pink lines are guides to the eye. **b.** Spectrogram of the simulated polarization at the sample surface after the THz pump. The simulation takes into account of the electric polarization due to the E_u mode. Both the E_u mode and the chirped mode in the experimental spectrogram are well captured. **c.** Relation between the PP dispersion $\omega(k)$ and the spectrogram $\omega(t)$. Upper panel: schematics of the physical picture of the chirped mode. The ultrashort broadband THz pump pulse is converted to a PP wavepacket inside NiI_2 (white). Different frequency components travel with different group velocity to the back of the sample and reflects back to the front (red, green, and purple pulses). Smaller frequency components travel faster. The shaded purple region is the region SHG probe can sense. **d.** Reconstructed PP dispersion from the spectrogram in **a**. The red curve is obtained by integrating Eq.(5.5) with experimentally determined $\omega(t)$ and the violet curve is a Lorentz model fitting.

frequency/time line cuts with Gaussian functions. We perform the Gaussian fitting along constant-frequency cuts for PP component smaller than 3.5 THz (Fig. 5.7b) and constant-time cuts for larger than 3.5 THz (Fig. 5.7c). The uncertainty of this method will be determined by the superposition of the experimental sampling step uncertainty (taken to be half of the experimental time/frequency resolution) and the uncertainty of the peak position obtained by the Gaussian fittings. The final uncertainty window is shown by the solid filled region in Fig. 5.7d. The time resolution is found to be better than 0.05 ps and the frequency resolution better than 0.03 THz.

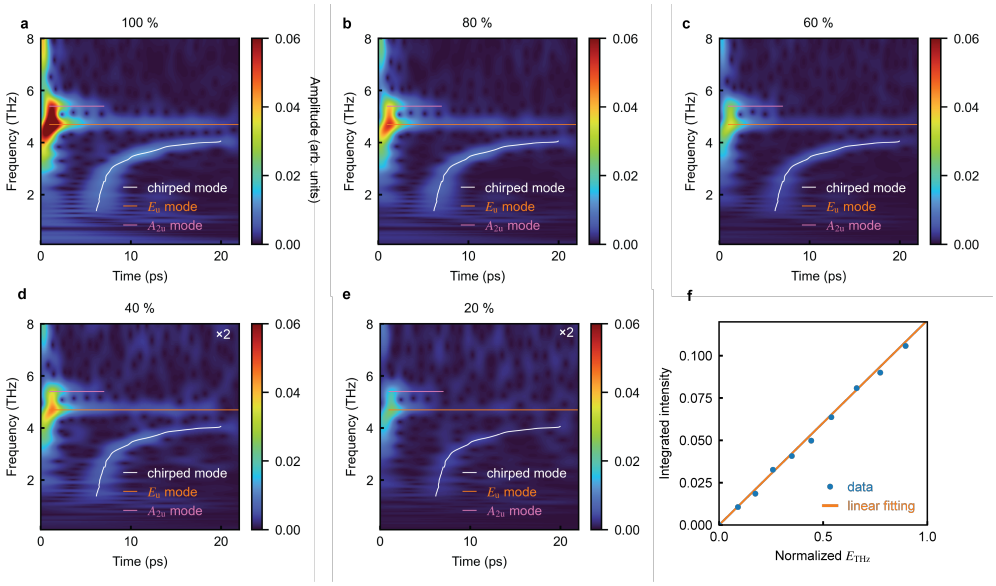

Figure 5.6: THz field strength dependence of the phonon polariton. a-e. Phonon polariton observed in spectrogram at different THz field strength. They all fall on to a same $\omega(t)$ relation (white curve). The data in **d** and **e** are multiplied by a factor two to enhance clarity. **f.** The integrated intensity of the phonon polariton along the $\omega(t)$ curve as a function of pump THz field strength. The orange line is a linear fitting to the data.

5.4 Simulation of the chirped propagating mode

To further establish this conclusion, we perform a comprehensive finite-difference-time-domain (FDTD) simulation of the THz optical response of NiI_2. To capture the essence of the experiment, we model the system as a THz plane wave incident perpendicularly to the sample surface. This approximation is valid since, given the THz refractive index of NiI_2 ($n \gtrsim 3$) [188], the angle between the THz wavevector inside the sample and the sample normal has only a small effect. We input the profile of our THz pulse (see Figure 5.1b) and combine Maxwell's equations with the dynamical response of the E_u phonon mode, which can be modeled by a damped harmonic oscillator.

The PP simulations were performed with the finite-difference time-domain (FDTD) method [191], using an open-source software package [192]. Figure 5.5b shows the result of simulation in one spatial dimension. A more realistic simulation with focused THz beam and oblique incidence produces similar results.

The sample is modeled by a Lorentz polarization model with a single resonance at the E_u phonon mode frequency, where we treat the IR-active phonon mode as a harmonic oscillator

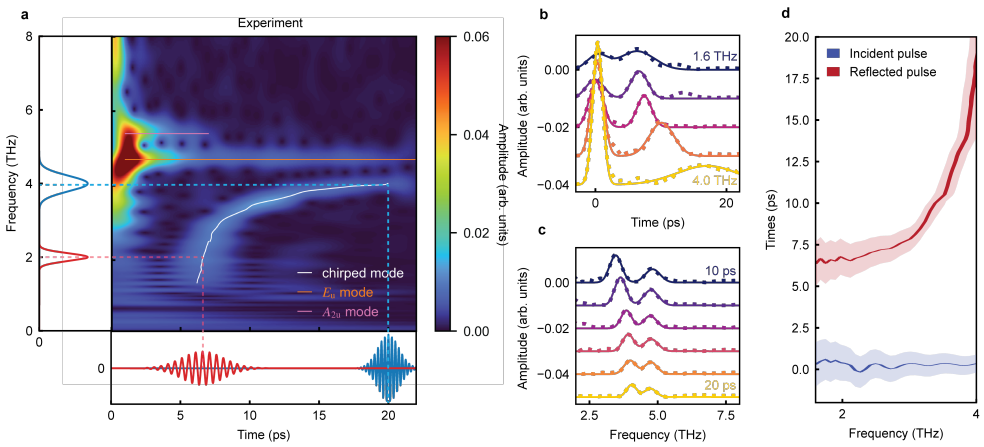

Figure 5.7: Time and frequency resolution of the wavelet analysis. a. Wavelet transformed spectrogram aligned with representative wavelet. The real part of the time-domain wavelets are shown in the lower panel, and the frequency-domain wavelet is shown in the left panel. **b.** Constant-frequency linecuts of the spectrogram and and their fittings with two Gaussian peaks. The left (near zero delay) and the right peaks correspond to the incident and the reflected pulses, respectively. **c.** Constant-time linecuts of the spectrogram and their fitting with two Gaussian peaks. The left (lower frequency) and the right peaks correspond to the reflected PP and the localized phonon, respectively. **d.** Frequency-resolved timing of the incident (blue) and the reflected (red) pulses. The light-shaded region shows the wavelet uncertainty window. The solid-shaded region shows our time and frequency resolution.

with certain damping rate:

$$\left(\frac{\partial^2}{\partial t^2}+\Gamma\frac{\partial}{\partial t}+\omega_{\mathrm{T}}^2\right)P_{\mathrm{L}}=\varepsilon_0\varepsilon_{\mathrm{r}\infty}(\omega_{\mathrm{L}}^2-\omega_{\mathrm{T}}^2)E, \tag{5.3}$$

where ω_{T} and ω_{L} are the transverse and the longitudinal phonon frequency of the E_{u} mode. Γ is the damping rate of the phonon polariton. ε_0 is the vacuum permeability constant and $\varepsilon_{\mathrm{r}\infty}$ is the relative permeability at the high frequency limit. The parameters ω_{T}, ω_{L}, and $\varepsilon_{\mathrm{r}\infty}$ are taken from [188]. Decay rate Γ is set to 0.04 THz to approximate the experimental measured decay rate. The total electric polarization of the sample is given by

$$P=\varepsilon_0(\varepsilon_{\mathrm{r}\infty}-1)E+P_{\mathrm{L}}=\varepsilon_0(\varepsilon_{\mathrm{r}\infty}+\varepsilon_{\mathrm{rL}}-1)E, \tag{5.4}$$

where P_{L} is the phonon contribution and $\varepsilon_0(\varepsilon_{\mathrm{r}\infty}-1)E$ is the electronic contribution.

The THz pump is modeled by a plane wave incident from the sample surface with the same time trace as measured by electric-optical sampling (Figure 5.1d). The total electric polarization P at the sample front surface is collected as a function of time, whose spectro-

gram is shown in Figure 5.5b. The FDTD simulation is performed with a grid size of 1 μm and time step of 2 fs.

The electric polarization at the sample surface as a function of time is used to model our experimental SH data. The result of these simulations is shown in Figure 5.5b and we find a similar chirped response as in the experiment, confirming that the chirped response indeed arises from a propagating PP wavepacket, and that the E_{u} phonon mode is responsible for the formation of the observed PP.

Therefore, we conclude that the chirped mode originates from the propagating wavepackets of the PP (shown in the schematics in Figure 5.5c). As the free space strong THz field hits the sample surface, it resonantly excites a set of PP wavepackets which propagate in the medium. As the polariton frequency approaches the phonon resonance it becomes increasingly phonon-like and its group velocity decreases. As a result, the time each frequency components of the PP (red, green and purple lines in Figure 5.5c) needs to travel to the back surface and then return to the front surface of the sample is different and is captured by the frequency-delay time relation of the chirped mode.

5.4.1 Fitting the experimental data

We use this result to extract the travel time of the different frequency components $t(\omega)$ of the polariton wavepacket, from which the dispersion relation of the PP can be directly deduced (Figure 5.5c). The time (t) and frequency (ω) information of the PP feature is extracted by Gaussian fitting of linecuts of the spectrogram, which yields a time uncertainty of 0.05 ps and a frequency uncertainty of 0.03 THz, as discussed in the next section. This time-frequency resolution is comparable to that achieved by time-domain THz spectroscopy. The group velocity of the PP $v_{\mathrm{g}}(\omega)$ can be straightforwardly extracted as $v_{\mathrm{g}}(\omega) = \frac{2l}{t(\omega)}$. Here $2l$ denotes the optical path length, which is approximated by twice of the sample thickness, with an error of less than 3%. The dispersion relation $\omega(k)$ is related to the group velocity through $v_{\mathrm{g}}(\omega) = \frac{\mathrm{d}\omega}{\mathrm{d}k}$ and we can obtain it by integrating the above relation:

$$\int_{\omega_0}^{\omega} t(\omega')\mathrm{d}\omega' = 2l(k - k_0). \tag{5.5}$$

Therefore, the dispersion relation is reconstructed with only one undetermined additive constant k_0, which can be determined by fitting to polariton dispersion models or requiring the extrapolation of the dispersion relation to satisfy certain constraints. The reconstructed PP dispersion relation of NiI_2 is shown in Figure 5.5d together with a fit using a Lorentz model without damping (see below). The uncertainty of the derived dispersion relation is shown by the errorbars at representative points, which is discussed in detail in the next section.

The averaged frequency error is 0.03 THz and wavevector error is 9 mm^{-1}. In addition, we note that the same analysis can be applied if we probe the transmitted PP at the back side of the sample [193]. However, the crucial information on the PP attenuation will be lost, as discussed later.

5.4.2 Lorentz model fitting of the PP dispersion relation

After the numerical integration given by Eq. (5.5), a dispersion curve is obtained. We first fit the integrated dispersion curve with theoretical PP dispersion without damping as the observed small damping has negligible effect on the real part of the dispersion:

$$\omega(k)^2 = \frac{1}{2\varepsilon_{r\infty}}\left(c^2k^2 + \varepsilon_{r\infty}\omega_L^2 \pm \sqrt{(c^2k^2 + \varepsilon_{r\infty}\omega_L^2)^2 - 4\varepsilon_{r\infty}c^2k^2\omega_T^2}\right), \tag{5.6}$$

where c is the speed of light. The fitted values are $\omega_T = 4.68$ THz, $\omega_L = 5.27$ THz, which are in good agreement with previous FTIR results in [188].

To include damping, it is more intuitive to consider the following differential equations[194]:

$$\begin{aligned} \ddot{Q}_1 + \Gamma_1\dot{Q}_1 &= -\omega_T^2 Q_1 + b_{1E}E, \\ P &= b_{E1}Q_1 + (\varepsilon_{r\infty} - 1)\varepsilon_0 E, \end{aligned} \tag{5.7}$$

where Q is the phonon mode coordinate, b_{1E} and b_{E1} are coupling coefficients, which are related to ω_L by $b_{1E}b_{E1} = \varepsilon_{r\infty}\varepsilon_0(\omega_L^2 - \omega_T^2)$. By coupling Eq. (5.7) to Maxwell's equations, the dispersion relation is obtained as

$$k + i\kappa = \frac{\omega}{c}\sqrt{\varepsilon_{r\infty} - \frac{b_{1E}b_{E1}/\varepsilon_0}{\omega^2 - \omega_T^2 + i\omega\Gamma_1}}. \tag{5.8}$$

Based on Eq. (5.7), coupling to other modes can be straightforwardly implemented by adding another coordinate Q_2 [195]:

$$\begin{aligned} \ddot{Q}_1 + \Gamma_1\dot{Q}_1 &= -\omega_T^2 Q_1 + b_{1E}E + b_{12}Q_2, \\ \ddot{Q}_2 + \Gamma_2\dot{Q}_2 &= -\omega_2^2 Q_2 + b_{21}Q_1, \\ P &= b_{E1}Q_1 + (\varepsilon_{r\infty} - 1)\varepsilon_0 E. \end{aligned} \tag{5.9}$$

b_{12} and b_{21} are coupling constants between mode Q_1 and Q_2. The terms involving b_{2E} and b_{E2} are omitted since we do not observe SH modulation at frequency ω_2. The PP dispersion

in this case is

$$k + i\kappa = \frac{\omega}{c}\sqrt{\varepsilon_{r\infty} - \frac{b_{1E}b_{E1}/\varepsilon_0}{\omega^2 - \omega_T^2 + i\omega\Gamma_1 - \frac{b_{12}b_{21}}{\omega^2-\omega_2^2+i\omega\Gamma_2}}}. \tag{5.10}$$

The fitting with Eq. (5.10) is presented in Figure 5.9b-c, which gives $\frac{\Gamma_1}{2\pi} = (0.05 \pm 0.01)$ THz, $\frac{\Gamma_2}{2\pi} = (1.04 \pm 0.04)$ THz, and correction factor $S = 1.28 \pm 0.01$.

5.5 Extraction of the dissipative part of the polariton dispersion

Besides the real part of the dispersion relation, the attenuation of the PP with propagation length can also be extracted from our time-of-flight method, which is related to the imaginary part (κ) of the dispersion ($\tilde{k} = k + i\kappa$). We can extract the PP oscillation amplitude as the amplitude of the spectrogram in Figure 5.5 a within the incident pulse A_0 (Figure 5.9a blue line) and the reflected pulse A_1 (Figure 5.9a red line) at different frequencies. They are related to each other by the imaginary part of the wavevector κ and the reflection coefficient r at the boundary by

$$\frac{A_1}{A_0} = e^{-2\kappa l} r(1 + r)S, \tag{5.11}$$

where the factor $(1 + r)$ accounts for the contribution of both the reflected pulse and its further reflection at the front surface. S is a order-one constant correction factor that accounts for the slight spatial offset between the incident pulse and the reflected pulse. The frequency dependence of κ, as obtained from Eq. (5.11), is shown in Figure 5.9b. The divergence of κ near the phonon resonance frequency is observed, which is consistent with the damped harmonic oscillator model. Notably, a shoulder-like peak in κ is observed around $\omega_2 = 3.1$THz. We rule out the possibility of this peak originating from data analysis or our experimental configuration. Such anomalous damping behavior is due to coupling of the E_u mode to another mode, which opens additional energy dissipation pathway to the coupled mode [195], [196]. Since $\kappa(\omega)$ does not change with the THz fluence (see Figure 5.8), we conclude that this is a bi-linear coupling between the E_u mode to another mode. The frequency of the shoulder-like peak in κ is close to a magnon mode in NiI_2 [186], indicating that our observation is a potential signature of magnon-phonon coupling. The real and the imaginary parts of the dispersion can be simultaneously fitted with the bi-linear coupling model [195] (Figure 5.9b and c). The coupling strength between the two modes is $\frac{b_{12}b_{21}}{(2\pi)^4} = (1.7 \pm 0.1)$ THz^4, while the E_u mode oscillator strength $\frac{b_{1E}b_{E1}}{(2\pi)^2\varepsilon_0} = (61 \pm 2)$ THz^2. The observation of the magnon-phonon coupling is due to the type-II multiferroic nature of NiI_2, and hints towards controlling the magnetization across the sample with PP.

In addition, the amplitude of the PP can also be measured by comparing with the static

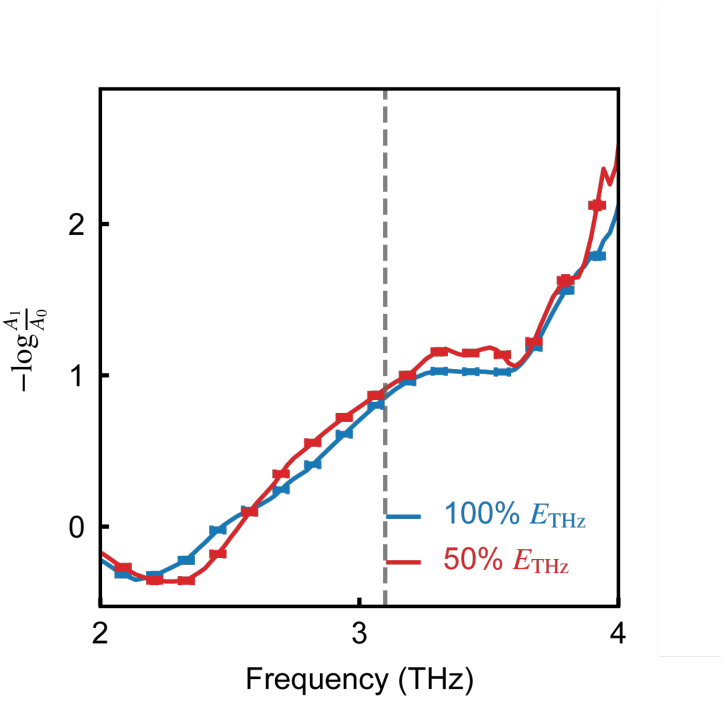

Figure 5.8: Bilinear mode coupling. The logarithm of the ratio between the reflected and the incident pulse amplitudes as a function of frequency at 100% E_{THz} (blue curve) and 50% E_{THz} (red curve). The dashed line shows the frequency of the coupled mode as obtained by bi-linear model fitting. The error bars are shown at representative points.

SH signal from NiI_2. The blue curve in Figure 5.9 shows the SH oscillation amplitude normalized by the static SH. The observed SH signal is proportional to the polariton induced electric dipole, which includes contribution from both electrons and phonons (see also in Methods section). When the phonon resonance frequency is approached, the real part of the dielectric function ε_r increases yet the polariton damping also increases, leading to a peak in the polarization amplitude below the resonance frequency (around 3.5 THz in Figure 5.9). The estimated phonon component is shown as the orange line of Figure 5.9. The peak of the phonon component is about 0.2% of the static SH signal in the low temperature multiferroic phase. As shown in Figure 5.10, we can separate the contributions from electronic and phonon polarizations using the parameters from the fitting in Figure 5.5d. The peak of the phonon component is about 0.2% of the static SH signal in the low temperature multiferroic phase.

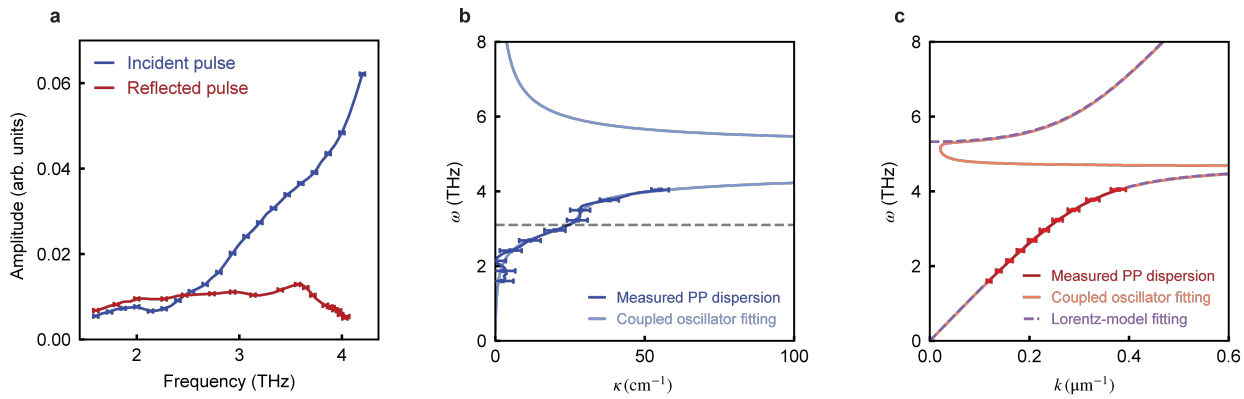

Figure 5.9: Obtaining the imaginary part of the PP dispersion relation from the spectrogram. a. The amplitude of the incident pulse (blue curve) and the reflected pulse (red curve) as a function of frequency extracted from the spectrogram in Figure 5.5a. The error bars show the standard error of the amplitude and frequency at representative points. **b.** The experimentally measured imaginary part of the dispersion relation obtained from Eq. (5.11) (dark blue curve) and its fitting with coupled Lorentz oscillator model (light blue curve). **c.** The red curve shows the real part of the dispersion relation as in Figure 5.5d. The dashed violet curve is the fitting with Lorentz model without damping as in Figure 5.5d. The orange curve is the fitting with bi-linear coupling model. The error bars in **b** and **c** show the standard error of wavevector and frequency of our constructed dispersion relation at representative points.

5.6 Application of the time-of-flight technique on $MnPS_3$

While in NiI_2 only the lower branch of the PP is visible due to finite THz bandwidth, in principle, our time-of-flight approach is sensitive to both the lower and upper PP branches (see Figure 5.11). To demonstrate the versatility of this time-of-flight approach, we carried out a similar measurement on a different non-centrosymmetric vdW magnet $MnPS_3$ [197]. In this experiment, we not only observe the dispersively chirped mode, but also a second replica at larger time delays, which originates from multiple reflections of the PP in the sample (see Figure 5.11b). Notably, the upper branch of the PP is also visible. The reconstructed PP dispersion relation of $MnPS_3$ is presented in Figure 5.11c. The light matter coupling strength is $\frac{b_{1E}b_{E1}}{4\pi^2\varepsilon_0} = (50.6 \pm 0.4)$ THz^2, indicating a weaker coupling to in-plane polarized light in the 1-5 THz range compared to NiI_2.

5.7 Conclusions

Compared with other methods for studying PPs, our time-of-flight approach offers several unique advantages. With a single scan, a broad bandwidth of phonon polariton dispersion can

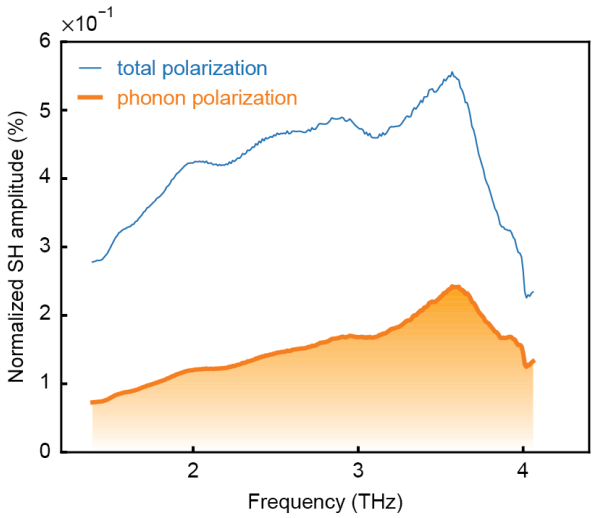

Figure 5.10: PP induced electric polarization. The blue curve is the total polarization of the PP returning to the sample surface. The orange curve is the lattice contribution to the polarization.

be obtained, as long as its attenuation coefficient is below 100 cm^{-1} for typical samples. This eliminates the need for repeated measurements with varying incidence angles or wavelengths. Larger attenuation coefficients usually only appear close to phonon resonances, where the PP is predominantly composed of non-propagating evanescent waves. The accessible range of the polariton dispersion can potentially be further extended by the use of broader bandwidth THz pulse. While time-domain THz spectroscopies have been used to investigate PPs, they require additional alignments to sample the THz pulse in an electro-optic sampling crystal. In contrast, our method enables sampling the time-dependent, phase-resolved PP amplitude directly at the sample surface. This aspect also allows the study of PPs over microscopic length scales, smaller than the THz diffraction limit. Since we are decoding the back-reflected THz PP in both time-frequency space, we are less affected by the overlapping back-reflected response that can limit the frequency resolution of a time-domain THz spectroscopy. Finally, anharmonic PP effects can potentially be observed in crystals with large nonlinearities, provided with our high THz field strength.

In summary, we demonstrated a time-resolved technique to measure both the real and the imaginary parts of coherent PP dispersion. This time-of-flight method is based on broadband THz excitation of a PP wavepacket and its detection using time-resolved SH, which offers technical advantages over traditional methods. Utilizing linear or nonlinear probing in the NIR or visible spectrum, as demonstrated here, shifts the achievable spatial resolution down to the ~ 1 μm range far beyond what conventional TDTS can achieve. Our time-of-flight

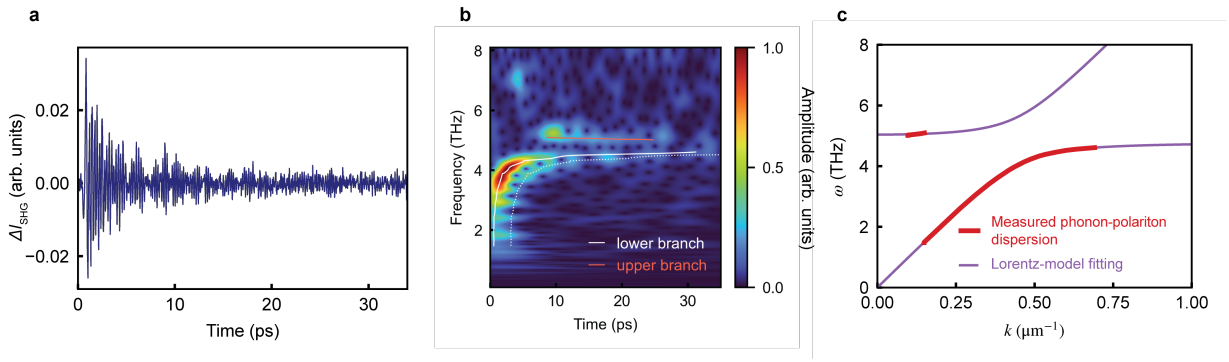

Figure 5.11: Phonon polariton observed in $MnPS_3$.
textbfa. THz pump SHG probe trace on $MnPS_3$. **b.** Spectrogram of the trace in **a**. **c.** the reconstructed phonon polariton dispersion relation from the spectrogram in **b**.

approach can also be extended to other polaritonic modes, such as magnon polariton. We expect that this method will be highly useful for the study of low energy collective modes and their interactions with light. It may also help enable the use of large amplitude PP oscillations as a tool for ultrafast control of material properties.

Chapter 6

Coherent detection of hidden magnetostriction effect

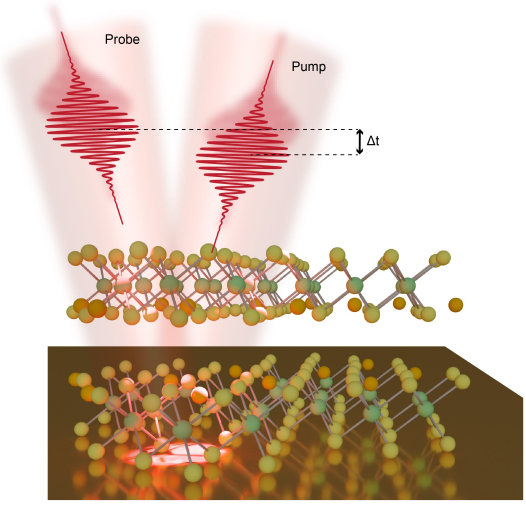

Contents

Strong interactions between various degrees of freedom can give rise to exotic phases of matter characterized by complex order parameters and emergent collective excitations. While traditional techniques like scattering and transport measurements can probe the amplitudes of these excitations, they generally lack sensitivity to their phases [198]. Consequently, novel methods that can detect phase are necessary to understand ground states with phase modulations [199] and interactions that couple to the phase of collective modes. In this study, we utilize phase-resolved coherent phonon spectroscopy (CPS) to uncover a hidden spin-lattice coupling in the van der Waals (vdW) antiferromagnet $FePS_3$, a phenomenon that has eluded conventional phase-insensitive probes such as Raman and X-ray scattering. Through comparative analysis and analytical calculations, we demonstrate that the magnetic order in $FePS_3$ selectively couples to trigonal distortions via partially filled t_{2g} orbitals. This magnetoelastic coupling is linear in terms of magnetic order and lattice parameters, making these distortions undetectable by inelastic scattering techniques. Our findings not only reveal the elusive spin-lattice coupling in $FePS_3$, but also establish phase-resolved CPS as a powerful tool for investigating hidden interactions.

This chapter is based on the following published work:

E. Ergeçen[†], B. Ilyas[†], *et al.* Coherent detection of hidden spin-lattice coupling in a van der Waals antiferromagnet. *Proceedings of the National Academy of Sciences* , **120** (12) e2208968120 (2023) [20]

The author of this dissertation contributed to the following aspects of the work: designing and constructing the experimental setup, conducting the experiments, analyzing and interpreting the experimental data, and writing the manuscript.

6.1 The microscopic origin of spin-lattice interactions

van der Waals (vdW) materials and their heterostructures exhibit a range of tunable correlated phenomena, resulting from the interplay between lattice, spins, and orbitals. These

phenomena include unconventional superconductivity [6] and charge-ordered states [200]. Recently, vdW magnets have emerged as platforms for studying strong spin-lattice interactions [201]–[203]. For instance, the stacking configuration between adjacent layers can modify the interlayer exchange interactions [204], leading to diverse magnetic ground states [93], such as the coexistence of distinct magnetic states with mesoscopic periodicity defined by the twist angle [205]–[207].

Despite the various phases emerging from strong spin-lattice coupling in vdW magnets, their microscopic origins remain poorly understood, necessitating new techniques with both magnetic and structural sensitivity. This is particularly relevant for $FePS_3$, a prototypical vdW antiferromagnet exhibiting easy-axis zigzag antiferromagnetic order below its Néel temperature (T_N = 118 K) [121]. $FePS_3$ displays a unique set of magnetically active low-energy collective modes [208]–[211], interpreted as zone-folded phonon modes, indicating strong spin-lattice coupling. However, the structural phonon modes above the Néel temperature do not show any frequency renormalization, which is a hallmark of strong spin-phonon coupling [212], [213]. Despite the emergence of new magnetically enabled phonons with the onset of magnetic order, the microscopic mechanisms causing the disparity between these new collective modes and structural phonon modes, as well as the nature of spin-lattice coupling in $FePS_3$, remain unresolved.

In this chapter, we use phase-resolved coherent phonon spectroscopy (CPS) to reveal a mode-selective spin-lattice coupling in $FePS_3$ that has remained hidden to Raman and X-ray scattering techniques [208], [210], [211]. CPS allows us to resolve both the amplitudes and phases of phonons in $FePS_3$ by coherently driving them and observing their real-time oscillations. Below the Néel temperature (T_N), this hidden spin-lattice interaction is indicated by a sudden change in the phase and amplitude of the 7.51 THz phonon mode. This interaction is specific to this mode, as the 11.45 THz mode shows no change in its phase or amplitude. To identify the origin of this mode-selective change, we compare our results with $NiPS_3$, an isostructural analog of $FePS_3$ [122], [214]. Through crystal field calculations, we determine that the effect is due to a magnetoelastic coupling between t_{2g} orbitals and trigonal distortion, which closely matches the symmetry of the 7.51 THz A_{1g} mode. Our analysis clarifies the source of the observed mode-specific spin-phonon coupling in $FePS_3$.

6.2 Experimental methods

6.2.1 Sample preparation

$FePS_3$ crystals were synthesized via a chemical vapor transport method as detailed in Ref. [215]. All powdered elements: iron (99.99% purity), phosphorus (99.99%), and sul-

fur (99.998%), were obtained from Sigma-Aldrich and prepared inside an argon-filled glove box. The starting materials were weighed in the correct stoichiometric ratio, with an additional 5 wt% of sulfur added to account for its high vapor pressure. After synthesis, we conducted a chemical analysis of the single-crystal samples using a COXEM EM-30 scanning electron microscope with a Bruker QUANTAX 70 energy dispersive X-ray system to confirm stoichiometry. We also performed XRD checks using a Rigaku Miniflex II commercial diffractometer. Before optical measurements, we determined the crystal axes of the samples using an X-ray diffractometer. To ensure a clean surface free from contamination and oxidation, the samples were cleaved and placed into a high vacuum ($\sim 10^{-7}$ torr).

6.2.2 Phase-resolved coherent phonon spectroscopy

We used the output from a Ti:sapphire oscillator (Cascade-5, KMLabs), centered at 760 nm (1.63 eV) with a pulse duration of ∼25 fs. The laser operated at an 80 MHz repetition rate. Before splitting the output into pump and probe branches, we compensated for group velocity dispersion (GVD) using a pair of chirp mirrors and N-BK7 wedges to maintain the pulse duration at the sample position. The pump and probe pulses were separately characterized at the sample position using frequency-resolved optical gating techniques, confirming a pulse duration of around 25 fs. To enhance the signal-to-noise ratio, we modulated the pump intensity at 100 kHz. The probe signal from the photodiode was sent to a lock-in amplifier (Stanford Research SR830) synchronized to the chopping frequency (100 kHz). For faster data acquisition and averaging, the pump-probe delay was rapidly scanned at a rate of 5 Hz using an oscillating mirror (APE ScanDelay USB). Detailed schematics of the setup are provided in Figure 7.2

6.3 Mode selective spin-phonon interaction

6.3.1 Transient reflectivity at room temperature

In our experimental setup, a low-intensity and ultrashort pump pulse is used to displacively excite coherent phonons of A_{1g} and E_g symmetries without quenching the magnetic order. Following the pump excitation, a lower-intensity probe pulse tracks the coherent phonon oscillations as a function of the pump-probe delay time, Δt. The pump has a center wavelength of 760 nm (1.63 eV) and a pulse bandwidth of 60 nm, covering the charge transfer gap in this energy range [216], [217]. Figure 6.1b shows the transient reflectivity trace of $FePS_3$ at room temperature. In addition to the incoherent electronic decay, the signal includes an oscillatory component composed of two Fourier components (inset of Figure 6.1b), with

frequencies of 7.51 THz and 11.45 THz. The lattice distortions associated with these A_{1g} symmetry phonon modes are depicted in Figure 6.1a. The 7.51 THz mode corresponds to an out-of-plane breathing mode of sulfur atoms, while the 11.45 THz mode involves the in-plane motion of sulfur atoms.

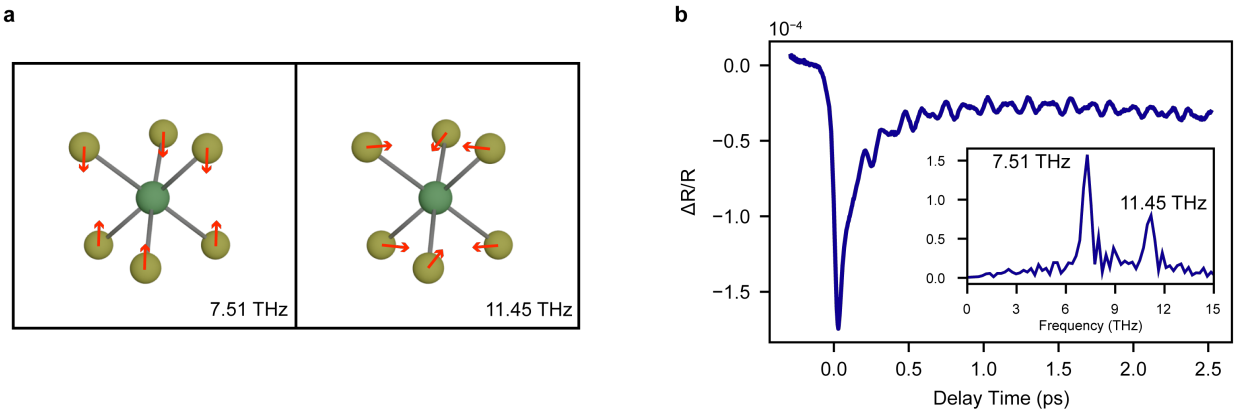

Figure 6.1: Coherent phonon spectroscopy on $FePS_3$. a. In $FePS_3$, six sulfur (yellow) atoms in an octahedral configuration surround iron (green) atoms. Arrows depict the octahedral distortions corresponding to two A_{1g} phonons with frequencies 7.51 THz and 11.45 THz. **b** The transient reflectivity trace of $FePS_3$ obtained at room temperature (293 K) consists of an incoherent electronic decay signal and oscillatory features originating from coherent phonons. The Fourier spectrum (inset) of these oscillations reveals two phonon modes with frequencies matching the A_{1g} phonons shown in **a**. .

6.3.2 Temperature dependence

To investigate the effects of spin-lattice coupling on the coherent phonon spectrum, we conducted temperature-dependent phase-resolved CPS on $FePS_3$ and monitored the changes in transient reflectivity as a function of temperature (Figure 6.2a). Around 90 K, the signal develops a long-lived component, indicating a change in electronic structure due to the magnetic order. Concurrently, we observe changes in the coherent phonon oscillations (Figure 6.2b), which are isolated by subtracting the incoherent background using a single exponential fit. Figure 6.3a displays the temperature-dependent Fourier transform of the coherent phonon oscillations. Below ∼90 K, a new mode at 3.28 THz emerges in the coherent phonon spectrum. This low-energy mode, previously observed in Raman spectroscopy below T_N, is attributed to magnetic zone-folding [208], [211], signaling the onset of magnetic order. We use this mode as an indicator of magnetic order in our experimental scheme. The discrepancy between the reported Néel temperature (118 K) and the observed Néel temperature (90 K) is attributed to laser-induced average heating in our experiments. As shown in Figure 6.3 a and c, the

emergence of the 3.28 THz mode, which marks the onset of magnetic order, coincides with a clear downturn in the amplitude of the 7.51 THz mode. Upon further cooling, this coherent phonon oscillation diminishes around 80 K and then recovers as the temperature continues to drop. In contrast, the 11.45 THz mode shows negligible change across T_N.

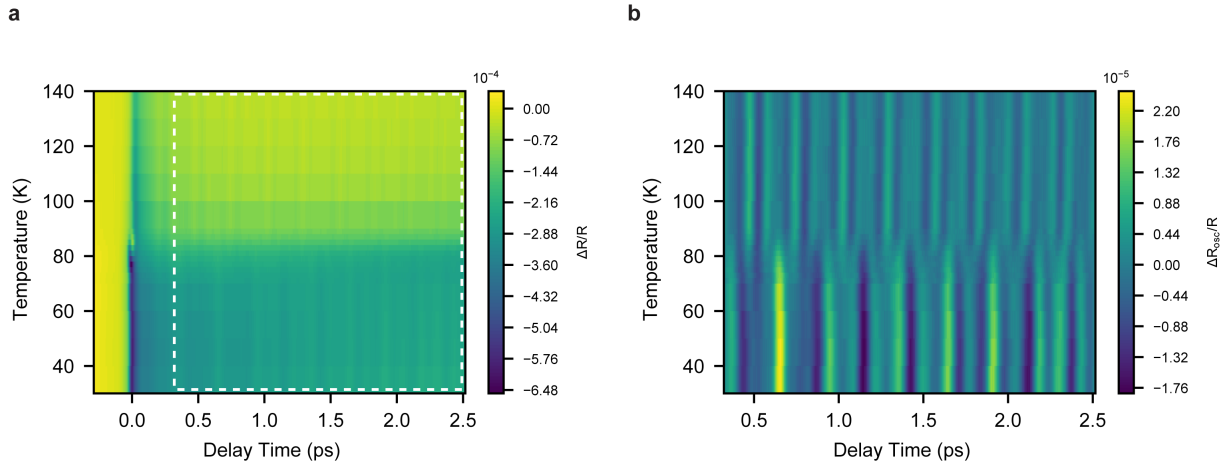

Figure 6.2: Magnetic order induced changes in coherent phonons. a. The temperature dependent coherent phonon spectroscopy on $FePS_3$ exhibits a pronounced change near ∼90 K . **b.** The oscillatory part of the traces in the region marked by a dashed white box, extracted by fitting the incoherent background with a single exponential.

To further investigate the time-domain evolution of these phonon modes, we applied Fourier filtering. The filtered spectral regions and the corresponding time traces are presented in Figure 6.3b. Notably, the 7.51 THz mode exhibits a π phase shift at low temperatures, which is not observed in the 11.45 THz phonon mode, as shown in Figure 6.3d. Figure 6.3c also displays the phase-corrected coherent phonon amplitudes, where the π phase shift corresponds to a negative mode amplitude. The 3.28 THz phonon mode demonstrates order parameter behavior, indicating that the pump pulse does not disrupt the magnetic order in these samples across all temperatures. The amplitude of the 7.51 THz mode begins to decline at the onset of magnetic order, with its decrease mirroring the order parameter behavior of the 3.28 THz mode. This behavior is significantly suppressed in the 11.45 THz phonon mode, suggesting a weaker spin coupling compared to the 7.51 THz mode.

6.3.3 Contrasting CPS and Raman spectra

The frequencies of both phonon modes are consistent with the Raman results. However, unlike CPS, the Raman scattering amplitudes for the 7.51 THz and 11.45 THz modes do not exhibit any temperature dependence, as shown in Figure 6.4. Despite both Raman and

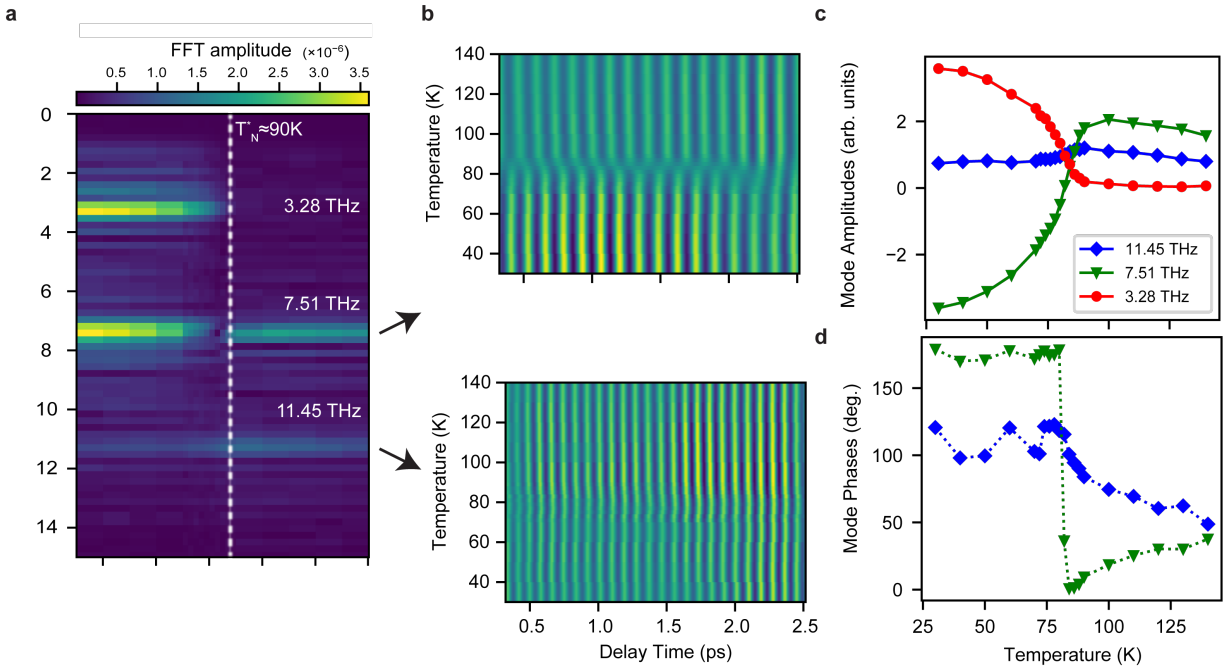

Figure 6.3: The Néel order selectively couples to the 7.51 THz phonon mode. a. Below ∼90 K, the temperature-dependent Fourier spectra of oscillations reveal the emergence of a new phonon mode at 3.28 THz. Fourier filtered time traces for the 7.51 THz and 11.45 THz modes are shown in **b**. **c** and **d** present the temperature-dependent phase-corrected amplitudes and phases of these phonons. The 3.28 THz mode exhibits order parameter-like behavior, with its onset coinciding with the magnetic order. Following the appearance of this mode, the 7.51 THz mode experiences a π-phase shift, resulting in a sign change in its phase-corrected amplitude. In contrast, the amplitude of the 11.45 THz mode shows no discernable change.

CPS being sensitive to phonon modes, they excite and detect phonons differently. Raman scattering measures phonon-induced changes in polarizability, known as the Raman matrix element ($|\frac{\partial \epsilon}{\partial Q}|^2$), by transitioning between the ground state and the single phonon excited state [218]. This suggests that in $FePS_3$, the Raman matrix elements of both A_{1g} phonons remain constant across all temperatures. In contrast, CPS relies on the generation of pump-induced coherent phonons through displacive or impulsive processes [219]. Therefore, the observed mode amplitude in CPS is given by:

$$R_{\text{osc}} = \sum_i \frac{\partial R}{\partial \epsilon} \frac{\partial \epsilon}{\partial Q_i} \Delta Q_i \tag{6.1}$$

here ΔQ_i represents the initial displacement of a phonon after photoexcitation, ϵ is the dielectric constant, and R is the reflectivity as a function of the dielectric constants. Since the Raman matrix elements remain constant across all temperatures, the observed temperature-dependent changes in amplitude and phase in CPS can be attributed to variations in ΔQ_i.

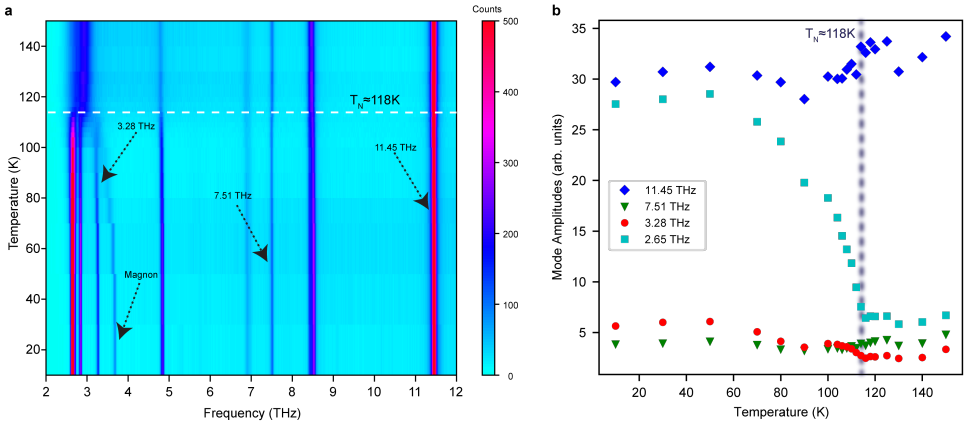

Figure 6.4: Temperature dependent Raman spectra of $FePS_3$. a. Raman spectra in a temperature range that spans above and below T_N. White dashed line marks the transition temperature. Phonon modes with 3.28 THz, 7.51 THz, 11.45 THz frequencies and a magnon are labeled. **b.** Temperature evolution of amplitudes of selected phonons. 7.51 THz and 11.45 THz modes show no discernable change across Néel temperature.

6.3.4 Photoexcited electronic free energy landscape

To investigate the underlying mechanisms behind the mode-selective behavior and the influence of magnetic order on phonon phase shifts, we examine the free energy landscape before and after photoexcitation. In the case of ultrafast excitations, the initial displacement of phonons (ΔQ) corresponds to the difference between the minimum energy lattice configurations before and after pump excitation. This process, known as displacive excitation of coherent phonons, is illustrated for $FePS_3$ in Figure 6.5, where the upper and lower free energy surfaces represent the photoexcited and equilibrium states, respectively. Generally, the equilibrium and photoexcited free energy landscapes exhibit different minima due to the presence of excited electrons. Below the Néel temperature (T_N), the equilibrium atomic positions undergo shifts due to magnetoelastic coupling, with the magnitude of displacement along specific mode directions determined by the strength of mode-selective spin-phonon

coupling. If the magnetoelastic coupling between the magnetic order parameter (N) and the phonon position operators is linear, it alters the phonon displacements without affecting their frequencies and Raman matrix elements. The mathematical expression describing this scenario is detailed in the following.

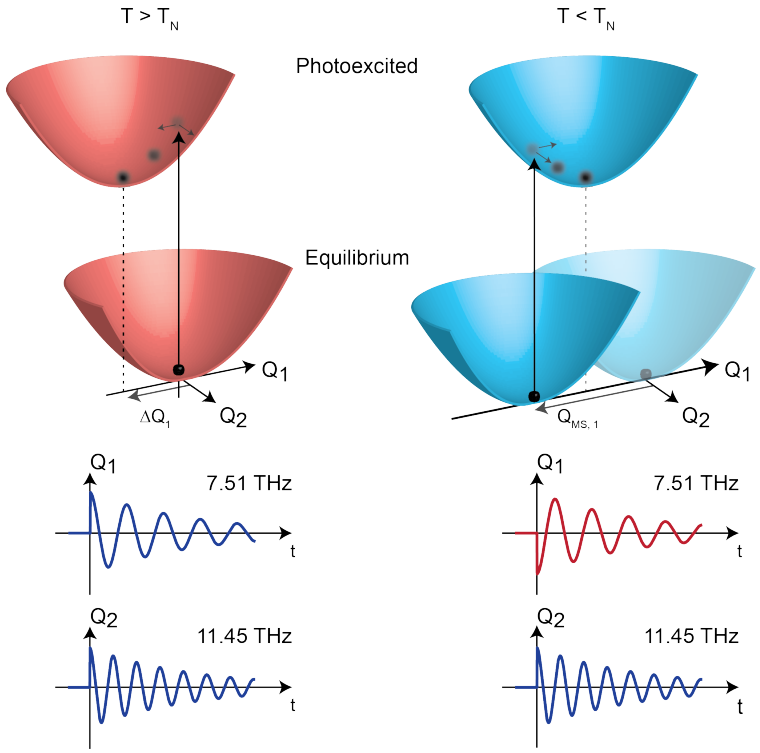

Figure 6.5: Magnetostriction induces a mode-selective π-phase shift in coherent phonon oscillations. a. Upper panels show the equilibrium and photoexcited free energy landscapes. Q_1 and Q_2 are generalized atomic coordinates along the motion axis of 7.51 THz and 11.45 THz phonons, respectively. Above T_N, photoexcitation launches coherent phonons displacively due to a relative shift between photoexcited and equilibrium free energy landscape minima (e.g ΔQ_1 along the Q_1 axis). Below T_N, magnetostriction induces an anisotropic shift of the equilibrium landscape, which is much stronger along the Q_1 axis ($Q_{MS,\,1}$) than in Q_2 axis. This results in π-phase shift of the 7.51 THz mode, while 11.45 THz mode remains unaffected. This scenario is depicted in the lower panels which show the coherent oscillations of each mode in time domain below and above T_N.

The free energy functional that describes our system can be expressed as:

$$F_{\text{equilibrium}} = \frac{p_1^2}{2m_1} + \frac{1}{2}m_1\omega_1^2Q_1^2 + \frac{p_2^2}{2m_2} + \frac{1}{2}m_2\omega_1^2Q_2^2 + g_1N^2Q_1 + g_2N^2Q_2 \tag{6.2}$$

where Q_1, p_1, Q_2, and p_2 represent the positions and momenta of the Raman phonon modes, while g_1 and g_2 denote the magnetoelastic coupling constants corresponding to the 7.51 THz (ω_1) and 11.45 THz (ω_2) phonon modes, respectively. The linear coupling between the

magnetic order parameter N and the phonon position operators induces changes in phonon displacements without affecting their frequencies or Raman matrix elements. This linear coupling, permitted by symmetry as Raman modes are even under inversion, alters the phonon positions in response to the magnetic order. Given the observed changes in the 7.51 THz phonon mode concurrent with the onset of magnetic order compared to the 11.45 THz phonon mode, it suggests that the magnetoelastic coefficient (g_1) for the 7.51 THz mode is considerably higher than that of the 11.45 THz mode (g_2).

6.4 The role of d-shell electronic configurations in the magnetoelastic coupling

6.4.1 Comparison with the nickel-based counterpart

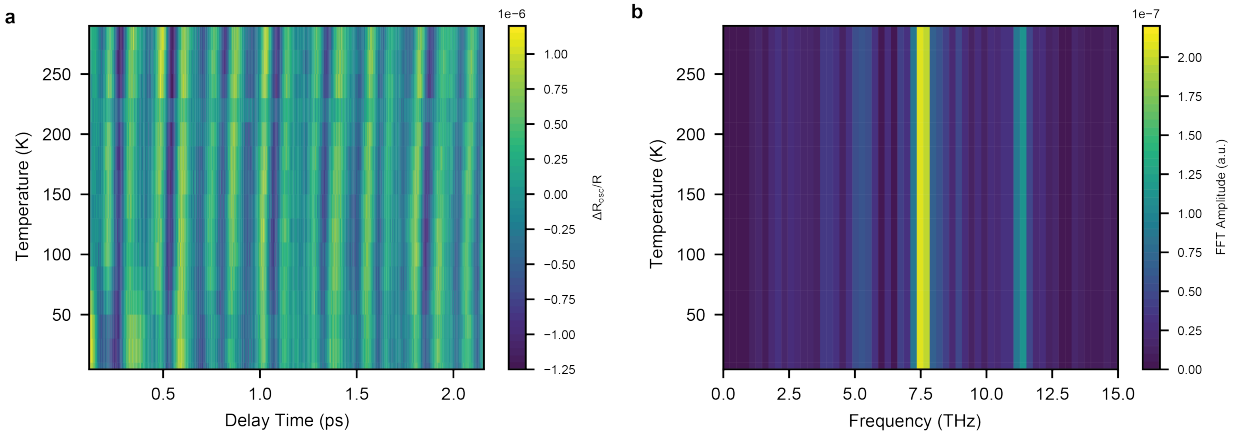

Figure 6.6: Coherent phonon spectroscopy of $NiPS_3$. a. Time traces of coherent phonon oscillations of $NiPS_3$, extracted from pump-probe signal by fitting the incoherent background with a single exponential. No discernible change was observed across the T_N = 155K. **b.** Fourier transform of oscillations. Three distinct modes was detected: 5.1,THz, 7.5 THz and 11.4 THz. The frequencies of 7.5 THz and 11.4 THz modes match well with modes observed in $FePS_3$. The striking contrast from iron compound is that the modes (amplitude and phase) remain unaffected by magnetic ordering.

While our phenomenological model effectively describes the experimental observations of mode-selective spin-lattice coupling, it lacks a microscopic explanation for the mode specificity and the linear coupling between phonons and magnetic order. To uncover the underlying microscopic mechanisms, we compare the coherent phonon spectra of $FePS_3$ to those of $NiPS_3$, an isostructural counterpart. Both systems exhibit zigzag AFM order with similar exchange coupling constants [91], [220], [221]. Additionally, their optical spectra reflect

comparable bandgaps [216], [222], [223]. The key distinction lies in the electronic configurations of the transition metal ions. Ni^{2+} ions ($3d^8$) possess two additional d-electrons compared to Fe^{2+} ions ($3d^6$). Despite both $NiPS_3$ (see Figure 6.6) and $FePS_3$ exhibiting phonon modes at 7.51 and 11.45 THz with similar symmetries, the former does not display any temperature-dependent phase or amplitude changes below the Néel temperature (T_N). This observation leads us to attribute the mode-selective spin-lattice coupling in $FePS_3$ to its localized d-orbital electron configuration.

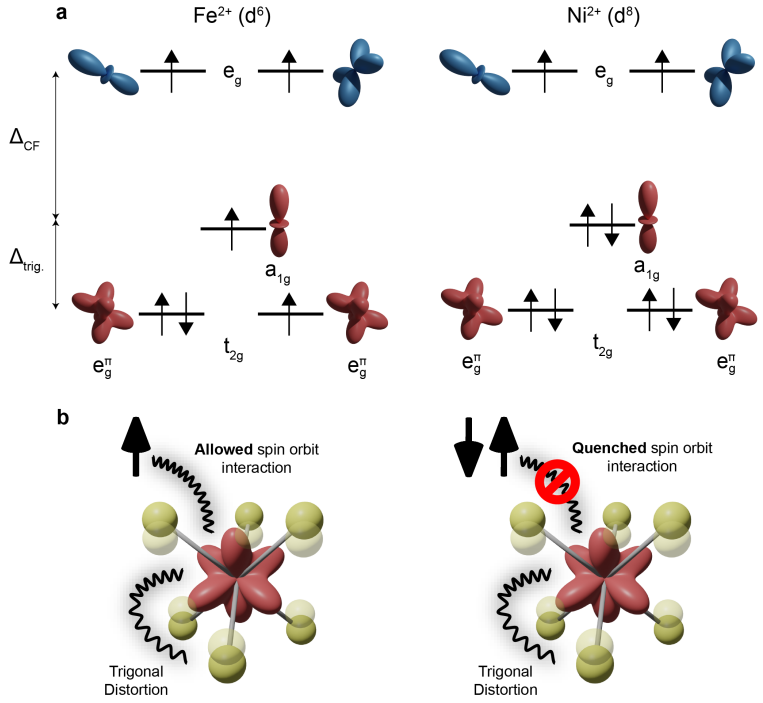

Figure 6.7: Spins in e_g^π levels selectively couple to trigonal distortions resulting in mode-selective magnetostriction. a. Electronic configurations of Fe^{2+} and Ni^{2+} ions in a trigonally contracted octahedral environment of sulfur atoms. In $FePS_3$, transition metal ions host two unpaired spins in e_g^π orbitals and two unpaired spins in e_g orbitals with quenched orbital angular momenta. On the other hand, in $NiPS_3$, transition metal ions host two additional electrons in e_g^π orbitals compared to $FePS_3$. **b.** Two unpaired spins in e_g^π orbitals of $FePS_3$ allow efficient coupling between the magnetic order and trigonal distortions. This magnetoelastic effect is due to spin-orbit coupling mediated virtual transitions between e_g^π and a_{1g} orbitals. This effect is absent in $NiPS_3$ (shown on the right), since the t_{2g} levels are fully occupied.

The d-orbital electron configurations of Ni^{2+} and Fe^{2+} ions are depicted in Figure 6.7a. In both compounds, the transition metal ions are surrounded by ligands arranged in octahedral configurations, accompanied by trigonal distortions [122]. Both Fe^{2+} and Ni^{2+} ions exhibit two unpaired spins in their e_g orbitals. In iron compounds, the t_{2g} levels are partially filled, while in nickel compounds, these levels are fully occupied. Thus, we can attribute the

microscopic origin of mode-selective magnetoelasticity in $FePS_3$ to the t_{2g} orbitals.

6.4.2 Spin order induced trigonal distortion

To investigate the magnetoelastic effects in $FePS_3$, we conduct a theoretical analysis of the system at the single octahedra level, with a specific focus on the low-energy t_{2g} manifold. In the context of trigonal distortions, the Hamiltonian governing the low-energy t_{2g} manifold is described as follows [122]:

$$H = (\Delta_{\text{trig.}} + \alpha u)L_z^2 + \lambda LS + \frac{1}{2}Bu^2 \tag{6.3}$$

where $\Delta_{\text{trig.}}$ represents the existing trigonal splitting, λ denotes the spin-orbit coupling constant, H stands for the external magnetic field, B corresponds to the elastic constant associated with trigonal distortions, and α quantifies the change in energy following changes in trigonal distortions. The quantization axis aligns along the (111) direction of the octahedra and the c-axis of the crystal. Despite the absence of a direct coupling between the structural distortion u and the spin operator S, spin-orbit coupling generates an effective Hamiltonian, proportional to $H_{\text{eff, magnetoelastic}} = -\frac{\alpha\lambda^2}{\Delta^2}uS_z^2$. This term implies that the z-component of spins selectively displaces the octahedra along the trigonal distortion. It does not induce changes in its elastic properties, which would manifest as a coupling quadratic term in u and would modify the normal mode frequencies. Moreover, this microscopic treatment yields the value of trigonal distortion as $u_0 = \frac{\alpha\lambda^2}{B\Delta^2}S_z^2$. Following pump excitation, this value alters due to the pump-induced change in the magnetic system, given by $\delta u_0 = \frac{2\alpha\lambda^2}{B\Delta^2}S_z\delta S_z$. This expression mirrors the magnetic order-dependent phonon displacement (ΔQ) expression and provides a microscopic explanation for spin-dependent coherent phonon oscillations on a single-ion level.

Our microscopic examination of mode-selective magnetoelasticity, based on single-ion anisotropy, holds true for $FePS_3$ on a bulk level. Firstly, below the magnetic transition, the expectation value of S_z^2 remains constant for different octahedra constituting the material. Consequently, each individual layer of $FePS_3$ experiences a uniform trigonal distortion, allowing the replacement of the S_z operator with the antiferromagnetic order parameter N. Additionally, the spin-orbit coupling in this material arises from on-site e_g^π d-orbitals. Unlike other vdW magnets such as CrI_3 [224], [225], where the spin-orbit coupling stems from ligands, our single-ion treatment remains applicable for bulk $FePS_3$.

The trigonal distortions induced by the mode-selective magnetoelasticity on the single octahedral level translate to out-of-plane motion of sulfur atoms on a bulk scale. Consequently, the mode-selective magnetoelasticity will interact differently with phonon modes,

depending on their spatial projection on trigonal distortions or the out-of-plane motion of sulfur atoms. As depicted in Figure 6.1a, the 7.51 THz A_{1g} phonon mode directly corresponds to the out-of-plane oscillation of sulfur atoms and thus directly relates to the trigonal distortion of octahedra. Conversely, as the 11.45 THz phonon mode involves the in-plane motion of sulfur atoms, the coupling between this phonon mode and the trigonal distortions is negligible. Moreover, as illustrated in Figure 6.7b, this magnetoelastic coupling is absent in $NiPS_3$ due to its fully filled t_{2g} d-shell.

6.5 Conclusions

In conclusion, through coherent phonon spectroscopy, we unveil mode-selective magnetoelasticity in $FePS_3$, a phenomenon previously undetectable with phase-insensitive measurements. This effect alters both the amplitude and phase of the coherent phonon signal of the 7.51 THz A_{1g} phonon mode without frequency renormalization below the magnetic transition temperature. By conducting a comparative analysis between $FePS_3$ and $NiPS_3$, we identify the mode-selective nature of spin-lattice coupling and highlight the crucial role of trigonal distortions in these materials. Our findings not only shed light on mode-selective magnetoelasticity in $FePS_3$ but also reconcile the distinction between magnetically induced phonon modes and pre-existing phonon modes. We propose that perturbations directly influencing the trigonal distortions in $FePS_3$, such as pressure [226] and nonlinear phononics [227], [228], could manipulate the magnetic order or induce nonequilibrium magnetic phases inaccessible in equilibrium. Moreover, we anticipate that coherent phonon spectroscopy could be extended as a highly sensitive tool for probing hidden spin-lattice coupling in van der Waals magnet monolayers and other systems exhibiting strong spin-lattice interactions.

Chapter 7

Magnetically brightened dark electron-phonon bound states

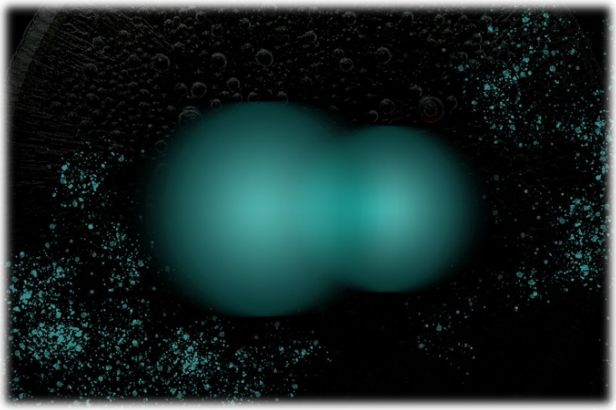

Contents

In van der Waals (vdW) materials, the strong interaction between various degrees of freedom can cause elementary excitations to hybridize into bound states with mixed characteristics. Properly identifying the nature and composition of these bound states is essential for understanding their ground state properties and excitation spectra. In this study, we use ultrafast spectroscopy to uncover bound states of d-orbitals and phonons in the 2D vdW antiferromagnet $NiPS_3$. These bound states are indicated by equally spaced phonon replicas in the frequency domain. These electronic transitions are dipole forbidden above the Néel temperature but become detectable with magnetic order. By driving this phonon and tracking its amplitude spectrally, we determine that the electronic origin of these bound states is localized d–d excitations. Our data reveal that the electron-phonon coupling strength in this system surpasses the highest known value in 2D systems. These findings position $NiPS_3$ as a platform for studying strong interactions between spins, orbitals, and the lattice, and open new possibilities for the coherent control of 2D magnets.

This chapter is based on the following published work:

E. Ergeçen†, B. Ilyas†, *et al.* Magnetically brightened dark electron-phonon bound states in a van der Waals antiferromagnet. *Nature Communications* **13**, 98 (2022) [222]

The author of this dissertation contributed to the following aspects of the work: designing and constructing the experimental setup, conducting the experiments, analyzing and interpreting the experimental data, and writing the manuscript.

7.1 Strong electron-lattice coupling

The interaction between electrons and the lattice is fundamental to many physical phenomena observed in 2D vdW materials, such as interlayer exciton-phonon states [229] and enhanced superconductivity [230]. A key indicator of strong electron-phonon coupling is the presence of electron-phonon bound states, which result from coherent coupling between electronic and vibrational levels. Experiments like photoemission [231] and optical spectroscopy [232] have shown that these hybrid excitations in 2D vdW materials produce spectral replicas spaced equally by a phonon

frequency. These states provide a way to quantify electron-phonon coupling without relying on physical models.

In vdW magnets, the lattice significantly influences the magnetic ground state properties. For instance, changes in the stacking configuration can transform the bulk vdW ferromagnet CrI_3 into an antiferromagnet in its few-layer limit [202]. Spin-lattice coupling is also evident in the vibrational modes of vdW magnets [224], seen as energy renormalization below the magnetic ordering temperature. Beyond strong lattice coupling, magnetic ordering creates new electronic states, which serve as proxies for antiferromagnetic order in 2D limits, such as d-d transitions in transition metals [223] and spin-orbit entangled excitons [233][234].

This strong coupling between different degrees of freedom in vdW magnets can result in novel bound states with mixed characteristics. These hybrid excitations could enable new functionalities for manipulating optical and electronic properties. Despite their potential, the full promise of these excitations in vdW magnets has yet to be realized. The main challenge lies in identifying and characterizing these excitations, particularly in materials with multiple electronic excitations and collective modes. This task requires spectral tools capable of distinguishing the various bosonic and fermionic components involved in bound state formation.

In this chapter, we describe the use of coherent ultrafast spectroscopy with energy and time resolution to detect bound states of localized d-orbitals and a phonon in the 2D antiferromagnetic vdW insulator $NiPS_3$. These bound states are optically dark above the Néel temperature (T_N) and become optically accessible below T_N. They appear as equally spaced replica peaks in transient absorption spectra, with energy spacing corresponding to the 7.5 THz (253 cm^{-1}) A_{1g} Raman active phonon mode. To determine the electronic origin of these spectral progressions, we use energy-resolved coherent phonon spectroscopy to coherently launch this phonon mode and observe it in both time and frequency domains. Our data clearly show that the phonon replicas originate from localized d-d electronic transitions.

7.2 Experimental methods

7.2.1 Sample synthesis and characterization

Our $NiPS_3$ crystals were synthesized via a chemical vapor transport method, as detailed in Ref. [215]. All powdered elements (obtained from Sigma-Aldrich), including nickel (99.99% purity), phosphorus (99.99%), and sulfur (99.998%), were prepared within an argon-filled glove box. After accurately weighing the starting materials in the proper stoichiometric ratio, we added an extra 5 wt% of sulfur to account for its high vapor pressure. Following synthesis, we conducted chemical analysis of the single-crystal samples using a COXEM EM-30 scanning electron microscope equipped with a Bruker QUANTAX 70 energy dispersive X-ray system to confirm the correct stoichiometry. Additionally, X-ray diffraction (XRD) was performed using a commercial diffractometer (Rigaku Miniflex II). Prior to optical measurements, we determined the crystal axes of the samples using an X-ray diffractometer. Samples were cleaved before placement into high vacuum conditions ($\sim 10^{-7}$

torr) to expose a fresh surface free from contamination and oxidation.

7.2.2 Broadband transient absorption spectroscopy.

The 1038 nm (1.19 eV) output from a commercial Yb:KGW regenerative amplifier laser system (PHAROS SP-10-600-PP, Light Conversion), operating at 100 kHz, was divided into pump and probe arms. In the probe arm, the beam was focused onto a calcium fluoride (CaF_2) crystal to generate a whitelight continuum, covering the spectrum from 1.4 eV to 2 eV. The pump arm was used to seed the optical parametric amplifier (ORPHEUS, Light Conversion), enabling wavelength tuning of the pump. Both pump and probe arms were focused onto the sample at an incidence angle of 20 degrees, with pump and probe beam spot diameters of 50 μm and 40 μm, respectively, measured using a knife-edge method. The pump fluence at the sample position was measured to be 4.3 mJ/cm^2. The reflected probe beam was directed to a monochromator and a photodiode for lock-in detection. The monochromator's spectral resolution was 1 nm. The time resolution of this experiment was approximately 200 fs. Detailed schematics of the setup are provided in Figure 7.1.

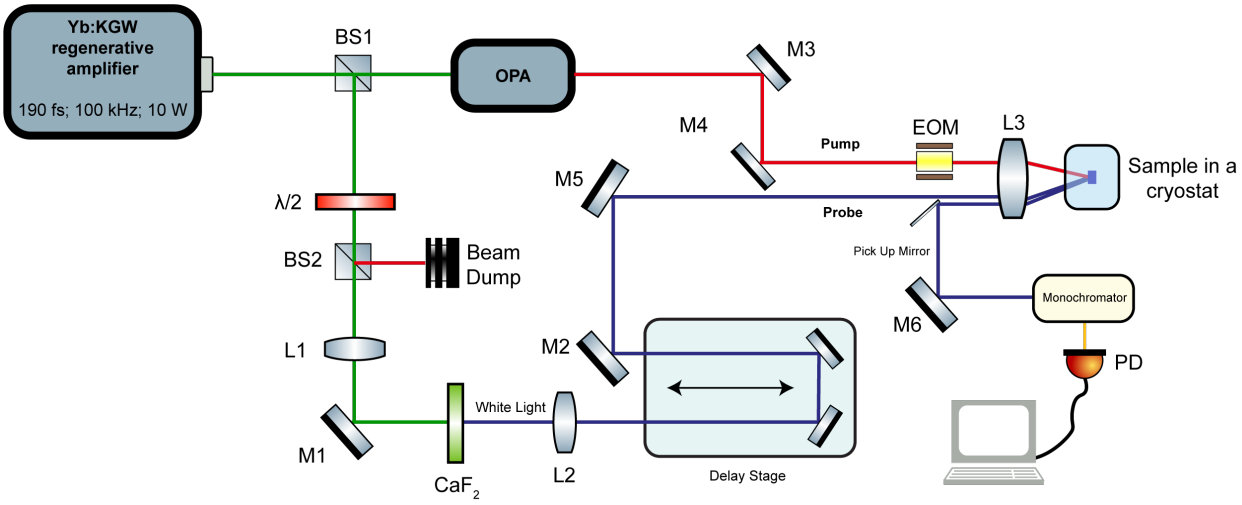

Figure 7.1: Experimental scheme of the broadband transient absorption spectroscopy. "BS" - Beam Splitter and "$\lambda/2$" - Half Waveplate, are used to control the laser power incident on the whitelight continuum generation crystal CaF_2; "M" - Mirror; "PD" - Photodiode; "L" - Lens; "OPA" - Optical Parametric Amplifier; "EOM" - Electro-Optic Modulator .

7.2.3 Energy resolved coherent phonon spectroscopy.

A Ti:sapphire oscillator (Cascade-5, KMLabs) output, centered at 760 nm (1.63 eV) and with a pulse duration of approximately 25 fs, was utilized. The laser operated at a repetition rate of 80 MHz, and no cumulative heating effect was observed. Prior to splitting the output into pump and

probe branches, group velocity dispersion (GVD) was precompensated using chirp mirrors and N-BK7 wedges to maintain short pulses at the sample position. Both pump and probe pulses were individually characterized at the sample position using the frequency-resolved optical gating technique (FROG). The measured pulse duration was ∼25 fs. To enhance the signal-to-noise ratio of our setup, the pump intensity was modulated at 100 kHz. For faster data acquisition and averaging, the pump-probe delay was rapidly scanned at a rate of 5 Hz using an oscillating mirror (APE Scan-Delay USB). The reflected probe beam was directed either directly to a photodiode for spectrally integrated experiments or through the monochromator for spectrally resolved experiments. The spectral resolution of the monochromator was 3 nm. The signal from the photodiode was then fed into a lock-in amplifier (Stanford Research SR830) synchronized to the chopping frequency. Detailed schematics of the setup are provided in the supplementary information (Figure 7.2).

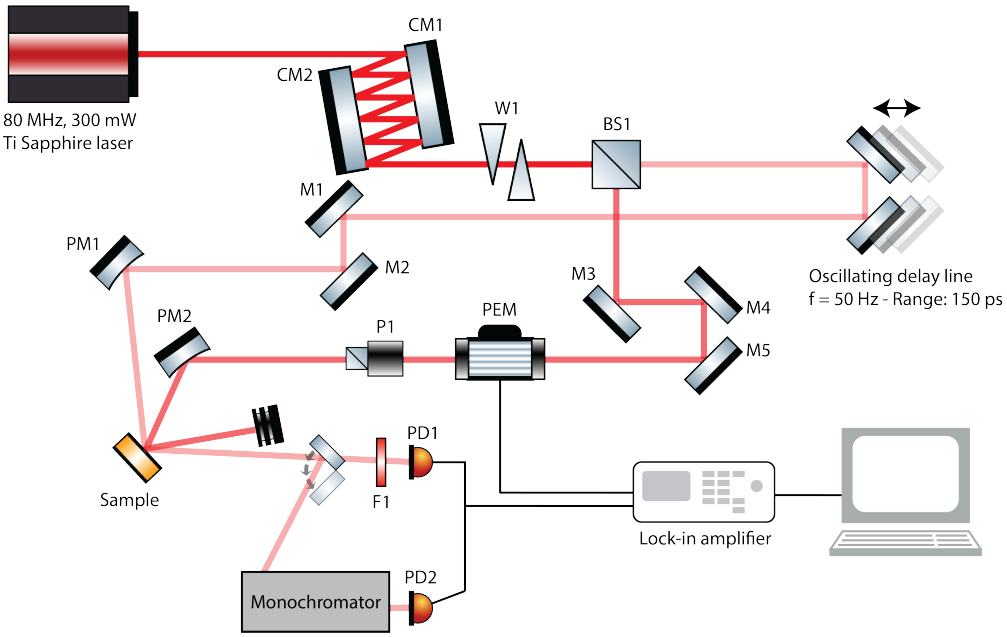

Figure 7.2: Experimental scheme of the energy resolved coherent phonon spectroscopy. "BS" - Beam Splitter; "$\lambda/2$" - Half Waveplate; "M" - Mirror; "PM" - Parabolic Mirror; "CM" - Chirped Mirror; "W" - Wedge; "P" - Polarizer; "PD" - Photodiode; "L" - Lens; "EOM" - Electro-Optics Modulator; "PEM" - Photoelastic Modulator. .

7.3 Detection of electron-phonon bound states

7.3.1 Optical, structural and magnetic properties of $NiPS_3$

$NiPS_3$ is a member of transition metal thiophosphates (MPX_3, M: Fe, Mn, Ni and X: S, Se) layered crystal family [121]. In $NiPS_3$, nickel atoms are arranged in a honeycomb lattice (See Figure 7.3). Below the Néel temperature (∼150 K), spins localized at nickel sites align in-plane, ferromagnetically

along zigzag chains, and antiferromagnetically between adjacent chains, with a slight out-of-plane canting of spin orientations [235]. At low temperatures, the system exhibits several spectral features in the near-infrared and visible spectrum, including spin-orbit-entangled excitons and on-site d-d transitions, as observed in linear absorption measurements [223], [236]. These features are close to the band edge absorption at 1.8 eV.

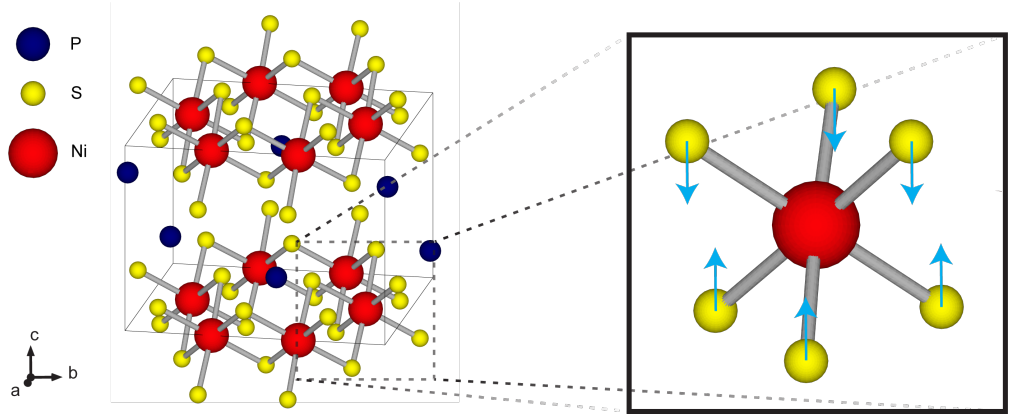

Figure 7.3: Crystal structure of $NiPS_3$. Octahedron as shown in the solid square, formed by a nickel (red) and six sulfur (yellow) atoms. Phosphorus atoms are shown in dark blue. Arrows indicate the A_{1g} phononic displacements for the 7.5 THz A_{1g} mode .

7.3.2 Low temperature transient absorption spectrum

To investigate the equilibrium and non-equilibrium optical properties of $NiPS_3$, we use broadband transient absorption spectroscopy with a high dynamic range. In this experimental setup, high-intensity (4.3 mJ/cm^2) ultrashort pulses at 1.88 eV efficiently generate electron and hole pairs, heating up the magnetic and electronic systems. The demagnetizing effect of high-intensity optical pulses, extensively studied in magnets [237]–[239], is known to bleach any spectral responses related to magnetic ordering. Following photoexcitation, a broadband probe pulse, spanning 1.4 eV to 2 eV, measures changes in the reflectivity spectrum. The probe energy and delay time dependence is shown in Figure 7.4. Transient reflectivity changes observed 2 picoseconds after the pump pulse are shown in Figure 7.5b. Below 1.53 eV, the spectrum reveals two sharp absorption lines (Peaks I and II in Figure 7.5b) between 1.45 eV and 1.50 eV, previously identified as a spin-orbit-entangled exciton and a magnon sideband [223].

7.3.3 Pump photon energy and fluence dependence

Figure 7.6a displays the pump wavelength dependence of the transient absorption spectra, measured 2 ps after the pump pulses. The pump fluences for all wavelengths were ~4.33 mJ/cm^2. We observe the highest transient response when the pump energy exceeds the bandgap of $NiPS_3$ (1.8 eV). This indicates that the transient response is primarily due to the thermal heating of electronic

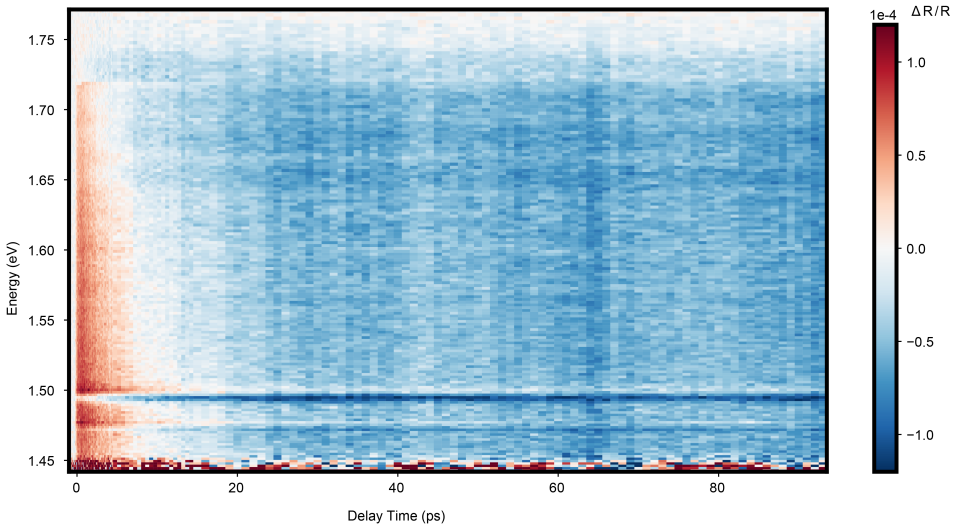

Figure 7.4: Time dependence of absorption. Two narrow lines in the lower side are peak I (exciton) and peak II. Due to their previously reported exceptionally sharp bandwidth, their lifetimes are at least 100 ps. Besides that the spectral oscillations also last for long ($>$ 100 ps) after excitation. This shows that the spectral oscillations are indeed equilibrium phenomena. The data was taken at 30K.

and magnetic subsystems, resulting from the efficient generation of electron-hole pairs. Figure 7.6b shows the fluence dependence of magnetic exciton absorption peaks. The oscillator strengths of both peaks (I and II) increase linearly with pump intensities. All experiments were conducted at 10K.

7.3.4 Temperature dependence

These features only become visible below the antiferromagnetic ordering temperature (approximately 150 K), confirming their magnetic origin (Figure 7.7a). Above 1.53 eV, the spectrum is dominated by a broad peak associated with localized electronic transitions among d-orbitals [236]. Notably, fine oscillations resembling spectral replicas are observed on top of the transition peak near 1.7 eV (Figure 7.5b). The temperature-dependent data (Figure 7.7) indicates that the onset of these spectral structures coincides with the Néel temperature. The Fourier transform of the spectral replicas shows a broad distribution between 25 and 35 meV, peaking around 28.5 meV (Figure 7.5b inset).

Spectral replicas are common in molecular systems with strong vibronic coupling [240], in semiconductors with localized excitations [232], [241]–[243], and in engineered quantum systems [244]–[246]. For $NiPS_3$, one possible explanation for the regularly spaced spectral replicas is the dressing of an electronic excitation, such as excitons or d-d transitions, with a bosonic field like a phonon or magnon. We exclude the coupling between electronic excitations and magnons as the cause of these replicas because magnon modes soften near the critical temperature, yet the energy spacing of

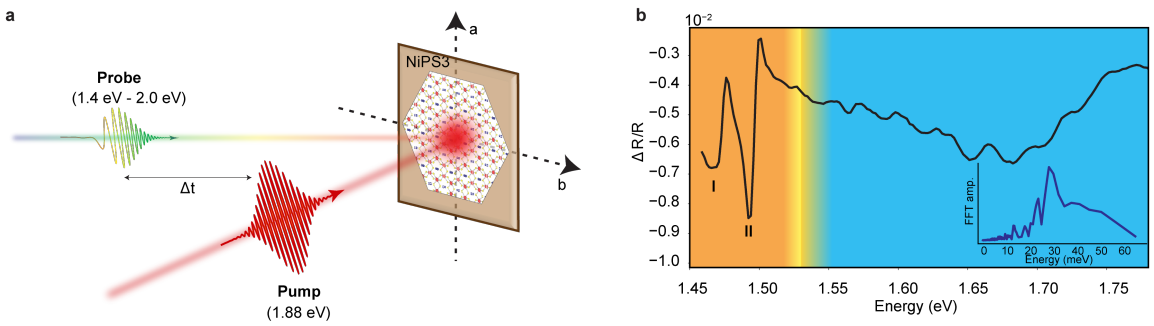

Figure 7.5: Phonon replicas in the transient absorption spectrum of $NiPS_3$. a. Schematic of the broadband transient absorption spectroscopy setup. An excitation pulse with energy (1.88 eV) larger than the bandgap excites the system, and a following probe pulse with a whitelight continuum measures the transient reflectivity across a broad spectral range, with a spectral resolution of 1.5 meV. **b.** Spectral dependence of transient reflectivity measured at 10K, 2 ps after the pump. Previously reported coherent many-body spin-orbit-entangled excitons (orange region) and a broad d-d transition (blue region) can clearly be seen. Two sharp features are labeled as Peak I and Peak II which have been previously identified as a spin-orbit-entangled exciton and a magnon sideband [223]. The d-d peak is dressed by phonons, with at least 9 replicas visible, indicating a strong coupling between them. The inset shows the Fourier transform of the extracted spectral oscillations, with a mode peaking at 28.5 meV, which is close to the 7.5 THz A_{1g} phonon energy.

the replicas remains unchanged with increasing temperature (see Figure 7.7). Raman spectroscopy results [215], [224] corroborate that the energy spacing between replicas matches an A_{1g} phonon mode, responsible for out-of-plane even-symmetry vibrations of sulfur atoms (Figure 7.3). This suggests that the observed replicas originate from the 7.5 THz (253 cm^{-1}) A_{1g} phonon mode.

7.4 Identification of the electronic nature of the bound state

While we have identified the phonons as the bosonic field involved in the hybrid state formation, the electronic component remains unresolved from our transient absorption measurements. The coupling of this phonon mode to either d-d transitions or spin-orbit-entangled excitons could explain the emergence of replicas. Since spectral responses related to both of these electronic elements appear at the Néel temperature [236], the temperature dependence alone cannot distinguish between these scenarios and pinpoint the exact electronic origin of the replicas.

To address the question of phonon coupling with different spectral regions, we use energy-resolved coherent phonon spectroscopy (see Methods). Unlike the high-intensity (∼4.33 mJ/cm^2) and longer pulse duration (∼200 fs) used in broadband transient absorption spectroscopy, this experimental setup employs a low-intensity (∼1 $\mu J/cm^2$) and ultrashort (∼25 fs) pump pulse to im-

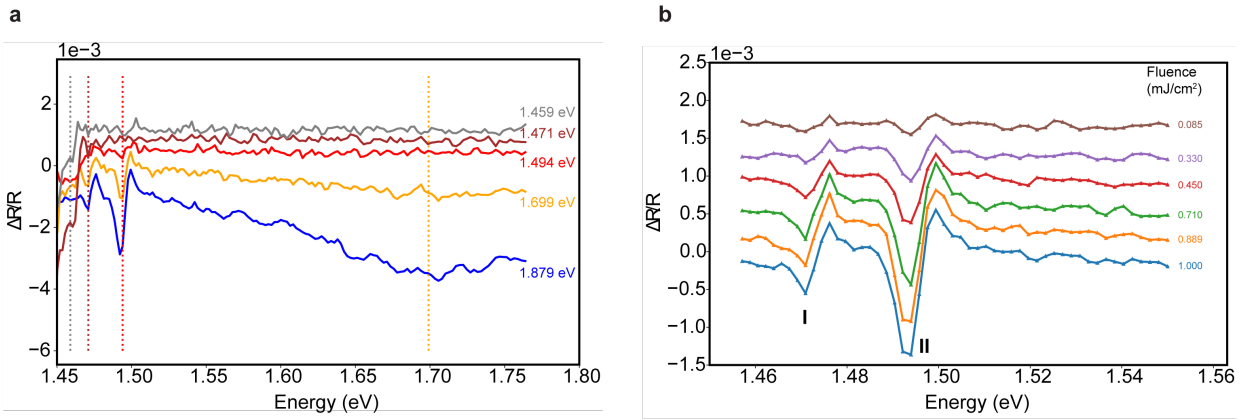

Figure 7.6: Pump photon energy and fluence dependence. a. Pump energy dependence of the response. Only pumping above the optical bandgap gives high response and the oscillatory features start to become clear. **b.** Pump fluence dependence of the excitonic intensities. Both (**a**) and (**b**) were taken at 10K.

pulsively or displacively drive the phonon modes with A_{1g} and E_g symmetries without disturbing the underlying magnetic order. Following the pump excitation, a broadband and ultrashort probe pulse tracks these phonon oscillations as a function of both time and wavelength. The energy-integrated coherent phonon spectroscopy traces in Figure 7.8 show an oscillatory component, representing coherently excited phonon modes, superimposed on an incoherent electronic relaxation. The Fourier transform of these oscillations is shown in the inset of Figure 7.8. We observe two A_{1g} phonons at 7.5 THz (253 cm^{-1}) and 11.5 THz (384 cm^{-1}), and one E_g phonon at 5.2 THz (173 cm^{-1}). The energy of the dominant mode (7.5 THz) matches well with the energy spacing of the replicas.

To investigate this phonon mode's coupling strength to d-d transitions and spin-orbit-entangled excitons, we compare oscillation amplitudes from different spectral regions by spectrally separating the broadband probe pulse using a filter (Figure 7.8) or a monochromator (Figure 7.9). Initially, we use a low-pass filter with a cutoff at 1.53 eV to focus on the dynamics of the excitons and suppress the response from d-d transitions. Transient reflectivity traces obtained with and without the low-pass filter, shown in Figure 7.8, reveal a significant observation: While most of the incoherent response is localized below 1.53 eV, where the excitons reside, the A_{1g} phonon mode oscillations are absent in this spectral region. This absence implies a negligible coupling of the A_{1g} phonon mode to spin-orbit-entangled excitons.

The finer spectral dependence of the phonon amplitude obtained with a monochromator is shown in Figure 7.9. Coherent phonon oscillations begin to appear above 1.53 eV and are absent in the region associated with spin-orbit-entangled excitons. This observation indicates that spin-orbit-entangled excitons do not contribute to the formation of spectral replicas. Since coherent phonon oscillations are only detected in the spectral region of d-d transitions, we conclude that the replica peaks result from the hybridization between localized d-d levels and a Raman active optical phonon.

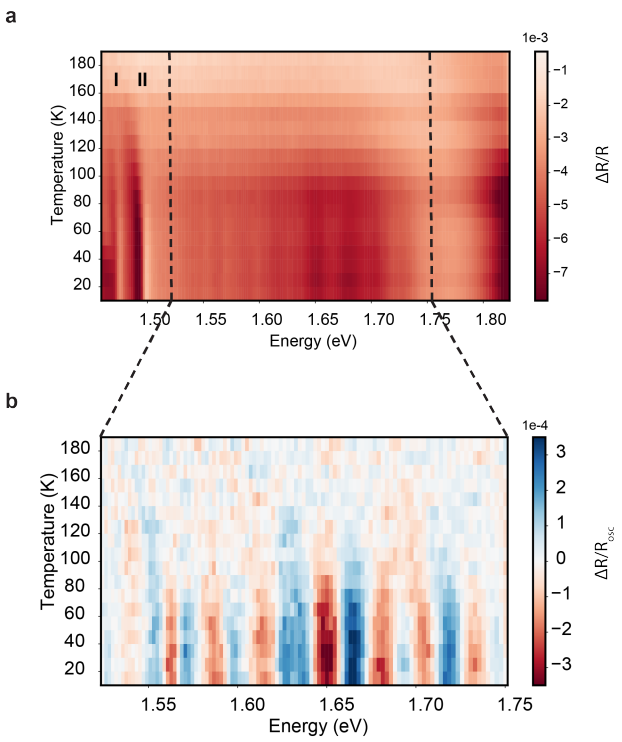

Figure 7.7: Temperature dependence of phonon replicas. a. Temperature dependence of the spin-orbit-entangled excitons and spectral oscillations. Exciton states become visible below the Néel temperature, as reported previously. Phonon dressed d-d excitations also follow the Néel order. **b.** Enlarged view of the d-d transition region. Background is subtracted using fifth order polynomial fit.

7.5 Minimal model of electron-phonon coupling

7.5.1 The Hamiltonian and the spectral function

The energy level splitting of a d-d transition is proportional to the distance between the transition metal ion and the surrounding ligands. In $NiPS_3$, as illustrated in Figure 7.3, a 7.5 THz phonon with A_{1g} symmetry modulates the interatomic octahedral distances, thereby affecting the energy splittings between d-levels. Consequently, the dynamics of our system can be effectively captured by the following Hamiltonian of this minimal model:

$$H = H_{\mathrm{dd}} + H_{\mathrm{ph}} + H_{\mathrm{int}} \tag{7.1}$$

where the terms of the Hamiltonian respectively correspond to the d-d electronic transitions, the phonon mode and the interaction between them.

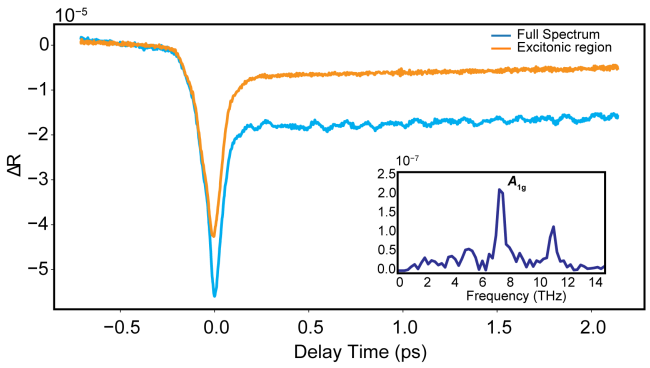

Figure 7.8: Coherent phonon spectroscopy traces obtained below the Néel temperature (77 K), with ∼25 fs temporal resolution. The blue trace represents the energy integrated coherent phonon spectroscopy trace. The oscillatory part of the energy integrated transient reflectivity was extracted after subtracting an exponential background from the raw data. Energy integrated coherent phonon spectroscopy reveals three distinct high frequency optical phonons at 5.2 THz, 7.5 THz and 11.5 THz. The Fourier amplitudes of the oscillations are shown in the inset. The orange line represents the data obtained with a long pass filter (cut-off energy: 1.53 eV) that excludes the d-d level transition. This spectrally separates the spin-orbit-entangled exciton from d-d levels. The 7.5 THz phonon mode modulates the d-d transition region, whereas the region with excitons is not being modulated by that mode.

Specifically, the Hamiltonian can be expressed as:

$$H_{\mathrm{dd}} = \hbar\omega_{\mathrm{dd}} d^{\dagger} d \tag{7.2}$$

$$H_{\mathrm{ph}} = \hbar\omega_{\mathrm{ph}} (a^{\dagger} a + \frac{1}{2}) \tag{7.3}$$

$$H_{\mathrm{int}} = M d^{\dagger} d (a + a^{\dagger}) \tag{7.4}$$

Here, $d^{\dagger}$ and d are the creation and annihilation operators for the d-electrons, $\hbar\omega_{\mathrm{dd}}$ are the energy levels of the d-electrons, $\hbar\omega_{\mathrm{ph}}$ is the energy of the phonon mode, $a^{\dagger}$ and a are the creation and annihilation operators for the phonon. The coupling constant can be written as $M = \sqrt{g}\omega_{ph}$ [247], where g is called the dimensionless Huang-Rhys factor, which quantifies electron-phonon coupling strength. This Hamiltonian is exactly diagonalizable with a unitary transformation [247] and the spectral function $A(\omega)$ has a form of Poisson distribution:

$$A(\omega) = 2\pi e^{-g} \sum_{n=0}^{\infty} \frac{g^n}{n!} L(\omega - \omega_{dd} + \Delta - \omega_{ph} n) \tag{2}$$

where L is a function corresponds to the lineshape of undressed d-d transition, n is the number of phonons and Δ is the renormalization energy of d-d transition due to hybridization with phonons, which is equal to $g\omega_{ph}$.

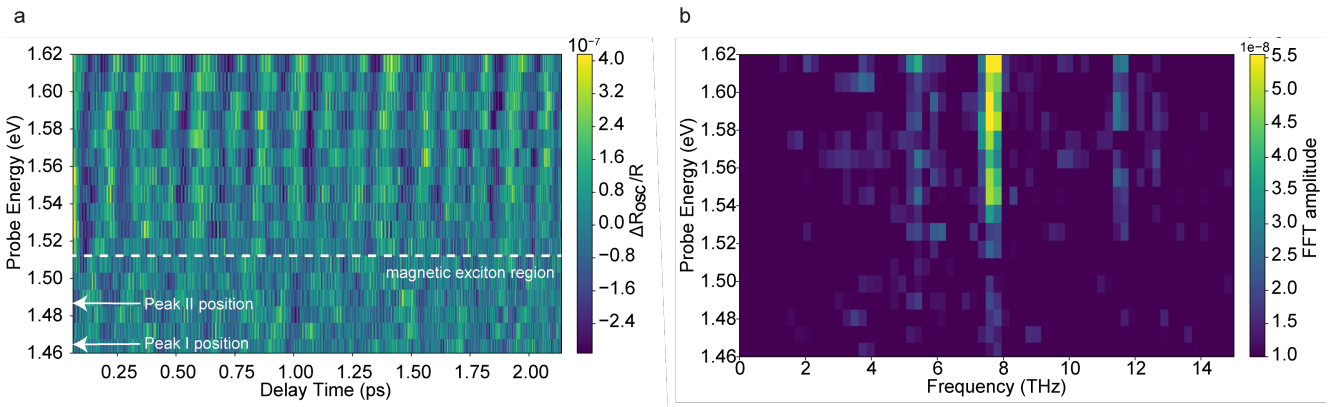

Figure 7.9: Energy-resolved coherent phonon spectroscopy a. Energy-resolved coherent phonon time traces. For finer energy resolution, the probe beam was sent to monochromator and coherent phonon oscillations in the energy region between 1.46 eV and 1.62 eV, was measured. The data clearly shows that the modulations are mainly present in the spectral region near d-d transition. **b.** Fourier spectra of **a.**

7.5.2 Fitting results and large g factor

To extract the electronic transition energy and the g factor, we fit our transient absorption traces to this spectral function, as shown in Figure 7.10. The g factor, estimated from the fit, is approximately 10. This exceptionally high value indicates a strong coupling between the d-levels and the vibrational modes that modulate the octahedral distances.

These spectral features start to become apparent at temperatures where the thermal occupation of a 7.5 THz (253 cm^{-1}) phonon mode is negligible. The amplitudes of the replicas increase as the temperature decreases, indicating the formation of coherence between the d-d excitations and phonons. Moreover, the extracted amplitude of each phonon replica peak follows a Poisson distribution rather than a Bose-Einstein distribution, which describes a thermal state [245]. This observation suggests that the spectral replicas correspond to a coherent superposition between the d-d electronic transition and different phonon number states, rather than a thermal ensemble.

7.6 Optical selection rules and local breaking of the inversion symmetry

Typically, transitions between d-orbitals are considered optically forbidden in a centrosymmetric environment due to dipole selection rules. The transition from $^3A_{2g} \rightarrow {}^3T_{1g}$ is a spin allowed, parity forbidden single electron transition (see Figure 7.11) and the corresponding level splitting is ~1.7 eV. Another transition from $^3A_{2g} \rightarrow {}^3T_{2g}$ (1.1 eV) is also observed in a broadband absorption experiment [236] at low temperatures. However, these transitions can become optically accessible if there are perturbations that temporarily or permanently disrupt local inversion symmetry at

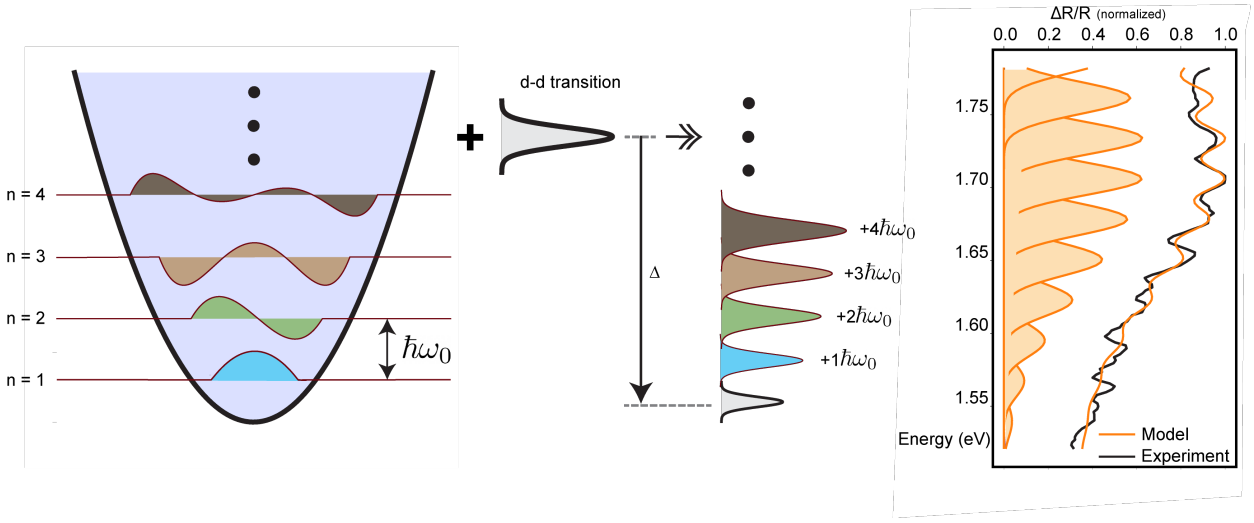

Figure 7.10: Extracting the Huang-Rhys factor. On the left, phonon eigenstates with equal spacings are illustrated. The coupling of the d-d transition to phonon degrees of freedom results in a broad absorption peak with superimposed oscillatory features and an energy shift denoted by Δ. This model aligns well with the experimental data. We fit the absorption spectrum using a minimal model that includes a sum of linewidth functions (either Gaussian or Lorentzian), each weighted by a Poisson distribution. The free parameter of this distribution corresponds to the dimensionless Huang-Rhys factor g.

nickel sites. While stacking faults and lattice defects can break inversion symmetry on a global or local scale, they are unlikely to cause d-d transitions to coincide with magnetic order. Conversely, when inversion symmetry is transiently disrupted by odd-symmetry phonons, the spectral weight of d-d transitions is expected to increase with temperature due to the thermal occupation of phonon modes [240]. However, in the case of $NiPS_3$, the d-d transition only becomes visible below the Néel temperature, as depicted in Figure 7.7, ruling out a scenario where phonons break inversion symmetry. This observation, consistent with linear absorption measurements [236], suggests a mechanism that breaks local inversion symmetry at nickel sites as a consequence of magnetic order.

In Figure 7.12, we illustrate the local environment of nickel sites both above and below the ordering temperature. At high temperatures, all sulfur atoms are positioned between identical nickel ions without any particular spin orientation, maintaining local inversion symmetry. However, at lower temperatures, sulfur atoms positioned between two anti-aligned spins (highlighted in orange) become distinct from those adjacent to two aligned nickel spins (highlighted in yellow) due to the charge transfer nature of $NiPS_3$ [223]. As the exchange interaction is mediated by sulfur atoms, their spin and charge configurations are influenced by surrounding nickel spin orientations, resulting in distinguishable ligands. Below the Néel temperature, this dissimilarity between sulfur atoms breaks local inversion symmetry, as the inversion operation centered at a nickel ion connects two sulfur atoms of different types as illustrated in Figure 7.12. Consequently, even though the antiferromagnetic order maintains global inversion symmetry in $NiPS_3$ [248], as shown in Figure 7.11, the

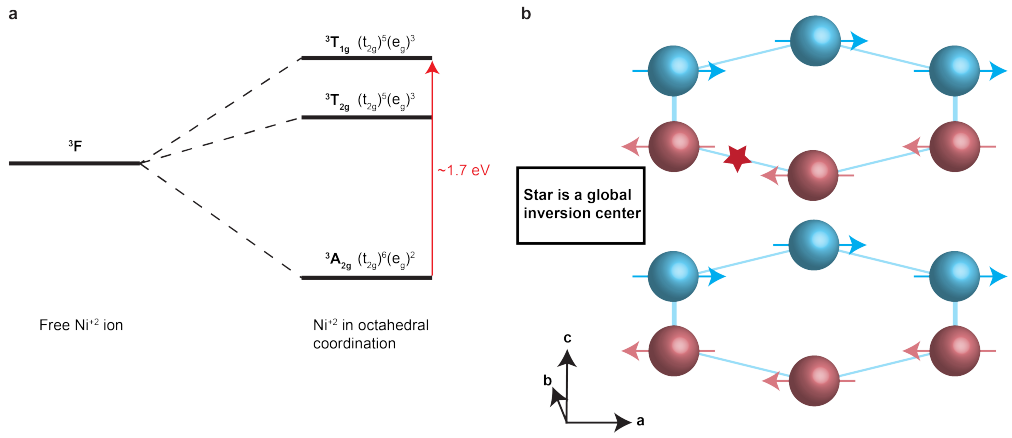

Figure 7.11: Electronic transitions and inversion symmetry in $NiPS_3$. a. The energy levels of a Ni^{+2} ion in octahedral coordination and when it is a free ion. In octahedral coordination, the ground state of Ni^{+2} is the $^3A_{2g}$ triplet, with six electrons in the lower-lying t_{2g} level and two electrons in the higher e_g level. The absorption band of interest is indicated by a red arrow, corresponding to the $^3A_{2g} \rightarrow {}^3T_{1g}$ transition. This transition involves a single electron, is spin-allowed, but electric dipole forbidden. **b.** The magnetic structure of $NiPS_3$. The blue and red spheres represent nickel ions, with arrows indicating the spin vector. A red star marks an inversion center of the crystal. This figure is inspired by Chu et al. [248].

local inversion symmetry at nickel sites is broken, allowing electronic transitions between d-levels to become dipole allowed.

7.7 Conclusion

In summary, our study reveals magnetically brightened dark electron-phonon bound states involving a localized d-d transition and the A_{1g} phonon mode in $NiPS_3$. Employing ultrafast techniques to suppress magnetic order and coherently initiate phonon modes, we dissect the intricate structure of spectral replicas and definitively identify their bosonic and fermionic constituents. The extracted coupling strength between d-orbitals and phonons is remarkably high ($g \sim 10$), surpassing the previously known highest value in van der Waals materials, CrI_3 [232] ($g = 1.5$), by nearly an order of magnitude. Our investigation demonstrates that in $NiPS_3$, the distinct in-gap electronic states are not only strongly coupled to photons and magnons [223], [233], [234], but also to phonons. These spectrally separated in-gap states hint at the potential use of different optical stimuli to achieve effective magnon-phonon coupling [227]. Moreover, in transition metal thiophosphates, the crystal field splitting dictates magnetic anisotropy and plays a pivotal role in determining the type of magnetic order [122], [249]. Thus, our findings suggest that metastable magnetic states could be engineered in $NiPS_3$ through precise control of crystal field splittings. This strong coupling offers opportunities to manipulate d-d electronic transitions either transiently via nonlinear phonon driving [57] or in equilibrium through strain or pressure. Furthermore, our results indicate that van

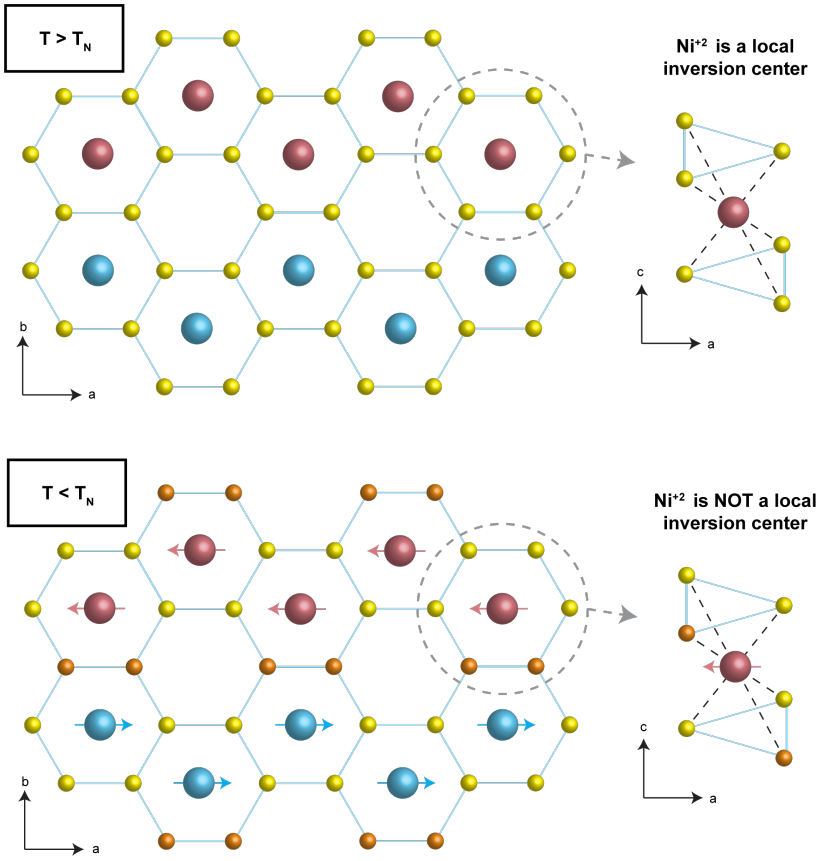

Figure 7.12: Spin order induced local inversion symmetry breaking. With the onset of magnetic ordering, the local environment around nickel sites breaks the local inversion symmetry making the electric-dipole forbidden d-d transition visible in absorption spectrum. For T $> T_{\mathrm{N}}$, all sulfur atoms (yellow) are equivalent and hence nickel site is a local inversion center. For T $< T_{\mathrm{N}}$, nickel atoms are no longer local inversion centers, as the magnetic order creates two sets of distinguishable sulfur atoms: hose between opposite spins (orange) and those between parallel spins (yellow). These different sulfur atoms break local inversion at nickel sites, as illustrated on the right.

der Waals magnets could serve as ideal platforms for engineering novel phases of matter through phonon-driven Floquet states [250], [251].

Chapter 8

Discovery of monolayer van der Waals multiferroic

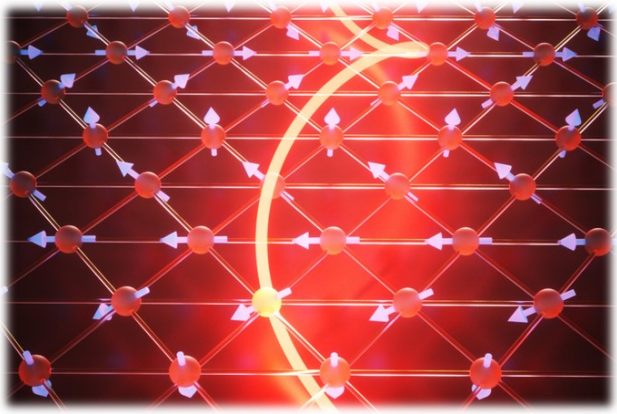

Contents

Multiferroic materials have garnered significant interest for their exceptional static [252]–[254] and dynamical [255]–[257] magnetoelectric properties. In particular, type-II multiferroics exhibit an inversion-symmetry-breaking magnetic order, which directly induces a ferroelectric polarization through various mechanisms, such as the spin-current effect or the inverse Dzyaloshinskii-Moriya effect [106], [254]. This intrinsic coupling between magnetic and dipolar order parameters results in record-strength magnetoelectric effects [254], [258]. Two-dimensional materials with intrinsic multiferroic properties have long been sought for harnessing magnetoelectric coupling in nanoelectronic devices [97], [252], [259]. Here, we report the discovery of type-II multiferroic order in a single atomic layer of the transition metal-based van der Waals material NiI_2. The multiferroic state of NiI_2 is characterized by a proper-screw spin helix with a specific handedness, which couples to the charge degrees of freedom to produce a chirality-controlled electrical polarization. We employ circular dichroic Raman measurements to directly probe the magneto-chiral ground state and its electromagnon modes originating from dynamic magnetoelectric coupling. Additionally, through birefringence and second-harmonic generation measurements, we detect a highly anisotropic electronic state that simultaneously breaks three-fold rotational and inversion symmetry, supporting polar order. The evolution of the optical signatures as a function of temperature and layer number reveals an ordered magnetic, polar state that persists down to the ultrathin limit of monolayer NiI_2. These observations establish NiI_2 and transition metal dihalides as a new platform for studying emergent multiferroic phenomena, chiral magnetic textures, and ferroelectricity in the two-dimensional limit.

This chapter is based on the following published work:

Q. Song†, C. A. Occhialini†, E. Ergeçen†, B. Ilyas†, *et al.* Evidence for a single-layer van der Waals multiferroic. *Nature* **602**, 601-605 (2022) [186]

The author of this dissertation contributed to the following aspects of the work: conducting SHG spectroscopy experiments, analyzing and interpreting the SHG data, and writing the manuscript.

8.1 Search for two-dimensional multiferroic materials

The recent discovery of intrinsic magnetic order in atomically-thin van der Waals (vdW) materials has created new opportunities for the study of collective spin phenomena in free-standing two-dimensional (2D) systems and nanoscale devices . In past years, significant efforts have been made to achieve direct electrical control and manipulation of magnetic properties in 2D [97], [259], but the mechanisms remain elusive. A more promising avenue towards realizing electrical control of 2D magnetism may be found in vdW materials with intrinsic type-II multiferroicity. In type-II multiferroics, the direct coupling between the magnetic and ferroelectric order parameters is enabled by the presence of a spin configuration lacking inversion symmetry [260]–[262], resulting in a large and robust magnetoelectric response [254], [258], [263].

Among possible multiferroic vdW materials, several families have been identified [264]–[266], most prominently the transition metal dihalides (MH_2, M = transition metal, H = halogen). Of particular promise is the magnetic semiconductor NiI_2 [264], [267]–[270], which is host to a rich phase diagram including a type-II multiferroic ground state [253], [271]. NiI_2 crystallizes in the rhombohedral $R\bar{3}m$ structure at room temperature, forming a triangular lattice of Ni^{2+} ions ($3d^8$, $S = 1$) which are stacked along the c-axis and held together by weak interlayer bonding (Figure 8.1a). The 2D triangular lattice geometrically frustrates the intralayer magnetic exchange interactions that govern the long-range ordering of the local Ni spins [267], [268], [272]. This leads to a sequence of magnetic phase transitions in NiI_2, first to an antiferromagnetic (AFM) state at $T_{N,1} \simeq 75$ K, and then to a proper-screw helimagnetic ground state below $T_{N,2} \simeq 59.5$ K. The latter exhibits long wavelength helical magnetic structure with propagation vector $\mathbf{Q} = (0.138, 0, 1.457)$ reciprocal lattice units (r.l.u.) [273] (Figure 8.1b). The helimagnetic transition is concomitant with the appearance of an in-plane electrical polarization perpendicular to the ordering vector [253] as well as crystal symmetry lowering from rhombohedral to monoclinic [273].

In this chapter, we investigate the multiferroic states in bulk and few-layer NiI_2 crystals[274]. Due to the complexity of the ground state, which simultaneously breaks mirror, rotational, and inversion symmetries, we employ a suite of complementary optical techniques to track the multiple signatures of the polar and magneto-chiral orders, as a function of temperature and layer number. Optical birefringence is found to originate from a lowering of the lattice symmetry at both the $T_{N,1}$ and $T_{N,2}$ transitions, and is consistent with a breaking of **c**-axis three-fold rotational symmetry (C_{3z}) and a reduction to a single in-plane two-fold symmetry operation (C_2) [275]. We further use second harmonic generation (SHG) as a probe of inversion-symmetry breaking, which, together with lowering of rotational symmetry to C_2, enables to track the presence of polar order down to the single-layer limit. To confirm the presence of magnetochiral order in the helimagnetic phase of NiI_2, we perform Raman spectroscopy with circularly polarized light to resolve a coupled spin-lattice electromagnon excitation with strong optical activity as a signature of spin chirality. These experimental findings are supported by first-principles and Monte Carlo simulations, altogether

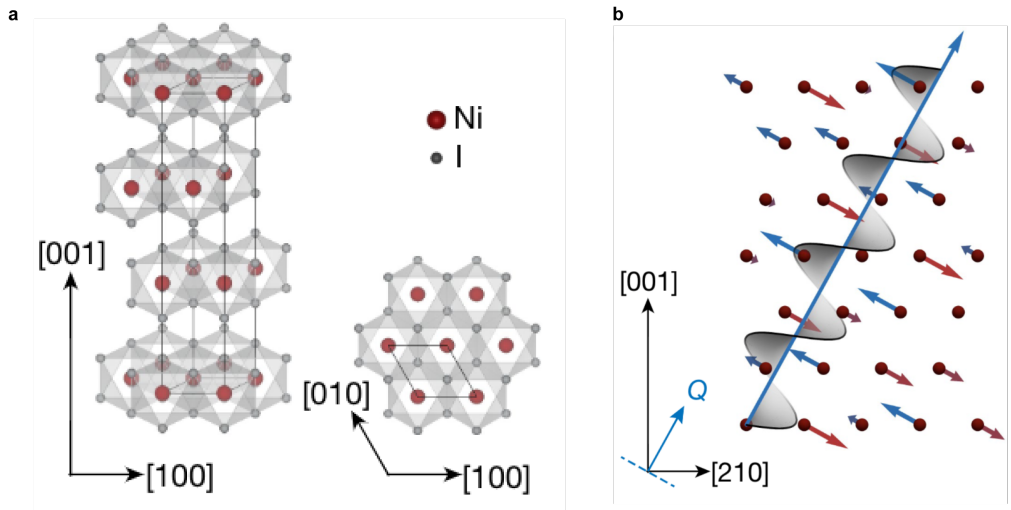

Figure 8.1: Crystal and magnetic structure of NiI_2. **a**, The high-temperature $R\bar{3}m$ structure of NiI_2. **b**, The helical magnetic structure of bulk NiI_2 below $T_{N,2} = 59.5$ K. .

providing robust evidence for the persistence of type-II multiferroic order down to single-layer NiI_2.

8.2 Experimental methods

8.2.1 Growth and characterization of bulk and few-layer NiI_2 crystals

Bulk-like NiI_2 crystals were grown on 300 nm SiO_2/Si and few-layer crystals were grown on hexagonal boron nitride (hBN) substrates via physical vapor deposition (PVD) in a horizontal single-zone furnace equipped with a 0.5 in. diameter quartz tube at ambient pressure. hBN was mechanically exfoliated and transferred onto 300 nm SiO_2/Si substrates, then annealed in vacuum at 700 °C for 1 h prior to the growth. In a typical synthesis, 0.1 g of NiI_2 powder (99.5%, anhydrous, Alfa Aesar) was positioned at the center of the furnace as the source material and the SiO_2/Si substrate was placed downstream at the maximum temperature gradient point. The furnace was purged by pumping the quartz tube below 0.1 Torr and then refilled with 99.99% Ar gas three times. When growing bulk-like NiI_2 crystals, the furnace was heated to 450°C in 15 minutes and held at that temperature for 10 minutes. For few-layer NiI_2 samples, the furnace was heated to 380-420°C in 15 minutes and then the SiO_2/Si substrate was taken out immediately and stored inside a nitrogen-filled glove box ($O_2 < 0.5$ ppm, $H_2O < 0.5$ ppm). The sample thickness was determined by atomic force microscopy (AFMWorkshop HR), which was performed inside a separate nitrogen-filled glovebox ($O_2 < 100$ ppm, $H_2O < 1$ ppm), using a silicon probe in tapping mode. The electron diffraction (JEOL HRTEM) was performed on a 7 nm thick PVD grown NiI_2 flake using a transmission electron microscope. The flake was picked up and dropped down using the dry transfer technique onto a SiNx membrane with 2 μm pores (NORCADA)[276].

Single crystal NiI_2 was grown by chemical vapor transport (CVT), from elemental precursors

with molar ratio Ni:I=1:2, at a temperature gradient 700°C to 500°C. The magnetic susceptibility was measured during field cooling at 0.9 T applied out of plane, using a Magnetic Property Measurement System (MPMS-3, Quantum Design Inc.). X-ray diffraction of CVT grown crystals was performed in Bragg geometry using Cu K_α radiation (PANalytical), and the refined unit cell at room temperature is $a = 3.91$ Å, $c = 19.93$ Å.

8.2.2 Layer-dependent second harmonic generation spectroscopy

In second harmonic generation (SHG) microscopy, an objective lens (Olympus LMPlanFL-N 50x) focuses an ultrashort laser beam onto the sample located in a cryostat (Janis ST-500). For wavelength dependent SHG experiments, we used a optical parametric amplifier (ORPHEUS, Light Conversion) seeded with a regenerative amplifier (PHAROS SP-10-600-PP, Light Conversion) These allowed us to tune the output wavelength in a wide spectral range. The estimated spot size on the sample is $\sim 2\mu m$. The laser fluence incident on the sample was set to 1 mJ/cm^2. No sample damage or degradation was observed during the measurements. Upon reflection, the second harmonic component of the beam radiated from sample was selected out by a dichroic mirror and a monochromator with 2 nm spectral resolution. The second harmonic photons were detected and counted using a photomultiplier tube (Hamamatsu PMT) and a dual-channel gated photon-counter (Stanford Research SR400). To decrease the background and dark counts, the photon counter was synchronized and gated with laser pulses. To perform SHG imaging (Figure 8.5), we keep the sample location fixed and rotate a motorized mirror to scan the laser across the sample. The polarization angle of the pulses were controlled using a wire-grid polarizer and a half-waveplate respectively to obtain the polarization resolved second harmonic traces (Figure 8.6).

8.2.3 Optical birefringence measurements

A supercontinuum light source (NKT Photonics, Fianium) monochromatized to $\lambda = 532$ nm/550 nm and a bandwidth of approximately 1 nm was used as excitation for angular-dependent linear dichroism and birefringence-induced polarization rotation measurements, respectively. All measurements were performed at normal incidence in a Montana Instruments closed-cycle optical cryostat. Linear dichroism measurements were performed with a photo-elastic modulator (PEM-100, Hinds Instruments) on the incident path of the optical setup. The beam incident on the PEM is prepared in linear polarization making an angle of 45° with the respect to the PEM fast axis and amplitude modulated with a mechanical chopper. The PEM retardance was set to 0.5λ to modulate the incident polarization between ±45° linear polarization states. The light is then focused onto the sample using a 50x objective lens. The backscattered light is measured by an amplified photodiode (ThorLabs PDA100A2), whose output is connected to a lock-in amplifier (Stanford Instruments SR865A) referenced to the second harmonic of the fundamental PEM frequency $f = 50$ kHz. The total reflectance of the sample, used as a normalization, is monitored by a second lock-in amplifier

referenced to the chopping frequency $f = 557$ Hz.
To perform angular-dependent linear dichroism measurements, the angle of the perpendicular linear polarization states created by the PEM is varied across the crystal using a zero-order half-wave plate placed just before the objective. In order to ensure the angular-dependence is recorded from a uniform, mono-domain region of the sample, polarized microscopy images were first recorded at the base temperature $T = 5$ K. The sample was held at this temperature for the duration of the angular-dependent measurements in order to maintain the same distribution of birefringent domains. Birefringence-induced polarization rotation measurements on the few- and single-layer samples were performed with the PEM on the detection path of the optical setup with a retardance amplitude of 0.486λ, using a lock-in amplifier at the second harmonic of the fundamental PEM frequency for signal collection. The unrotated incident beam is kept parallel to the PEM fast-axis and analyzed by a polarizer at 45 deg. before being measured by the photodiode. This setup provided a sensitivity down to 10 μrad.
Polarized microscopy was performed with a broadband visible LED light source, a standard CMOS-based monochrome camera and Glan-Thompson polarizers on both the input and output light paths in reflection geometry. A detuning of 0.5 (2.0) degrees from a cross-polarized configuration was used to maximize the contrast from birefringent domains and a 5 (2) second integration time was used for the images of few-layer (bulk) samples. Cross-polarized contrast images were obtained as a function of temperature by auto-correlating the images for different temperatures to overlap with a high-temperature ($T > T_{N,1}$) reference, and subtracting the low and high temperature images.

8.2.4 Raman spectroscopy measurements

Polarized Raman experiments were performed in a back-scattering geometry using a confocal microscope spectrometer (Horiba LabRAM HR Evolution) with a 50x objective lens and 532 nm laser excitation at a power of 300μW (40μW) for bulk (few-layer) samples, respectively. Scattered light was dispersed by a 1800 lines/mm grating and detected with a liquid nitrogen cooled charge-coupled device (CCD) camera. The spectrometer integration time was 30/60 minutes for bulk/few-layer samples, and each scan was taken twice and then averaged before analysis. Polarized Raman spectra were recorded with a linearly polarized incident beam. For angle-resolved polarized Raman spectroscopy (ARPRS) measurements, an achromatic half-wave plate was placed just before the objective and rotated in steps of 7.5° from 0° to 180°. An analyzer was placed in front of the spectrometer entrance and kept vertical/horizontal for parallel (XX)/perpendicular (XY) configurations, respectively. For circularly polarized measurements, an achromatic quarter-wave plate was placed in front of the objective with fast axis oriented at +/- 45 degrees with respect to the incident linear polarization for σ^+/σ^- circular incident polarization, respectively. For the reported circularly polarized spectra, no analyzing polarizer is used. Temperature-dependent measurements in the range $5 - 300$ K were performed using a Montana Instruments closed-cycle optical cryostat.

8.2.5 Device fabrication for bulk photovoltaic effect measurements.

The photocurrent device was fabricated by depositing two Ti(5nm)/Au(50 nm) electrodes on a sapphire substrate using a 20 μm wide wire mask. A PVD-grown bulk-like NiI_2 flake was then picked up and dropped down across the gap using a polymer-based dry transfer technique. To minimize the exposure to moisture, the polymer was dissolved in anhydrous chloroform inside the glovebox. To ensure a good and uniform electric contact, a carbon copy of the metal pads was created using the same dry transfer technique and stacked on top of the sample to provide a vertically symmetric contact. We used a 0.3 mW linearly-polarized 532 nm laser for the photocurrent measurement. The current was measured using a Keithley 2401 current meter, and the magnetic field was applied perpendicular to the electric field in plane using a 1 T electromagnet from Montana Instruments.

8.3 Optical probes of multiferroic order in bulk NiI_2

8.3.1 Linear dichroism: probe of broken rotational three-fold symmetry

We performed high-resolution, single-domain linear dichroism measurements on bulk NiI_2 – representing the difference in reflectivity ΔR between two perpendicular, linear polarization states – across the two transitions at $T_{N,1}$ and $T_{N,2}$ (Figure 8.3a). The appearance of optical birefringence indicates the breaking of the three-fold (C_{3z}) rotational symmetry in the parent $\bar{3}m$ point group (see Figure 8.2).

In the polarization angle dependent linear dichroism plots as shown in Figure 8.3a, Figure 8.9c and Figure 8.2, the reported angle corresponds to the angle of the primary polarization $\epsilon_{\parallel}(\theta)$ in the frame of the crystal axes. The recorded signal in the polar plots is then the reflectance $R_{\parallel}(\theta)$ along the direction of $\epsilon_{\parallel}(\theta)$ minus the reflectance $R_{\perp}(\theta)$ along the perpendicular polarization state $\epsilon_{\perp}(\theta)$, given by $\Delta R(\theta) := (R_{\parallel}(\theta) - R_{\perp}(\theta))/R_0$ where R_0 is the average reflectance. The difference is monitored directly by the oscillating component of the reflected light at the polarization modulation frequency f, as measured by a lock-in amplifier, while the average reflectance R_0 is monitored by the DC reflectance as measured by the same photodiode.

In the low-temperature C_2 point group, the the dielectric tensor takes on the form,

$$\epsilon = \begin{pmatrix} \epsilon_{xx} & 0 & \epsilon_{xz} \\ 0 & \epsilon_{yy} & 0 \\ \epsilon_{zx} & 0 & \epsilon_{zz} \end{pmatrix} \tag{8.1}$$

For light incident along the **c**-axis, the reflectivity tensor is then,

$$\mathbf{r} = \begin{pmatrix} r_{xx} & 0 \\ 0 & r_{yy} \end{pmatrix} \tag{8.2}$$

where the directions **x**- and **y**- are the principle axes. In the case of the C_2 point group, the principle-axis directions correspond to the unique C_2 axis (**y**) and the direction perpendicular to the C_2 axis (**x**). Defining $\theta = 0$ along the **x**-axis, the linear polarization states for the angular-dependent linear dichroism measurements are expressed as:

$$\epsilon_{\parallel}(\theta) = (\cos(\theta),\ \sin(\theta), 0)\,,\quad \epsilon_{\perp}(\theta) = (-\sin(\theta),\ \cos(\theta),\ 0) \tag{8.3}$$

In this case, the angle dependent reflectances for the two polarization states are given by,

$$R_{\parallel}(\theta) = r_{xx}^2\cos^2(\theta) + r_{yy}^2\sin^2(\theta),\quad R_{\perp}(\theta) = r_{xx}^2\sin^2(\theta) + r_{yy}^2\cos^2(\theta)$$

while the average reflactance $R_0 = (r_{xx}^2 + r_{yy}^2)/2$. The angular-dependent linear dichroism signal, as defined above, is then given by,

$$\Delta R(\theta) = \frac{(r_{xx}^2 - r_{yy}^2)}{R_0} := \delta\cos(2\theta)$$

where δ is the linear dichroism. We see that the resulting angular dependent dichroism signal reaches extrema when $\epsilon_{\parallel}(\theta)$ lies along one of the principle axes, displaying a positive peak when along the more reflective axis and a negative peak when along the less reflective axis.

In our measurements, both in the bulk and the single-layer limits, the registered curves are fit well to the expected $\propto \cos(2\theta)$ dependence on polarization angle, and display maxima oriented along the **a**-axes of the high-temperature rhombohedral phase. In the low-temperature phase, three-fold rotational symmetry about the **c**-axis is broken and one of the three **a**-axes becomes the unique C_2 axis of the monoclinic phase. Therefore the angular-dependent linear dichroism measurement directly identifies the three possible orientations of the local in-plane C_2 axis and confirms the principle axis orientation along the a-axis of the high temperature rhombohedral phase.

For the temperature-dependence of the three-fold rotational symmetry breaking in few-layer samples, we achieved a higher signal-to-noise ratio by measuring the birefringence-induced polarization rotation. In this case, a linear incident polarization state at an angle θ_i with respect to the crystal axes is reflected off the sample with a different polarization angle θ_f, where $\theta := \theta_i - \theta_f$ is the birefringence-induced polarization rotation.

For initial polarization,

$$\epsilon = (\cos(\theta_i),\ \sin(\theta_i),\ 0) \tag{8.4}$$

the birefringence induced polarization can be expressed in terms of the linear dichroism above as

$$\theta = \cos^{-1}\left(\frac{\sqrt{1+\delta}\ \cos^2(\theta_i) + \sin^2(\theta_i)}{\sqrt{(1+\delta)\ \cos^2(\theta_i) + \sin^2(\theta_i)}}\right) \simeq \frac{\delta}{4}\sin(2\theta_i) \tag{8.5}$$

expanded for small difference in reflectivity δ. Therefore, the dichroism-induced polarization rotation

is zero when the incident polarization is aligned along one of the principle axes, but has a non-zero value for all other incident polarization states and is directly proportional to the linear dichroism.

In the case of our measurements on the few-layer samples, temperature-dependence was recorded on domains such that the incident polarization made an angle of either $\pm 30°$ or $\pm 45°$ with respect to the principle axes. This lead to typical values of the polarization rotation of 1-2 mrad in the 1L, 3-4 mrad in the 2L and 6-7 mrad in the 4L samples.

The temperature dependence of ΔR bears a striking resemblance to the magnetic susceptibility (χ_{mag}, Figure 8.3a), with a kink at $T_{N,1}$ and a sharp jump at $T_{N,2}$. Therefore, the reduction in the lattice rotational symmetry is a direct proxy for the change in the magnetic ground state. We further record the dependence of the linear dichroism signal on the angle of linear incident polarization with respect to the crystallographic axes, $\Delta R(\theta)$. These results (inset of Figure 8.3a and Figure 8.2) display a maximum dichroism of positive sign (blue lobes) for polarization parallel to the crystallographic **a**-axis and display the expected two-fold rotational symmetry, confirming that the low-temperature phase is characterized by a local, unique C_2 axis.

8.3.2 Second harmonic generation: probe of ferroelectric order

To confirm the polar nature of the low-temperature symmetry group, we measured SHG in bulk NiI_2 from a mono-domain region identified through SHG imaging (Figure 8.3b and Figure 8.6). Electric-dipole SHG (ED-SHG) is used as a direct probe of inversion-symmetry breaking [277].

For NiI_2, the second harmonic radiated from the sample can be written as:

$$S(2\omega) = \mu_0 \frac{\partial^2 P}{\partial t^2} + \mu_0 \nabla \times \frac{\partial M}{\partial t}$$

In frequency and momentum domain, this expression takes the following form:

$$S(2\omega) = -4\omega^2 \mu_0 P(2\omega) + 4\omega \mu_0 k \times M(2\omega)$$

where k represents the wavevector along the propagation direction. For normal incidence, k is along z-axis. The first term in this equation represents electric dipole (ED) contribution to SHG, which is only present for non-centrosymmetric systems. On the other hand, the second term corresponds to magnetic dipole (MD) contribution to SHG, which can be present in magnetic systems, such as antiferromagnets, even without inversion symmetry breaking. These two contributions can be decomposed with polarization analysis of SHG signal.

For MD contribution, the magnetization at second harmonic can be written as:

$$M_i(2\omega) = \chi^{(2)}_{ijk,mag} E_j(\omega) E_k(\omega)$$

where $\chi^{(2)}_{ijk,mag}$ corresponds to the magnetic SHG tensor. For ED contribution, the polarization at second harmonic can be written as:

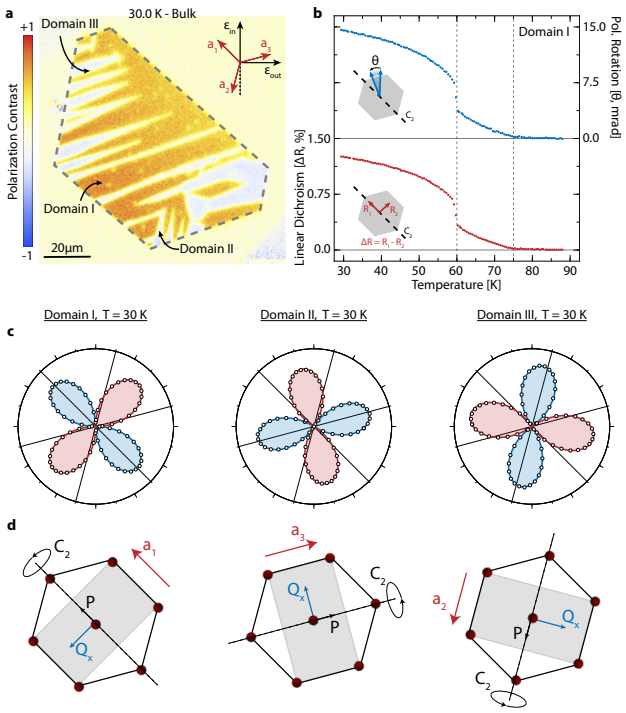

Figure 8.2: Linear dichroism and birefringence-induced polarization rotation measurements. **a**, Polarized microscopy image of bulk NiI_2. The positions where the optical measurements were performed are labelled as Domain I-III. **b**, Comparison of the temperature-dependent birefringence-induced polarization rotation (top) and linear dichroism (bottom) on Domain I. **c**, Angular-dependent linear dichroism measurements from the three distinct domains identified in **a**. Radial lines indicate the crystallographic a-axes determined from the edges of the as-grown PVD sample. **d**, Schematics of the domains as identified from AD-LD measurements in **c**, denoting the local C_2 axis orientation, the polar vector P and the in-plane component of the helimagnetic ordering vector $\mathbf{Q}$.

$$P_i(2\omega) = \chi^{(2)}_{ijk,elec} E_j(\omega) E_k(\omega)$$

The non-zero elements of $\chi^{(2)}_{ijk,elec}$ and $\chi^{(2)}_{ijk,mag}$ are determined by crystal symmetries. For monoclinic monoclinic C_2 symmetry, the non-zero elements of both $\chi^{(2)}_{ijk,elec}$ and $\chi^{(2)}_{ijk,mag}$ relevant for a fundamental field propagating along z-axis are: $\chi^{(2)}_{xxy}$, $\chi^{(2)}_{xyx}$, $\chi^{(2)}_{yxx}$, $\chi^{(2)}_{yyy}$ where y denotes the normal vector direction perpendicular to the mirror plane.

To extract the ED and MD contributions from the SHG signal, we fit our SHG polarization dependent traces in order to obtain the tensor elements both for electric and magnetic dipole SHG tensors. The polarization dependent SHG signal is collected as a function of incident electric field angle rotated along propagation axis (z-axis) and two polarization channels, parallel and perpendicular. The overall emitted second harmonic field can be represented as $S(2\omega, \theta)$ where the incident electric field is equal to $E_{inc} = E_0(\cos(\theta)x + \sin(\theta)y)$. The SHG intensity in the parallel channel is

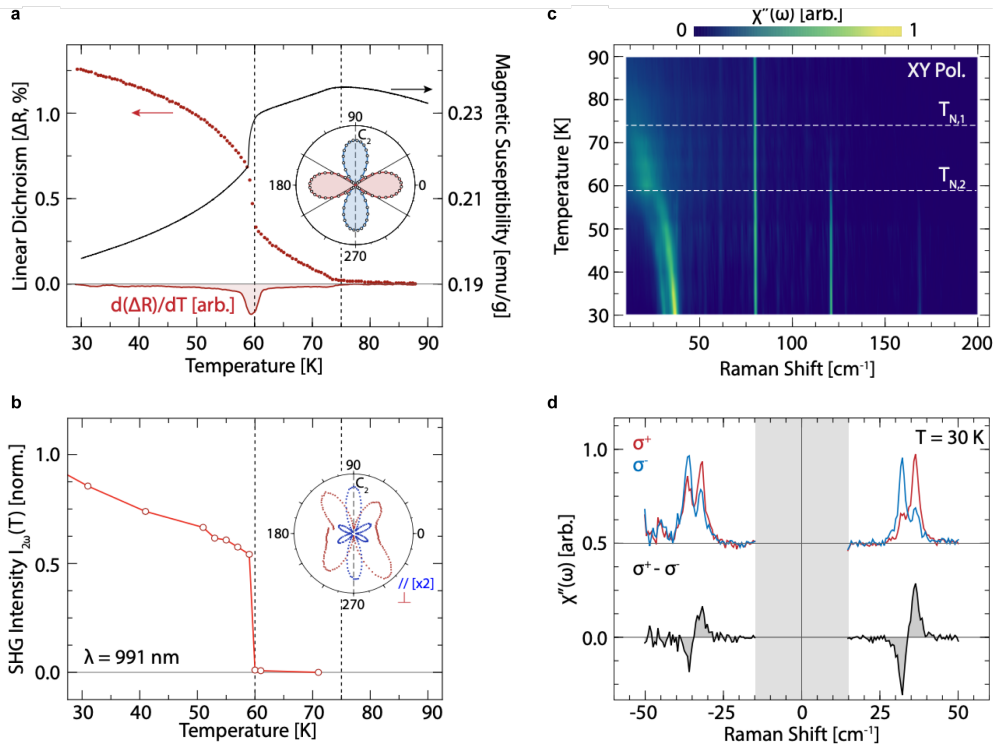

Figure 8.3: Optical characterization of multiferroic order. **a**, Temperature-dependent linear dichroism ($\Delta R(T)$) measurements on a mono-domain region of bulk NiI_2, overlaid on the magnetic susceptibility χ_{mag}. The inset shows the angular-dependence of ΔR at $T = 30$ K – radial lines indicate the crystallographic **a** axes and the dashed line corresponds to the local C_2 axis. **b**, Below band gap ($\lambda = 991$ nm) temperature-dependent SHG in bulk NiI_2. The inset shows rotational anisotropy SHG patterns for a mono-domain region in the $\parallel$ and $\perp$ polarization channels with the dashed line corresponding to the C_2 axis orientation. Vertical dashed lines in **a**,**b** indicate the $T_{N,1}$ and $T_{N,2}$ transitions. **c**, Temperature-dependent Raman spectra in the XY polarization channel. **d**, Circular-polarized Stokes and Anti-Stokes Raman spectra of the soft mode excitations for σ^+/σ^- incident polarization (top) and the net Raman optical activity ($\sigma^+ - \sigma^-$) (bottom).

equal to $|(\cos(\theta)x + \sin(\theta)y)S(2\omega, \theta)|^2$, whereas the SHG intensity in the parallel channel is equal to $|(-\sin(\theta)x + \cos(\theta)y)S(2\omega, \theta)|^2$.

The fit results for three different fundamental wavelengths (991, 826, 780 nm) are given in Figure 8.6. NiI_2 is transparent for 991 nm, whereas 826 and 780 nm excitations reside within the broad $d - d$ transition. In addition to the changes in values of nonlinear tensor elements as a function of excitation wavelength, the ED and MD contributions can change as a function of excitation wavelength. In magnetic systems, the MD contributions are enhanced in the vicinity of localized $d - d$ transitions. As shown in the fits for SHG traces obtained with 826 and 780 nm fundamental, both MD and ED contributions are required to fit the polarization dependent SHG data. This result is expected as both of these wavelengths are close to the localized $d-d$ transition. On the other hand, the SHG traces obtained with 991 nm fundamental can easily be fit with only

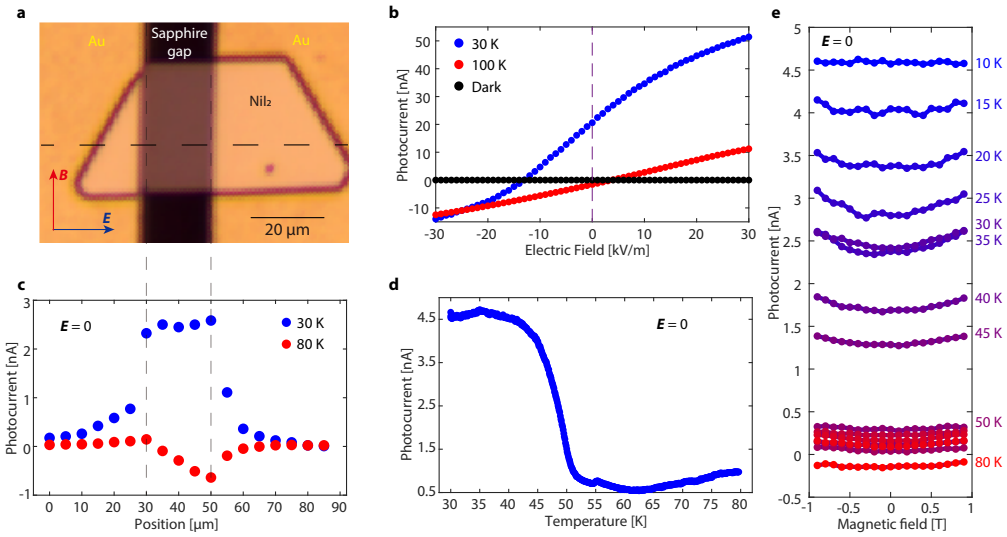

Figure 8.4: Bulk photovoltaic effect. **a**, Optical image of the BPE device. A PVD grown bulk-like NiI_2 flake was transferred across a sapphire gap, bridging two gold pads as electrodes. The electric field was applied between the electrodes and in a direction nearly parallel to the **a**-axis, while the magnetic field was applied perpendicular to the electric field in plane. **b**, The electric field dependence of the photocurrent at 30 K, in the multiferroic phase and at 100 K, in the paramagnetic phase, reveals the presence of a polarization-induced internal electric field the multiferroic phase. **c**, The position dependence of the photocurrent along the dashed line in **a**, under zero bias shows a major contribution of the photocurrent from the NiI_2 between the electrodes. **d**, The temperature dependence of the zero-bias photocurrent shows a strong enhancement in the multiferroic phase. **e**, The external magnetic field increased the zero-bias photocurrent by 10-15%, which we ascribe to an increase of the electric polarization from magnetoelectric coupling. Linearly polarized 532 nm light (0.3 mW power) was used in the BPE measurement.

ED contribution, implying that it is only sensitive to the inversion symmetry breaking ferroelectric order parameter.

Here, the pure electric-dipole SHG mechanism is ensured by tuning the energy of the fundamental beam to a wavelength $\lambda = 991$ nm that is below the optical band-gap and d-d transitions [275]. This is verified with rotational anisotropy SHG (RA-SHG) measurements, which agree well with the ED-SHG tensor elements predicted for the C_2 monoclinic point group in the helimagnetic phase (inset of Figure 8.3a, Figure 8.6). For wavelengths in the vicinity of the d-d transitions ($\lambda = 780$ and 826 nm), magnetic-dipole SHG originating purely from spin order, which does not necessitate inversion symmetry breaking, is also present (see Figure 8.6). The combined observation of ED-SHG (lattice inversion-symmetry breaking) and optical birefringence (rotational-symmetry breaking) directly confirms the presence of a polar phase in NiI_2 and an underlying single-$\mathbf{Q}$, helical magnetic ground state. Moreover, the SHG imaging of the monolayer NiI_2 is shown in Figure 8.5The resulting electrical polarization induces a bulk photovoltaic effect which was detected in photocurrent measurements on a thin NiI_2 flake (Figure 8.4).

8.3.3 Raman spectroscopy: probe of electromagnon mode

To underscore the connection between the optical signatures of polar order and the underlying magnetic state, we have performed Raman measurements ($\lambda = 532$ nm) on bulk NiI_2.

The irreducible representations of NiI_2 (space group $R\bar{3}m$) A_{1g}, $E_{g,1}$, $E_{g,2}$ have Raman tensors $\tilde{R}$ of the following form:

A_{1g}	$E_{g,1}$	$E_{g,2}$
$\begin{pmatrix} a & 0 & 0 \\ 0 & a & 0 \\ 0 & 0 & b \end{pmatrix}$	$\begin{pmatrix} c & 0 & 0 \\ 0 & -c & d \\ 0 & d & 0 \end{pmatrix}$	$\begin{pmatrix} 0 & -c & -d \\ -c & 0 & 0 \\ -d & 0 & 0 \end{pmatrix}$

At low temperature, NiI_2 transitions into the monoclinic structure. The Raman tensors of A_g phonon modes, M magnon modes have the following form:

A_g	M
$\begin{pmatrix} a & d & 0 \\ d & b & 0 \\ 0 & 0 & c \end{pmatrix}$	$\begin{pmatrix} 0 & ie & 0 \\ -ie & 0 & if \\ 0 & -if & 0 \end{pmatrix}$

The Raman scattering intensity is $I \propto |\boldsymbol{e_s^*} \cdot \tilde{R} \cdot \boldsymbol{e_i}|^2$, where the $\boldsymbol{e_i}$ and $\boldsymbol{e_s}$ are the polarization vectors of the incident and scattered light, respectively. In the back-scattering geometry, the incident light polarization is $\boldsymbol{e_i} = (\cos(\theta),\ \sin(\theta),\ 0)$ and the scattered light polarization is $\boldsymbol{e_s} = (\cos(\theta),\ \sin(\theta),\ 0)$ for parallel configuration (XX), and $\boldsymbol{e_s} = (-\sin(\theta),\ \cos(\theta),\ 0)$ for perpendicular configuration (XY), where θ is the angle between the Raman principle axis and the incident polarization angle.

Angle resolved polarized Raman spectroscopy (ARPRS) measurements can distinguish each mode based on the symmetry analysis of the Raman intensity as a function of polarization angle. At low temperature in the perpendicular configuration (XY), the Raman intensity of each mode is:

$$I(A_g) \propto \left| \frac{b-a}{2} \sin(2\theta) + d\cos(2\theta) \right|^2, \quad I(M) \propto |e|^2$$

Figure 8.8 shows the ARPRS of bulk NiI_2 at 30 K in monoclinic phase. From the calculation above, the ARPRS pattern of a phonon mode should display a polar plot with four lobes and four nodes (zero intensity) while the ARPRS of a magnon mode should be a constant. The 79.9 cm^{-1} and 80.2 cm^{-1} modes are two closely spaced phonon modes (corresponding to E_g modes at room temperature) that are out of phase, which is similar to what observed in the ARPRS plots of CrI_3 and $CrCl_3$ in the monoclinic phase[278], [279]. The 120.8 cm^{-1} and 168.8 cm^{-1} are magnon modes, and the 120.8 cm^{-1} mode onsets at $T_{N,1}$, which indicates that it is an antiferromagnetic magnon. The 31 cm^{-1} and 37.5 cm^{-1} modes appear only in the multiferroic phase and are not consistent with either pure phonon or pure magnon excitations from the ARPRS analysis.

The dichroic contrast of the Raman intensity in different circularly polarized channels supports the previous assignment of each Raman mode via selection rules (Figure 8.7c). In the monoclinic structure, the intensity of the phonon and magnon modes are as follows:

$$I_L(A_g) = I_R(A_g) \propto \frac{a^2 + b^2 + 2d^2}{2}, \quad I_L(M) = I_R(M) \propto |e|^2$$

where $L(R)$ means left (right) circular polarized light in. The phonon and magnon modes in the monoclinic structure should appear in both channels, without any contrast in L/R. This agrees well with the 79.9 cm^{-1}, 80.2 cm^{-1}, and 128 cm^{-1} phonon modes (Figure 8.8a, b). This consideration, in conjunction with the angular independent ARPRS patterns, also confirms the magnetic origin of the 120.8 cm^{-1} and 168.8 cm^{-1} excitations. The 31 cm^{-1} and 37.5 cm^{-1} modes are more complex. Both excitations appear in L/R channels with different intensities and appear only in the multiferroic phase, which suggest that they may be phonon/magnon hybrids, or electromagnons modes[280].

Above $T_{N,1}$, the cross-polarized (XY) Raman spectrum of NiI_2 displays a single phonon at 80.2 cm^{-1} of E_g symmetry [274]. Our measurements reveal a major change in the Raman response in the magnetically-ordered phase, including the appearance of two new high-energy modes around 120.8, and 168.8 cm^{-1} (Figure 8.3c) which exhibit polarization selection rules corresponding to single magnon excitations [281], [282] (see Figure 8.7, 8.8). At low-energy transfer, a pronounced quasi-elastic signal (QES) develops on approaching $T_{N,1}$ [274] (Figure 8.3c). Below $T_{N,2}$, this broad excitation hardens into two sharp and distinct modes (Figure 8.3c, d), which display a much more complex set of selection rules compared to the higher energy magnon and phonon excitations (see Figure 8.7, 8.8) suggesting they are electromagnons [106], [254]–[257]. In support of this interpretation, circular polarized excitation reveals a large Raman optical activity (ROA) for the electromagnon peaks (Figure 8.3d) that is absent for all other phonon and magnon excitations (Figure 8.7). The presence of large ROA for the electromagnon underscores it as a direct signature of magneto-chiral order. The reversal of the ROA between Stokes and anti-Stokes scattering (Figure 8.3d) is in agreement with the optical selection rules observed for Raman-active magnetic excitations in previous studies [281].

8.4 Group theory analysis of the low-temperature phase

Our observations of birefringence in the **a**-**b** plane, the resolution of the principle axes of the birefringence as well as an electric-dipole allowed second harmonic generation together provide strong restrictions for the possible point groups in ground state of bulk and few-layer NiI_2. The high-temperature point group symmetry is $\bar{3}m$, for which both **a**-**b** plane birefringence and electric-dipole active SHG are symmetry forbidden. The development of birefringence necessitates the breaking of the 3-fold rotational symmetry about the **c**-axis, while SHG requires the breaking of inversion-symmetry. Among the possible sub-point groups of the parent phase, there are only three possible crystallographic (non-magnetic) points groups consistent with our observations of both of these ef-

fects: C_1 (1), C_i (m), and C_2 (2). All of these possible sub-point groups are polar as shown in the following table.

Point Group	**Birefringence in the a-b plane:**	**Electric-dipole SHG:**	**Polar?**
$\bar{3}m$ (D_{3d})	Forbidden	Forbidden	No
$\bar{3}$ (S_6)	Forbidden	Forbidden	No
$2/m$ (C_{2h})	Allowed	Forbidden	No
$3m$ (C_{3v})	Forbidden	Allowed	Yes
32 (D_3)	Forbidden	Allowed	No
3 (C_3)	Forbidden	Allowed	Yes
2 (C_2)	Allowed	Allowed	Yes
m (C_s)	Allowed	Allowed	Yes
$\bar{1}$ (C_i)	Allowed	Forbidden	No
1 (C_1)	Allowed	Allowed	Yes

In the bulk, the totality of data are consistent with an assignment of the C_2 point group below $T_{N,2} = 60$ K. The distinction between the possible points groups is unequivocally demonstrated by the SHG rotational anisotropy patterns for laser wavelengths below the band-gap where the signal is of pure electric-dipole origin (with the absence of magnetic-dipole SHG contributions). For this case, the SHG-RA patterns are well described by the C_2 point group tensor restrictions (see Figure 8.6). The SHG-RA patterns also uniquely determine the C_2 axis, which is parallel to the crystallographic **a**-axis of the $\bar{3}m$ structure, and forms the unique monoclinic **b**-axis in the low-temperature phase. The angular-dependent linear dichroism measurements further confirm this situation, which demonstrate three domains with principle axes oriented along the crystallographic **a** direction and relatively rotated by 120 degrees. These measurements show that the C_2 axis is the more highly reflective axis, displaying a strong dichroism of positive sign between the **a** axes and the perpendicular $\mathbf{b}^*$ axes.

In the few-layer samples, a consistent behavior is found with the point group symmetry observed in the bulk. Our results demonstrate that ED-active SHG is allowed down to the monolayer limit in addition to the presence of a strong birefringence. These observations restrict to the same three possible point groups for the ground state in the atomically-thin limit. The AD-LD measurements registered on three mono-domain regions of a monolayer sample confirm an identical behavior to the bulk, showing 3-domains with principle axes relatively oriented by 120 degrees. Furthermore, the axes with higher reflectivity are in close agreement with the **a**-axes (as determined by the as-grown edges of the samples), as opposed to the 30 degree rotated $\mathbf{a}^*$ axes, the same as found in the bulk. These observations, along with the smooth trend of these signatures as the layer number is reduced to the monolayer limit, strongly support the same assignment of the C_2 non-magnetic point group for low-temperature phase of few- and single-layer NiI_2.

8.5 Layer-dependence of multiferroic order

8.5.1 Linear dicroism

The baseline optical characterization of bulk samples serves as a blueprint for the exploration of the multiferroic state in few-layer NiI_2 samples. Figure 8.9a shows an optical image of 1- and 2-layer NiI_2 crystals grown by physical vapor deposition on hBN. The optical anisotropy of NiI_2 is directly captured using cross-polarized microscopy (see Experimental methods section), signaling the presence of birefringent domains on both the 1- and 2-layer regions at $T = 5$ K (Figure 8.9b). As temperature is increased, the birefringent domains vanish from the 1-layer region between $T = 15 - 25$ K, and from the 2-layer region between $T = 25 - 35$ K (Figure 8.9b). Crucially, a reduction of rotational symmetry from three-fold to two-fold is also observed in single-layer samples, as confirmed by angular dependent linear dichroism ($\Delta R(\theta)$) measurements (Figure 8.9c). Angle dependent linear dichroism traces collected in different domains, determined from the cross-polarized images, show the presence of unique two-fold (C_2) axes (highlighted by dashed lines in Figure 8.9c). The detailed layer dependence of the rotational symmetry breaking transition is obtained through birefringence-induced polarization rotation measurements ($\theta(T)$) in Figure 8.9d, which reveals a monotonic evolution of the transition temperatures from 1- to 4-layer samples. The transition temperatures are defined as the values of maximum slope of the polarization rotation signal (where $d\theta/dT$ is minimum), yielding 21 K for single-layer, 30 K for 2-layer, 39 K for 3-layer and 41 K for 4-layer flakes for 3- and 4-layer optical images and additional $\theta(T)$ data for 1-, 2-, and 4-layer).

8.5.2 Second harmonic generation

Temperature-dependent ED-SHG ($\lambda = 991$ nm) measurements from 4-, to 1-layer NiI_2 samples (Figure 8.9e) provide complementary information on the breaking of inversion symmetry down to the single layer limit. For all samples, the SHG intensity displays a clear drop near the transition temperatures derived from the birefringence data. The SHG signal from single-layer samples is genuine as demonstrated by temperature-dependent SHG imaging of multiple monolayer regions (see Figure 8.5). For these SHG spatial maps, we note a temperature-independent residual SHG contrast from single-layer NiI_2 samples which originates at the NiI_2/hBN interface due to surface inversion symmetry breaking. The breaking of inversion symmetry demonstrated through SHG and the 3-fold rotational symmetry breaking observed in birefringence measurements (Figure 8.9b) unequivocally establish the persistence of a polar ground state in few- and single-layer samples. Concurrently, Raman measurements reveal the persistence of the magnetic soft modes down to the two-layer limit (see Figure 8.10). The quantitative agreement of the transition temperatures from these independent measurements, as well as the smooth trend of these optical signatures as layer number is reduced from bulk to the monolayer, thus offer strong evidence for the survival of the polar, helimagnetic phase down to the monolayer limit in NiI_2.

8.6 Theoretical analysis of multiferroic phase in few-layer NiI_2

8.6.1 Magnetic Hamiltonian and Monte Carlo simulations

The observed reduction of the transition temperature as layer number is decreased is strongly indicative of the relevant role played by the interlayer exchange interaction, as also reported for other 2D magnets [93], [282]–[286], while the finite transition temperature detected in the monolayer sample indicate a non-negligible magnetic anisotropy.

To describe the magnetic properties of the system we adopted the 2D anisotropic Heisenberg model derived for NiI_2 monolayer [268] supplemented by a nearest-neighbour antiferromagnetic interlayer interaction accounting for the exchange between rhombohedral-stacked layers:

$$H = \frac{1}{2}\sum_{ij}\left(\mathbf{S}_i^{(e)}\cdot\mathbf{J}_{ij}\cdot\mathbf{S}_j^{(e)} + \mathbf{S}_i^{(o)}\cdot\mathbf{J}_{ij}\cdot\mathbf{S}_j^{(o)}\right) + \sum_i \mathbf{S}_i\cdot\mathbf{A}_{ii}\cdot\mathbf{S}_i + J_\perp\sum_{<ij>}\mathbf{S}_i^{(e)}\cdot\mathbf{S}_j^{(o)} \tag{8.6}$$

Here e and o label respectively even and odd layers perpendicular to the **c** axis, the first sum extends to third nearest neighbour within each plane while the last sum is restricted to nearest-neighbours belonging to different layers. We used the interlayer exchange $\mathbf{J}_{ij}$ and single-site anisotropy $\mathbf{A}_{ij}$ tensors evaluated from first principles for NiI_2 monolayer [268]; the non-negligible anisotropic terms guarantee a finite-temperature long-range magnetic order, with a triple-**Q** topological phase competing with single-**Q** spiral configuration. The anisotropic part of the exchange tensor has been accordingly rescaled to 60% of the ab initio estimate, thus favouring the spin-spiral solution, in agreement with the breaking of the three-fold rotational symmetry experimentally detected. We set the energy scale as $J_\parallel = -J^{\mathrm{1iso}}$, the ferromagnetic nearest-neighbour interlayer interaction.

We performed MC simulations using a standard Metropolis algorithm on rhombohedral-stacked triangular lattices (rhombohedral supercells in hexagonal setting) in slab geometry to simulate multilayer (bulk) NiI_2. We used 10^5 MC steps for thermalization and 5×10^5 MC steps for statistical averaging at each simulated temperature. Simulations have been performed on 24×24 lattices in slab geometry comprising up to 5 layers of triangular NiI_2 (and up to 2880 spins) with two-dimensional periodic boundary conditions (PBC), and on $8\times8\times8$ hexagonal supercells (comprising 1536 spins) with three-dimensional PBC for bulk rhombohedral system. The transition temperature is identified by the peak in the specific heat of the spin model. All MC results for multilayer slabs at different values of interlayer exchange $J_\perp$ are well described by a simple empirical function:

$$T_{\mathrm{c(N)}} = T_{\mathrm{c}}^{\text{1-layer}}\,\tanh\left(b\,\ln N + \frac{1}{2}\ln\frac{t+1}{t-1}\right), \tag{8.7}$$

where $t = T_{\mathrm{N},2}/T_{\mathrm{c}}^{\text{1-layer}}$ is the reduced temperature, N is the number of layers and the coefficient $b = 1.05$ has been obtained by fitting only the $J_\perp = 0.1\ J_\parallel$ data points.

We performed MC simulations to further investigate the role of the interlayer exchange interaction in affecting the helimagnetic transition temperature. Our starting model is the classical

2D anisotropic Heisenberg model recently introduced for NiI_2 monolayer [268], supplemented by a nearest-neighbour antiferromagnetic interlayer exchange $J_\perp$ in order to describe the bulk phase. The presence of anisotropic interactions guarantees a finite-temperature transition to a long-range ordered magnetic phase even in the monolayer (Figure 8.11c). On the other hand, the transition temperature of the bulk system is found to increase proportionally to $J_\perp$ (Figure 8.11a). Experimentally, the helimagnetic transition temperature of the 1-layer sample is strongly reduced from its bulk value, being $T_{\mathrm{N},2}/T_c^{\text{1-layer}} \simeq 2.8$. A linear extrapolation of the MC estimates for transition temperatures as a function of $J_\perp$ allows to estimate a quite large interlayer exchange, $J_\perp \sim 0.45\, J_\parallel$, where $J_\parallel$ is the dominant ferromagnetic intralayer interaction. Using $J_\parallel \simeq 7$ meV [268], the estimated interlayer exchange is $J_\perp = 3.15$ meV; this is in quite good agreement with the value we directly calculated by means of Density Functional Theory (DFT) calculations for 2-layer NiI_2, that is $J_\perp^{(\mathrm{DFT})} \sim 3$ meV. The evolution of transition temperatures as a function of the sample thickness has also been estimated with MC simulations for different number N of layers (N ranging from 1 to 5) and at fixed $J_\perp$. Remarkably, all MC estimates as well as the experimental data are well described by a simple empirical formula that depends only on the ratio of bulk and 1-layer transition temperatures, with no fitting parameters, as shown in Figure 8.11b.

8.6.2 Magnetism induced ferroelectricity: generalized KNB model

The possible onset of a magnetically induced electric polarization in 1-layer NiI_2 has been further investigated in the framework of the generalized spin-current (or Katsura-Nagaosa-Balatsky, gKNB) model [287], where an electric dipole may be induced by spin pairs according to the general expression $\mathbf{P}_{ij} = \mathbf{M} \cdot \mathbf{S}_i \times \mathbf{S}_j$. The 3×3 $\mathbf{M}$ tensor has been evaluated from first-principles, and then used to estimate the polarization of NiI_2 monolayer from MC simulations.

Within this generalised spin-current model gKNB [287], the total polarization is given by:

$$\mathbf{P} = \frac{1}{2N} \sum_{ij} \mathbf{M}_{ij} \cdot \mathbf{S}_i \times \mathbf{S}_j, \tag{8.8}$$

where N is the number of magnetic sites, and we restricted the sum to interlayer nearest-neighbours. The M-tensor has been evaluated from first principles for a spin pair parallel to the $\mathbf{a}$ axis using the four-state method [287] (the tensor of equivalent bonds is readily obtained by enforcing crystalline symmetries). The dominant tensor components found are $M_{22} = 348 \times 10^{-5}$ eÅ and $M_{23} = -520 \times 10^{-5}$ eÅ, the other components being zero or smaller than ~ 30 eÅ. Assuming a proper-screw spiral with positive/negative handedness $\tau = \pm 1$ propagating along the $\mathbf{a}$ (x) axis with pitch 2δ, the gKNB model predicts $P_x \equiv P_\parallel = 3\, M_{22} \sin(\tau\delta)/2$, in agreement with numerical MC calculations. For the proper-screw spiral propagating along the $\mathbf{Q} = (0.138,0,1.457)$ direction, with the spins rotating in a plane making an angle $\theta = 55°$ as observed in bulk NiI_2 [273], the electric polarization predicted by the gKNB model lies in the ab plane and is perpendicular to the in-plane projection of $\mathbf{Q}$, $P_\perp = \sqrt{3}[M_{22}\cos\theta - 2M_{23}\sin\theta]\sin(\tau 0.138)/2$. In both cases, handedness τ determines the

sign of **P**, that is always parallel to the crystallographic axis **a**.

As shown in Figure 8.11d, a proper-screw spiral propagating along the $\boldsymbol{a}$ lattice vector stabilizes below $T_c \lesssim 27$ K, in reasonable agreement with the experimental value of 21 K. The corresponding magnetic point group is the polar $21'$ group, with the twofold rotational axis and the electric polarization coinciding with the spiral propagation vector and hence with the **a** axis, in agreement with the optical measurements. Within the gKNB model, the handedness of the spin spiral uniquely determines if the electric polarization is parallel or antiparallel to the polar axis. We further notice that when the magnetic helix is slanted from the basal plane with a propagation vector $\mathbf{Q} = (0.138,0,1.457)$, as it occurs in bulk samples, the purely spin-induced polarization as evaluated from our estimated **M**-tensor is always parallel to the crystallographic **a** axis.

8.7 Defining factors of the multiferroic ground state

NiI_2, down to the 2D limit, is therefore an example of improper electronic ferroelectricity, where the electric polarization is driven by the emergence of an inversion-symmetry breaking magnetic order (such as the proper-screw spin helix) in an otherwise centrosymmetric lattice. The propensity for such spin-spiral ordering in the single-layer limit can be associated to the significant frustration of the intralayer exchange interactions on the underlying triangular lattice, along with crucial magnetic anisotropy effects [268]. Furthermore, NiI_2 shows superexchange mediated by the extended $5p$ states of the iodine ligands, the latter also introducing a significant spin-orbit coupling (SOC). As a result, non-negligible spin interactions beyond nearest neighbor Ni sites play a relevant role in the stabilization of the resulting proper-screw spin-helix, the latter giving rise to SOC-induced electric polarization, as described by the generalized KNB model [287]. In this framework, the observation of SHG and birefringence in monolayer NiI_2 is consistent with the proposed theoretical picture, providing a direct indication of a non-centrosymmetric polar magnetic texture that develops below the identified Curie temperature of 21 K. The observed suppression of the multiferroic transition temperature with reducing layer number further allowed us to clarify the role of the interlayer exchange interactions, which are known to contribute to the orientation of the spin-rotation plane and magnetic ordering vector in the bulk [272], [273].

Our results point to the crucial role of SOC and orbital extension of the ligands in modulating both the long-range magnetic interactions and the exchange anisotropy, ultimately determining the magnetic ground state among closely lying, competing phases [268]. This suggests that changing the ligand could be a powerful tuning knob to realize new exotic magnetic ground states in 2D, including helices, cycloids and skyrmions with unique topological and multiferroic properties [267], [268], [288]. In addition, our observations of a complex magnetic ground state in an atomically-thin vdW crystal introduces new avenues for exploring multiferroicity which are inherently unique to 2D systems. These include the robust and direct electrical control of magnetism through electrostatic doping or external fields and currents, or the realization of new interfacial multiferroic properties in

artificial vdW heterostructures. Moreover, 2D materials with gate-tunable magnetoelectric coupling might offer a new platform for continuous tuning of multiferroic systems toward quantum critical behavior [289]. While our optical measurements establish the persistence of multiferroicity in NiI_2 to the monolayer limit, further characterization through piezo-response force microscopy or high-sensitivity pyroelectric current measurements will be of great importance to confirm the electrical manifestations of multiferroicity and assess its potential for these future device applications.

8.8 Conclusions

In conclusion, our results represent the first observation of an intrinsic multiferroic phase in the single-layer limit. Multiple complementary optical signatures confirm the persistence of ferroelectricity and inversion-symmetry breaking magnetic order down to monolayer NiI_2 with a transition temperature of $T = 21$ K. These results usher the physics of type-II multiferroics into the playground of vdW materials. These findings open a new frontier for studying and optimizing the interplay of magnetic and dielectric properties in next-generation nanoscale devices.

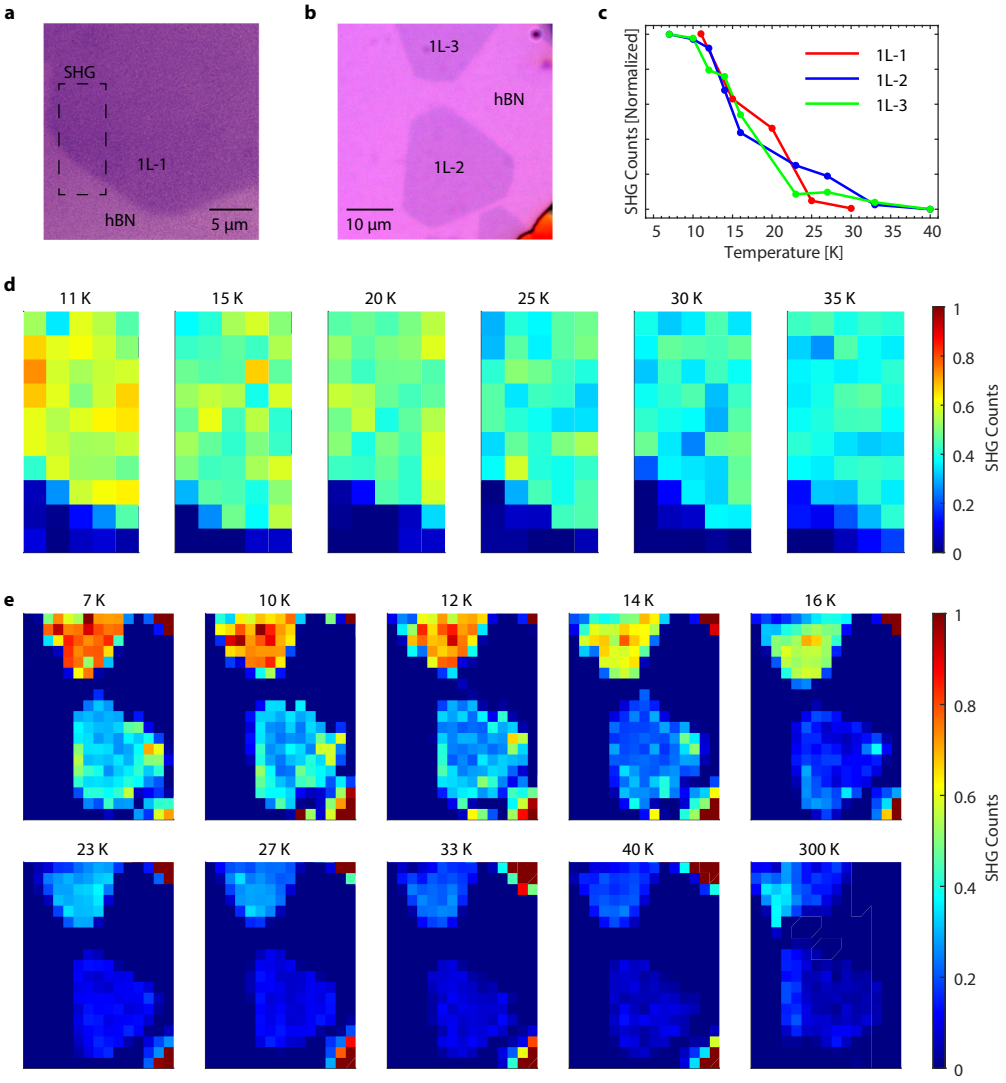

Figure 8.5: Temperature dependent Second Harmonic Generation imaging of the single-layer crystals. a, b, Optical images of the region where the SHG imaging was performed. **c**, Integrated SHG counts on three single-layer NiI_2 crystals show a transition around 20 K, which is consistent with the polarization rotation measurement. **d**, Temperature dependent SHG imaging of the rectangular region in **a** using 780 nm excitation. **e**, Temperature dependent SHG imaging of the region in **b** using 991 nm laser. Colorbar: SHG counts.

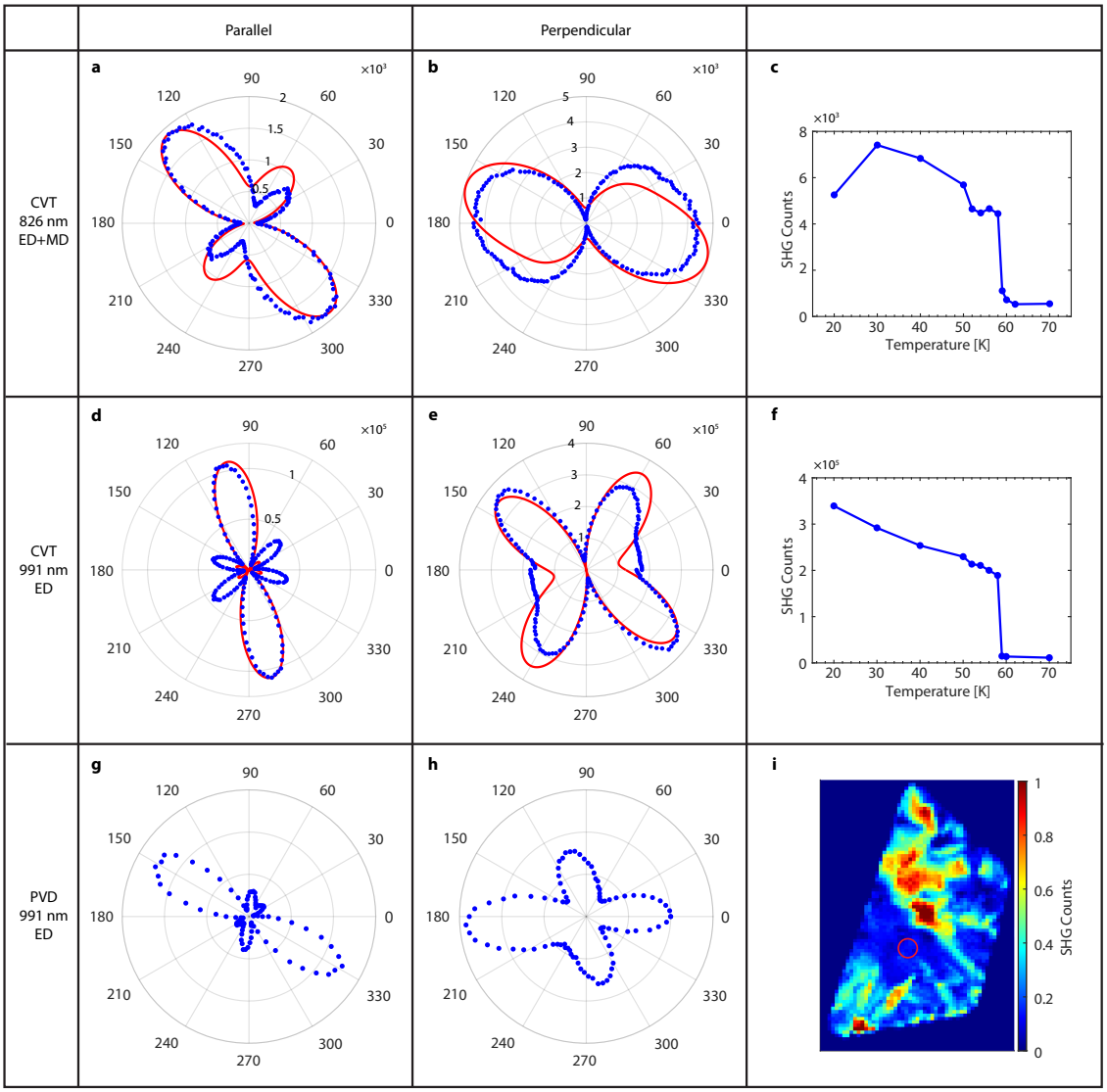

Figure 8.6: Wavelength-dependent second harmonic generation. Rotational anisotropy SHG (RA-SHG), fits to nonlinear tensor elements and their temperature dependence on a single domain CVT grown bulk NiI_2 using **a-c**, 826 nm laser, and **d-f**, 991 nm laser. The RA-SHG traces obtained with 826 nm can only be fit with a combination of electric dipole (ED) and magnetic dipole (MD) radiation, whereas the RA-SHG traces obtained with 991 nm only exhibit ED component. **g, h**, RA-SHG on PVD grown bulk NiI_2 samples shows the same signatures as the CVT grown samples. **i** SHG imaging of the PVD sample at 15 K. The red circle shows the single domain region where the RA-SHG was taken.

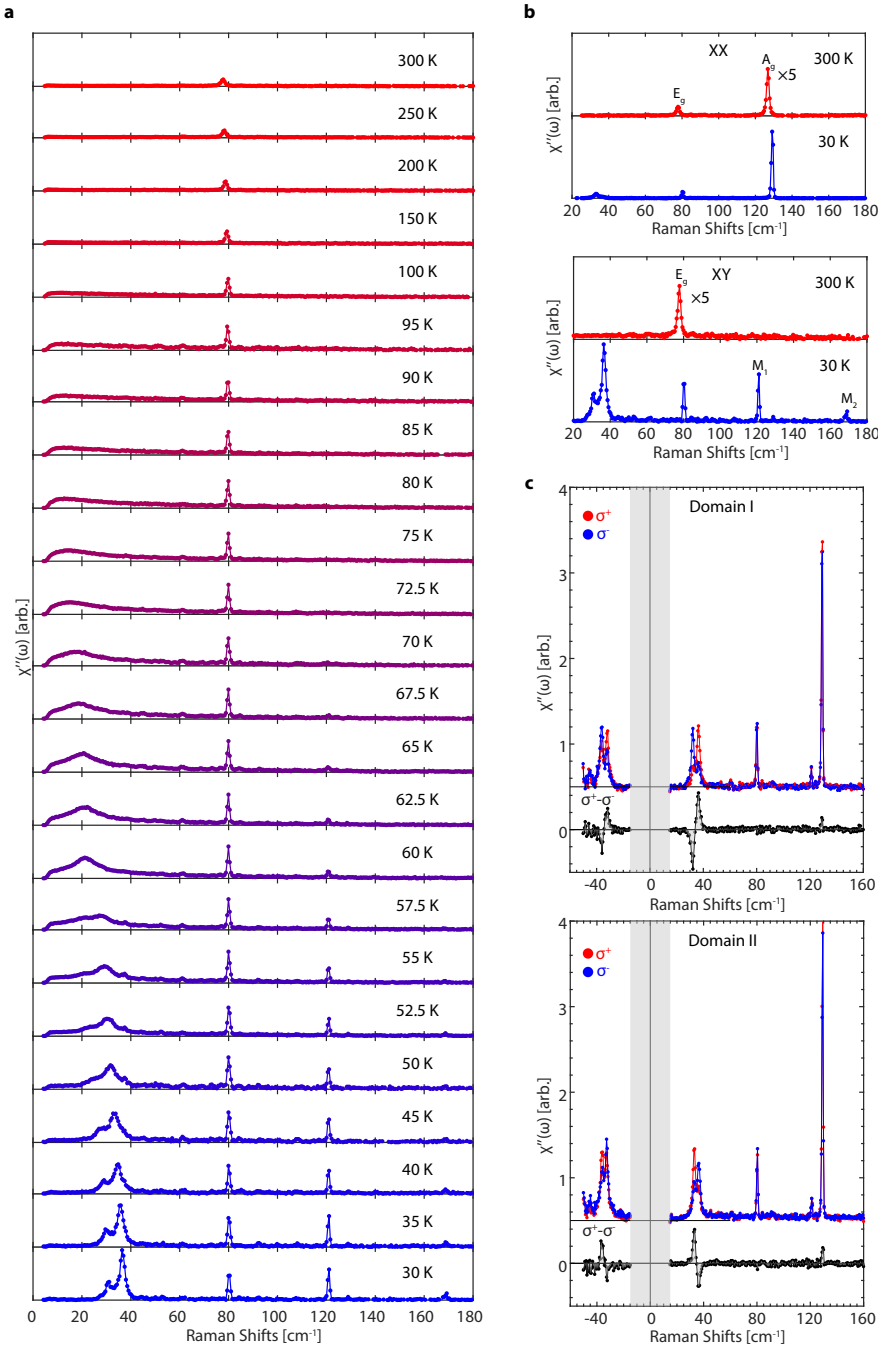

Figure 8.7: Temperature-dependent polarized Raman spectra of bulk crystal. **a**, Raman data in the cross-polarized XY channel from 30 K to 300 K. **b**, Comparison of the cross-polarized (XY) and parallel-polarized (XX) channels at high and low temperature. **c**, Circularly polarized Raman spectra at 30 K on domain I and domain II regions for σ^+/σ^- incident polarization (top) and the net ROA ($\sigma^+ - \sigma^-$) (bottom).

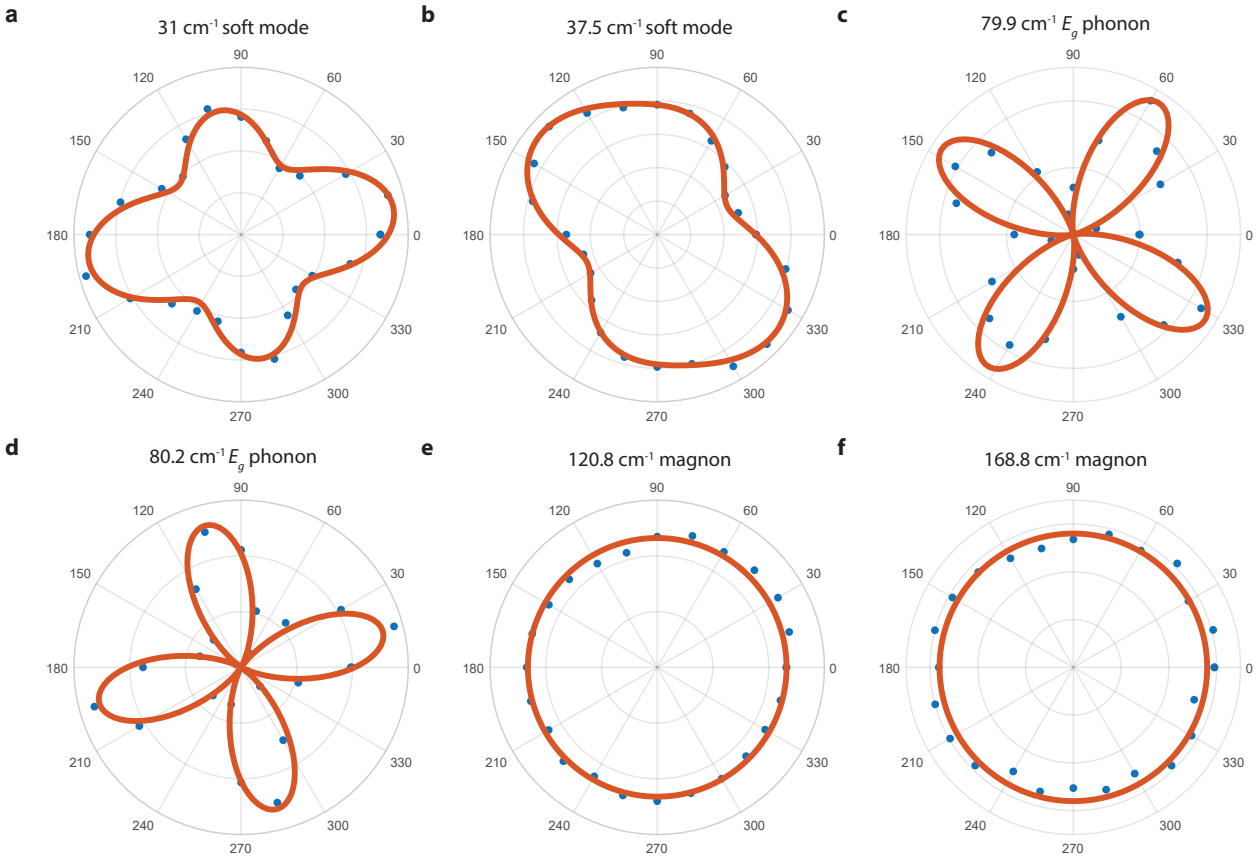

Figure 8.8: Angle Resolved Polarized Raman Spectroscopy (ARPRS) in cross-polarized (XY) configuration. a, b, The ARPRS polar plots of the 31 cm^{-1} and 37 cm^{-1} modes appearing in the multiferroic phase. Neither agrees with a pure phonon or magnon mode, suggesting they may be consistent with electromagnons. **c, d**, The 80 cm^{-1} peak is composed of two phonons below $T_{N,2}$, one at 79.9 cm^{-1} and the other at 80.2 cm^{-1}. These closely-spaced phonon modes display out-of-phase modulation with respect to the incident linear polarization and both display an E_g symmetry with respect to the high-temperature $R\bar{3}m$ phase. **e, f**, The 120.8 cm^{-1} and 168.8 cm^{-1} are magnon modes. Red lines: ARPRS fits to the Raman tensors for different mode symmetries.

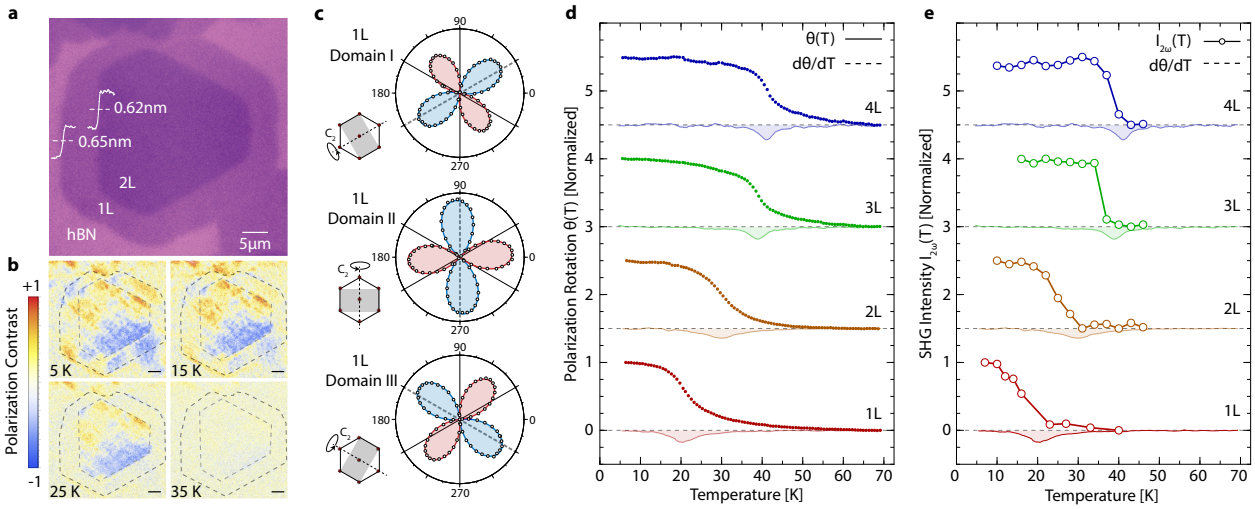

Figure 8.9: Birefringence and Second Harmonic Generation in Few- and Single-layer. **a**, Optical image of 1- and 2-layer NiI_2 samples grown on hBN with atomic step height profiles measured by AFM (scale bar: 5 μm). **b**, Temperature-dependent polarized microscopy images on the same region in **a**. Dashed lines demarcate the 1- and 2-layer regions (scale bars: 5 μm). **c**, Angular-dependent linear dichroism $\Delta R(\theta)$ measurements in monolayer NiI_2 on three monodomain regions determined from polarized microscopy, as in **c**. Radial lines indicate the crystallographic **a**-axes and the dashed lines indicates the orientation of the local C_2 axis, as shown in the schematics at the left. **d**, Temperature-dependent, birefringence-induced polarization rotation $\theta(T)$ measurements acquired in monodomain regions of 1- to 4-layer NiI_2 samples. **e**, Temperature dependent electric-dipole SHG ($\lambda = 991$ nm) intensity for 1- to 4-layer samples. Error bars in the SHG data are smaller than the size of the data points. Dashed curves in **d** and **e** represent $d\theta/dT$ calculated from layer-dependent $\theta(T)$ data in **d**. Data are normalized to the value at 5 K and offset vertically for clarity.

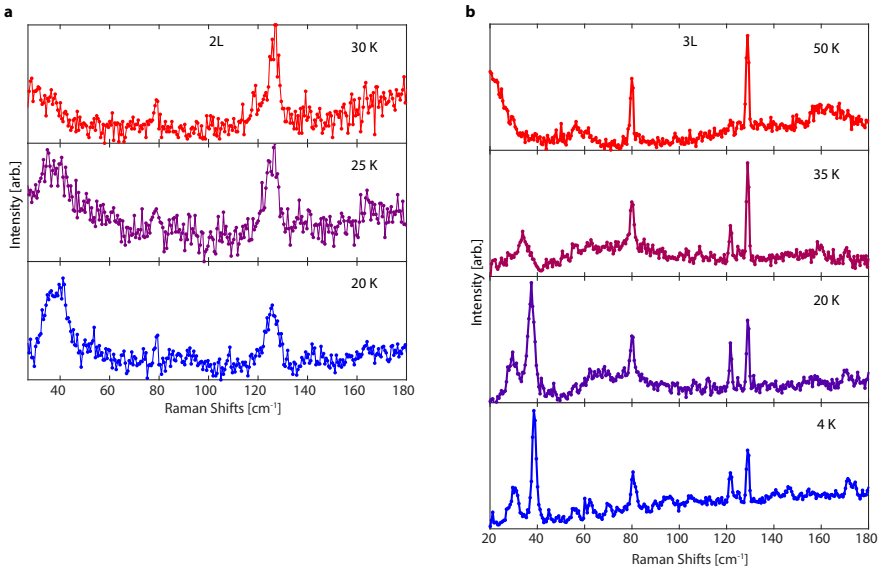

Figure 8.10: Temperature dependent Raman Spectroscopy of two- and three-layer in cross-polarized (XY) configuration. The soft modes at around 38 cm^{-1} in **a**, 2-layer and **b**, 3-layer built up below 25 K and 35 K respectively, which are consistent with the transition temperature measured from polarization rotation and SHG.

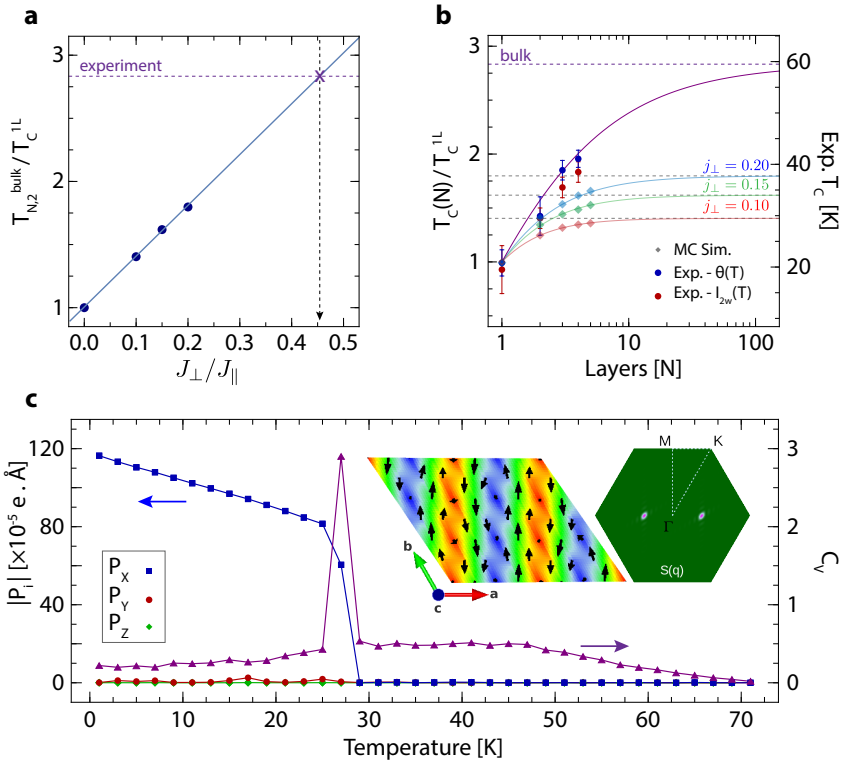

Figure 8.11: Layer-Dependent Magnetic Transition Temperatures and the Ground State of Single-Layer NiI_2. **Ta**, Evolution of the reduced temperature t as a function of the interlayer exchange $J_\perp/J_\parallel$, where $t = T_{N,2}/T_c^{1-layer}$ is the ratio of bulk and 1-layer transition temperatures. Circles denote Monte Carlo estimates, the solid line linearly extrapolates t to larger $J_\perp$. Horizontal dashed line indicates the experimental reduced temperature, $t =\simeq 2.8$, while the vertical one points to the estimated $J_\perp \simeq 0.45 J_\parallel$. **b**, Evolution of the critical temperature as a function of the number of layers (N). Full symbols (open diamonds) denote the Monte Carlo (experimental) estimates and full lines correspond to the empirical relation. Dotted horizontal lines represent the bulk transition temperature corresponding to the effective interlayer interaction. **c**, Electrical polarization components in units of $10^{-5} e$Å (absolute value, closed square) and specific heat (stars) as a function of temperature, relative to the proper-screw spiral order represented in the insets (spin texture – black arrows represent in-plane components of spins, colormap indicates the out-of-plane spin component, s_z=+(-)1 red(blue)- and $S(\mathbf{Q})$, respectively), as obtained via Monte Carlo simulations.

References

[1] R. B. Laughlin and D. Pines, "The theory of everything," *Proceedings of the national academy of sciences*, vol. 97, no. 1, pp. 28–31, 2000.

[2] F. Bloch, "Über die quantenmechanik der elektronen in kristallgittern," *Zeitschrift für physik*, vol. 52, no. 7, pp. 555–600, 1929.

[3] B. Keimer, S. A. Kivelson, M. R. Norman, S. Uchida, and J. Zaanen, "From quantum matter to high-temperature superconductivity in copper oxides," *Nature*, vol. 518, no. 7538, pp. 179–186, 2015.

[4] R. Bistritzer and A. H. MacDonald, "Moiré bands in twisted double-layer graphene," *Proceedings of the National Academy of Sciences*, vol. 108, no. 30, pp. 12 233–12 237, 2011.

[5] Y. Cao, V. Fatemi, A. Demir, S. Fang, S. L. Tomarken, J. Y. Luo, J. D. Sanchez-Yamagishi, K. Watanabe, T. Taniguchi, E. Kaxiras, *et al.*, "Correlated insulator behaviour at half-filling in magic-angle graphene superlattices," *Nature*, vol. 556, no. 7699, pp. 80–84, 2018.

[6] Y. Cao, V. Fatemi, S. Fang, K. Watanabe, T. Taniguchi, E. Kaxiras, and P. Jarillo-Herrero, "Unconventional superconductivity in magic-angle graphene superlattices," *Nature*, vol. 556, no. 7699, pp. 43–50, 2018, ISSN: 14764687. DOI: 10.1038/nature26160.

[7] J. Cai, E. Anderson, C. Wang, X. Zhang, X. Liu, W. Holtzmann, Y. Zhang, F. Fan, T. Taniguchi, K. Watanabe, *et al.*, "Signatures of fractional quantum anomalous hall states in twisted mote2," *Nature*, vol. 622, no. 7981, pp. 63–68, 2023.

[8] J. Bardeen, L. N. Cooper, and J. R. Schrieffer, "Theory of superconductivity," *Physical review*, vol. 108, no. 5, p. 1175, 1957.

[9] A. Kirilyuk, A. V. Kimel, and T. Rasing, "Ultrafast optical manipulation of magnetic order," *Reviews of Modern Physics*, vol. 82, no. 3, pp. 2731–2784, 2010.

[10] D. N. Basov, A. Asenjo-Garcia, P. James Schuck, X. Zhu, and A. Rubio, "Polariton panorama," *Frontiers in Optics and Photonics*, vol. 10, no. 1, pp. 565–593, 2021. DOI: 10.1515/9783110710687-044.

[11] R. F. Ribeiro, L. A. Martínez-Martínez, M. Du, J. Campos-Gonzalez-Angulo, and J. Yuen-Zhou, "Polariton chemistry: Controlling molecular dynamics with optical cavities," *Chemical science*, vol. 9, no. 30, pp. 6325–6339, 2018.

[12] K. W. Böer and U. W. Pohl, "Excitons," in *Semiconductor physics*, Springer, 2023, pp. 529–591.

[13] J. Madéo, M. K. Man, C. Sahoo, M. Campbell, V. Pareek, E. L. Wong, A. Al-Mahboob, N. S. Chan, A. Karmakar, B. M. K. Mariserla, *et al.*, "Directly visualizing the momentum-forbidden dark excitons and their dynamics in atomically thin semiconductors," *Science*, vol. 370, no. 6521, pp. 1199–1204, 2020.

[14] M. Mitrano, A. Cantaluppi, D. Nicoletti, S. Kaiser, A. Perucchi, S. Lupi, P. Di Pietro, D. Pontiroli, M. Riccò, S. R. Clark, *et al.*, "Possible light-induced superconductivity in k 3 c 60 at high temperature," *Nature*, vol. 530, no. 7591, pp. 461–464, 2016.

[15] T. Nova, A. Disa, M. Fechner, and A. Cavalleri, "Metastable ferroelectricity in optically strained srtio3," *Science*, vol. 364, no. 6445, pp. 1075–1079, 2019.

[16] X. Li, T. Qiu, J. Zhang, E. Baldini, J. Lu, A. M. Rappe, and K. A. Nelson, "Terahertz field–induced ferroelectricity in quantum paraelectric SrTiO3," *Science*, vol. 364, no. 6445, pp. 1079–1082, 2019, ISSN: 10959203. DOI: 10.1126/science.aaw4913.

[17] A. S. Disa, J. Curtis, M. Fechner, A. Liu, T. F. Nova, P. Narang, A. V. Boris, B. Keimer, and A. Cavalleri, "Optical Stabilization of Fluctuating High Temperature Ferromagnetism in YTiO3," *arXiv*, 2021. URL: https://arxiv.org/abs/2111.13622.

[18] H. Zeiger, J. Vidal, T. Cheng, E. Ippen, G. Dresselhaus, and M. Dresselhaus, "Theory for displacive excitation of coherent phonons," *Physical Review B*, vol. 45, no. 2, p. 768, 1992.

[19] S. Gerber, S. L. Yang, D. Zhu, *et al.*, "Femtosecond electron-phonon lock-in by photoemission and x-ray free-electron laser," *Science*, vol. 357, no. 6346, pp. 71–75, 2017, ISSN: 10959203. DOI: 10.1126/science.aak9946.

[20] E. Ergeçen, B. Ilyas, J. Kim, J. Park, M. B. Yilmaz, T. Luo, D. Xiao, S. Okamoto, J.-G. Park, and N. Gedik, "Coherent detection of hidden spin–lattice coupling in a van der waals antiferromagnet," *Proceedings of the National Academy of Sciences*, vol. 120, no. 12, e2208968120, 2023.

[21] D. M. Juraschek and S. F. Maehrlein, "Sum-frequency ionic Raman scattering," *Physical Review B*, vol. 97, no. 17, p. 174 302, May 2018. DOI: 10.1103/PhysRevB.97.174302. URL: https://link.aps.org/doi/10.1103/PhysRevB.97.174302.

[22] G. Khalsa, N. A. Benedek, and J. Moses, "Ultrafast control of material optical properties via the infrared resonant raman effect," *Phys. Rev. X*, vol. 11, p. 021 067, 2 Jun. 2021. DOI: 10.1103/PhysRevX.11.021067. URL: https://link.aps.org/doi/10.1103/PhysRevX.11.021067.

[23] T. G. Blank, K. A. Grishunin, K. Zvezdin, N. Hai, J. Wu, S.-H. Su, J.-C. Huang, A. Zvezdin, and A. V. Kimel, "Two-dimensional terahertz spectroscopy of nonlinear phononics in the topological insulator mnbi 2 te 4," *Physical review letters*, vol. 131, no. 2, p. 026 902, 2023.

[24] E. A. Mashkovich, K. A. Grishunin, R. M. Dubrovin, A. K. Zvezdin, R. V. Pisarev, and A. V. Kimel, "Terahertz light–driven coupling of antiferromagnetic spins to lattice," *Science*, vol. 374, no. 6575, pp. 1608–1611, Dec. 2021, ISSN: 10959203. DOI: 10.1126/SCIENCE.ABK1121. URL: https://www.science.org.

[25] L. Zhao, C. Belvin, R. Liang, D. Bonn, W. Hardy, N. Armitage, and D. Hsieh, "A global inversion-symmetry-broken phase inside the pseudogap region of yba2cu3o y," *Nature Physics*, vol. 13, no. 3, pp. 250–254, 2017.

[26] Y. Wang, H. Steinberg, P. Jarillo-Herrero, and N. Gedik, "Observation of floquet-bloch states on the surface of a topological insulator," *Science*, vol. 342, no. 6157, pp. 453–457, 2013.

[27] D. Basov, R. Averitt, and D. Hsieh, "Towards properties on demand in quantum materials," *Nature materials*, vol. 16, no. 11, pp. 1077–1088, 2017.

[28] G. R. Fowles, *Introduction to modern optics*. Courier Corporation, 1989.

[29] T. Nakagawa, "Surface magneto-optic kerr effect," *Compendium of Surface and Interface Analysis*, pp. 667–671, 2018.

[30] M. H. Christensen, T. Birol, B. M. Andersen, and R. M. Fernandes, "Loop currents in a v 3 sb 5 kagome metals: Multipolar and toroidal magnetic orders," *Physical Review B*, vol. 106, no. 14, p. 144 504, 2022.

[31] Y. Xu, Z. Ni, Y. Liu, B. R. Ortiz, Q. Deng, S. D. Wilson, B. Yan, L. Balents, and L. Wu, "Three-state nematicity and magneto-optical kerr effect in the charge density waves in kagome superconductors," *Nature physics*, vol. 18, no. 12, pp. 1470–1475, 2022.

[32] D. R. Saykin, C. Farhang, E. D. Kountz, D. Chen, B. R. Ortiz, C. Shekhar, C. Felser, S. D. Wilson, R. Thomale, J. Xia, *et al.*, "High resolution polar kerr effect studies of csv 3 sb 5: Tests for time-reversal symmetry breaking below the charge-order transition," *Physical Review Letters*, vol. 131, no. 1, p. 016 901, 2023.

[33] E. Collett, *Field guide to polarization*. Spie Bellingham, WA, 2005.

[34] H. Zhang, Z. Ni, C. E. Stevens, A. Bai, F. Peiris, J. R. Hendrickson, L. Wu, and D. Jariwala, "Cavity-enhanced linear dichroism in a van der Waals antiferromagnet," *Nature Photonics*, vol. 16, no. 4, pp. 311–317, 2022, ISSN: 1749-4893. DOI: 10.1038/s41566-022-00970-8. URL: https://doi.org/10.1038/s41566-022-00970-8.

[35] J. Harter, L. Niu, A. Woss, and D. Hsieh, "High-speed measurement of rotational anisotropy nonlinear optical harmonic generation using position-sensitive detection," *Optics letters*, vol. 40, no. 20, pp. 4671–4674, 2015.

[36] L. Zhao, D. Torchinsky, H. Chu, V. Ivanov, R. Lifshitz, R. Flint, T. Qi, G. Cao, and D. Hsieh, "Evidence of an odd-parity hidden order in a spin–orbit coupled correlated iridate," *Nature Physics*, vol. 12, no. 1, pp. 32–36, 2016.

[37] M. Fiebig, V. V. Pavlov, and R. V. Pisarev, "Second-harmonic generation as a tool for studying electronic and magnetic structures of crystals," *JOSA B*, vol. 22, no. 1, pp. 96–118, 2005.

[38] S. Toyoda, M. Fiebig, T.-h. Arima, Y. Tokura, and N. Ogawa, "Nonreciprocal second harmonic generation in a magnetoelectric material," *Science Advances*, vol. 7, no. 16, eabe2793, 2021.

[39] A. de la Torre, D. M. Kennes, M. Claassen, S. Gerber, J. W. McIver, and M. A. Sentef, "Colloquium: Nonthermal pathways to ultrafast control in quantum materials," *Reviews of Modern Physics*, vol. 93, no. 4, p. 41 002, Oct. 2021. DOI: 10.1103/RevModPhys.93.041002. URL: https://link.aps.org/doi/10.1103/RevModPhys.93.041002.

[40] L. Stojchevska, I. Vaskivskyi, T. Mertelj, P. Kusar, D. Svetin, S. Brazovskii, and D. Mihailovic, "Ultrafast switching to a stable hidden quantum state in an electronic crystal," *Science*, vol. 344, no. 6180, pp. 177–180, Apr. 2014, ISSN: 10959203. DOI: 10.1126/SCIENCE.1241591/SUPPL{_}FILE/STOJCHEVSKA.SM.PDF. URL: https://www.science.org/doi/10.1126/science.1241591.

[41] A. Mraz, R. Venturini, D. Svetin, V. Sever, I. A. Mihailovic, I. Vaskivskyi, B. Ambrozic, G. Dražić, M. D'Antuono, D. Stornaiuolo, *et al.*, "Charge configuration memory devices: Energy efficiency and switching speed," *Nano Letters*, vol. 22, no. 12, pp. 4814–4821, 2022.

[42] M. Rini, Z. Hao, R. Schoenlein, C. Giannetti, F. Parmigiani, S. Fourmaux, J. Kieffer, A. Fujimori, M. Onoda, S. Wall, *et al.*, "Optical switching in vo2 films by below-gap excitation," *Applied Physics Letters*, vol. 92, no. 18, 2008.

[43] I. Vaskivskyi, J. Gospodaric, S. Brazovskii, D. Svetin, P. Sutar, E. Goreshnik, I. A. Mihailovic, T. Mertelj, and D. Mihailovic, "Controlling the metal-to-insulator relaxation of the metastable hidden quantum state in 1t-tas2," *Science advances*, vol. 1, no. 6, e1500168, 2015.

[44] J. Chang, E. Blackburn, A. Holmes, N. B. Christensen, J. Larsen, J. Mesot, R. Liang, D. Bonn, W. Hardy, A. Watenphul, *et al.*, "Direct observation of competition between superconductivity and charge density wave order in yba2cu3o6. 67," *Nature Physics*, vol. 8, no. 12, pp. 871–876, 2012.

[45] S. Wandel, F. Boschini, E. da Silva Neto, L. Shen, M. Na, S. Zohar, Y. Wang, S. Welch, M. Seaberg, J. Koralek, *et al.*, "Enhanced charge density wave coherence in a light-quenched, high-temperature superconductor," *Science*, vol. 376, no. 6595, pp. 860–864, 2022.

[46] A. Kogar, A. Zong, P. E. Dolgirev, *et al.*, "Light-induced charge density wave in LaTe3," *Nature Physics*, vol. 16, no. 2, pp. 159–163, 2020, ISSN: 1745-2481. DOI: 10.1038/s41567-019-0705-3. URL: https://doi.org/10.1038/s41567-019-0705-3.

[47] Z. Chang, L. Fang, V. Fedorov, C. Geiger, S. Ghimire, C. Heide, N. Ishii, J. Itatani, C. Joshi, Y. Kobayashi, *et al.*, "Intense infrared lasers for strong-field science," *Advances in Optics and Photonics*, vol. 14, no. 4, pp. 652–782, 2022.

[48] M. Alverson, S. G. Baird, R. Murdock, J. Johnson, T. D. Sparks, *et al.*, "Generative adversarial networks and diffusion models in material discovery," *Digital Discovery*, vol. 3, no. 1, pp. 62–80, 2024.

[49] G. A. Valdivia-Berroeta, Z. B. Zaccardi, S. K. Pettit, S.-H. Ho, B. W. Palmer, M. J. Lutz, C. Rader, B. P. Hunter, N. K. Green, C. Barlow, *et al.*, "Data mining for terahertz generation crystals," *Advanced Materials*, vol. 34, no. 16, p. 2 107 900, 2022.

[50] J. Hebling, K.-L. Yeh, M. C. Hoffmann, B. Bartal, and K. A. Nelson, "Generation of high-power terahertz pulses by tilted-pulse-front excitation and their application possibilities," *Journal of the Optical Society of America B*, vol. 25, no. 7, B6–B19, 2008. DOI: 10.1364/JOSAB.25.0000B6. URL: https://opg.optica.org/josab/abstract.cfm?URI=josab-25-7-B6.

[51] P. Chevalier, A. Amirzhan, F. Wang, M. Piccardo, S. G. Johnson, F. Capasso, and H. O. Everitt, "Widely tunable compact terahertz gas lasers," *Science*, vol. 366, no. 6467, pp. 856–860, 2019.

[52] B. Green, S. Kovalev, V. Asgekar, G. Geloni, U. Lehnert, T. Golz, M. Kuntzsch, C. Bauer, J. Hauser, J. Voigtlaender, *et al.*, "High-field high-repetition-rate sources for the coherent thz control of matter," *Scientific reports*, vol. 6, no. 1, p. 22 256, 2016.

[53] H. A. Hafez, S. Kovalev, J.-C. Deinert, Z. Mics, B. Green, N. Awari, M. Chen, S. Germanskiy, U. Lehnert, J. Teichert, *et al.*, "Extremely efficient terahertz high-harmonic generation in graphene by hot dirac fermions," *Nature*, vol. 561, no. 7724, pp. 507–511, 2018.

[54] T. F. Nova, A. Cartella, A. Cantaluppi, M. Först, D. Bossini, R. V. Mikhaylovskiy, A. V. Kimel, R. Merlin, and A. Cavalleri, "An effective magnetic field from optically driven phonons," *Nature Physics*, vol. 13, no. 2, pp. 132–136, 2017, ISSN: 1745-2481. DOI: 10.1038/nphys3925. URL: https://doi.org/10.1038/nphys3925.

[55] G. Cerullo, A. Baltuška, O. D. Mücke, and C. Vozzi, "Few-optical-cycle light pulses with passive carrier-envelope phase stabilization," *Laser & Photonics Reviews*, vol. 5, no. 3, pp. 323–351, 2011.

[56] B. Liu, H. Bromberger, A. Cartella, T. Gebert, M. Först, and A. Cavalleri, "Generation of narrowband, high-intensity, carrier-envelope phase-stable pulses tunable between 4 and 18 thz," *Optics letters*, vol. 42, no. 1, pp. 129–131, 2017.

[57] D. Fausti, R. I. Tobey, N. Dean, S. Kaiser, A. Dienst, M. C. Hoffmann, S. Pyon, T. Takayama, H. Takagi, and A. Cavalleri, "Light-induced superconductivity in a stripe-ordered cuprate," *Science*, vol. 331, no. 6014, pp. 189–191, 2011, ISSN: 00368075. DOI: 10.1126/science.1197294.

[58] M. Budden, T. Gebert, M. Buzzi, G. Jotzu, E. Wang, T. Matsuyama, G. Meier, Y. Laplace, D. Pontiroli, M. Riccò, *et al.*, "Evidence for metastable photo-induced superconductivity in k3c60," *Nature Physics*, vol. 17, no. 5, pp. 611–618, 2021.

[59] S. Fava, G. De Vecchi, G. Jotzu, M. Buzzi, T. Gebert, Y. Liu, B. Keimer, and A. Cavalleri, "Magnetic field expulsion in optically driven yba _2 cu _3 o _{6.48}," *arXiv preprint arXiv:2405.00848*, 2024.

[60] A. Yamanaka, M. Kataoka, Y. Inaba, K. Inoue, B. Hehlen, and E. Courtens, "Evidence for competing orderings in strontium titanate from hyper-raman scattering spectroscopy," *Europhysics letters*, vol. 50, no. 5, p. 688, 2000.

[61] A. Durán, E. Martínez, J. Díaz, and J. Siqueiros, "Ferroelectricity at room temperature in pr-doped srtio3," *Journal of applied physics*, vol. 97, no. 10, 2005.

[62] R. Xu, J. Huang, E. S. Barnard, S. S. Hong, P. Singh, E. K. Wong, T. Jansen, V. Harbola, J. Xiao, B. Y. Wang, *et al.*, "Strain-induced room-temperature ferroelectricity in srtio3 membranes," *Nature communications*, vol. 11, no. 1, p. 3141, 2020.

[63] X. Li, T. Qiu, J. Zhang, E. Baldini, J. Lu, A. M. Rappe, and K. A. Nelson, "Terahertz field–induced ferroelectricity in quantum paraelectric SrTiO3," *Science*, vol. 364, no. 6445, pp. 1079–1082, Jun. 2019. DOI: 10.1126/science.aaw4913. URL: https://doi.org/10.1126/science.aaw4913.

[64] T. F. Nova, A. S. Disa, M. Fechner, and A. Cavalleri, "Metastable ferroelectricity in optically strained SrTiO3," *Science*, vol. 364, no. 6445, pp. 1075–1079, Jun. 2019. DOI: 10.1126/science.aaw4911. URL: https://doi.org/10.1126/science.aaw4911.

[65] M. Fechner, M. Först, G. Orenstein, V. Krapivin, A. Disa, M. Buzzi, A. von Hoegen, G. de la Pena, Q. Nguyen, R. Mankowsky, *et al.*, "Quenched lattice fluctuations in optically driven srtio3," *Nature Materials*, vol. 23, no. 3, pp. 363–368, 2024.

[66] G. Orenstein, V. Krapivin, Y. Huang, Z. Zhan, G. d. l. P. Munoz, R. A. Duncan, Q. Nguyen, J. Stanton, S. Teitelbaum, H. Yavas, *et al.*, "Observation of polarization density waves in srtio3," *arXiv preprint arXiv:2403.17203*, 2024.

[67] A. Borovik-Romanov, "Piezomagnetism in the antiferromagnetic fluorides of cobalt and mangamse," *Soviet Phys JETP*, vol. 11, no. 4, 1960.

[68] T. Moriya, "Piezomagnetism in cof2," *Journal of Physics and Chemistry of Solids*, vol. 11, no. 1-2, pp. 73–77, 1959.

[69] F. A. Lindemann, "The calculation of molecular eigen-frequencies," Tech. Rep., 1984.

[70] A. S. Disa, M. Fechner, T. F. Nova, B. Liu, M. Först, D. Prabhakaran, P. G. Radaelli, and A. Cavalleri, "Polarizing an antiferromagnet by optical engineering of the crystal field," *Nature Physics*, vol. 16, no. 9, pp. 937–941, Sep. 2020, ISSN: 17452481. DOI: 10.1038/s41567-020-0936-3.

[71] S. Mukamel, "Principles of nonlinear optical spectroscopy," *(No Title)*, 1995.

[72] M. Woerner, W. Kuehn, P. Bowlan, K. Reimann, and T. Elsaesser, "Ultrafast two-dimensional terahertz spectroscopy of elementary excitations in solids," *New Journal of Physics*, vol. 15, no. 2, p. 025 039, 2013.

[73] J. Lu, X. Li, H. Y. Hwang, B. K. Ofori-Okai, T. Kurihara, T. Suemoto, and K. A. Nelson, "Coherent two-dimensional terahertz magnetic resonance spectroscopy of collective spin waves," *Physical review letters*, vol. 118, no. 20, p. 207 204, 2017.

[74] Z. Zhang, F. Y. Gao, J. B. Curtis, Z.-J. Liu, Y.-C. Chien, A. von Hoegen, M. T. Wong, T. Kurihara, T. Suemoto, P. Narang, *et al.*, "Terahertz field-induced nonlinear coupling of two magnon modes in an antiferromagnet," *Nature Physics*, pp. 1–6, 2024.

[75] F. Y. Gao, Z. Zhang, Z.-J. Liu, and K. A. Nelson, "High-speed two-dimensional terahertz spectroscopy with echelon-based shot-to-shot balanced detection," *Optics Letters*, vol. 47, no. 14, pp. 3479–3482, 2022.

[76] Z. Zhang, F. Y. Gao, Y.-C. Chien, Z.-J. Liu, J. B. Curtis, E. R. Sung, X. Ma, W. Ren, S. Cao, P. Narang, *et al.*, "Terahertz-field-driven magnon upconversion in an antiferromagnet," *Nature Physics*, pp. 1–6, 2024.

[77] F. Mahmood, D. Chaudhuri, S. Gopalakrishnan, R. Nandkishore, and N. Armitage, "Observation of a marginal fermi glass," *Nature Physics*, vol. 17, no. 5, pp. 627–631, 2021.

[78] Y. Wan and N. Armitage, "Resolving continua of fractional excitations by spinon echo in thz 2d coherent spectroscopy," *Physical review letters*, vol. 122, no. 25, p. 257 401, 2019.

[79] A. Liu and A. Disa, "Excitation-dependent features and artifacts in 2-d terahertz spectroscopy," *arXiv preprint arXiv:2405.00971*, 2024.

[80] M. Garg and K. Kern, "Attosecond coherent manipulation of electrons in tunneling microscopy," *Science*, vol. 367, no. 6476, pp. 411–415, 2020.

[81] T. L. Cocker, D. Peller, P. Yu, J. Repp, and R. Huber, "Tracking the ultrafast motion of a single molecule by femtosecond orbital imaging," *Nature*, vol. 539, no. 7628, pp. 263–267, 2016.

[82] D. H. Auston, "Picosecond optoelectronic switching and gating in silicon," *Applied Physics Letters*, vol. 26, no. 3, pp. 101–103, 1975.

[83] P. Gallagher, C.-S. Yang, T. Lyu, F. Tian, R. Kou, H. Zhang, K. Watanabe, T. Taniguchi, and F. Wang, "Quantum-critical conductivity of the dirac fluid in graphene," *Science*, vol. 364, no. 6436, pp. 158–162, 2019.

[84] W. Zhao, S. Wang, S. Chen, Z. Zhang, K. Watanabe, T. Taniguchi, A. Zettl, and F. Wang, "Observation of hydrodynamic plasmons and energy waves in graphene," *Nature*, vol. 614, no. 7949, pp. 688–693, 2023.

[85] S. Xu, Y. Li, R. A. Vitalone, R. Jing, A. J. Sternbach, S. Zhang, J. Ingham, M. Delor, J. McIver, M. Yankowitz, *et al.*, "Electronic interactions in dirac fluids visualized by nano-terahertz spacetime mapping," *arXiv preprint arXiv:2311.11502*, 2023.

[86] F.-F. Stiewe, T. Winkel, Y. Sasaki, T. Tubandt, T. Kleinke, C. Denker, U. Martens, N. Meyer, T. S. Parvini, S. Mizukami, *et al.*, "Spintronic emitters for super-resolution in thz-spectral imaging," *Applied Physics Letters*, vol. 120, no. 3, 2022.

[87] A. Zong, B. R. Nebgen, S.-C. Lin, J. A. Spies, and M. Zuerch, "Emerging ultrafast techniques for studying quantum materials," *Nature Reviews Materials*, vol. 8, no. 4, pp. 224–240, 2023.

[88] N. D. Mermin, "Crystalline order in two dimensions," *Physical review*, vol. 176, no. 1, p. 250, 1968.

[89] N. D. Mermin and H. Wagner, "Absence of ferromagnetism or antiferromagnetism in one-or two-dimensional isotropic heisenberg models," *Physical Review Letters*, vol. 17, no. 22, p. 1133, 1966.

[90] M. A. McGuire, H. Dixit, V. R. Cooper, and B. C. Sales, "Coupling of crystal structure and magnetism in the layered, ferromagnetic insulator cri3," *Chemistry of Materials*, vol. 27, no. 2, pp. 612–620, 2015.

[91] N. Sivadas, M. W. Daniels, R. H. Swendsen, S. Okamoto, and D. Xiao, "Magnetic ground state of semiconducting transition-metal trichalcogenide monolayers," *Physical Review B - Condensed Matter and Materials Physics*, vol. 91, no. 23, 2015, ISSN: 1550235X. DOI: 10.1103/PhysRevB.91.235425.

[92] M.-W. Lin, H. L. Zhuang, J. Yan, T. Z. Ward, A. A. Puretzky, C. M. Rouleau, Z. Gai, L. Liang, V. Meunier, B. G. Sumpter, *et al.*, "Ultrathin nanosheets of crsite 3: A semiconducting two-dimensional ferromagnetic material," *Journal of Materials Chemistry C*, vol. 4, no. 2, pp. 315–322, 2016.

[93] B. Huang, G. Clark, E. Navarro-Moratalla, *et al.*, "Layer-dependent ferromagnetism in a van der Waals crystal down to the monolayer limit," *Nature*, vol. 546, no. 7657, pp. 270–273, 2017, ISSN: 14764687. DOI: 10.1038/nature22391.

[94] C. Gong, L. Li, Z. Li, *et al.*, "Discovery of intrinsic ferromagnetism in two-dimensional van der Waals crystals," *Nature*, vol. 546, no. 7657, pp. 265–269, 2017, ISSN: 14764687. DOI: 10.1038/nature22060.

[95] T. Song, X. Cai, M. W.-Y. Tu, X. Zhang, B. Huang, N. P. Wilson, K. L. Seyler, L. Zhu, T. Taniguchi, K. Watanabe, *et al.*, "Giant tunneling magnetoresistance in spin-filter van der waals heterostructures," *Science*, vol. 360, no. 6394, pp. 1214–1218, 2018.

[96] T. Song, Q.-C. Sun, E. Anderson, C. Wang, J. Qian, T. Taniguchi, K. Watanabe, M. A. McGuire, R. Stöhr, D. Xiao, *et al.*, "Direct visualization of magnetic domains and moiré magnetism in twisted 2d magnets," *Science*, vol. 374, no. 6571, pp. 1140–1144, 2021.

[97] B. Huang, G. Clark, D. R. Klein, *et al.*, "Electrical control of 2d magnetism in bilayer CrI_3," *Nature Nanotechnology*, vol. 13, no. 7, pp. 544–548, 2018, ISSN: 17483395. DOI: 10.1038/s41565-018-0121-3.

[98] J.-U. Lee, S. Lee, J. H. Ryoo, S. Kang, T. Y. Kim, P. Kim, C.-H. Park, J.-G. Park, and H. Cheong, "Ising-Type Magnetic Ordering in Atomically Thin FePS3," *Nano Letters*, vol. 16, no. 12, pp. 7433–7438, Dec. 2016, ISSN: 1530-6984. DOI: 10.1021/acs.nanolett.6b03052. URL: https://doi.org/10.1021/acs.nanolett.6b03052.

[99] X. Wang, K. Du, Y. Y. F. Liu, P. Hu, J. Zhang, Q. Zhang, M. H. S. Owen, X. Lu, C. K. Gan, P. Sengupta, *et al.*, "Raman spectroscopy of atomically thin two-dimensional magnetic iron phosphorus trisulfide (feps3) crystals," *2D Materials*, vol. 3, no. 3, p. 031 009, 2016.

[100] Q. Zhang, M. Ozerov, E. V. Boström, J. Cui, N. Suri, Q. Jiang, C. Wang, F. Wu, K. Hwangbo, and J.-H. Chu, "Coherent strong-coupling of terahertz magnons and phonons in a Van der Waals antiferromagnetic insulator," *arXiv preprint arXiv:2108.11619*, 2021.

[101] K. Kim, S. Y. Lim, J.-U. Lee, S. Lee, T. Y. Kim, K. Park, G. S. Jeon, C.-H. Park, J.-G. Park, and H. Cheong, "Suppression of magnetic ordering in XXZ-type antiferromagnetic monolayer NiPS3," *Nature Communications*, vol. 10, no. 1, p. 345, 2019, ISSN: 2041-1723. DOI: 10.1038/s41467-018-08284-6. URL: https://doi.org/10.1038/s41467-018-08284-6.

[102] V. Berezinskii, "Destruction of long-range order in one-dimensional and two-dimensional systems having a continuous symmetry group i. classical systems," *Sov. Phys. JETP*, vol. 32, no. 3, pp. 493–500, 1971.

[103] J. M. Kosterlitz and D. J. Thouless, "Ordering, metastability and phase transitions in two-dimensional systems," in *Basic Notions Of Condensed Matter Physics*, CRC Press, 2018, pp. 493–515.

[104] S. Kang, K. Kim, B. H. Kim, *et al.*, "Coherent many-body exciton in van der Waals antiferromagnet NiPS3," *Nature*, vol. 583, no. 7818, pp. 785–789, Jul. 2020, ISSN: 14764687. DOI: 10.1038/S41586-020-2520-5.

[105] X. Wang, J. Cao, Z. Lu, *et al.*, "Spin-induced linear polarization of photoluminescence in antiferromagnetic van der Waals crystals," *Nature Materials*, vol. 20, no. 7, pp. 964–970, 2021, ISSN: 1476-4660. DOI: 10.1038/s41563-021-00968-7. URL: https://doi.org/10.1038/s41563-021-00968-7.

[106] D. Khomskii, "Classifying multiferroics: Mechanisms and effects," *Physics*, vol. 2, 2009, ISSN: 1943-2879. DOI: 10.1103/physics.2.20.

[107] T. Kurumaji, S. Seki, S. Ishiwata, H. Murakawa, Y. Kaneko, and Y. Tokura, "Magnetoelectric responses induced by domain rearrangement and spin structural change in triangular-lattice helimagnets NiI2 and CoI 2," *Physical Review B - Condensed Matter and Materials Physics*, vol. 87, no. 1, Jan. 2013, ISSN: 10980121. DOI: 10.1103/PHYSREVB.87.014429.

[108] M. Mitrano, A. Cantaluppi, D. Nicoletti, *et al.*, "Possible light-induced superconductivity in K3C60 at high temperature," *Nature*, vol. 530, no. 7591, pp. 461–464, 2016, ISSN: 1476-4687. DOI: 10.1038/nature16522. URL: https://doi.org/10.1038/nature16522.

[109] A. S. McLeod, J. Zhang, M. Q. Gu, *et al.*, "Multi-messenger nanoprobes of hidden magnetism in a strained manganite," *Nature Materials*, vol. 19, no. 4, pp. 397–404, Apr. 2020, ISSN: 14764660. DOI: 10.1038/S41563-019-0533-Y.

[110] A. S. Disa, J. Curtis, M. Fechner, *et al.*, "Photo-induced high-temperature ferromagnetism in YTiO3," *Nature*, vol. 617, no. 7959, pp. 73–78, 2023, ISSN: 1476-4687. DOI: 10.1038/s41586-023-05853-8. URL: https://doi.org/10.1038/s41586-023-05853-8.

[111] J. Schmalian, D. Pines, and B. Stojković, "Weak Pseudogap Behavior in the Underdoped Cuprate Superconductors," *Physical Review Letters*, vol. 80, no. 17, pp. 3839–3842, Apr. 1998. DOI: 10.1103/PhysRevLett.80.3839. URL: https://link.aps.org/doi/10.1103/PhysRevLett.80.3839.

[112] T. A. Sedrakyan and A. V. Chubukov, "Pseudogap in underdoped cuprates and spin-density-wave fluctuations," *Physical Review B*, vol. 81, no. 17, p. 174 536, May 2010. DOI: 10.1103/PhysRevB.81.174536. URL: https://link.aps.org/doi/10.1103/PhysRevB.81.174536.

[113] M. Ye and A. V. Chubukov, "Hubbard model on a triangular lattice: Pseudogap due to spin density wave fluctuations," *Physical Review B*, vol. 100, p. 35 135, 2019. DOI: 10.1103/PhysRevB.100.035135.

[114] K. A. Miiller, W. Berlinger, and E. Tosatti, "Indication for a novel phase in the quantum paraelectric regime of SrTi03," *Z. Phys. B-Condensed Matter*, vol. 84, p. 277 583, 1991.

[115] S. Latini, D. Shin, S. A. Sato, C. Schäfer, U. D. Giovannini, H. Hübener, and A. Rubio, "The ferroelectric photo ground state of $SrTiO_3$: Cavity materials engineering," *Proceedings of the National Academy of Sciences*, vol. 118, no. 31, Jul. 2021. DOI: 10.1073/pnas.2105618118. URL: https://doi.org/10.1073/pnas.2105618118.

[116] E. Viñas Boström, A. Sriram, M. Claassen, and A. Rubio, "Controlling the magnetic state of the proximate quantum spin liquid α-$RuCl_3$ with an optical cavity," *arXiv:2211.07247*, 2022.

[117] D. Afanasiev, J. R. Hortensius, B. A. Ivanov, A. Sasani, E. Bousquet, Y. M. Blanter, R. V. Mikhaylovskiy, A. V. Kimel, and A. D. Caviglia, "Ultrafast control of magnetic interactions via light-driven phonons," *Nature Materials*, vol. 20, no. 5, pp. 607–611, May 2021, ISSN: 14764660. DOI: 10.1038/S41563-021-00922-7.

[118] R. Brec, D. M. Schleich, G. Ouvrard, A. Louisy, and J. Rouxel, "Physical properties of lithium intercalation compounds of the layered transition-metal chalcogenophosphites," *Inorganic Chemistry*, vol. 18, no. 7, pp. 1814–1818, Jul. 1979, ISSN: 0020-1669. DOI: 10.1021/ic50197a018. URL: https://doi.org/10.1021/ic50197a018.

[119] K. Kim, S. Y. Lim, J. Kim, *et al.*, "Antiferromagnetic ordering in van der Waals 2D magnetic material MnPS3 probed by Raman spectroscopy," *2D Materials*, vol. 6, no. 4, p. 041 001, 2019, ISSN: 2053-1583. DOI: 10.1088/2053-1583/ab27d5. URL: https://dx.doi.org/10.1088/2053-1583/ab27d5.

[120] G. Long, H. Henck, M. Gibertini, D. Dumcenco, Z. Wang, T. Taniguchi, K. Watanabe, E. Giannini, and A. F. Morpurgo, "Persistence of Magnetism in Atomically Thin MnPS3 Crystals," *Nano Letters*, vol. 20, no. 4, pp. 2452–2459, Apr. 2020, ISSN: 1530-6984. DOI: 10.1021/acs.nanolett.9b05165. URL: https://doi.org/10.1021/acs.nanolett.9b05165.

[121] G. Le Flem, R. Brec, G. Ouvard, A. Louisy, and P. Segransan, "Magnetic interactions in the layer compounds MPX3 (M = Mn, Fe, Ni; X = S, Se)," *Journal of Physics and Chemistry of Solids*, vol. 43, no. 5, pp. 455–461, 1982. URL: https://www.sciencedirect.com/science/article/pii/0022369782901561.

[122] P. A. Joy and S. Vasudevan, "Magnetism in the layered transition-metal thiophosphates MPS3 (M=Mn, Fe, and Ni)," *Physical Review B*, vol. 46, no. 9, pp. 5425–5433, 1992, ISSN: 01631829. DOI: 10.1103/PhysRevB.46.5425.

[123] E. Ergeçen, B. Ilyas, J. Kim, J. Park, M. B. Yilmaz, T. Luo, D. Xiao, S. Okamoto, J.-G. Park, and N. Gedik, "Coherent detection of hidden spin–lattice coupling in a van der Waals antiferromagnet," *Proceedings of the National Academy of Sciences*, vol. 120, no. 12, e2208968120, Mar. 2023. DOI: 10.1073/pnas.2208968120. URL: https://doi.org/10.1073/pnas.2208968120.

[124] F. Zhou, K. Hwangbo, Q. Zhang, *et al.*, "Dynamical criticality of spin-shear coupling in van der Waals antiferromagnets," *Nature Communications*, vol. 13, no. 1, p. 6598, Nov. 2022, ISSN: 2041-1723. DOI: 10.1038/s41467-022-34376-5. URL: https://www.nature.com/articles/s41467-022-34376-5.

[125] K. Hwangbo, Q. Zhang, Q. Jiang, *et al.*, "Highly anisotropic excitons and multiple phonon bound states in a van der Waals antiferromagnetic insulator," *Nature Nanotechnology*, vol. 16, no. 6, pp. 655–660, Jun. 2021, ISSN: 17483395. DOI: 10.1038/s41565-021-00873-9.

[126] E. Ergeçen, B. Ilyas, D. Mao, H. C. Po, M. B. Yilmaz, J. Kim, J. G. Park, T. Senthil, and N. Gedik, "Magnetically brightened dark electron-phonon bound states in a van der Waals antiferromagnet," *Nature Communications*, vol. 13, no. 1, Dec. 2022, ISSN: 20411723. DOI: 10.1038/S41467-021-27741-3.

[127] C. A. Belvin, E. Baldini, I. O. Ozel, *et al.*, "Exciton-driven antiferromagnetic metal in a correlated van der Waals insulator," *Nature Communications*, vol. 12, no. 1, Dec. 2021, ISSN: 20411723. DOI: 10.1038/s41467-021-25164-8.

[128] D. Afanasiev, J. R. Hortensius, M. Matthiesen, *et al.*, "Controlling the anisotropy of a van der Waals antiferromagnet with light," *Science Advances*, vol. 7, no. 23, eabf3096, Oct. 2020, ISSN: 23752548. DOI: 10.1126/sciadv.abf3096. URL: http://arxiv.org/abs/2010.05062%20http://dx.doi.org/10.1126/sciadv.abf3096%20https://doi.org/10.1126/sciadv.abf3096.

[129] D. Khusyainov, T. Gareev, V. Radovskaia, *et al.*, "Ultrafast laser-induced spin–lattice dynamics in the van der Waals antiferromagnet CoPS3," *APL Materials*, vol. 11, no. 7, p. 071 104, Jul. 2023, ISSN: 2166-532X. DOI: 10.1063/5.0146128. URL: https://doi.org/10.1063/5.0146128.

[130] A. R. Wildes, M. E. Zhitomirsky, T. Ziman, D. Lançon, and H. C. Walker, "Evidence for biquadratic exchange in the quasi-two-dimensional antiferromagnet FePS 3," *Journal of Applied Physics*, vol. 127, no. 22, p. 223 903, Jun. 2020, ISSN: 0021-8979. DOI: 10.1063/5.0009114. URL: https://pubs.aip.org/aip/jap/article/127/22/223903/1065459/Evidence-for-biquadratic-exchange-in-the-quasi-two.

[131] A. R. Wildes, K. C. Rule, R. I. Bewley, M. Enderle, and T. J. Hicks, "The magnon dynamics and spin exchange parameters of FePS3," *Journal of Physics Condensed Matter*, vol. 24, no. 41, p. 8, 2012, ISSN: 09538984. DOI: 10.1088/0953-8984/24/41/416004. URL: https://dx.doi.org/10.1088/0953-8984/24/41/416004.

[132] A. Zong, Q. Zhang, F. Zhou, *et al.*, "Spin-mediated shear oscillators in a van der waals antiferromagnet," *Nature*, vol. 620, pp. 988–993, 7976 2023, ISSN: 1476-4687. DOI: 10.1038/s41586-023-06279-y. URL: https://doi.org/10.1038/s41586-023-06279-y.

[133] A. McCreary, J. R. Simpson, T. T. Mai, R. D. McMichael, J. E. Douglas, N. Butch, C. Dennis, R. Valdés Aguilar, and A. R. Hight Walker, "Quasi-two-dimensional magnon identification in antiferromagnetic FePS3 via magneto-Raman spectroscopy," *Physical Review B*, vol. 101, no. 6, p. 64 416, Feb. 2020. DOI: 10.1103/PhysRevB.101.064416. URL: https://link.aps.org/doi/10.1103/PhysRevB.101.064416.

[134] S. Liu, A. G. del Águila, D. Bhowmick, *et al.*, "Direct observation of magnon-phonon strong coupling in two-dimensional antiferromagnet at high magnetic fields," *Physical Review Letters*, vol. 127, p. 97 401, 9 Aug. 2021. DOI: 10.1103/PhysRevLett.127.097401. URL: https://link.aps.org/doi/10.1103/PhysRevLett.127.097401.

[135] D. Vaclavkova, M. Palit, J. Wyzula, *et al.*, "Magnon polarons in the van der Waals antiferromagnet FePS3," *Physical Review B*, vol. 104, no. 13, p. 134 437, Oct. 2021. DOI: 10.1103/PhysRevB.104.134437. URL: https://link.aps.org/doi/10.1103/PhysRevB.104.134437.

[136] K. Momma and F. Izumi, "VESTA 3 for three-dimensional visualization of crystal, volumetric and morphology data," *Journal of applied crystallography*, vol. 44, no. 6, pp. 1272–1276, 2011, ISSN: 1600-5767.

[137] F. Mertens, D. Mönkebüscher, U. Parlak, *et al.*, "Ultrafast Coherent THz Lattice Dynamics Coupled to Spins in the van der Waals Antiferromagnet FePS3," *Advanced Materials*, vol. 35, no. 6, p. 2 208 355, Feb. 2023, ISSN: 15214095. DOI: 10.1002/adma.202208355. URL: https://onlinelibrary.wiley.com/doi/full/10.1002/adma.202208355%20https://onlinelibrary.wiley.com/doi/abs/10.1002/adma.202208355%20https://onlinelibrary.wiley.com/doi/10.1002/adma.202208355%20https://doi.org/10.1002/adma.202208355.

[138] X.-X. Zhang, S. Jiang, J. Lee, C. Lee, K. F. Mak, and J. Shan, "Spin Dynamics Slowdown near the Antiferromagnetic Critical Point in Atomically Thin FePS3," *Nano Letters*, vol. 21, no. 12, pp. 5045–5052, Jun. 2021, ISSN: 1530-6984. DOI: 10.1021/acs.nanolett.1c00870. URL: https://doi.org/10.1021/acs.nanolett.1c00870.

[139] Q. Zhang, K. Hwangbo, C. Wang, Q. Jiang, J. H. Chu, H. Wen, D. Xiao, and X. Xu, "Observation of Giant Optical Linear Dichroism in a Zigzag Antiferromagnet FePS3," *Nano Letters*, vol. 21, no. 16, pp. 6938–6945, 2021, ISSN: 15306992. DOI: 10.1021/acs.nanolett.1c02188. URL: https://doi.org/10.1021/acs.nanolett.1c02188.

[140] M. C. Hoffmann, N. C. Brandt, H. Y. Hwang, K.-L. L. Yeh, and K. A. Nelson, "Terahertz Kerr effect," *Applied Physics Letters*, vol. 95, no. 23, p. 231 105, Dec. 2009, ISSN: 00036951. DOI: 10.1063/1.3271520. URL: https://doi.org/10.1063/1.3271520.

[141] D. Lançon, H. C. Walker, E. Ressouche, B. Ouladdiaf, K. C. Rule, G. J. Mcintyre, T. J. Hicks, H. M. Rønnow, and A. R. Wildes, "Magnetic structure and magnon dynamics of the quasi-two-dimensional antiferromagnet FePS3," *Physical Review B*, vol. 94, no. 21, p. 214 407, Dec. 2016, ISSN: 24699969. DOI: 10.1103/PhysRevB.94.214407. URL: https://link.aps.org/doi/10.1103/PhysRevB.94.214407.

[142] Z. Zhang, J. Zhang, Z.-J. Liu, *et al.*, "Discovery of enhanced lattice dynamics in a single-layered hybrid perovskite," *arXiv:2301.03501*, 2023.

[143] G. Ouvrard, R. Brec, and J. Rouxel, "Structural determination of some MPS3 layered phases (M = Mn, Fe, Co, Ni and Cd)," *Materials Research Bulletin*, vol. 20, no. 10, pp. 1181–1189, 1985, ISSN: 00255408. DOI: 10.1016/0025-5408(85)90092-3. URL: https://www.sciencedirect.com/science/article/pii/0025540885900923.

[144] J. Cui, E. V. Boström, M. Ozerov, *et al.*, "Chirality selective magnon-phonon hybridization and magnon-induced chiral phonons in a layered zigzag antiferromagnet," *Nature Communications*, vol. 14, no. 1, Jun. 2023. DOI: 10.1038/s41467-023-39123-y. URL: https://doi.org/10.1038/s41467-023-39123-y.

[145] X. Gonze, B. Amadon, G. Antonius, *et al.*, "The Abinitproject: Impact, environment and recent developments," *Computer Physics Communications*, vol. 248, p. 107 042, 2020, ISSN: 0010-4655. DOI: https://doi.org/10.1016/j.cpc.2019.107042. URL: https://www.sciencedirect.com/science/article/pii/S0010465519303741.

[146] X. Gonze, "First-principles responses of solids to atomic displacements and homogeneous electric fields: Implementation of a conjugate-gradient algorithm," *Physical Review B*, vol. 55, no. 16, pp. 10 337–10 354, Apr. 1997. DOI: 10.1103/PhysRevB.55.10337. URL: https://link.aps.org/doi/10.1103/PhysRevB.55.10337.

[147] B. Amadon, F. Lechermann, A. Georges, F. Jollet, T. O. Wehling, and A. I. Lichtenstein, "Plane-wave based electronic structure calculations for correlated materials using dynamical mean-field theory and projected local orbitals," *Physical Review B*, vol. 77, no. 20, p. 205 112, May 2008. DOI: 10.1103/PhysRevB.77.205112. URL: https://link.aps.org/doi/10.1103/PhysRevB.77.205112.

[148] M. Torrent, F. Jollet, F. Bottin, G. Zérah, and X. Gonze, "Implementation of the projector augmented-wave method in the ABINIT code: Application to the study of iron under pressure," *Computational Materials Science*, vol. 42, no. 2, pp. 337–351, 2008, ISSN: 0927-0256. DOI: https://doi.org/10.1016/j.commatsci.2007.07.020. URL: https://www.sciencedirect.com/science/article/pii/S0927025607002108.

[149] G. Pizzi, V. Vitale, R. Arita, *et al.*, "Wannier90 as a community code: new features and applications," *Journal of Physics: Condensed Matter*, vol. 32, no. 16, p. 165 902, 2020, ISSN: 0953-8984. DOI: 10.1088/1361-648X/ab51ff. URL: https://dx.doi.org/10.1088/1361-648X/ab51ff.

[150] X. He, N. Helbig, M. J. Verstraete, and E. Bousquet, "TB2J: A python package for computing magnetic interaction parameters," *Computer Physics Communications*, vol. 264, p. 107 938, 2021, ISSN: 0010-4655. DOI: https://doi.org/10.1016/j.cpc.2021.107938. URL: https://www.sciencedirect.com/science/article/pii/S0010465521000679.

[151] Y. Lee, S. Son, C. Kim, *et al.*, "Giant Magnetic Anisotropy in the Atomically Thin van der Waals Antiferromagnet FePS3," *Advanced Electronic Materials*, vol. 9, no. 2, p. 2 200 650, 2023. DOI: https://doi.org/10.1002/aelm.202200650. URL: https://onlinelibrary.wiley.com/doi/abs/10.1002/aelm.202200650.

[152] P. Padmanabhan, F. L. Buessen, R. Tutchton, *et al.*, "Coherent helicity-dependent spin-phonon oscillations in the ferromagnetic van der waals crystal cri3," *Nature Communications*, vol. 13, p. 4473, 1 2022, ISSN: 2041-1723. DOI: 10.1038/s41467-022-31786-3. URL: https://doi.org/10.1038/s41467-022-31786-3.

[153] H. Padmanabhan, M. Poore, P. K. Kim, *et al.*, "Interlayer magnetophononic coupling in mnbi2te4," *Nature Communications*, vol. 13, p. 1929, 1 2022, ISSN: 2041-1723. DOI: 10.1038/s41467-022-29545-5. URL: https://doi.org/10.1038/s41467-022-29545-5.

[154] A. M. Ferrenberg, J. Xu, and D. P. Landau, "Pushing the limits of Monte Carlo simulations for the three-dimensional Ising model," *Physical Review E*, vol. 97, no. 4, p. 43 301, Apr. 2018. DOI: 10.1103/PhysRevE.97.043301. URL: https://link.aps.org/doi/10.1103/PhysRevE.97.043301.

[155] P. C. Hohenberg and B. I. Halperin, "Theory of dynamic critical phenomena," *Rev. Mod. Phys.*, vol. 49, pp. 435–479, 3 Jul. 1977. DOI: 10.1103/RevModPhys.49.435. URL: https://link.aps.org/doi/10.1103/RevModPhys.49.435.

[156] F. Formisano, R. M. Dubrovin, R. V. Pisarev, A. M. Kalashnikova, and A. V. Kimel, "Laser-induced THz magnetism of antiferromagnetic CoF2," *Journal of Physics: Condensed Matter*, vol. 34, no. 22, p. 225 801, Mar. 2022, ISSN: 0953-8984. DOI: 10.1088/1361-648X/AC5C20. URL: https://iopscience.iop.org/article/10.1088/1361-648X/ac5c20%20https://iopscience.iop.org/article/10.1088/1361-648X/ac5c20/meta.

[157] D. J. Higley, K. Hirsch, G. L. Dakovski, *et al.*, "Femtosecond X-ray magnetic circular dichroism absorption spectroscopy at an X-ray free electron laser," *Review of Scientific Instruments*, vol. 87, no. 3, p. 033 110, Mar. 2016, ISSN: 0034-6748. DOI: 10.1063/1.4944410. URL: https://doi.org/10.1063/1.4944410.

[158] C. Bostedt, S. Boutet, D. M. Fritz, Z. Huang, H. J. Lee, H. T. Lemke, A. Robert, W. F. Schlotter, J. J. Turner, and G. J. Williams, "Linac Coherent Light Source: The first five years," *Reviews of Modern Physics*, vol. 88, no. 1, p. 15 007, Mar. 2016. DOI: 10.1103/RevModPhys.88.015007. URL: https://link.aps.org/doi/10.1103/RevModPhys.88.015007.

[159] S. Zayko, O. Kfir, M. Heigl, M. Lohmann, M. Sivis, M. Albrecht, and C. Ropers, "Ultrafast high-harmonic nanoscopy of magnetization dynamics," *Nature Communications*, vol. 12, no. 1, p. 6337, 2021, ISSN: 2041-1723. DOI: 10.1038/s41467-021-26594-0. URL: https://doi.org/10.1038/s41467-021-26594-0.

[160] T. Luo, B. Ilyas, A. v. Hoegen, Y. Lee, J. Park, J.-G. Park, and N. Gedik, "Time-of-flight detection of terahertz phonon-polariton," *Nature Communications*, vol. 15, no. 1, pp. 1–8, 2024.

[161] A. Frisk Kockum, A. Miranowicz, S. De Liberato, S. Savasta, and F. Nori, "Ultrastrong coupling between light and matter," *Nature Reviews Physics*, vol. 1, no. 1, pp. 19–40, 2019, ISSN: 25225820. DOI: 10.1038/s42254-018-0006-2. URL: http://dx.doi.org/10.1038/s42254-018-0006-2.

[162] M. Hohenleutner, F. Langer, O. Schubert, M. Knorr, U. Huttner, S. W. Koch, M. Kira, and R. Huber, "Real-time observation of interfering crystal electrons in high-harmonic generation," *Nature*, vol. 523, no. 7562, pp. 572–575, Jul. 2015, ISSN: 14764687. DOI: 10.1038/nature14652. URL: https://www.nature.com/articles/nature14652.

[163] P. B. Corkum and F. Krausz, "Attosecond science," *Nature Physics*, vol. 3, no. 6, pp. 381–387, Jun. 2007, ISSN: 1745-2473. DOI: 10.1038/nphys620. URL: https://www.nature.com/articles/nphys620.

[164] O. D. Mücke, T. Tritschler, M. Wegener, U. Morgner, and F. X. Kärtner, "Signatures of Carrier-Wave Rabi Flopping in GaAs," *Physical Review Letters*, vol. 87, no. 5, p. 057 401, Jul. 2001, ISSN: 0031-9007. DOI: 10.1103/PhysRevLett.87.057401. URL: https://journals.aps.org/prl/abstract/10.1103/PhysRevLett.87.057401%20https://link.aps.org/doi/10.1103/PhysRevLett.87.057401.

[165] D. N. Basov, M. M. Fogler, and F. J. García de Abajo, "Polaritons in van der Waals materials," *Science*, vol. 354, no. 6309, p. 195, Oct. 2016, ISSN: 0036-8075. DOI: 10.1126/science.aag1992. URL: http://dx.doi.%20https://www.science.org/doi/10.1126/science.aag1992.

[166] C. Haffner, W. Heni, Y. Fedoryshyn, *et al.*, "All-plasmonic Mach-Zehnder modulator enabling optical high-speed communication at the microscale," *Nature Photonics*, vol. 9, no. 8, pp. 525–528, Jul. 2015, ISSN: 17494893. DOI: 10.1038/nphoton.2015.127. URL: https://www.nature.com/articles/nphoton.2015.127.

[167] D. Ballarini, M. De Giorgi, E. Cancellieri, R. Houdré, E. Giacobino, R. Cingolani, A. Bramati, G. Gigli, and D. Sanvitto, "All-optical polariton transistor," *Nature Communications*, vol. 4, no. 1, p. 1778, Apr. 2013, ISSN: 2041-1723. DOI: 10.1038/ncomms2734. URL: https://www.nature.com/articles/ncomms2734.

[168] S. Dai, Z. Fei, Q. Ma, *et al.*, "Tunable phonon polaritons in atomically thin van der Waals crystals of boron nitride," *Science*, vol. 343, no. 6175, pp. 1125–1129, Mar. 2014, ISSN: 10959203. DOI: 10.1126/science.1246833. URL: https://www.science.org/doi/10.1126/science.1246833.

[169] R. Macêdo and R. E. Camley, "Engineering terahertz surface magnon-polaritons in hyperbolic antiferromagnets," *Physical Review B*, vol. 99, no. 1, p. 014 437, Jan. 2019, ISSN: 2469-9950. DOI: 10.1103/PhysRevB.99.014437. URL: https://link.aps.org/doi/10.1103/PhysRevB.99.014437.

[170] J. Sloan, N. Rivera, J. D. Joannopoulos, I. Kaminer, and M. Soljačić, "Controlling spins with surface magnon polaritons," *Physical Review B*, vol. 100, no. 23, p. 235 453, Dec. 2019, ISSN: 24699969. DOI: 10.1103/PhysRevB.100.235453. URL: https://journals.aps.org/prb/abstract/10.1103/PhysRevB.100.235453.

[171] P. Sivarajah, A. Steinbacher, B. Dastrup, J. Lu, M. Xiang, W. Ren, S. Kamba, S. Cao, and K. A. Nelson, "THz-frequency magnon-phonon-polaritons in the collective strong-coupling regime," *Journal of Applied Physics*, vol. 125, no. 21, p. 213 103, 2019, ISSN: 10897550. DOI: 10.1063/1.5083849. URL: https://doi.org/10.1063/1.5083849.

[172] Z. Fei, M. E. Scott, D. J. Gosztola, *et al.*, "Nano-optical imaging of WS e2 waveguide modes revealing light-exciton interactions," *Physical Review B*, vol. 94, no. 8, p. 081 402, Aug. 2016, ISSN: 24699969. DOI: 10.1103/PhysRevB.94.081402. URL: https://journals.aps.org/prb/abstract/10.1103/PhysRevB.94.081402.

[173] F. Dirnberger, R. Bushati, B. Datta, A. Kumar, A. H. MacDonald, E. Baldini, and V. M. Menon, "Spin-correlated exciton–polaritons in a van der Waals magnet," *Nature Nanotechnology*, vol. 17, no. 10, pp. 1060–1064, Sep. 2022, ISSN: 17483395. DOI: 10.1038/s41565-022-01204-2. URL: https://www.nature.com/articles/s41565-022-01204-2.

[174] T. Feurer, J. C. Vaughan, and K. A. Nelson, "Spatiotemporal coherent control of lattice vibrational waves," *Science*, vol. 299, no. 5605, pp. 374–377, Jan. 2003, ISSN: 00368075. DOI: 10.1126/science.1078726. URL: www.sciencemag.org.

[175] T. Feurer, N. S. Stoyanov, D. W. Ward, J. C. Vaughan, E. R. Statz, and K. A. Nelson, "Terahertz Polaritonics," *Annual Review of Materials Research*, vol. 37, no. 1, pp. 317–350, Aug. 2007, ISSN: 1531-7331. DOI: 10.1146/annurev.matsci.37.052506.084327. URL: https://www.annualreviews.org/doi/10.1146/annurev.matsci.37.052506.084327.

[176] M. Henstridge, M. Först, E. Rowe, M. Fechner, and A. Cavalleri, "Nonlocal nonlinear phononics," *Nature Physics*, vol. 18, no. 4, pp. 457–461, Mar. 2022, ISSN: 17452481. DOI: 10.1038/s41567-022-01512-3. URL: https://www.nature.com/articles/s41567-022-01512-3.

[177] H. J. Bakker, S. Hunsche, and H. Kurz, "Coherent phonon polaritons as probes of anharmonic phonons in ferroelectrics," *Reviews of Modern Physics*, vol. 70, no. 2, pp. 523–536, 1998, ISSN: 00346861. DOI: 10.1103/revmodphys.70.523.

[178] A. Von Hoegen, R. Mankowsky, M. Fechner, M. Först, and A. Cavalleri, "Probing the interatomic potential of solids with strong-field nonlinear phononics," *Nature*, vol. 555, no. 7694, pp. 79–82, Feb. 2018, ISSN: 14764687. DOI: 10.1038/nature25484. URL: https://www.nature.com/articles/nature25484.

[179] C. H. Henry and J. J. Hopfield, "Raman scattering by Polaritons," *Physical Review Letters*, vol. 15, no. 25, pp. 964–966, Dec. 1965, ISSN: 00319007. DOI: 10.1103/PhysRevLett.15.964. URL: https://link.aps.org/doi/10.1103/PhysRevLett.15.964.

[180] R. Claus, "Light scattering by optical phonons and polaritons in perfect crystals," *Physica Status Solidi (B)*, vol. 50, no. 1, pp. 11–32, Mar. 1972, ISSN: 15213951. DOI: 10.1002/pssb.2220500102. URL: https://onlinelibrary.wiley.com/doi/10.1002/pssb.2220500102.

[181] H. J. Bakker, S. Hunsche, and H. Kurz, "Investigation of anharmonic lattice vibrations with coherent phonon polaritons," *Physical Review B*, vol. 50, no. 2, pp. 914–920, Jul. 1994, ISSN: 01631829. DOI: 10.1103/PhysRevB.50.914. URL: https://link.aps.org/doi/10.1103/PhysRevB.50.914.

[182] Y. Ikegaya, H. Sakaibara, Y. Minami, I. Katayama, and J. Takeda, "Real-time observation of phonon-polariton dynamics in ferroelectric LiNbO3 in time-frequency space," *Applied Physics Letters*, vol. 107, no. 6, p. 062 901, Aug. 2015, ISSN: 0003-6951. DOI: 10.1063/1.4928480. URL: http://dx.doi.org/10.1063/1.4928480%20https://pubs.aip.org/apl/article/107/6/062901/29356/Real-time-observation-of-phonon-polariton-dynamics.

[183] B. E. Knighton, B. S. Dastrup, C. L. Johnson, and J. A. Johnson, "Measurement of a phonon-polariton dispersion curve by varying the excitation wavelength," *Physical Review B*, vol. 97, no. 21, p. 214 307, Jun. 2018, ISSN: 2469-9950. DOI: 10.1103/PhysRevB.97.214307. URL: https://link.aps.org/doi/10.1103/PhysRevB.97.214307.

[184] S. Kojima, N. Tsumura, M. W. Takeda, and S. Nishizawa, "Far-infrared phonon-polariton dispersion probed by terahertz time-domain spectroscopy," *Physical Review B*, vol. 67, no. 3, p. 035 102, Jan. 2003, ISSN: 0163-1829. DOI: 10.1103/PhysRevB.67.035102. URL: https://link.aps.org/doi/10.1103/PhysRevB.67.035102.

[185] R. G. Ulbrich and G. W. Fehrenbach, "Polariton wave packet propagation in the exciton resonance of a semiconductor," *Physical Review Letters*, vol. 43, no. 13, pp. 963–966, 1979, ISSN: 00319007. DOI: 10.1103/PhysRevLett.43.963.

[186] Q. Song, C. A. Occhialini, E. Ergeçen, *et al.*, "Evidence for a single-layer van der Waals multiferroic," *Nature*, vol. 602, no. 7898, pp. 601–605, Feb. 2022, ISSN: 14764687. DOI: 10.1038/S41586-021-04337-X.

[187] T. Kurumaji, S. Seki, S. Ishiwata, H. Murakawa, Y. Kaneko, and Y. Tokura, "Magnetoelectric responses induced by domain rearrangement and spin structural change in triangular-lattice helimagnets NiI2 and CoI2," *Physical Review B*, vol. 87, no. 1, p. 014 429, Jan. 2013, ISSN: 1098-0121. DOI: 10.1103/PhysRevB.87.014429. URL: https://link.aps.org/doi/10.1103/PhysRevB.87.014429.

[188] S. R. Kuindersma, "A far-infrared study of the lattice vibrations of NiI2 and CoI2," *Physica Status Solidi (B)*, vol. 107, no. 2, K163–K166, 1981, ISSN: 15213951. DOI: 10.1002/pssb.2221070264.

[189] S. R. Kuindersma, P. R. Boudewijn, and C. Haas, "Near-Infrared d–d Transitions of NiI2, CdI2:Ni2+, and CoI2," *Physica Status Solidi (B)*, vol. 108, no. 1, pp. 187–194, 1981, ISSN: 15213951. DOI: 10.1002/pssb.2221080122.

[190] S. Son, Y. Lee, J. H. Kim, *et al.*, "Multiferroic-Enabled Magnetic-Excitons in 2D Quantum-Entangled Van der Waals Antiferromagnet NiI2," *Advanced Materials*, vol. 34, no. 10, p. 2 109 144, Mar. 2022, ISSN: 15214095. DOI: 10.1002/adma.202109144. URL: https://onlinelibrary.wiley.com/doi/10.1002/adma.202109144.

[191] A. Taflove, S. C. Hagness, and M. Piket-May, "Computational Electromagnetics: The Finite-Difference Time-Domain Method," in *The Electrical Engineering Handbook*, 2004, pp. 629–670, ISBN: 9780121709600. DOI: 10.1016/B978-012170960-0/50046-3.

[192] A. F. Oskooi, D. Roundy, M. Ibanescu, P. Bermel, J. D. Joannopoulos, and S. G. Johnson, "Meep: A flexible free-software package for electromagnetic simulations by the FDTD method," *Computer Physics Communications*, vol. 181, no. 3, pp. 687–702, Mar. 2010, ISSN: 00104655. DOI: 10.1016/j.cpc.2009.11.008.

[193] T. Lin, R. Xu, X. Chen, Y. Guan, M. Yao, J. Zhang, X. Li, and H. Zhu, "Sub-wavelength, phase-sensitive microscopy of third-order nonlinearity in terahertz frequencies," Preprint at https://doi.org/10.1364/opticaopen.220, Jun. 2023. DOI: 10.1364/opticaopen.22066295.v2. URL: /articles/preprint/Sub-wavelength_phase-sensitive_microscopy_of_third-order_nonlinearity_in_terahertz_frequencies/22066295/2%20https://doi.org/10.1364/opticaopen.22066295.v2.

[194] K. Huang, "Lattice vibrations and optical waves in ionic crystals," *Nature*, vol. 167, no. 4254, pp. 779–780, 1951, ISSN: 00280836. DOI: 10.1038/167779b0. URL: https://www.nature.com/articles/167779b0.

[195] G. P. Wiederrecht, T. P. Dougherty, L. Dhar, K. A. Nelson, D. E. Leaird, and A. M. Weiner, "Explanation of anomalous polariton dynamics in LiTaO3," *Physical Review B*, vol. 51, no. 2, pp. 916–931, Jan. 1995, ISSN: 01631829. DOI: 10.1103/PhysRevB.51.916. URL: https://journals.aps.org/prb/abstract/10.1103/PhysRevB.51.916%20https://link.aps.org/doi/10.1103/PhysRevB.51.916.

[196] T. Kuribayashi, T. Motoyama, Y. Arashida, I. Katayama, and J. Takeda, "Anharmonic phonon-polariton dynamics in ferroelectric LiNbO3 studied with single-shot pump-probe imaging spectroscopy," *Journal of Applied Physics*, vol. 123, no. 17, p. 174 103, May 2018, ISSN: 10897550. DOI: 10.1063/1.5021379. URL: /aip/jap/article/123/17/174103/155310/Anharmonic-phonon-polariton-dynamics-in.

[197] H. Chu, C. J. Roh, J. O. Island, C. Li, S. Lee, J. Chen, J.-G. Park, A. F. Young, J. S. Lee, and D. Hsieh, "Linear Magnetoelectric Phase in Ultrathin MnPS3 Probed by Optical Second Harmonic Generation," *Physical Review Letters*, vol. 124, no. 2, p. 027 601, Jan. 2020, ISSN: 0031-9007. DOI: 10.1103/PhysRevLett.124.027601. URL: https://link.aps.org/doi/10.1103/PhysRevLett.124.027601.

[198] P. Coleman, *Introduction to Many-Body Physics*. 2015. DOI: 10.1017/cbo9781139020916.

[199] M. H. Hamidian, S. D. Edkins, S. H. Joo, *et al.*, "Detection of a Cooper-pair density wave in Bi2Sr2CaCu2O8+x," *Nature*, vol. 532, no. 7599, 2016, ISSN: 14764687. DOI: 10.1038/nature17411.

[200] Y. Xu, S. Liu, D. A. Rhodes, K. Watanabe, T. Taniguchi, J. Hone, V. Elser, K. F. Mak, and J. Shan, "Correlated insulating states at fractional fillings of moiré superlattices," *Nature*, vol. 587, no. 7833, pp. 214–218, 2020, ISSN: 14764687. DOI: 10.1038/s41586-020-2868-6.

[201] M. Gibertini, M. Koperski, A. F. Morpurgo, and K. S. Novoselov, "Magnetic 2D materials and heterostructures," *Nature Nanotechnology*, vol. 14, no. 5, pp. 408–419, 2019, ISSN: 17483395. DOI: 10.1038/s41565-019-0438-6.

[202] B. Huang, M. A. McGuire, A. F. May, D. Xiao, P. Jarillo-Herrero, and X. Xu, "Emergent phenomena and proximity effects in two-dimensional magnets and heterostructures," *Nature Materials*, vol. 19, no. 12, pp. 1276–1289, 2020, ISSN: 14764660. DOI: 10.1038/s41563-020-0791-8.

[203] K. S. Burch, D. Mandrus, and J. G. Park, "Magnetism in two-dimensional van der Waals materials," *Nature*, vol. 563, no. 7729, pp. 47–52, 2018, ISSN: 14764687. DOI: 10.1038/s41586-018-0631-z.

[204] N. Sivadas, S. Okamoto, X. Xu, C. J. Fennie, and D. Xiao, "Stacking-dependent magnetism in bilayer cri3," *Nano letters*, vol. 18, no. 12, pp. 7658–7664, 2018.

[205] T. Song, Q. C. Sun, E. Anderson, *et al.*, "Direct visualization of magnetic domains and moiré magnetism in twisted 2D magnets," *Science*, vol. 374, no. 6571, pp. 1140–1144, 2021, ISSN: 10959203. DOI: 10.1126/science.abj7478.

[206] Y. Xu, A. Ray, Y. T. Shao, *et al.*, "Coexisting ferromagnetic–antiferromagnetic state in twisted bilayer CrI3," *Nature Nanotechnology*, 2021, ISSN: 17483395. DOI: 10.1038/s41565-021-01014-y.

[207] H. Xie, X. Luo, G. Ye, *et al.*, "Twist engineering of the two-dimensional magnetism in double bilayer chromium triiodide homostructures," *Nature Physics*, 2021, ISSN: 1745-2473. DOI: 10.1038/s41567-021-01408-8. arXiv: 2103.13537.

[208] J. U. Lee, S. Lee, J. H. Ryoo, S. Kang, T. Y. Kim, P. Kim, C. H. Park, J. G. Park, and H. Cheong, "Ising-Type Magnetic Ordering in Atomically Thin FePS3," *Nano Letters*, vol. 16, no. 12, pp. 7433–7438, 2016, ISSN: 15306992. DOI: 10.1021/acs.nanolett.6b03052. arXiv: 1608.04169.

[209] D. Lançon, H. C. Walker, E. Ressouche, B. Ouladdiaf, K. C. Rule, G. J. McIntyre, T. J. Hicks, H. M. Rønnow, and A. R. Wildes, "Magnetic structure and magnon dynamics of the quasi-two-dimensional antiferromagnet FePS3," *Physical Review B*, vol. 94, no. 21, 2016, ISSN: 24699969. DOI: 10.1103/PhysRevB.94.214407.

[210] M. Scagliotti, M. Jouanne, M. Balkanski, G. Ouvrard, and G. Benedek, "Raman scattering in antiferromagnetic FePS3 and FePSe3 crystals," *Physical Review B*, vol. 35, no. 13, pp. 7097–7104, 1987, ISSN: 01631829. DOI: 10.1103/PhysRevB.35.7097.

[211] A. Ghosh, M. Palit, S. Maity, V. Dwij, S. Rana, and S. Datta, "Spin-phonon coupling and magnon scattering in few-layer antiferromagnetic FePS3," *Physical Review B*, vol. 103, no. 6, 2021, ISSN: 24699969. DOI: 10.1103/PhysRevB.103.064431.

[212] J. Hong, A. Stroppa, J. Añiguez, S. Picozzi, and D. Vanderbilt, "Spin-phonon coupling effects in transition-metal perovskites: A DFT+U and hybrid-functional study," *Physical Review B - Condensed Matter and Materials Physics*, vol. 85, no. 5, 2012, ISSN: 10980121. DOI: 10.1103/PhysRevB.85.054417. arXiv: 1112.5205.

[213] J. Vermette, S. Jandl, and M. M. Gospodinov, "Raman study of spin-phonon coupling in ErMnO3," *Journal of Physics Condensed Matter*, vol. 20, no. 42, 2008, ISSN: 09538984. DOI: 10.1088/0953-8984/20/42/425219.

[214] G. Ouvrard, R. Brec, and J. Rouxel, "Structural determination of some MPS3 layered phases (M = Mn, Fe, Co, Ni and Cd)," *Materials Research Bulletin*, vol. 20, no. 10, pp. 1181–1189, 1985, ISSN: 00255408. DOI: 10.1016/0025-5408(85)90092-3.

[215] C. T. Kuo, M. Neumann, K. Balamurugan, *et al.*, "Exfoliation and Raman Spectroscopic Fingerprint of Few-Layer NiPS 3 Van der Waals Crystals," *Scientific Reports*, vol. 6, no. May 2015, pp. 1–10, 2016, ISSN: 20452322. DOI: 10.1038/srep20904. URL: http://dx.doi.org/10.1038/srep20904.

[216] M. Piacentini, F. S. Khumalo, G. Leveque, C. G. Olson, and D. W. Lynch, "X-ray photoemission and optical spectra of NiPS3, FePS3 and ZnPS3," *Chemical Physics*, vol. 72, no. 1-2, pp. 61–71, 1982, ISSN: 03010104. DOI: 10.1016/0301-0104(82)87066-3.

[217] Q. Zhang, K. Hwangbo, C. Wang, Q. Jiang, J. H. Chu, H. Wen, D. Xiao, and X. Xu, "Observation of Giant Optical Linear Dichroism in a Zigzag Antiferromagnet FePS3," *Nano Letters*, vol. 21, no. 16, pp. 6938–6945, 2021, ISSN: 15306992. DOI: 10.1021/acs.nanolett.1c02188.

[218] R. Loudon, "The Raman effect in crystals," *Advances in Physics*, vol. 13, no. 52, pp. 423–482, 1964, ISSN: 14606976. DOI: 10.1080/00018736400101051.

[219] H. J. Zeiger, J. Vidal, T. K. Cheng, E. P. Ippen, G. Dresselhaus, and M. S. Dresselhaus, "Theory for displacive excitation of coherent phonons," *Physical Review B*, vol. 45, no. 2, pp. 768–778, 1992, ISSN: 01631829. DOI: 10.1103/PhysRevB.45.768.

[220] D. Lançon, R. A. Ewings, T. Guidi, F. Formisano, and A. R. Wildes, "Magnetic exchange parameters and anisotropy of the quasi-two-dimensional antiferromagnet NiPS3," *Physical Review B*, vol. 98, no. 13, 2018, ISSN: 24699969. DOI: 10.1103/PhysRevB.98.134414. arXiv: 1808.01480.

[221] T. Y. Kim and C.-H. Park, "Magnetic Anisotropy and Magnetic Ordering of Transition-Metal Phosphorus Trisulfides," *Nano Letters*, vol. 21, no. 23, pp. 10 114–10 121, 2021, ISSN: 1530-6984. DOI: 10.1021/acs.nanolett.1c03992.

[222] E. Ergeçen, B. Ilyas, D. Mao, H. C. Po, M. B. Yilmaz, J. Kim, J.-G. Park, T. Senthil, and N. Gedik, "Magnetically brightened dark electron-phonon bound states in a van der waals antiferromagnet," *Nature Communications*, vol. 13, no. 1, p. 98, 2022.

[223] S. Kang, K. Kim, B. H. Kim, *et al.*, "Coherent many-body exciton in van der Waals antiferromagnet NiPS3," *Nature*, vol. 583, no. 7818, pp. 785–789, 2020, ISSN: 14764687. DOI: 10.1038/s41586-020-2520-5.

[224] K. Kim, S. Y. Lim, J. U. Lee, S. Lee, T. Y. Kim, K. Park, G. S. Jeon, C. H. Park, J. G. Park, and H. Cheong, "Suppression of magnetic ordering in XXZ-type antiferromagnetic monolayer NiPS 3," *Nature Communications*, vol. 10, no. 1, pp. 1–9, 2019, ISSN: 20411723. DOI: 10.1038/s41467-018-08284-6.

[225] J. L. Lado and J. Fernández-Rossier, "On the origin of magnetic anisotropy in two dimensional CrI3," *2D Materials*, vol. 4, no. 3, 2017, ISSN: 20531583. DOI: 10.1088/2053-1583/aa75ed. arXiv: 1704.03849.

[226] M. J. Coak, D. M. Jarvis, H. Hamidov, *et al.*, "Emergent Magnetic Phases in Pressure-Tuned van der Waals Antiferromagnet FePS3," *Physical Review X*, vol. 11, no. 1, 2021, ISSN: 21603308. DOI: 10.1103/PhysRevX.11.011024.

[227] A. S. Disa, M. Fechner, T. F. Nova, B. Liu, M. Först, D. Prabhakaran, P. G. Radaelli, and A. Cavalleri, "Polarizing an antiferromagnet by optical engineering of the crystal field," *Nature Physics*, vol. 16, no. 9, pp. 937–941, 2020, ISSN: 17452481. DOI: 10.1038/s41567-020-0936-3.

[228] M. Rodriguez-Vega, Z.-X. Lin, A. Leonardo, A. Ernst, M. G. Vergniory, and G. A. Fiete, "Light-driven topological and magnetic phase transitions in thin layer antiferromagnets," *The Journal of Physical Chemistry Letters*, vol. 13, no. 18, pp. 4152–4158, 2022, PMID: 35507411. DOI: 10.1021/acs.jpclett.2c00070. eprint: https://doi.org/10.1021/acs.jpclett.2c00070. URL: https://doi.org/10.1021/acs.jpclett.2c00070.

[229] C. Jin, J. Kim, J. Suh, *et al.*, "Interlayer electron-phonon coupling in WSe 2/hBN heterostructures," *Nature Physics*, vol. 13, no. 2, pp. 127–131, 2017, ISSN: 17452481. DOI: 10.1038/nphys3928.

[230] J. F. Ge, Z. L. Liu, C. Liu, C. L. Gao, D. Qian, Q. K. Xue, Y. Liu, and J. F. Jia, "Superconductivity above 100 K in single-layer FeSe films on doped SrTiO3," *Nature Materials*, vol. 14, no. 3, pp. 285–289, 2015, ISSN: 14764660. DOI: 10.1038/nmat4153.

[231] S. N. Rebec, T. Jia, C. Zhang, M. Hashimoto, D. H. Lu, R. G. Moore, and Z. X. Shen, "Coexistence of Replica Bands and Superconductivity in FeSe Monolayer Films," *Physical Review Letters*, vol. 118, no. 6, p. 067 002, 2017, ISSN: 10797114. DOI: 10.1103/PhysRevLett.118.067002.

[232] W. Jin, H. H. Kim, Z. Ye, G. Ye, L. Rojas, X. Luo, B. Yang, F. Yin, J. S. A. Horng, S. Tian, *et al.*, "Observation of the polaronic character of excitons in a two-dimensional semiconducting magnet cri3," *Nature communications*, vol. 11, no. 1, p. 4780, 2020.

[233] X. Wang, J. Cao, Z. Lu, *et al.*, "Spin-induced linear polarization of photoluminescence in antiferromagnetic van der waals crystals," *Nature Materials*, vol. 20, pp. 1–7, 7 2021, ISSN: 14764660. DOI: 10.1038/s41563-021-00968-7.

[234] K. Hwangbo, Q. Zhang, Q. Jiang, *et al.*, "Highly anisotropic excitons and multiple phonon bound states in a van der waals antiferromagnetic insulator," *Nature Nanotechnology*, vol. 16, pp. 655–660, 6 2021, ISSN: 17483395. DOI: 10.1038/s41565-021-00873-9.

[235] A. R. Wildes, V. Simonet, E. Ressouche, *et al.*, "Magnetic structure of the quasi-two-dimensional antiferromagnet," *Physical Review B*, vol. 92, no. 22, p. 224 408, 2015, ISSN: 1098-0121.

[236] S. Y. Kim, T. Y. Kim, L. J. Sandilands, *et al.*, "Charge-Spin Correlation in van der Waals Antiferromagnet NiPS3," *Physical Review Letters*, vol. 120, no. 13, p. 136 402, 2018, ISSN: 10797114. DOI: 10.1103/PhysRevLett.120.136402.

[237] M. Fiebig, N. P. Duong, T. Satoh, B. B. Van Aken, K. Miyano, Y. Tomioka, and Y. Tokura, "Ultrafast magnetization dynamics of antiferromagnetic compounds," *Journal of Physics D: Applied Physics*, vol. 41, no. 16, p. 164 005, 2008, ISSN: 00223727. DOI: 10.1088/0022-3727/41/16/164005.

[238] N. P. Duong, T. Satoh, and M. Fiebig, "Ultrafast manipulation of antiferromagnetism of NiO," *Physical Review Letters*, vol. 93, no. 11, p. 117 402, 2004, ISSN: 00319007. DOI: 10.1103/PhysRevLett.93.117402.

[239] J. Y. Bigot, M. Vomir, and E. Beaurepaire, "Coherent ultrafast magnetism induced by femtosecond laser pulses," *Nature Physics*, vol. 5, no. 7, 2009, ISSN: 17452481. DOI: 10.1038/nphys1285.

[240] C. Flint, "Vibronic spectra of coordination compounds," *Coordination Chemistry Reviews*, vol. 14, no. 1, pp. 47–66, 1974, ISSN: 0010-8545. DOI: https://doi.org/10.1016/S0010-8545(00)82033-0. URL: https://www.sciencedirect.com/science/article/pii/S0010854500820330.

[241] J. J. Hopfield, D. G. Thomas, and R. T. Lynch, "Isoelectronic donors and acceptors," *Physical Review Letters*, vol. 17, no. 6, p. 312, 1966, ISSN: 00319007. DOI: 10.1103/PhysRevLett.17.312.

[242] C. H. Henry, P. J. Dean, and J. D. Cuthbert, "New red pair luminescence from GaP," *Physical Review*, vol. 166, no. 3, p. 754, 1968, ISSN: 0031899X. DOI: 10.1103/PhysRev.166.754.

[243] I. Paradisanos, G. Wang, E. M. Alexeev, A. R. Cadore, X. Marie, A. C. Ferrari, M. M. Glazov, and B. Urbaszek, "Efficient phonon cascades in WSe2 monolayers," *Nature Communications*, vol. 12, no. 1, pp. 1–7, 2021, ISSN: 20411723. DOI: 10.1038/s41467-020-20244-7.

[244] P. Arrangoiz-Arriola, E. A. Wollack, Z. Wang, M. Pechal, W. Jiang, T. P. McKenna, J. D. Witmer, R. Van Laer, and A. H. Safavi-Naeini, "Resolving the energy levels of a nanomechanical oscillator," *Nature*, vol. 571, no. 7766, 2019, ISSN: 14764687. DOI: 10.1038/s41586-019-1386-x.

[245] D. I. Schuster, A. A. Houck, J. A. Schreier, *et al.*, "Resolving photon number states in a superconducting circuit," *Nature*, vol. 445, no. 7127, pp. 515–518, 2007, ISSN: 14764687. DOI: 10.1038/nature05461.

[246] D. Lachance-Quirion, Y. Tabuchi, S. Ishino, A. Noguchi, T. Ishikawa, R. Yamazaki, and Y. Nakamura, "Resolving quanta of collective spin excitations in a millimeter-sized ferromagnet," *Science Advances*, vol. 3, no. 7, e1603150, 2017, ISSN: 23752548. DOI: 10.1126/sciadv.1603150.

[247] G. D. Mahan, *Many-Particle Physics*. Springer, 2000. DOI: 10.1007/978-1-4757-5714-9.

[248] H. Chu, C. J. Roh, J. O. Island, C. Li, S. Lee, J. Chen, J.-G. Park, A. F. Young, J. S. Lee, and D. Hsieh, "Linear Magnetoelectric Phase in Ultrathin MnPS3 Probed by Optical Second Harmonic Generation," *Phys. Rev. Lett.*, vol. 124, p. 027 601, 2 2020. DOI: 10.1103/PhysRevLett.124.027601. URL: https://link.aps.org/doi/10.1103/PhysRevLett.124.027601.

[249] D. Afanasiev, J. R. Hortensius, M. Matthiesen, *et al.*, "Controlling the anisotropy of a van der waals antiferromagnet with light," *Science Advances*, vol. 7, eabf3096, 23 2021, ISSN: 23752548. DOI: 10.1126/sciadv.abf3096.

[250] H. Hübener, U. De Giovannini, and A. Rubio, "Phonon Driven Floquet Matter," *Nano Letters*, vol. 18, no. 2, pp. 1535–1542, 2018, ISSN: 15306992. DOI: 10.1021/acs.nanolett.7b05391.

[251] S. Chaudhary, A. Haim, Y. Peng, and G. Refael, "Phonon-induced Floquet topological phases protected by space-time symmetries," *Physical Review Research*, vol. 2, no. 4, p. 043 431, 2020, ISSN: 2643-1564. DOI: 10.1103/physrevresearch.2.043431.

[252] F. Matsukura, Y. Tokura, and H. Ohno, "Control of magnetism by electric fields," *Nature Nanotechnology*, vol. 10, no. 3, pp. 209–220, 2015, ISSN: 17483395. DOI: 10.1038/nnano.2015.22.

[253] T. Kurumaji, S. Seki, S. Ishiwata, H. Murakawa, Y. Kaneko, and Y. Tokura, "Magnetoelectric responses induced by domain rearrangement and spin structural change in triangular-lattice helimagnets NiI_2 and CoI_2," *Physical Review B - Condensed Matter and Materials Physics*, vol. 87, no. 1, pp. 1–9, 2013, ISSN: 10980121. DOI: 10.1103/PhysRevB.87.014429.

[254] Y. Tokura, S. Seki, and N. Nagaosa, "Multiferroics of spin origin," *Reports on Progress in Physics*, vol. 77, no. 7, 2014, ISSN: 00344885. DOI: 10.1088/0034-4885/77/7/076501.

[255] A. Pimenov, A. A. Mukhin, V. Y. Ivanov, V. D. Travkin, A. M. Balbashov, and A. Loidl, "Possible evidence for electromagnons in multiferroic manganites," *Nature Physics*, vol. 2, no. 2, pp. 97–100, 2006, ISSN: 17452481. DOI: 10.1038/nphys212.

[256] P. Rovillain, M. Cazayous, Y. Gallais, A. Sacuto, M. A. Measson, and H. Sakata, "Magnetoelectric excitations in multiferroic $TbMnO_3$ by Raman scattering," *Physical Review B - Condensed Matter and Materials Physics*, vol. 81, no. 5, pp. 1–5, 2010. DOI: 10.1103/PhysRevB.81.054428.

[257] S. Kibayashi, Y. Takahashi, S. Seki, and Y. Tokura, "Magnetochiral dichroism resonant with electromagnons in a helimagnet," *Nature Communications*, vol. 5, pp. 1–7, 2014, ISSN: 20411723. DOI: 10.1038/ncomms5583.

[258] N. A. Spaldin and R. Ramesh, "Advances in magnetoelectric multiferroics," *Nature Materials*, vol. 18, no. 3, pp. 203–212, 2019, ISSN: 14764660. DOI: 10.1038/s41563-018-0275-2.

[259] S. Jiang, L. Li, Z. Wang, K. F. Mak, and J. Shan, "Controlling magnetism in 2d CrI_3 by electrostatic doping," *Nature Nanotechnology*, vol. 13, no. 7, pp. 549–553, 2018, ISSN: 17483395. DOI: 10.1038/s41565-018-0135-x.

[260] D. N. Astrov, "The magnetoelectric effect in antiferromagnetics," *Sov. Phys. – JETP*, vol. 11, p. 708, 1960. DOI: 10.1063/1.1728630.

[261] G. T. Rado and V. J. Folen, "Observation of the magnetically induced magnetoelectric effect and evidence for antiferromagnetic domains," *Physical Review Letters*, vol. 7, no. 8, pp. 310–311, Oct. 1961. DOI: 10.1103/PhysRevLett.7.310.

[262] R. E. Newnham, J. J. Kramer, W. A. Schulze, and L. E. Cross, "Magnetoferroelectricity in Cr_2BeO_4," *Journal of Applied Physics*, vol. 49, no. 12, pp. 6088–6091, Dec. 1978, ISSN: 0021-8979. DOI: 10.1063/1.324527.

[263] T. Kimura, T. Goto, H. Shintani, K. Ishizaka, T. Arima, and Y. Tokura, "Magnetic control of ferroelectric polarization," *Nature*, vol. 426, no. 6962, pp. 55–58, 2003, ISSN: 1476-4687. DOI: 10.1038/nature02018. (visited on 05/25/2021).

[264] M. A. McGuire, "Crystal and magnetic structures in layered, transition metal dihalides and trihalides," *Crystals*, vol. 7, no. 5, 2017, ISSN: 20734352. DOI: 10.3390/cryst7050121.

[265] K. F. Mak, J. Shan, and D. C. Ralph, "Probing and controlling magnetic states in 2d layered magnetic materials," *Nature Reviews Physics*, vol. 1, no. 11, pp. 646–661, 2019, ISSN: 25225820. DOI: 10.1038/s42254-019-0110-y.

[266] Y. Lai, Z. Song, Y. Wan, *et al.*, "Two-dimensional ferromagnetism and driven ferroelectricity in van der Waals $CuCrP_2S_6$," *Nanoscale*, vol. 11, pp. 5163–5170, 12 2019. DOI: 10.1039/C9NR00738E.

[267] A. S. Botana and M. R. Norman, "Electronic structure and magnetism of transition metal dihalides: Bulk to monolayer," *Physical Review Materials*, vol. 3, no. 4, p. 44 001, 2019, ISSN: 24759953. DOI: 10.1103/PhysRevMaterials.3.044001.

[268] D. Amoroso, P. Barone, and S. Picozzi, "Spontaneous skyrmionic lattice from anisotropic symmetric exchange in a Ni-halide monolayer," *Nature Communications*, vol. 11, no. 1, pp. 1–9, 2020, ISSN: 20411723. DOI: 10.1038/s41467-020-19535-w.

[269] I. Pollini, J. Thomas, and A. Lenselink, "Optical properties of layered transition-metal iodides," *Physical Review B*, vol. 30, no. 4, pp. 2140–2148, 1984, ISSN: 01631829. DOI: 10.1103/PhysRevB.30.2140.

[270] H. Ju, Y. Lee, K.-T. Kim, I. H. Choi, C. J. Roh, S. Son, P. Park, J. H. Kim, T. S. Jung, J. H. Kim, *et al.*, "Possible persistence of multiferroic order down to bilayer limit of van der Waals material NiI_2," *Nano Letters*, 2021. DOI: 10.1021/acs.nanolett.1c01095.

[271] T. Kurumaji, "Spiral spin structures and skyrmions in multiferroics," *Physical Sciences Reviews*, vol. 5, 1 Jan. 2020, ISSN: 2365659X. DOI: 10.1515/psr-2019-0016.

[272] J. M. Friedt, J. P. Sanchez, and G. K. Shenoy, "Electronic and magnetic properties of metal diiodides MI_2 (M=V, Cr, Mn, Fe, Co, Ni, and Cd) from ^{129}I Mössbauer spectroscopy," *Journal of Chemical Physics*, vol. 65, no. 12, pp. 5093–5102, 1976, ISSN: 00219606. DOI: 10.1063/1.433072.

[273] S. Kuindersma, J. Sanchez, and C. Haas, "Magnetic and structural investigations on NiI_2 and CoI_2," *Physica B+C*, vol. 111, no. 2, pp. 231–248, 1981, ISSN: 0378-4363. DOI: 10.1016/0378-4363(81)90100-5.

[274] H. Liu, X. Wang, J. Wu, Y. Chen, J. Wan, R. Wen, J. Yang, Y. Liu, Z. Song, and L. Xie, "Vapor deposition of magnetic van der Waals NiI_2 crystals," *ACS Nano*, vol. 14, no. 8, pp. 10 544–10 551, 2020, ISSN: 1936086X. DOI: 10.1021/acsnano.0c04499.

[275] S. R. Kumdersma, P. R. Boudewijn, and C. Haas, "Near infrared d-d transitions of NiI_2, CdI_2:Ni^{2+}, and CoI_2," *Phys. Stat.Sol. (b)*, vol. 108, pp. 187–194, 1981. DOI: 10.1002/pssb.2221080122.

[276] P. Zomer, M. Guimarães, J. Brant, N. Tombros, and B. Van Wees, "Fast pick up technique for high quality heterostructures of bilayer graphene and hexagonal boron nitride," *Applied Physics Letters*, vol. 105, no. 1, p. 013 101, 2014. DOI: 10.1063/1.4886096.

[277] J. Xiao, H. Zhu, Y. Wang, *et al.*, "Intrinsic two-dimensional ferroelectricity with dipole locking," *Physical Review Letters*, vol. 120, no. 22, p. 227 601, 2018, ISSN: 10797114. DOI: 10.1103/PhysRevLett.120.227601.

[278] A. Pimenov, A. Shuvaev, A. Loidl, F. Schrettle, A. A. Mukhin, V. D. Travkin, V. Y. Ivanov, and A. M. Balbashov, "Magnetic and magnetoelectric excitations in $TbMnO_3$," *Physical Review Letters*, vol. 102, 10 Mar. 2009, ISSN: 00319007. DOI: 10.1103/PhysRevLett.102.107203.

[279] D. R. Klein, D. MacNeill, Q. Song, *et al.*, "Enhancement of interlayer exchange in an ultrathin two-dimensional magnet," *Nature Physics*, vol. 15, pp. 1255–1260, 12 Dec. 2019, ISSN: 17452481. DOI: 10.1038/s41567-019-0651-0.

[280] D. T. Larson and E. Kaxiras, "Raman spectrum of CrI_3: An ab initio study," *Physical Review B*, vol. 98, 8 Aug. 2018, ISSN: 24699969. DOI: 10.1103/PhysRevB.98.085406.

[281] J. Cenker, B. Huang, N. Suri, *et al.*, "Direct observation of two-dimensional magnons in atomically thin CrI_3," *Nature Physics*, vol. 17, no. 1, pp. 20–25, 2021, ISSN: 17452481. DOI: 10.1038/s41567-020-0999-1.

[282] W. Jin, H. H. Kim, Z. Ye, *et al.*, "Raman fingerprint of two terahertz spin wave branches in a two-dimensional honeycomb Ising ferromagnet," *Nature Communications*, vol. 9, no. 1, pp. 1–7, 2018, ISSN: 20411723. DOI: 10.1038/s41467-018-07547-6.

[283] Y. Deng, Y. Yu, Y. Song, *et al.*, "Gate-tunable room-temperature ferromagnetism in two-dimensional Fe_3GeTe_2," *Nature*, vol. 563, no. 7729, pp. 94–99, 2018, ISSN: 14764687. DOI: 10.1038/s41586-018-0626-9.

[284] N. Sivadas, S. Okamoto, X. Xu, C. J. Fennie, and D. Xiao, "Stacking-dependent magnetism in bilayer CrI_3," *Nano Letters*, vol. 18, no. 12, pp. 7658–7664, 2018. DOI: 10.1021/acs.nanolett.8b03321.

[285] M. Akram, H. LaBollita, D. Dey, J. Kapeghian, O. Erten, and A. S. Botana, "Moiré skyrmions and chiral magnetic phases in twisted CrX_3 (X = I, Br, and Cl) bilayers," *Nano Letters*, vol. 21, no. 15, pp. 6633–6639, 2021. DOI: 10.1021/acs.nanolett.1c02096.

[286] T. P. T. Nguyen, K. Yamauchi, T. Oguchi, D. Amoroso, and S. Picozzi, "Electric-field tuning of the magnetic properties of bilayer VI_3: A first-principles study," *Phys. Rev. B*, vol. 104, p. 014 414, 1 Aug. 2021. DOI: 10.1103/PhysRevB.104.014414.

[287] H. J. Xiang, E. J. Kan, Y. Zhang, M.-H. Whangbo, and X. G. Gong, "General theory for the ferroelectric polarization induced by spin-spiral order," *Phys. Rev. Lett.*, vol. 107, p. 157 202, 15 Oct. 2011. DOI: 10.1103/PhysRevLett.107.157202.

[288] T. B. Prayitno, "Controlling phase transition in monolayer metal diiodides XI_2 (X: Fe, Co, and Ni) by carrier doping," *Journal of Physics: Condensed Matter*, vol. 33, p. 335 803, Jun. 2021, ISSN: 0953-8984. DOI: 10.1088/1361-648X/ac0937.

[289] A. Narayan, A. Cano, A. V. Balatsky, and N. A. Spaldin, "Multiferroic quantum criticality," *Nature Materials*, vol. 18, no. 3, pp. 223–228, Mar. 2019, ISSN: 1476-4660. DOI: 10.1038/s41563-018-0255-6. (visited on 05/25/2021).